Shear and Flexural Behavior of Prefabricated Hybrid Steel Joist Girders Supporting FRC Slabs

A Thesis Submitted to the Department of Civil Engineering in the University of Babylon in Partial Fulfillment of the Requirements for The Degree of Doctor of Philosophy in Engineering/Civil Engineering/ Structural

Republic of Iraq
Ministry of Higher Education
and Scientific Research
University of Babylon
College of Engineering
Department of Civil Engineering

Shear and Flexural Behavior of Prefabricated Hybrid Steel Joist Girders Supporting FRC Slabs

A Thesis Submitted to the Department of Civil Engineering in the University of Babylon in Partial Fulfillment of the Requirements for The Degree of Doctor of Philosophy in Structural Engineering

By

Jenan Neama Yaser Almusawi

(B.Sc. Civil Engineering, University of Kufa, 1998)
(M.Sc. Structural Engineering, University of Kufa, 2002)

Supervised By

Prof. Dr. Haitham Hasan Muteb Aldaami

June 2022 Dhul Hijjah 1443

Acknowledgments

In the name of Allah, the most gracious, the most merciful Praise be to Allah, who has granted me the syncretizing and enabled me to perform this thesis.

I would like to seize this opportunity to express my sincere thanks to my supervisors, Professor Dr. Haitham H. Muteb, for reviewing my thesis and guidance throughout the course of the project. I had the honor of being under his guidance and supervision.

My eternal cheerleaders, my mother and my father whom were always keen to know what I am doing and how I am proceeding in detail, until this significant moment is reached.

I am very grateful to my husband Dr. Bashar H. Alyasery who supported me and encouraged me at every step, and no description can represent his distinguished efforts.

I would like to provide the gratitude to the staffs whom assistant me in engineering collage of university of Babylon and also in the faculty of engineering in Kufa University, especially the staff of the laboratories of Civil Engineering and laboratories of Engineering Consulting Bureau at the Kufa University, and the staff of the Company for Inspection and Engineering Rehabilitation/ ministry of industrial and minerals of Iraq in Baghdad, also to Al-Nawafith Company for producing sand and gravel filters.

I would also like to thank my family to whom I owe gratitude and appreciation that could never be repaid. Thank you for all the sacrifices you have made, and for the support, you have constantly given.

Finally, a special thanks I would awarded for all who helped me in the experimental tests.

Great Thanks for All

Jenan N. Yaser Almusawi

2022

ABSTRACT

The experimental program of the present study consisted of fabricating and testing two groups of specimens; all specimens were tested under monotonic load. The first group consisted of ten hybrid open web steel joists (HOWSJs) specimens; each pair of this specimens had the same cross-section and had three variables. The first variable was the shape of the cross-section of the joist, the second variable was the span to depth ratio of steel joists, and the third variable was the effect of the diameter of interior web members on the shear, flexural and lateral torsional buckling behavior of the HOWSJs.

The second group consists of seven composite open web steel joists (COWSJs) specimens. Three specimens were tested with different cross-section shapes of HOWSJs, to study the effect of the shape of the cross-section on the behavior of the composite open web steel joist. While four specimens were had the same cross-section of the HOWSJ but at the same time, many variables were investigated when testing these specimens. These variables were the effective width of the concrete slab deck, the span to depth ratio of HOWSJs, and the type of the concrete slab; where two types of concrete were used in this study to cast the deck, which were a steel fiber reinforced concrete (SFRC) and non fibrous concrete (NC).

In this study, a new type of shear connector was used, so a push-out test was performed to determine the shear strength and stiffness of the shear connectors embedded in both non fibrous concrete and steel fiber reinforced concrete. The shear resistance experimental results for this type of shear stud were compared with some standard design codes, and the results showed that these equations could be used to calculate the shear resistance of shear studs for both NC and SFRC.

The experimental results of the HOWSJs showed that the length to depth ratio (L/D) affected the analysis behavior of the joists. Therefore, Thus, when the L/D decreased, the improvement of the ultimate capacity was very slight, about 1.81 %; this slight increase was in the case of using the same bar diameter for the interior web used in prefabricated joists with L/D of 5.1 and joists with L/D of 3.6; but, when the interior web's bar diameter was increased by about (24.48 %), which led to a decrease in the slenderness ratio of the diagonal interior web members for HOWSJ, the increasing in the ultimate capacity of became about 25.7% and the deflection decreased by about 11.3%. Also, the shape of the cross-section of HOWSJ had a considerable effect on the behavior of the steel joist, where for the HOWSJ, which was fabricated by welding the angles of the top and bottom chord back to back, the ultimate capacity was increased almost (7.4%) and (14.5%) when compared with specimens which fabricated by welding the angles of chord either face to face

without gap or face to face with a gap, while the ductility index of the HOWSJ specimens which had face to face with gap cross-section was 1.52 and 1.35 times the ductility index of the HOWSJ specimens which had back to back and face to face without gap cross-section shape, respectively.

The lateral-torsional buckling experimental and theoretical investigation showed that the specimens which had face-to-face with gap cross-section were more stable against the lateral deformations than the other two cross-sections, where they have had a rotation and lateral deflection less than specimens with a cross-section of back to back welded angles by about (25.1%) and (30.7%), respectively. Also, they had a rotation and lateral deflection less than of specimens with a cross-section of face to face without gap welded angles by about (7.3%) and (11.2%), respectively.

Regarding the composite open web steel joists group, the experimental work results showed that using SFRC to cast the slab improved slightly composite steel joists' strength, stiffness, and ductility compared with using NC slab. On the other hand, increasing the span/depth ratio of HOWSJ for the two types of concrete slab has normalized deflections that are approximately (31%) greater than COWSJs with a lower L/D ratio. While decreasing the span/depth ratio improves the ultimate load capacity just about (3.66%) and (4.31%) for the NC and SFRC slabs, respectively.

Using the deck slab of SFRC in the COWSJ specimens for the three cross-sections shapes of HOWSJ used in this study was enhanced the ultimate load capacity, stiffness, toughness and improved the stability of interior web members and chords, within a reasonable ductility comparing with the results of HOWSJ specimens.

Finally, a finite element analysis was performed by ABAQUS program software to simulate the experimental program carried out in the present study. It was found that there was a good convergence between the experimental and ABAQUS results, where the highest difference in the ultimate flexural capacity was less than (8%) and (9.5%) for the HOWSJs and the COWSJs, respectively. While the largest difference in the deflection at the ultimate load did not exceed (10.72%) for both groups. The differences in rotation deformation and lateral deflection of the HOWSJs were less than (9%) and (6%), respectively.

TABLE OF CONTENTS

LIST OF TABLES

LIST OF FIGURES

LIST OF SYMBOLS

A_b: Cross-sectional area of the bottom chord, mm^2.

A_n: Net cross-sectional area of the joist bottom chord, mm^2.

A_{stud}: Stud's cross-sectional area, mm^2.

a: Depth of compressive block, mm.

b_e: Effective width of concrete slab over the composite joist, mm.

$b^{'}$: Length of the angle's leg, mm.

C_w: Warping constant of HOWSJ, mm^6.

d_b: Dimeter of the interioe web members, mm.

d_{stud}: Shear stud diameter, mm.

d_e: Vertical distance from the centroid of composite joist bottom chord to the centroid of resistance of the concrete in compression, mm.

d_j: Out-to-out depth of joist, mm.

E_c, E_cm: Concrete modulus of elasticity, MPa.

E_s : Modulus of elasticity of steel, MPa.

E_{Iy} : Lateral bending stiffness, $N.mm^2$.

$f_c^{\prime}$: Concrete's cylinder compressive strength, MPa.

f_{ck}: Concrete's cube compressive strength, MPa.

F_{ub}: Ultimate tensile strength of bottom chord, MPa.

F_{yb}: Specified minimum yield stress of the bottom chord, MPa.

F_{ustud}: Stud's ultimate tensile strength, MPa.

G_s: Shear modulus of elasticity of steel, MPa.

G_C: Shear modulus of elasticity of concrete, MPa.

GJ: Torsional rigidity, $N.mm^2$.

h: Depth of the HOWSJ, mm.

h_s: Distance between u_{uf} and u_{lf}, mm.

h_{stud}: Height of the shear stud, mm.

I: Moment of inertia, mm^4.

J: Saint-Venant torsional constant, mm^4.

L: Length of HOWSJ specimen, mm.

L_{db}: Length of diagonal interior web members, mm.

L_{vb}: Length of vertical interior web members, mm.

M_{cr}: Critical lateral torsional buckling moment, $N.mm$.

N: Number of shear connectors between mid-span and support.

NC: Non fibrous concrete.

P: Aplied load to the HOWSJ specimen, C.

P_{cr}: Static critical lateral torsional buckling load, mm.

SFC: Steel fiber concrete.

t_c: Minimum thickness of the concrete slab above the top of the metal deck, (mm).

$t^{'}$: Thickness of the angle's leg, mm.

u: Lateral deflection of the HOWSJ, mm.

u_{uf}: Measured lateral displacement of the top chord flange of HOWSJ, mm.

u_{lf}: Measured lateral displacement of the bottom chord flange of HOWSJ, mm.

u_w: Lateral deflection of one of the chord flanges due to warping, mm.

y': Vertical distance to centroidal axis of bottom chord measured from the bottom of the bottom chord, mm.

ϵ: Strain gauge reading.

ϕ: Angle of twist (or rotation) of HOWSJ, $degree$.

ν: Poisson's ratio.

CHAPTER 1

INTRODUCTION

1.1 General

Composite construction is when more than one material is used in one structural element to resist loads. Each different building material has a special prominent quality which distinguished it from other materials and there is no single material that can provide all the structural requirements. This is the reason of using different materials that can be arranged in an optimum geometric configuration, with the aim that only the desirable property of each material will be utilized by virtue of its designated position. Famous example is reinforced concrete, which has internal composite action between the concrete and the reinforcing bars. Another example in bridges, steel girders is used to support the concrete deck, which can be called external composite action.

The advantage of using composite steel-concrete structures is to get high stiffness allowing for smaller section sizes. This leads to weight reduction, lower deflection, and to span large distances compared to the contribution of their components acting separately [1] .

Composite beams offer several advantages over non-composite sections. Since the load is carried jointly by the concrete slab and the steel stem. The size of the steel section is smaller than otherwise would be required. This reduces the overall height of the building and the steel tonnage required, thus resulting in a direct cost reduction. A composite beam is also stiffer than a non-composite beam of the same size and thus experiences less deflection and floor vibrations [2].

Composite flooring also has a larger moment capacity and the metal decking in composite flooring acts as form-work for concrete decreases construction times. When used properly, composite construction will result in reduced building costs.

Therefore, composite steel-concrete structures are used widely in modern bridge and building construction. Composite construction simply aims to make both materials perform better together, or to strengthen the weaknesses of each material.

The challenge is to ensure that forces are transmitted effectively and safely between the two materials and there is full strain compatibility (composite action) at the interfaces, which means one neutral axis (better if within the concrete slab) allowing the concrete to take all the compression forces, while the steel bottom chord takes almost all the tension forces as shown in Figure 1.1 [3]. Without composite action, there is no strain compatibility at the interface between the two materials, two neutral axes, causing the steel and concrete to operate under both compression and tension, which leads to a smaller yielding/buckling load. The first forms of composite structures incorporated the use of steel and concrete for flexural members, and the issue of longitudinal slip between these elements was identified by Moore [4].

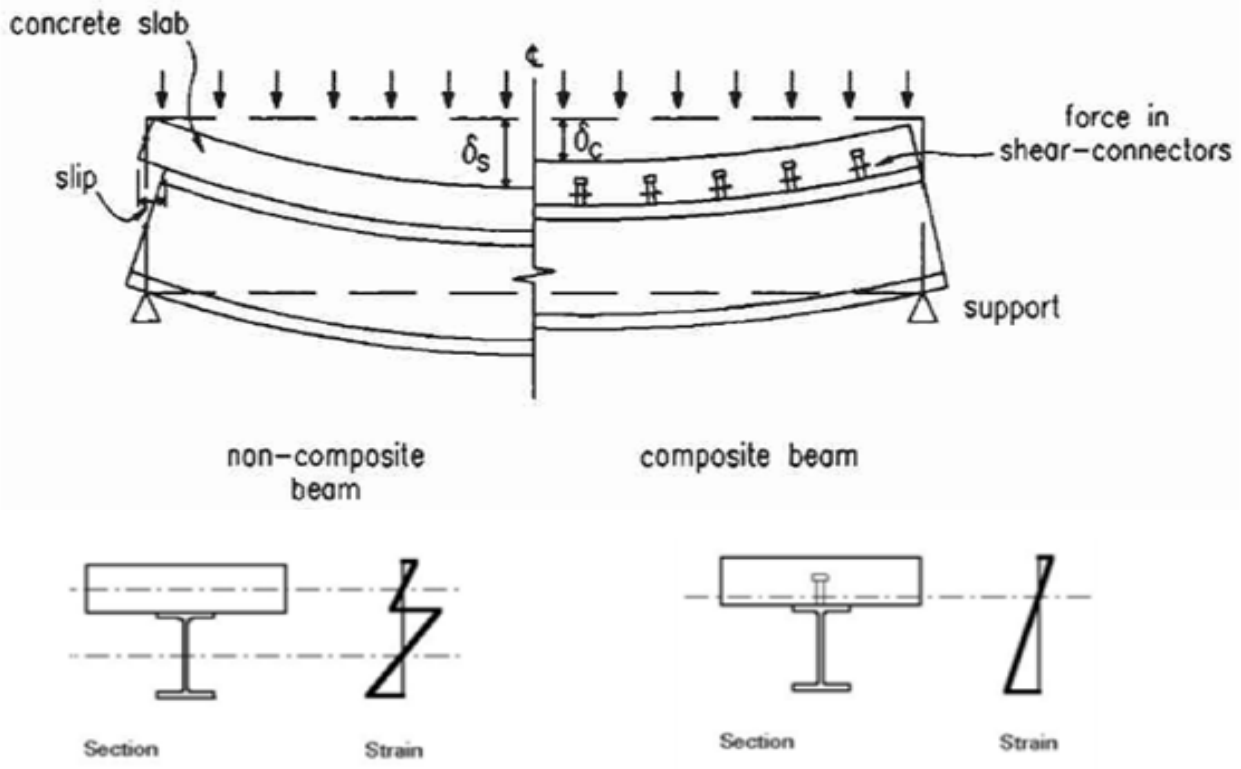

Figure 1.1 Non-composite vs. composite- neutral axis [3].

Nowadays, the construction community is looking for the best way to achieve composite action between steel and concrete in terms of reducing the installation time, higher safety level for workers, and lowest cost.

Composite steel construction is considered also as one of the most economical systems for constructing building floors. Composite floor systems typically involve structural steel beams, open-web steel joist, girders, or trusses with shear connectors supporting a concrete slab, forming an effective T-beam flexural member resisting primarily gravity loads [5].

1.2 Open Web Steel Joists (OWSJs)

Open Web Steel Joists (OWSJ) defines as steel trusses of relatively low mass with parallel or slightly pitched chords and triangulated web systems proportioned to span between walls, structural supporting members, or both, and to provide direct support for floor or roof decks. Specifically, joists can be designed to provide lateral support to compression elements of beams or columns, to participate in lateral-load-resisting systems, or as continuous joists, cantilevered joists, or joists having special support conditions. The advantages of OWSJ include enlarged effective depths with minimal increases in material as oppose to W-shape beams of similar depths, making them very efficient. The effective depth of an OWSJ is the distance between the centroid of the top and bottom chords. Due to the slim cross section of the top cord of OWSJ, it is highly desirable not only to ensure composite action, but also to ensure that the top cord is subjected to tension, and the N.A. lies in the concrete flange. Furthermore, Open-Web steel joists shall be designed for loads acting in the plane of the joist applied to the top chord assume to be prevented from lateral buckling by the deck.

Open web steel joists are proven they are standing strength to weight ratio, flexible and adaptable design characteristics, amazing durability, and economic advantages. (OWSJs) are marketable and readability simple internet steel product,

and its consists of five components, Figure 1.2 [6].

• The top chord

• The bottom chord

• The end web

• Bearing seat, and

• The interior web member or called (web members).

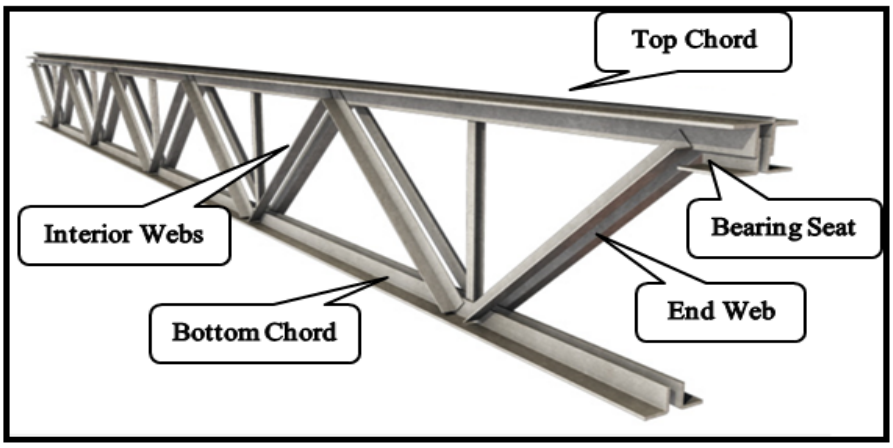

Figure 1.2 Open web steel joist.

In the other hand,these components are cut, bent, assembled and welded together to create an engineering product far superior in weight and cost to the monolithically parts. (OWSJs) are manufactured using hot rolled or cold formed steel. There are two categories of open web products :

1. Primary members are called joist girders, which are used to support a concentrated load applied by the secondary members (steel joist),and are supported by columns or other vertical structural elements. Like the joist there are significant weight and cost advantages for joist girders when compare to solid web wide flange beams.

2. Secondary members are called joists, which known by various names including (long spans, bar joist, or open web joists). Secondary members which are

horizontally sloped are used for direct support of floor and roof decks, all joists are considered secondary structural products in the primary structural members such as joist girders, steel columns and concrete or masonry walls.

There are various kinds of steel joist products are available for different engineering and construction applications:
A- The most basic product is bar joist k-series or short span k-series joist has over one hundred standardized designation.
B- Long span (LH) series and deep long span (DLH) series can manufactured with parallel, single pitched or double pitched chord.

1.3 Types of Open Web Steel Joists

Joists are supported at their ends which called the bearing point and under slung condition is when the bearing point is at the top chord. A square end condition is when the bearing point is at the bottom chord.

The top and bottom chords may be parallel or the top chord may be pitch to sloped, the pitch comes in two forms the top chord may be pitched two ways. Behind these elements produces six types of joists [6], Figure 1.3.
1- Parallel chords under slung,
2- Parallel chords square ends,
3- Top chord pitched one-way, under slung,
4- Top chord pitched one-way, square ends,
5- Top chord pitched two-way under slung, and
6- Top chord pitched two-way square ends.

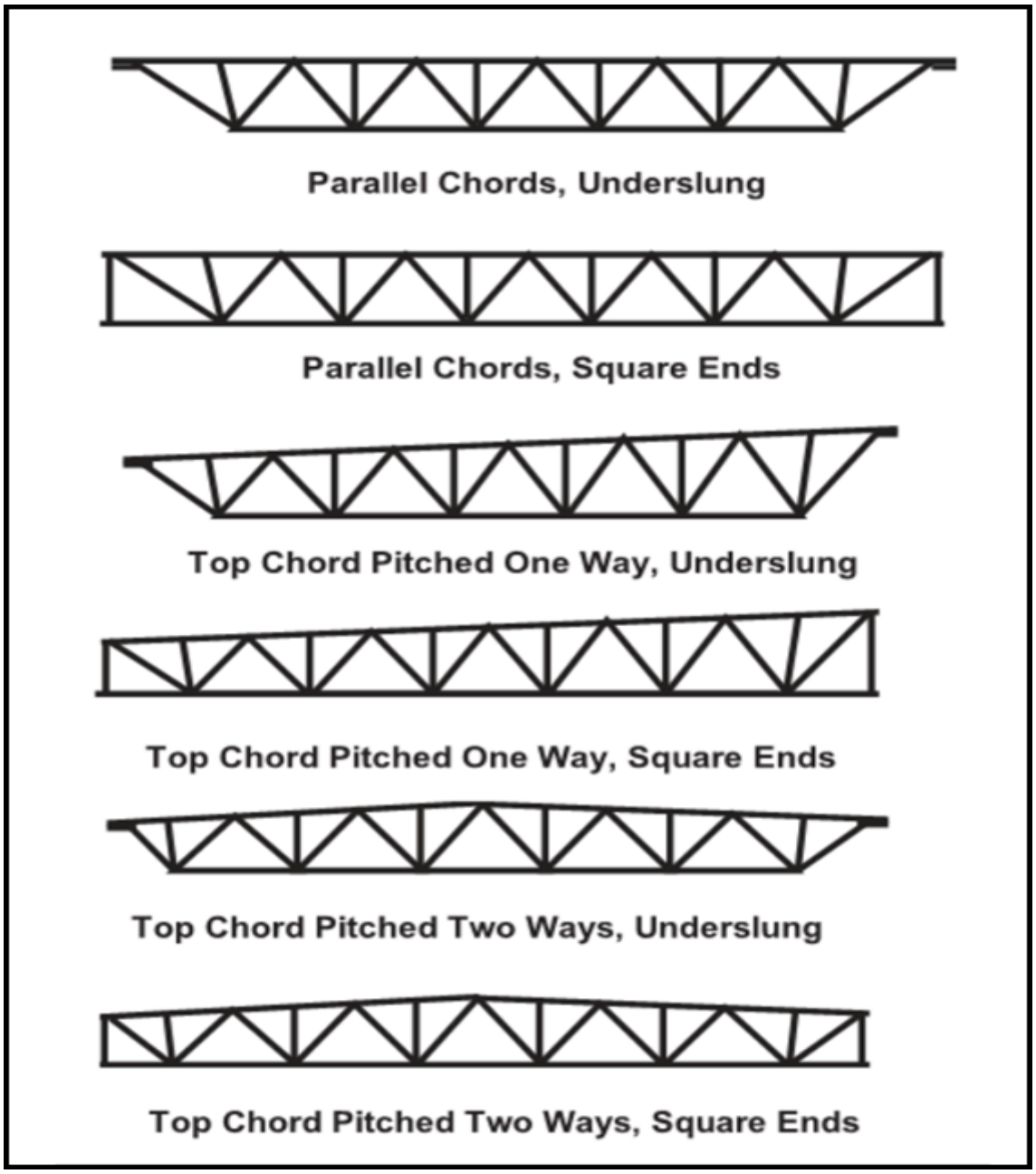

Figure 1.3 Types of open web steel joists.

1.4 Composite Concrete Steel Joists

The open web composite steel or composite joist CJ-series with parallel chords are capable of supporting large floor or roof, because the concrete slab is attached at the top chord and this create a composite action between the steel joist and the concrete slab. The shear connection between concrete and the joist is made by the welding shear stud through the steel deck to the underline CJ-series composite

steel joist. In typical steel frame construction, joist girders bear and columns steel are supported by the joist girders then the steel deck covered the steel joist and roofing or flooring material is placed for finishing the surface, Figure 1.4.

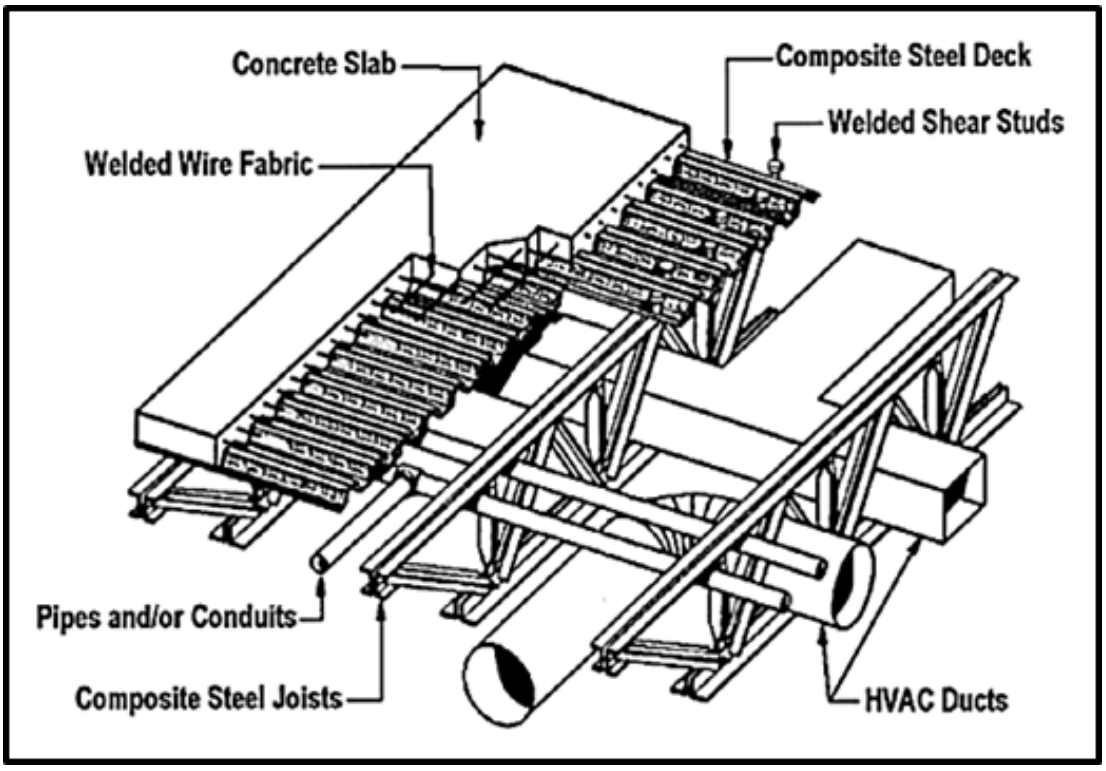

Figure 1.4 Composite joist system [3].

The steel joist institute (SJI) first published standard specification and load table in 1932. Since 1978 (SJI) regularly produces several publication, the main one is standards specifications load tables and weight tables for steel joists and joist girders. There are different economic advantages in using steel joist and joist girders.

• The cost and strength characteristic of steel is well documented.

• An engineering steel joist products are lighter than compared of monolithic products like I-beams and that's cost less.

• Because steel joist are made from of 90% recycled steel they have a much lower carbon formant and consequently are better for an environment as a whole.

• Standardization is another key advantage whereas all of the specification and load table requirements is recording for any specified joist, the allowable deflection,

camper, paint and another items are also listed as standards in the specifications.

• Another key advantage of using steel joists and joist girders is there open web construction, this allows ready passage and consent of the pipes, electric conducts and ducts of all sizes by running these materials through the open web of the joist, saving in floor height achieved thereby reducing the overall height and cost of the building, Figure 1.4.

• Joists are also easily erected, they are reliability light in weight and can be erected quickly under almost any weather condition.

• Flexibility is another advantage and like any other products, steel joist products are standardized in a wide selection of depths ranging from 8 to 120 inches and spans from 8 to 144 feet with varying in load conditions.

• With their unities construction they eliminate a need for job side assembly, preparations, forming, stripping, and the like.

• They provide an immediately available working plate from as soon as the joists are probable erected, bridged and welded in the place.

With this performance record and almost and unlimited ability of the joist manufacturers to design and manufactures these products steel joist are libraries, churches, museums, malls, industrial and manufacturing buildings, sport complexes, gymnasiums. Figure 1.5 shows an examples of building constructed by using open web steel girders [7].

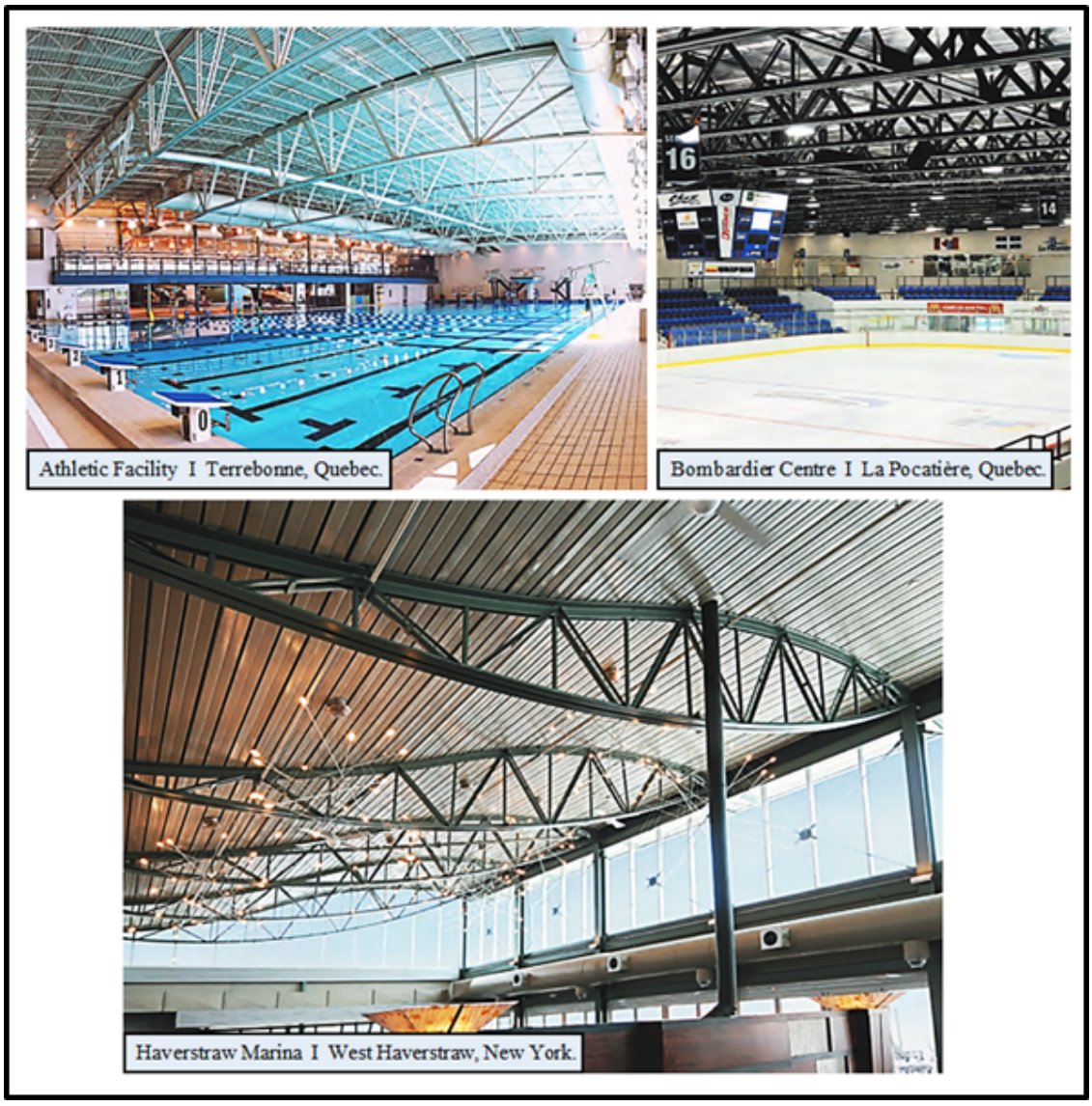

Figure 1.5 Different shapes of OWSJ girders [7].

1.5 Design Specification of Composite Steel Joist

The Steel Joist Institute (SJI)[6] published the first design specification of composite open web steel joists in 1928. The specification assumed that [8]:

• Top chord designed for compressive forces from non-composite dead load plus construction live load followed by a total composite load case check.

• Bottom chord designed for tension forces from composite dead and live loads.

• Webs designed to carry total vertical shear.

• Shear connectors applied to fully develop the bottom chord yield strength.

• Concrete slab analyzed using the transformed area concept.

• Deflection under composite loads analyzed using composite moment of inertia.

The distance, d_e (mm) between the centroid of the tension bottom chord and the centroid of the concrete compression block, shall be computed using a concrete stress of $0.85f'_c$ and an effective concrete width, b_e (mm) as shown in Figure 1.6.

$$d_e = d_j - y' + h_{deck} + t_c - \frac{a}{2} \tag{1.1}$$

$$a = \frac{M_n}{0.85f'_c b_e d_e} \leqslant t_c \tag{1.2}$$

where:

b_e : shall be taken as the sum of the effective widths for each side of the joist centerline, each of which shall be the lowest value of the following:

1. One-eighth of the joist span, center-to-center of supports;
2. One-half the distance to the centerline of the adjacent joist;
3. The distance to the edge of the slab.

$$M_u \leqslant \phi M_n \tag{1.3}$$

where:

ϕM_n: Minimum design flexural strength of composite section, (N.mm).

M_u: Required flexural strength determined from applied factored loads, (N.mm).

The design flexural strength of the composite section, ϕM_n shall be computed as the lowest value of the following limit states [8] :

a) Bottom Chord Tensile Yielding: $\phi_t = 0.9$

$$\phi M_n = \phi_t A_b F_{yb} d_e \tag{1.4}$$

b) Bottom Chord Tensile Rupture: $\phi_{tr} = 0.75$

$$\phi M_n = \phi_{tr} A_n F_{ub} d_e \tag{1.5}$$

c) Concrete Crushing: $\phi_{cc} = 0.85$

$$\phi M_n = \phi_{cc} 0.85 f'_c b_e t_c d_e \tag{1.6}$$

d) Shear Connector Strength: $\phi_{stud} = 0.9$

$$\phi M_n = \phi_{stud} N Q_n d_e \tag{1.7}$$

Where composite flexural strength is governed by the strength of shear connection as provided by Equation 1.7, the strength of shear connection, NQ_n, shall be no less than 50 percent of the bottom chord yield strength [6].

$$NQ_n \geqslant 0.5 A_b F_{yb} \tag{1.8}$$

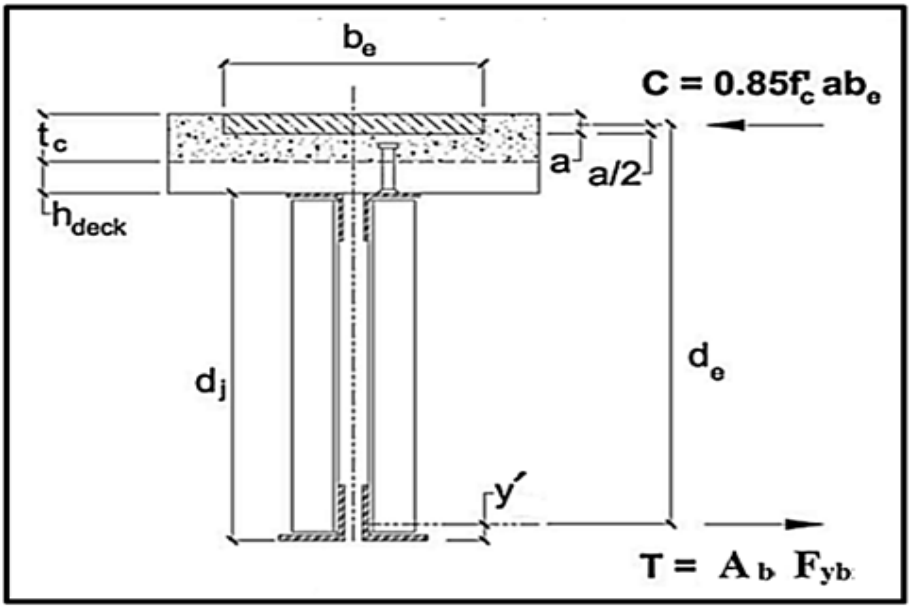

Figure 1.6 Composite steel joist flexural model [8].

1.6 Shear Connectors Designation and Placement

In comparison to non-composite action beams, the composite action increases the strength and stiffness of the girders. When steel joist and concrete deck floor is subjected to bending, the deck and joist tend to slip due to longitudinal shear at the interface, unless they are rigidly connected with shear connectors are used for this purpose, which creates strain compatibility behavior between the joist and deck, provided composite action. Composite action is achieved by connecting the steel girder to the concrete slab to permit transfer of horizontal shear force at the steel-concrete interface(Kwon, 2008) [9].

According to Standard specification for CJ-series composite steel joists [6], Shear studs, after installation, shall extend not less than (38 mm) above the top of the steel deck and there shall be at least (13 mm) of concrete cover above the top of the installed studs.

a) For studs in (38, 51, or 76) mm deep decks with ($d_{stud}/t_{topchord} \leqslant 2.7$):

$$Q_n = Min.[0.5A_{stud}\sqrt{f'_c E_c}, (R_p R_g A_{stud} F_{ustud}/1000)](kN) \tag{1.9}$$

b) For studs in (38, 51, or 76) mm deep decks with ($2.7 < (d_{stud}/t_{topchord}) \leqslant 3.0$):

$$Q_n = Min.[0.5A_{stud}\sqrt{f'_c E_c}, (R_p R_g A_{stud} F_{ustud}/1000) - 6.67(\frac{d_{stud}}{t_{topchord}} - 2.7)](kN) \tag{1.10}$$

Shear connectors required on each side of the point of maximum positive or negative bending moment, shall be distributed uniformly between that point and the adjacent points of zero moment, unless otherwise specified. However, the number of shear connectors placed between any concentrated load and the nearest point of zero moment shall be sufficient to develop the maximum moment required at the

concentrated load point [6].The transverse and longitudinal Shear Stud Spacing as recommended by SJI is shown in Figure 1.7 [8].

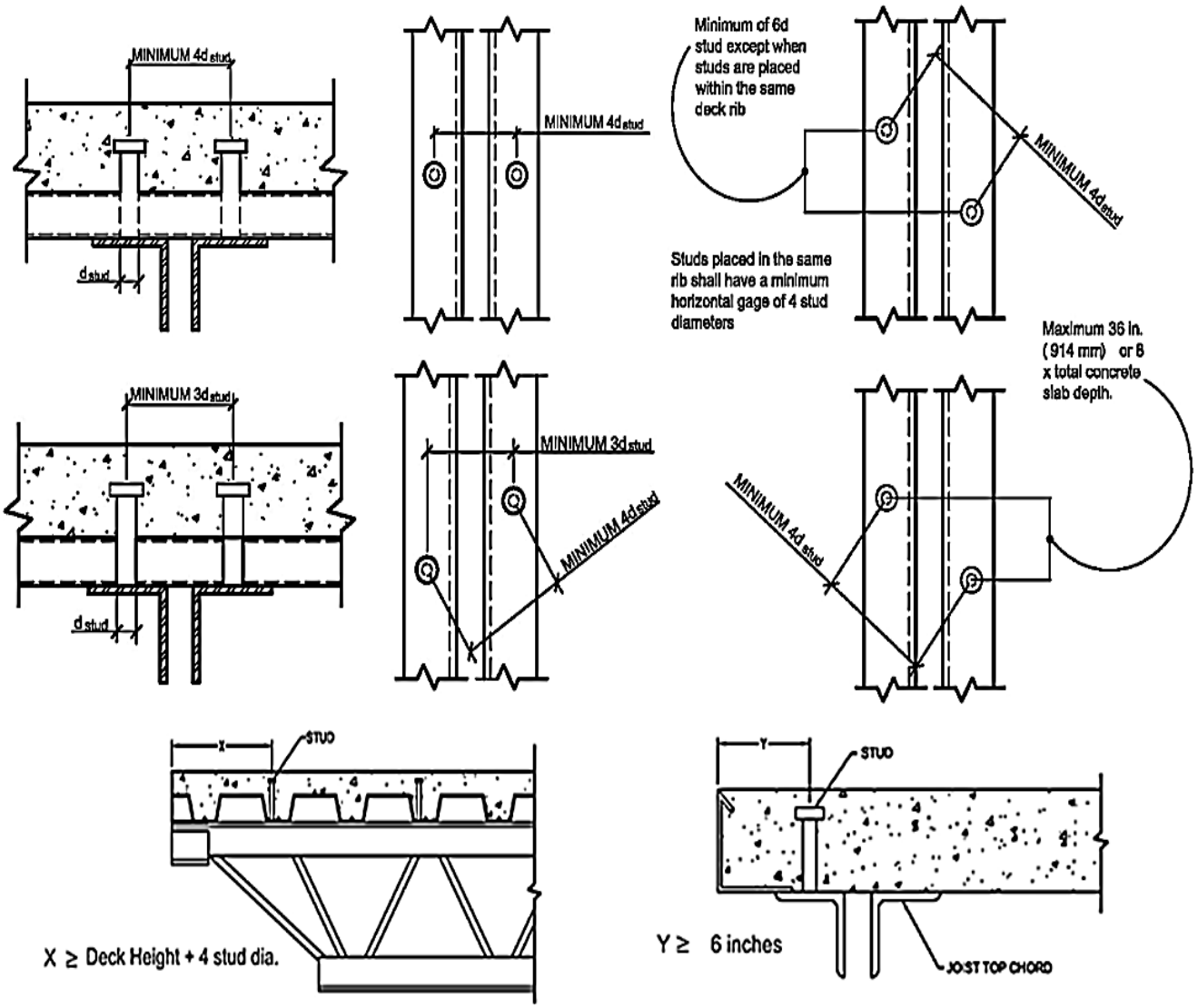

Figure 1.7 Distributions of the headed studs as recommended by SJI [8].

1.7 Bridging of Steel Joists

Bridging is a component of steel joists system, its purpose is to brace the joist against lateral displacement during erection and placing of construction load, whereas lateral displacement means the construction load causes the joist to destroy and roll over, this could result in the joist's falling. The number of rod of bridging is dependent on the length of the joist as well as the size of top and bottom chord,

and without bridging joist can easily turn over or loss their bearing. Once the construction load is applied to the joists the chord members tended displaced laterally, this could result in a serious accident.

Even if the joist is attached to a supporting members they can still fail, probe bridging solve this problem, the most common bridging material is angel, typical sizes range from (1×1 inch) to (2 1/2×2 1/2 inch), in special application even larger sizes may be used. There are many types of bridging as shown in Figure 1.8 such as cross, horizontal, erection, construction, permanent, and uplift bridging, and they should be anchorage to a fixed object such as a wall or beam [10].

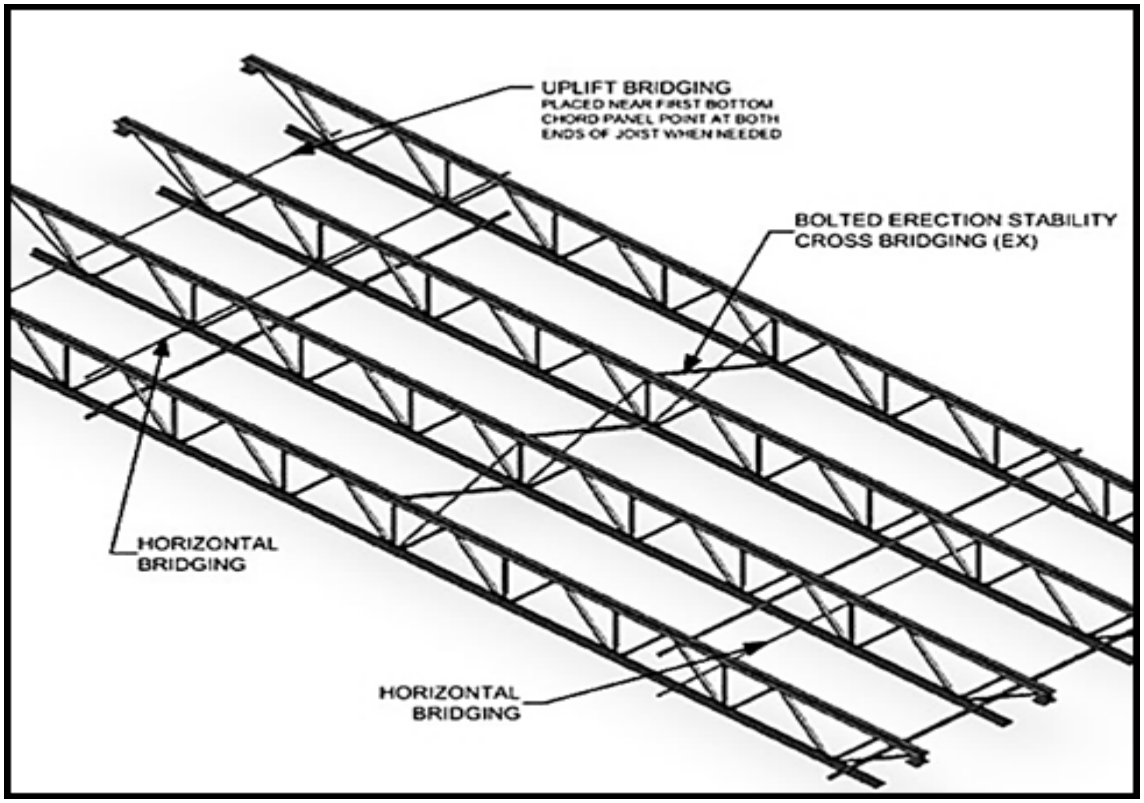

Figure 1.8 Types of bridging [10].

1.8 Fiber Reinforced Concrete (FRC)

Concrete is one of the most widely used construction material, it is strong under compression but weak in tension and it is brittle and have limited ductile behavior, therefore a form of reinforcement is needed for structure's stability. Discrete steel bars are used as a reinforcement in concrete structures but still there is possibility

of crack formation internally or externally and this way lead for the failure of the structures.

To increase the life of structures by increasing the fracture resistance of cementations materials, a multi-directional and closely spaced reinforcements which called fibers are frequently added, thus a composite material, fibers do not stop the cracks from forming but it keep the cracks small.

FRC is a concrete mix that contains short discrete fibers, they are uniformly distributed. Fibers give the concrete strength after cracking this is called toughness, the toughness and resistance to cycle and dynamic loads are increases (ACI 544.1R-1996) [11]. Also the toughness improving in compression brought by fibers is beneficial in prevention sudden and explosive failure under static loads and in assimilation of energy under dynamic loads (ACI 544.4R-1989) [12].

The fibers are classified into four types mainly such as [11].

1. Steel Fiber.
2. Glass Fiber.
3. Synthetic Fiber.
4. Natural Fiber.

Fiber strength, stiffness, and fiber's ability to bond with concrete are the basic fiber reinforcement characteristics. Bond is dependent on the aspect ratio of the fiber. Range for typical aspect ratios varies from about (20 to 100), while the length varies from (6.4 to 76 mm). Steel fibers have a relatively high resistance and modulus of elasticity as well as their bond with the mix can be enhanced by mechanical anchorage or surface roughness. Various steel fiber geometries are shown in Figure 1.9 [11].

The structural behavior of FRC in tension is:

• Delay and control in tensile cracking.

• By distribution of fibers, composite shows ductile behavior.

• Sharing of tensile stress.

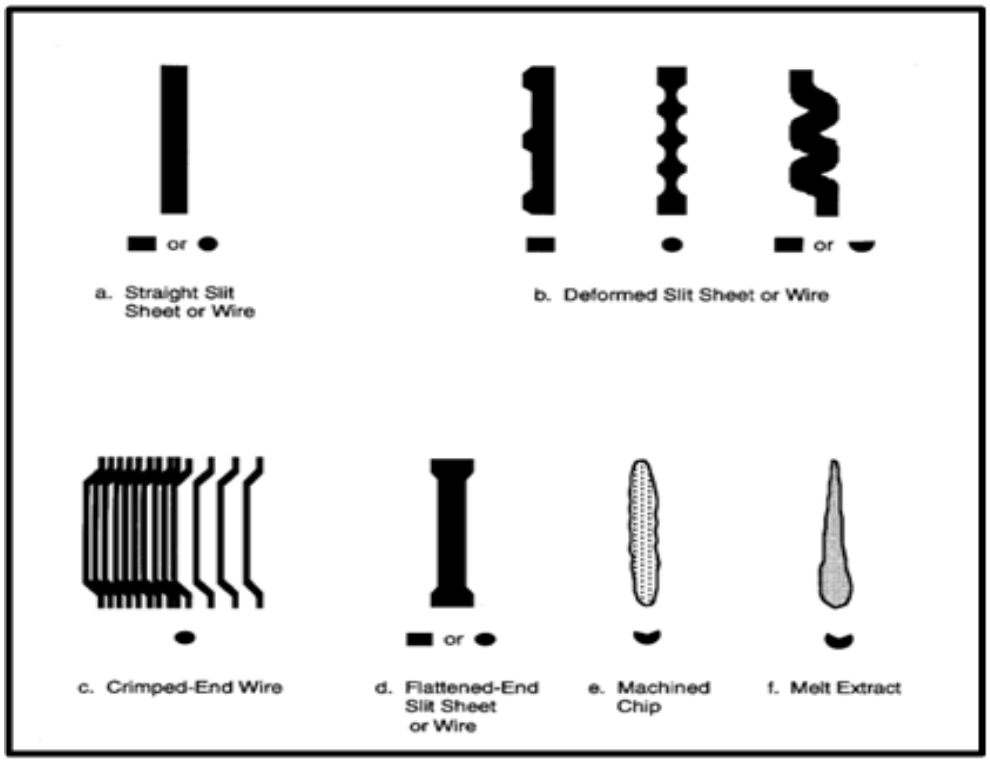

Figure 1.9 Various steel fiber geometries [11].

The structural behavior of FRC in compression is:

• 20% increase of compressive strength.

• Higher toughness: prevent failure in case of earth quick and blast type load.

There are different advantages in using FRC such that:

• Greater resistance to crack formation by bridging action of fibers, this increase durability, ductility, toughness, abrasion and shatter resistance of concrete; thus fibers increase the structural integrity.

• Flexural strength is improved up to 30% by decreasing the propagation of cracks.

• Increased moment capacity and torsional strength.

• An alternative way to reinforce concrete, thus fibers can reduce the quantity of rebars without loss of strength.

• Increase the resistance to impact load and also increase fire resistance.

• Less labour intensive than placing rebar.

• Can made into thin sheets and irregular shapes.

•FRC pavements offer good resistance.
•FRC slabs offer high strength while compared with conventional concrete slab.

Also, FRC has disadvantages such as:
• High cost of materials.
• Required more precise configuration than plain concrete.
• When quantity of fibers increased, the workability is decreased.
• If proper techniques and proportion are not used the fibers may also cause a finishing problem, with the fibers coming out of the concrete.

Table 1.1 shows the properties, advantages and disadvantages of each type of fibers. From this table it can be recognized that the most disadvantage of adding steel fiber in steel fiber reinforced concrete SFRC is the low workability and quickened stiffening of fresh concrete, which will increase the construction labor and time due to the higher vibrations needed to make SFRC functional. This problem can be partly overcome by the use of newly developed high-range super plasticizers which not only enhance operability of SFRC but also keep the mix flexibility for a longer time. Workability of SFRC is affected by volume fraction, fiber aspect ratio besides the consistency of plain concrete namely, where the workability decreases when fiber content increases, Endgington et al(1974)[13], as illustrate in Figure 1.10.

Also steel fibers have distinct advantages over other types of fibers due to their high-elastic modulus and a strong bond with the surrounding cementitious matrix. Steel fibers when added to concrete mix, get randomly distributed and act as crack arresters. Debonding and pulling out of fibers require more energy, thereby the toughness and resistance to dynamic and cyclic loads increases considerably [11].

SFRC is increasingly used day by day as a structural material due to the enhanced mechanical properties [14]. And ACI Committee 544 (ACI 544.4R-

Table 1.1 Summarized properties of types of fibers.

Type of Fiber	Properties	Advantages	Disadvantages
Steel Fiber	•Carbon steel fiber or stainless steel.	•High tensile and compressive strength.	•Reduction in workability.
	•Aspect ratio (l/d): (20-100).	•Reduction in quantity of rebars.	•Cost is high.
	•Length: (6.4-76) mm.	•Durable.	
	•Diameter: (0.25-0.75) mm.	•Provides tensile strength to concrete.	
	•Tensile strength: (275-2757) MPa.		
	•Young's modulus: (200000) MPa.		
Glass Fiber	•Length: (25-50) mm.	•Glass fiber are flexible.	•They has less ductility.
	•Diameter:(0.25-1) mm.	•High tensile strength.	•The cost of GFRC is higher than traditional concrete.
	•Tensile strength: (1034-3792) MPa.	•They don't corrode.	•GFRC is difficult to self-mix.
	•Young's modulus: (69000) MPa.	•Resistance to the thermal shock.	
	•Ultimate elongation: (1.5-3.5)%.	•Partial conductor of light.	
		•Used as a raw material of "transparent	
Synthetic Fiber	•Aramid, Carbon, Polypropylene, etc.	•Cheap and abundantly available.	•Low modulus of elasticity.
	•Diameter range: (0.25-0.75) mm.	•High chemical resistance.	
	•Tensile strength: (551-827) MPa.	•Resistance to corrosion.	
	•Young's modulus: (3450-4140) MPa.	•High melting point.	
	•Ultimate elongation: (16 -25)%.		
Natural Fiber	•Coir, Bamboo, Jute are examples.	•High impact strength.	•They many undergo organic decay.
	•Locally available fibers.	•Low cost.	

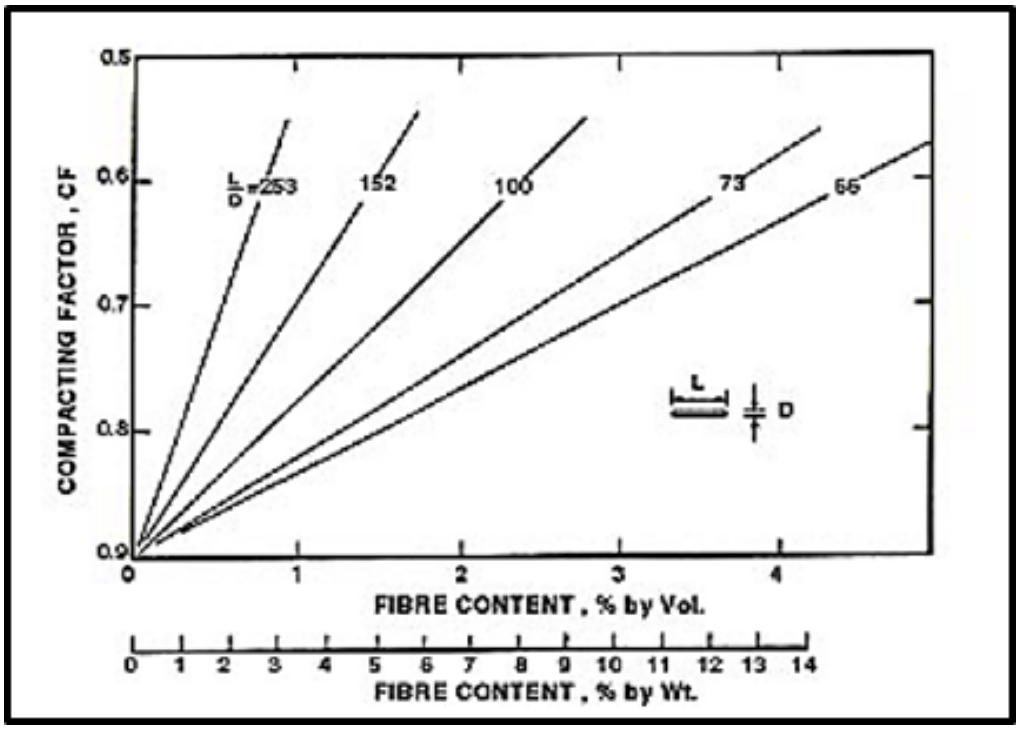

Figure 1.10 Effect of fiber aspect ratio on the workability [13].

1989)[12] had reported that the addition of steel fibers in concrete matrix improves mechanical properties of concrete such as flexural strength, tensile strength, compressive strength, toughness and energy absorption capacity at post-peak load. Steel fiber reinforced concrete has gained acceptance for a variety of applications, namely, industrial floors, bridge decks, pavement and overlays, hydraulic and marine structures, precast elements, tunnel linings, nuclear vessels, repair and rehabilitation works, blast resistance and penetration resistance structures.

Mixing of FRC needs careful precaution to avoid balling affect and segregation, whereas the increase in aspect ratio, volume percentage, and size of aggregate will increase the difficulties. This difficulty is usually overcome by slow, continuous uniform feeding of the fibers into the wet or dry mix.Suitable admixtures and vibrators is used for perfection, also mixing of fibers for large volume FRC can be easily done by the help of a machine.

1.9 Aims of the Study

Open web steel joists (OWSJs) are truss-type members which represent a smart load-bearing element because of their ability to transfer both tensile and compressive forces, and less material results not only in smaller costs but also in a lowered self-weight, where they are lighter than I-shaped steel profiles or as a channel. There are also many different advantages to using steel joist girders, such as the ability to transport the heating, ventilation, and air conditioning (HVAC) system, electrical wiring, and piping through their open path construction, and in addition, reducing vibration noticeability. The costs are lower because they can be made from recycled steel and are therefore better for the environment; from this advantage came the idea to conduct this study, in which different cross-sectional models were constructed using steel angles for the top and bottom chords and steel reinforcing bars for inner web elements to prefabricate a new product of hybrid open web steel joists (HOWSJs). Since these HOWSJs are a light structure, the result is a delicate stability structure in its various modes. An experimentally and numerically investigations were carried out in this study to determine this complex behavior. Three cross-sectional shapes of prefabricated steel joists were produced by welding two pairs of different configurations: back to back, face to face, and face to face with a gap. Generally, the increment in the depth of the steel joists could enlarge the web area but reduces web stability. Thereby, the interior web members' stability is essential in increasing the steel joists' strength capacity. Therefore, in this study, the effect of the diameter of the interior web members was also investigated. However, the HOWSJs will be improved their behavior when they are composited with a deck of non fibrous and steel fiber reinforced concrete. The main aims of this research were:

1- Investigating the behavior and the stability of new prefabricated hybrid open web steel joists (HOWSJs) in terms of ultimate strength, deflections, modes of failure, and strains under monotonic load.

2- Investigating the difference of the behavior between five groups were fabricated with different three shapes of cross section. Also studied the effect of span to the depth ratio, and the increased the diameter of interior web members on the behavior of HOWSJ .

3- Studying the lateral torsional behavior of prefabricated hybrid open web steel joists taking in consideration the change of cross section shape, span to the depth ratio, and the increase the diameter of interior web members.

4- Finding the optimum proportions to produce non fibrous concrete (NC) and steel fiber reinforced concrete (SFRC) of the deck slab of the composite section. Where mixtures of this study were proportioned using the specifications given in ACI-544.1R-96[11], and ACI 211.1-91 [15].

5- The experimental work includes manufacturing of new type of shear connectors which used in this study to achieve the composite action between the open web steel joist and concrete slab and finding the shear resistance for this type of shear connector by using the experimental push out test for (NC) and (SFRC).

6- Investigating the structural behavior of composite open web steel joists for three shapes of cross section of open web steel joist by using (SFRC) under monotonic loading in terms of ultimate strength, crack pattern, deflection, slip, and strains.

7- Examined the effect of the deck slab, which formed from (SFRC), to contribute with web for resisting the shear stress.

8- For one of three cross section shapes of open web steel joist the effect of type of concrete (NC) and (SFRC), span/depth ratio and width of concrete slab was studied on the carrying capacity of composite open web steel joists.

9- The prefabricated hybrid open web steel joists and composite open web steel joists, which had tested experimentally, will be analyzed numerically by using the software ABAQUS program, where the results were validated when compared with experimental results.

1.10 Layout of Thesis

The current thesis includes seven chapters, which are:

Chapter one: illustrate a general introduction to the open web steel joists and their properties, composite open web steel joists, fiber reinforced concrete, shear connectors designation and placement. The main aims of the current research are additionally incorporated into this chapter.

Chapter two: presents a comprehensive review of the previous experimental and theoretical studies concerning the behavior of composite open web steel joists, lateral torsional buckling of open web steel joists, fiber reinforced concrete, welding arc E6013 and push-out test.

Chapter three: this chapter presents all fabrication processes of composite open web steel joist, the material properties, the program of test and details of all specimens with the test method.

Chapter four: presents the results carried out experimentally, discussion and comparison of all tests. These tests were mechanical properties of materials, push out, open web steel joist and composite open web steel joist tests.

Chapter five: this chapter consists the results and their discussion of the lateral torsional buckling test of hybrid open web steel joist.

Chapter six:this chapter illustrates the finite element analysis by using ABAQUS software program to compare its results with the results of the experimental tests.

Chapter seven:this chapter presents the main conclusions from the results of the present study and suggested some recommendations for future works related to the subject of this study.

CHAPTER 2

LITERATURE REVIEW

2.1 General

Open Web Steel Joists (OWSJs) are charming for structural used in the pre-engineered metal building industry mainly as roof and floor support systems. OWSJ have great advantages than traditional wide flange steel beams and girders in the manufacture because of their capacity to sustain loads with long span and lightweight arrangements and they also offering sufficient opening for air ducts and other services.

There is no material that can provide all the structural requirements but each different material has a special distinguished characteristic which recognizes it from other materials, this is the reason of using more than one material that can be rigidly connected to each other to implement as one body, with the aim that only the eligible property of each material will be utilized by virtue of its designated position to bring out the strengths of each material as well as to strengthen the weakness of each individual material. The structure is then known as a composite structure and the relevant method of building as a composite construction.

Composite flooring is stiffer than non- composite flooring causing less deflection, furthermore:

• Composite flooring has a larger moment capacity, allowing for smaller section sizes.

• By using composite flooring it can be increased the length of spans.

• Composite action has a great effect on the stress and strain of a beam, because there is no strain compatibility at the interface between the two materials without composite action.

• With composite action, a single neutral axis (better if within the concrete slab),

allowing the concrete to take all the compression forces, while the steel beam takes almost all the tension forces.

Composite construction will result in reduced building costs, because the metal decking in composite flooring acts as formwork for concrete decreases construction times.

2.2 Review Studies on Composite Steel Joists

The first experimental research using to test open-web steel joists as part of a composite joist system was found in the 1960's by **Lembeck (1965)** [16].In this study, the double angle joist top chord was lowered to allow the round rod web members to extend into the concrete slab and form a shear connection with the overlying slab. Corrugated steel forms resting on the horizontal legs of the top chord angles supported the concrete slab. With the same theoretical design load when compared the results of conventional joists to composite steel joists, the later were stiffer and having about a 20 % reduction in deflection also approximately 14 % higher in ultimate moment is attained in composite steel joists than the conventional joists that were tested. The results also indicated that it was possible to achieve composite action in open-web steel joist construction by providing a longitudinal shear key along the one-piece top chord of the joists .

Followed by **Wang and Kale y (1967)**[17] where top and bottom chords of two composite joists were constructed from hat-shaped sections. The composite action was achieved by extending the webs above the top chord in addition to use shear connection of (12.7 mm) diameter filler rods welded to the top chord between the panel points without using shear connectors by adding continuous metal chairs into the top chord that were shaped like a bulb. Performance of the composite joists was compared with results of two additional non-composite tests. The comparison showed that mid span deflections were reduced to 39.8% and the maximum stresses of the lower chord were reduced to 78.1% .

Tide and Galambos (1970) [18] performed tests on five composite steel joists that used (9.5 mm) diameter × (51 mm) long shear studs welded to the joist top chords. A (76 mm) concrete slab was cast over each of the joist specimens. The main purpose of the research was to investigate the degree of composite action that could be obtained by studying the stud shear connector behavior in a composite system comprised of open-web steel joists, a cast-inplace concrete slab, and mechanical shear connectors holding the two together. The researchers varied the type and size of the joist top and bottom chords as well as the number and location of stud shear connectors. The web members were over-designed in all the test specimens to ensure there would be no web failures in the experiments. It wasn't until the mid 1980's that there was a renewed interest in composite design using open.

Cran (1972) [19] **and Atkinson and Cran (1972)** [20] tested composite steel joists supporting (38 mm) deep steel deck. Results from their study suggested that for joists spaced more than (1524 mm) apart and with joist spans greater than (10.97m), that composite joists were more economical than non-composite joists. Also The reports included the results of several push-out tests of shear connectors.

Azmi (1972) [21] conducted six tests on composite joists with (15.24 m) spans , deck depth (38 mm) and a slab thickness (65 mm). The author used three different joist chords which are: cold formed hat shape, hot rolled double angles, and a hot rolled hat shape. In addition to the test, a design model was developed that showed good correlation with the experimental data. The model was based on three levels of shear connection:Under-connected, balanced, and over-connected which related the stud shear strength to the tensile yield force in the bottom chord of the joist. In **(1975)** a finite difference method was developed by **Fahamy** [22] to analyze the behavior of composite steel joists in both the elastic and inelastic regime that considered two different methods for shear connection, puddle welds and shear studs.

Robinson and Fahmy (1978) [23] presented the experimental results and analysis of a number of composite open-web joists with metal deck. The idea was to demonstrate that composite with ribbed metal decking, would have sufficient ductility, and attain their computed ultimate flexural capacities. The experimental programs tested four types of OWSJ provided by three different manufacturing. The load was applied to the composite open-web joists at two points by means of a spreader beam. Test spans of the joists were either (15.25 m) or (15.6 m). Each joist supported (101.6 mm) thick concrete slab incorporating a (38.1 mm) deep ribbed metal floor of 14-gauge material. Stud connectors and arc spot welds were placed between the load points at approximately the same spacing as in the-shear spans. Test results showed that composite open-web joists with ribbed metal floors have greater stiffness, strength and ductility than non- composite open-web joists. All but one of the composite open-web joists tested attained at least or more than the calculated ultimate flexural capacity. The mode of failure was very much influenced by the degree of connection.

Leon and Curry (1987) [24] reported on the testing of two full-scale, 36 ft. (10.97 m) long span composite steel joists to failure. Each test specimen was constructed with 2 in. (51 mm) composite steel deck, 3/4 in. (19 mm) diameter headed shear studs, and normal weight concrete with a nominal strength of 4 ksi (27.6 MPa). **Alsamsam (1988)** [25] tested another two full-scale specimens to failure. The major result of the four tests was that the composite beam model could be used to predict the ultimate moment capacity of composite steel joists.

Patras and Azizinimini (1991) [26] tested two full-scale composite joists. The composite steel joists were (10.97 m) long with a nominal depth of (305 mm). Top and bottom chords of both specimens consisted of two equal leg angles welded back to back. Web members consisted of equal leg angles placed on the outside of the chords. Galvanized deck supported the (102 mm) total concrete slab. Shear connectors, (19 mm) diameter × (89 mm) long after welding, were welded

through the metal deck to the steel joist top chord angles. Light weight concrete was utilized for both specimens. Test specimen CH-1 was designed for a nominal strength of (20.7 MPa) while CH-2 was designed for a nominal concrete strength of (82.8 MPa). Crushing of the concrete adjacent to the shanks of the "Weak" position shear studs in CH-1 was observed while there was no noticeable concrete crushing in CH-2 in the vicinity of the shear studs. Test results also showed that the higher strength concrete in CH-2 exhibited a higher stiffness as expected. Ultimate load-carrying capacities were accurately predicted for both test specimens.

Brattland and Kennedy (1992) [27] studied the effect of concrete shrinkage on the behavior of composite steel joists. The authors tested two full-scale (11.58 m) specimens to failure, one at 65 days and the other at 85 days. It was found that the majority of the shrinkage occurred in the first 30 days. The failure loads that the specimens attained closely matched predictions based on an ultimate strength method with only the bottom chord in tension.

Easterling et al. (1993) [28] discussed the composite joist and slab systems. They tested four composite beams each of a single W16×31 section with a composite slab and composite deck with a total of (152.4 mm) thickness. The span of each specimen was (9 m). Welded wires were placed directly on the top of the deck and a total of 12 headed shear studs, (19 × 127) mm .They concluded that the hypothesis regarding the influence of the steel deck material properties on the stud strength must be evaluated at the same time and perhaps included as a modification to one of the existing methods. This hypothesis, while not conclusively verified, was supported by the results of the Virginia Tech research program. .

Mujagic et al. (2010) [29] presented an analytical and experimental findings pertaining to the design and behavior of composite truss members (composite open-web joists) with standoff screws as shear connectors. A procedure was presented

to predict the required and available slip of a particular joist member. Generally, brittle connections embodied in concrete rib failure have less slip capacity, and were found to be more appropriate for shorter members. Finally, a reliability study was performed and strength reduction factors were presented for both the strength prediction model and slip prediction equations to ensure the proper safety performance of the procedure, and that it can be easily adopted into design codes.

Hedaoo (2012) [30] presented the structural behavior of composite concrete slabs. The slab was created by composite interaction between the concrete and steel deck with embossments to improve their shear bond characteristics. However, it fails under longitudinal shear bond. Eighteen specimens are split into six sets of three specimens each in which all sets are tested for different shear span lengths under static and cyclic loadings on simply supported slabs.

Lakshmikandhan et al. (2013) [31] investigated the longitudinal shear transfer mechanism at the interface between steel and concrete. Three types of mechanical connectors schemes were investigated experimentally which were exhibited full shear interaction with negligible slip. These experiments were improved strength and stiffness of the deck and can effectively reduce the cost of formworks. The experts were noticed that the composite slab without shear connectors slips and fails at the earlier load level. The insertion of shear connector modifies the brittle behavior of the composite slab into ductile.

Ibrahim (2015) [3] investigated alternative connectors, which are puddle-welds and Hilti-screw to develop the composite action. The experimental work consisted of two full-scale specimens each consisted of (2400 mm) wide (6700 mm) long and (65 mm) thick concrete deck cast on top of corrugated steel sheets. The deck slab is supported over two OWSJ each of (250 mm) depth and spaced transversally at (1200 mm) with (600 mm) overhang on each side. Test results are presented in terms of load-strain and load-deflection relationships at different

locations over the concrete deck and across the depth and showed that both of these connectors are simple and save the construction time, but the puddle welds showed a stronger performance in terms of the deflections and strains compared with the Hilti-screw connector.

Hadeed (2018) [32] investigated many parameters on the behavior of composite open web steel joist. Seven specimens with same length (3 m) and span/depth ratio equal to 12 were tested under static loading. Shear connectors with 10 mm diameter were welded into double angles (2L 31.5×31.5×3) mm top chord. Six variables were adopted to study the flexural behavior and failure modes of these specimens. Web type and its inclination angle, under- and over-connected, uniform and non-uniform distribution of the shear connectors, casting the composite slab with normal and lightweight concrete, and using of long shear connectors were the parameters of this study. The experimental results showed that the bending analytical calculation needs to be multiplied by 0.7 reduction factor when small inclination angle of the web or long headed studs were used in the design of the composite open web joists, while the other five have to multiplied by 0.75.

De Seixas and De Miranda (2020) [33] developed innovative solutions for the composite floor system composed of with thin-walled trussed beams (or open-web joists) and one-way prefabricated concrete slab, according with the usual steel frame construction technology. According with the analysis of the experimental results, the three types of the proposed shear connectors, composed of thin-walled members and attached to the top chord of the trusses by means of self-drilling screws (4.2mm diameter). Also, the performance of the referred connectors was investigated with the help of three full-scale bending tests, which revealed important characteristics regarding the structural behavior of the composite floor systems in terms of bending capacity, flexural stiffness, degree of interaction between the steel

trusses and the concrete slabs, as well as strain distribution at mid-section. The experiments showed favorable results for both, the shear connectors behavior and the bending capacity of the proposed floor system.

2.3 Review of Literature on Behavior and the Lateral Buckling of Steel Beams and Joists

Because the steel structures are slender systems, thus buckling analysis is particularly important and its occurs suddenly and causes the system to collapse. The prefabricated hybrid open web steel joists (PHOWSJs) behavior which proposal in this study must be investigated such as its lateral torsional buckling. Steel joist are strong and stiff in their plane, but they are very flexible out-of-plane. They must, therefore, be properly braced prior to the application of any construction load. They are made of flexible interior shear web that support the top and bottom chords and their cross-sections are often mono-symmetric or unsymmetrical. Hot-rolled I-beams have relatively continuous thick webs that prevent web local and flange distortional buckling, hence lateral torsional buckling behavior of (PHOWSJs) are more complex than that of doubly symmetric hot-rolled beams. Also the material properties of steel joist sections such as the yield stress vary significantly depending on the location in the cross section. The residual stress pattern in open web steel joists is markedly different from that in hot-rolled I-beams.

Although of the growing usage of open web steel joists around the world, the methods for designing them against lateral torsional buckling are inadequate.

Past research on lateral–torsional buckling of steel beams has mainly concentrated on hot-rolled steel beams. The critical elastic lateral-torsional buckling of I-beams has been first investigated analytically by **Timoshenko and Gere (1961)** [34] . Timoshenko included effects of warping, which made it possible to describe the torsion of I-section beams correctly for different load cases

and different support conditions. Other researchers such as Wagner made further contributions that eventually led to a general theory on lateral-torsional buckling which can be found in the textbooks by Timoshenko and others. Before the 1960s the assessment of lateral-torsional buckling required extensive calculations by hand, which was a clear limiting factor due to the time needed.

Xykis and Galambos (1990) [35] developed a numerical methodology with the aid of the finite element method which provides a useful tool for the elastic buckling analysis of large rigid space frames, with thin- walled members in general and joist systems in particular. Even though the present methodology does not take into account warping, inclusion of its effect does not present any difficulties. The element stiffness matrix for second order (stability) analysis is formulated on the basis of open thin-walled element theory considering the coupling of torsional and flexural behavior in three dimensions under the assumption of small deformations. It has also been concluded that there are several factors that have a significant effects on the critical load of the structure, such as:

• A change in the boundary conditions at the ends of the horizontal bridging lines has a significant effect on the buckling load of the whole structure. The more restraints are imposed on the supports of the bridging lines, the higher the critical load becomes.

• The length of the bridging lines also has a considerable effect on the critical load of the structure.

• The configuration of the bridging lines (horizontal or X-bracing) also affects the critical load. Just by changing from horizontal to X-bracing one can notice a measurable increase in the load capacity of the joist system.

Galambos and Xykis (1991) [36] presented the results of two analytical studies on the elastic buckling strength of single and multiple braced trusses (steel joist) and compared to experimental results. The effect of the axial and flexural stiffness of the bracing, the brace end-conditions, the number of trusses in parallel,

and the effect of bracing only the top chord were investigated. The system of trusses and braces was shown schematically in Figure 2.1.The trusses to be braced are designated as 'joist' in this figure. Horizontal bridging was preferred because it was easier to install, but diagonal bridging was required for joists over (12 m) in length.

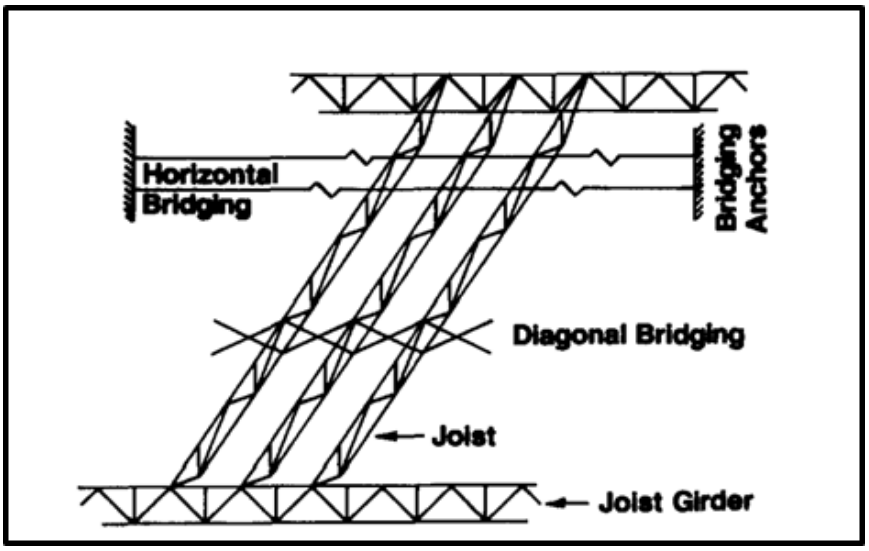

Figure 2.1 Joist and bridging system [36].

A number of conclusions were reached from these analytical experiments,

• The buckling capacity do not affect significantly when changing the support conditions at the ends of the bridging.

• The flexural stiffness of the bridging members has a significant effect on the buckling load.

• The buckling load was only slightly reduced if only the top chord was braced.

• The two finite element analyses gave comparably close results in overlapping cases.

• There was little difference between the two- and the three-joist systems if horizontal bridging was used, but the difference becomes significant if the bridging was diagonal.

• Diagonal bridging was more effective in increasing the buckling load than horizontal bridging.

In **(1999), Put et al.** [37] presented a paper which was concerned with the lateral buckling capacities of cold-formed lipped channel-section beams (CFCs). The paper describes a series of 10 lateral buckling tests on simply supported unbraced CFCs of two different cross sections, and a series of subsidiary tests, including tension tests, a stub-column test, section moment capacity tests, torsion tests, residual stress measurements, and measurements of initial crookedness and twist. It was argued that design code formulations based on those for hot-rolled I-beams may be inappropriate for CFCs, because of the very different cross-sectional shapes and methods of manufacture, and that there is a need for test data on the lateral buckling capacities of CFCs. The test beams failed catastrophically by local or distortional buckling of the most compressed element of the cross section, but often after quite large deformations developed as the inelastic buckling loads were approached. The modes of failure of the test beams were best discussed in terms of the elastic buckling modes shown in Figure 2.2. The lateral buckling results showed good agreement compared with design codes for hot-rolled sections and cold-formed sections.

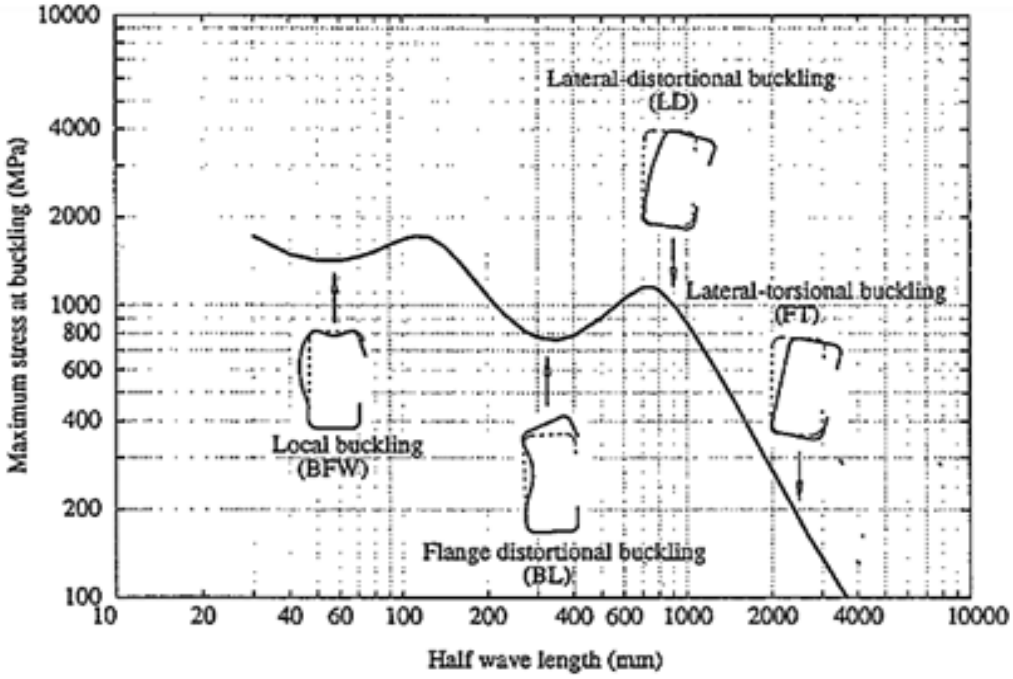

Figure 2.2 Elastic buckling modes of C10019 CFCs [37].

Distortional buckling experiments were carried out by **Zirakian and Showkati (2007)** [38] on simply supported fabricated steel I-beams with central concentrated load and an effective lateral brace at the mid-span of the top compression flange. The experimental beam strengths were compared with the design strengths predicted by the American AISC/LRFD and the Australian AS4100 specifications. Generally, the two specifications provide un conservative predictions in the inelastic range of structural response as the beam length decreases and inelastic behavior becomes more intense. Also there are many researches about cold formed steel beams.

Sharifi and Tohidi (2014) [39] presented a three-dimensional (3D) finite element model using ABAQUS for the elastic flexural torsional analysis of I-beams has been used to assess the effect of web opening on the lateral buckling moment capacity. Artificial neural network (ANN) approach has been also employed to derive empirical formulae for predicting the lateral-torsional buckling moment capacity of deteriorated steel I-beams with different sizes of rectangular web opening using obtained FE results. The analyzed specimens have been supposed to be subjected to equal and opposite end moments with an opening in mid span. It was found from the FE results that, the opening length has more effect than opening height on the strength reduction. The relationship between the buckling moments and the opening length ratio (b/L) under different opening height ratios (a/h) was depicted in Figure 2.3. It can be found from Figure 2.4 that the influence of the opening length ratio is more important and sensitive than the opening height ratio. In other words, the length of opening on the reduction strength is more than of the opening height. Comparison of the Figures 2.3 and 2.4 shows that the effect of opening height is not remarkable and it can be ignored until the 1/4 of cross section height. The results of this study can be used for better prediction of buckling life of web opening of steel beams by practice engineers.

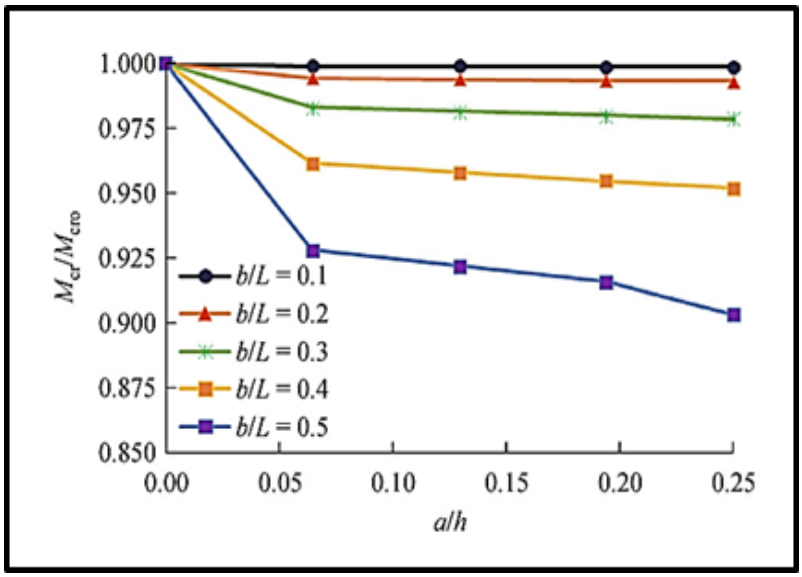

Figure 2.3 Relationships between the ultimate load-carrying capacity and the opening length ratio under different opening height ratios [39].

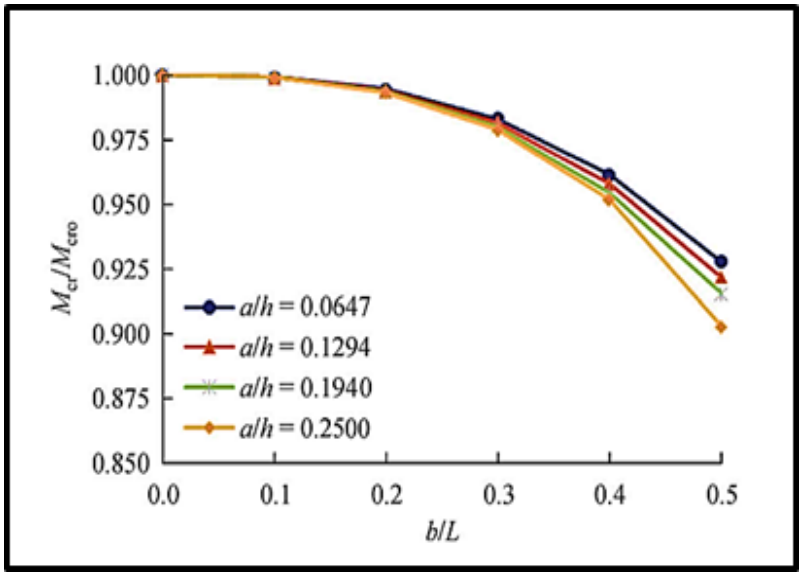

Figure 2.4 Relationships between the ultimate load-carrying capacity and the opening height ratio under different opening length ratios [39].

2.4 Review of Literature of Steel Fiber Reinforced Concrete

Cement concrete is the most extensively used construction material in the world. The reason for its extensive use is that it provides good workability and can be moulded to any shape. Ordinary cement concrete possesses a very low tensile strength, limited ductility and little resistance to crack. Internal micro cracks, leading to brittle failure of concrete. It has been found that different type of

fibers added in specific percentage to concrete improves the mechanical properties, durability and serviceability of the structure. It is now established that one of the important properties of Steel Fiber Reinforced Concrete (SFRC) is its superior resistance to crack and crack propagation.

The tensile strength of concrete is generally neglected in the design of reinforced concrete structures. When steel fibers are added to a concrete mix, the flexural tensile strength of the composite is increased by 2 to 3 times that of the plain concrete as reported by **Swamy and Mangat (1974)** [40] when researchers conducted a study on flexural strength of steel fiber reinforced concrete using a composite mechanics approach. The presence of fibers imparts to the composite a first cracking load distinct from the ultimate load and considerable post-cracking behavior, Figure 2.5 so that a substantial part of the ultimate flexural strength of the composite can be used in design. Equations were derived to predict the first crack and ultimate flexural strength of concrete reinforced with short discontinuous randomly oriented and uniformly dispersed steel fibers. The authors concluded that using a composite mechanics approach, first crack and ultimate flexural strength of SFRC can be predicted through the derived equations. Also it was reported that inherent properties of post-cracking behavior and crack control of material were of little danger to brittle failure or lack of durability.

Soroushian and Lee (1990) [41] conducted an experimental investigation on the distribution and orientation of fibers in steel fiber reinforced concrete, by counting the number of fibers per unit cross-sectional area of SFRC specimen incorporating various volume fractions of different fibers. Theoretical expressions were derived for the number of fibers per cross-sectional area in fiber reinforced concrete as a function of volume fraction and length, assuming the cross-sectional boundaries as the only factor distributing the 3-D random orientation of fibers. They made a comparison between number of fibers per cross-sectional area and the reorientation fibers in concrete.

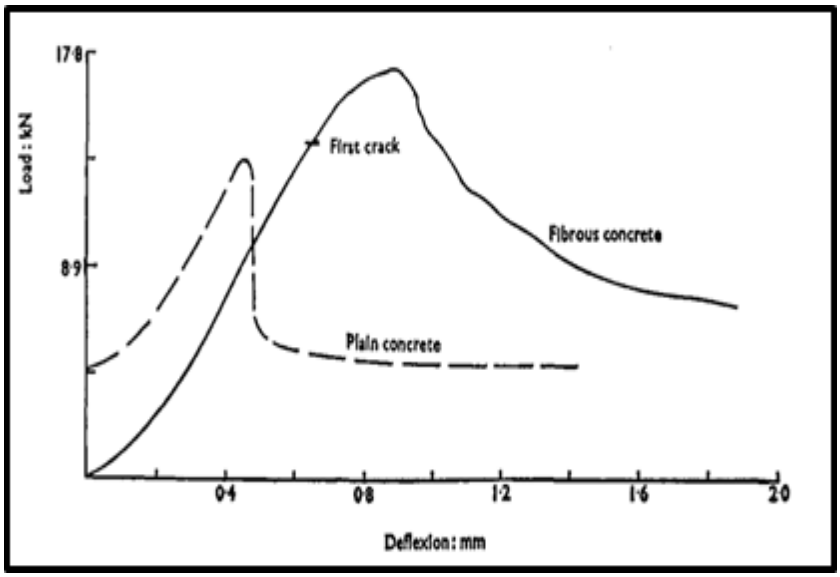

Figure 2.5 Typical load-deflection characteristics in flexure of plain unreinforced concrete and steel fiber reinforced concrete [40].

Nataraja et al. (1998) [42] conducted a study on steel fiber reinforced concrete under compression. The cylinder compressive strength ranged from 30 to 50 (N/mm^2). Round crimped fibers with three volume fractions of 0.5%, 0.75%, and 1.0%; and two aspect ratios of 55 and 82 were used. The effect of fiber addition to concrete on compressive strength was studied. It was concluded that the addition of fibers increased the compressive strength and toughness. Some empirical equations were also proposed for the compressive strength of concrete in terms of fiber reinforcing index.

Poon et al (2004) [43] studied the compressive behavior of FRC using steel and polypropylene fibers with and without pozzolan, at unheated condition and when subjected to elevated temperature. The results showed that after exposure to (600 and 800)^oC, the concrete mixes retained, respectively, 45% and 23% of their compressive strength, on average. SFRC was effective in minimizing the degradation of compressive strength after exposure to elevated temperature and showed the higher energy absorption capacity and when polypropylene fibers used in concrete reduced the energy absorption capacity.

fibers can be classified according to size, **L¨ofgren (2005)** [44] described an approach whereby the fibres are classified as macro-fibres when they are longer than the maximum aggregate size of the concrete, when their diameter is much greater than the cement grain size, and when the aspect ratio (length to diameter ratio) is less than 100. fibers with a cross-section diameter of the same order as the cement grains and a length of fiber less than the maximum aggregate size are classified as micro-fibres. Basically, macro-fibres increase the composite toughness by bridging macro-cracks, whereas micro-fibres increase resistance to micro-cracking prior to the formation of macro-cracks.

Nataraja et al.(2005) [45] have developed a practical rapid method of proportioning SFRC mixes. SFRC mixes having 28 day target strength of 30 MPa and 50 MPa were designed using this technique and examined its validation were the re-proportioning method suggested by **Nagaraj and Banu (1999)**[46] was used for SFRC mixes in this investigation. In addition, the impact resistance of proportioned plain and SFRC was studied at 7 and 28 days. The uniformity of concrete and proper distribution of fibers mainly depends on the mixing procedure. Cement and aggregates were mixed thoroughly and then fibers are added manually. While the mixing operation was in progress, 80% of water was added first and mixed for about 5 min then the remaining water was added and mixed thoroughly. After 24 hour the specimens were de-molded, immersed in portable water and cured until testing. The water was at a temperature of around 28^oC. It was observed that SFRC has developed significant impact resistance even for a small addition of steel fibers, whereas post crack resistance in impact was negligible in case of plain concrete. However, the percentage increase in post crack resistance was about 50% in SFRC.

Lau and Anson (2006) [47] have investigated the compressive strength, flexural strength, elastic modulus and porosity of concrete reinforced with 1% steel fiber (SFRC) subjected to different elevated heating temperature, ranging between

105^oC and 1200^oC. It were observed that for maximum exposure temperatures below 400^oC, the loss in compressive strength was relatively small and addition of steel fibers of 1% to the concrete increased the compressive strength of unheated concrete by 13%. When steel fibers are incorporated at 1%, an improvement of fire resistance and crack resistance as characterized by the residual strengths were observed.

Yazici et al. (2006) [48] investigated the effect of aspect ratio. Also, the fraction volume of the steel fiber reinforced concrete, SFRC, on the mechanical properties of the concrete. Three different types of end hooked with the aspect ratios of 45, 65, and 80 were used. In addition to three fraction volume contents of 0.5%, 1.0%, and 1.5% of steel fibers, were adopted. The experimental program consisted of ten mixtures, one as a control while the other nine were varied. The aggregate classified into three sizes of; 30% for size (0-3) mm, 30% for size (3-5) mm, and 40% for size (5-15) mm. The results showed that the increment content of steel fiber reduced the workability of mixture. The steel fiber possesses a higher aspect ratio with a high fraction content that will be enhanced the mechanical properties of the concrete, as listed in Table 2.1.

Table 2.1 Steel fiber content, aspect ratio, and test result [48].

Mix type	l/d, as-percent ratio	Fiber content% by volume	Compressive strength, MPa.	Split tensile strength, MPa	Flexural strength, MPa.
CC	0	0	49.1	4.06	5.94
SFRC1	45	0.5	50.8	4.5	6.14
SFRC2	45	1.5	53.7	4.69	6.32
SFRC3	45	0.5	57.7	5.69	7.75
SFRC4	65	0.5	53.5	4.51	6.24
SFRC5	65	1.0	58.3	4.77	8.08
SFRC6	65	1.5	56.4	6.26	9.33
SFRC7	80	0.5	56.0	4.58	6.42
SFRC8	80	1.0	58.3	5.18	9.74
SFRC9	80	1.5	52.1	5.9	10.76

Thomas and Ramaswamy (2007) [49] conducted an experimental investigation on mechanical properties of steel fiber reinforced concrete. Three different strengths such as normal strength (35 MPa), moderately high strength (65 MPa) and high strength (85 MPa) concrete mixes were considered for this study. Steel fibers of aspect ratio 55 with three different fiber volume fractions (0.5%, 1% and 1.5%) were used in the concrete mix. Based on 60 test data, regression analysis was done and empirical relations were proposed. It were concluded that the maximum increase in the compressive strength, modulus of elasticity, and Poisson's ration due to the addition of steel fibers was found to be quite small(less than 10%) and the maximum increase in the split tensile strength and modulus of rupture due to the addition of steel fibers, was found to be about 40% in various grades of concrete. The post-cracking response is significantly enhanced with fiber dosages across the different concrete grades.

Olivito and Zuccarello (2010) [50] conducted a number of experimental tests to investigate uniaxial compressive strength and tensile strength of steel fiber reinforced concrete. Different mixtures were prepared varying both mix-design and fiber length. Fibers content in volume was of 1% and 2% with aspect ratio (l_f/d_f) equle to 55 and their length equal to 22, 30, and 44 mm. Mechanical characterization was performed by means of uniaxial compression tests with the aim of deriving the ultimate compressive strength of fiber concrete. The tensile strength of steel fiber reinforced concrete (SFRC) was obtained both from an experimental procedure and by using an analytical model. The experimental tests showed the different behavior of SFRC with respect of the different fiber content and length. Based on the experimental results, an analytical model, reported in literature and used for the theoretical determination of direct tensile strength, was applied with the aim of making a comparison with experimental results. Experimental results showed that compressive strength of SFRC was less affected by the presence of fibers but the compressive strength of SFRC with

1% fibers content was little more than SFRC fibers content with 2% as shown in Figure 2.6. While Figure 2.7 shows the load–displacement curves for direct tensile tests obtained for the two types of specimens tested . However, failure mode considerably changes from fragile to ductile. Due to bridging effect of the fibers, the cubic specimens did not crush but held their integrity up to the end of the test. Also tests showed an increment for the maximum tensile strength for short fibers specimens, whereas the ultimate strain was higher for long fiber ones.

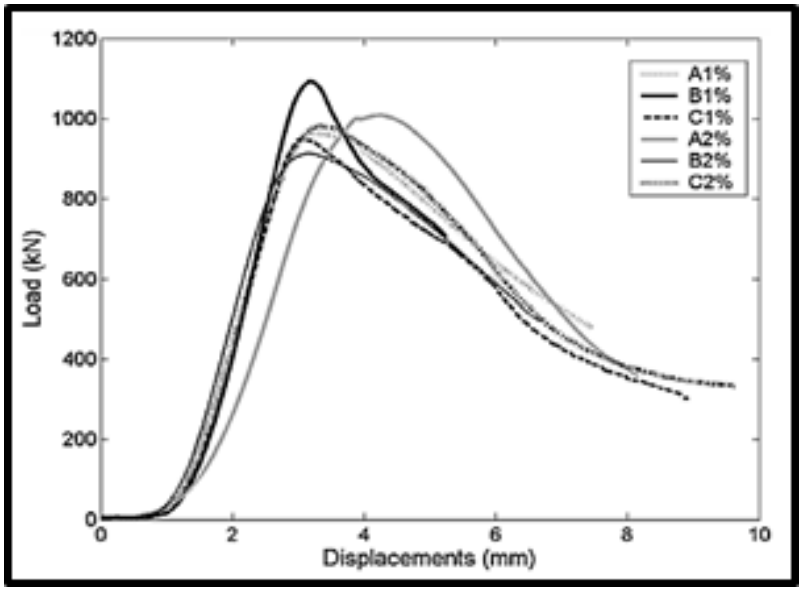

Figure 2.6 Load–displacement diagram relative to compression test [50].

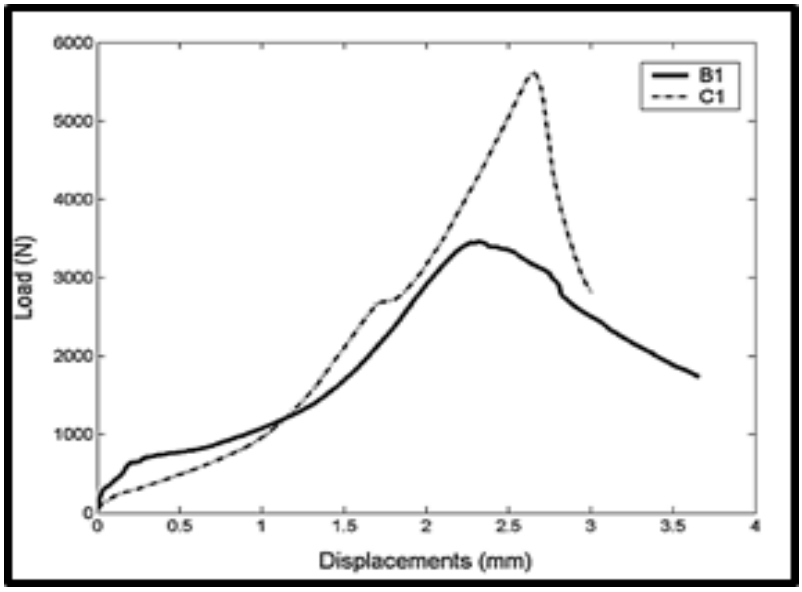

Figure 2.7 Load–displacement diagram relative to direct tensile test [50].

Islam et al.(2012) [51] provided an experimental investigation on the properties of fiber-reinforced composite concrete consisting of natural fibers (coconut coir) and rounded, straight steel fibers in a comparative manner for both normal-strength concrete (NSC) and high-strength concrete (HSC). The mixing procedure was recommended to be used it was that the aggregates were added into the mixer and mixed thoroughly till the aggregates are evenly mixed. Thereafter, fibers were added into the mixer uniformly by hand slowly and evenly to the concrete mix to encourage a uniform distribution of fibers throughout of the concrete. This prevents the congregation of the fibers on the paddle, which results in balling of fibers. Cement was added into the mixer and mixed until uniformity was achieved. Then, superplasticizer was added with the mixer for lower w/c ratio. Water was added into the mixer slowly after the cement was placed. Finally, the concrete was mixed about (3 min.). Figure 2.8 shows that the 90-day compressive strength decreases for fiber-reinforced concrete compared to control batch in NSC. For coir fiber and steel fiber, 90-day strength was not changed remarkably compared to 28-day strength. The effects and appearance of the test specimen for no fibers and with fibers after the test indicated clearly that the specimen containing no fibers fall off and failed in shear, while fiber-reinforced concrete specimens were still intact.

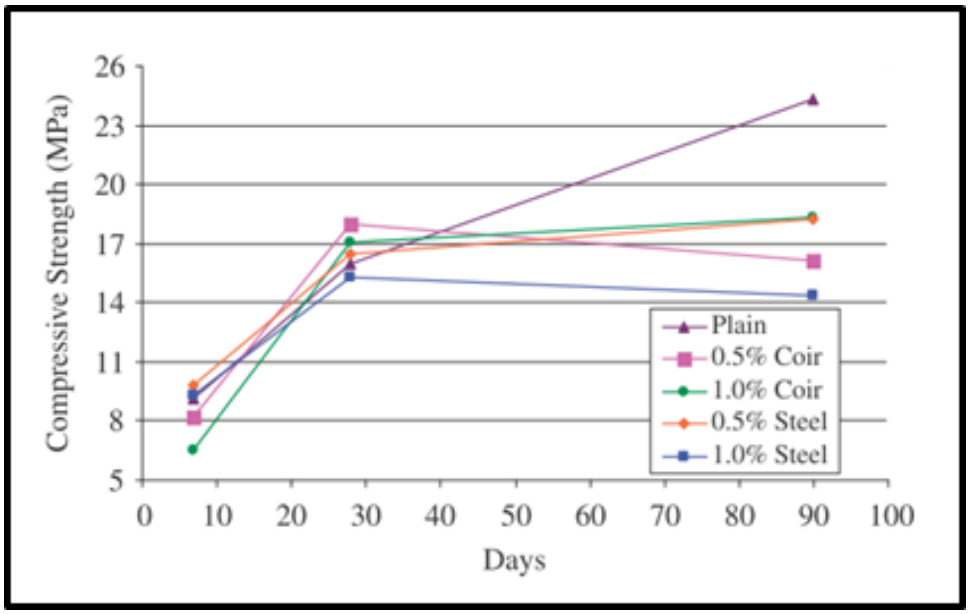

Figure 2.8 Average compressive strength (NSC) vs. age in days [51].

Mohod (2012) [52] studied the effect of fibers on the compressive and flexural strength of concrete for M 30 grade by varying the percentage of fibers in concrete. Fiber content were varied by 0.25%, 0.50%, 0.75%, 1%, 1.5%, and 2% by volume of cement. The results of fiber reinforced concrete for 3days, 7 days and 28 days curing with varied percentage of fiber were studied and it has been found that there was significant strength improvement in SFRC. The optimum fiber content while studying the compressive strength of cube was found to be 1% and 0.75% for flexural strength of the beam. Also, it has been observed that with the increase in fiber content up to the optimum value increases the strength of concrete. The Slump cone test results revealed that workability gets reduced with the increase in fiber content. Figures 2.9 and 2.10 shows the variation of compressive and flexural strength respectively with respect to (%) of fiber content. the plain cement concrete specimens have shown a typical crack propagation pattern which leaded into splitting of beam in two piece geometry. But due to addition of steel fibers in concrete cracks gets ceased which results into the ductile behavior of SFRC.

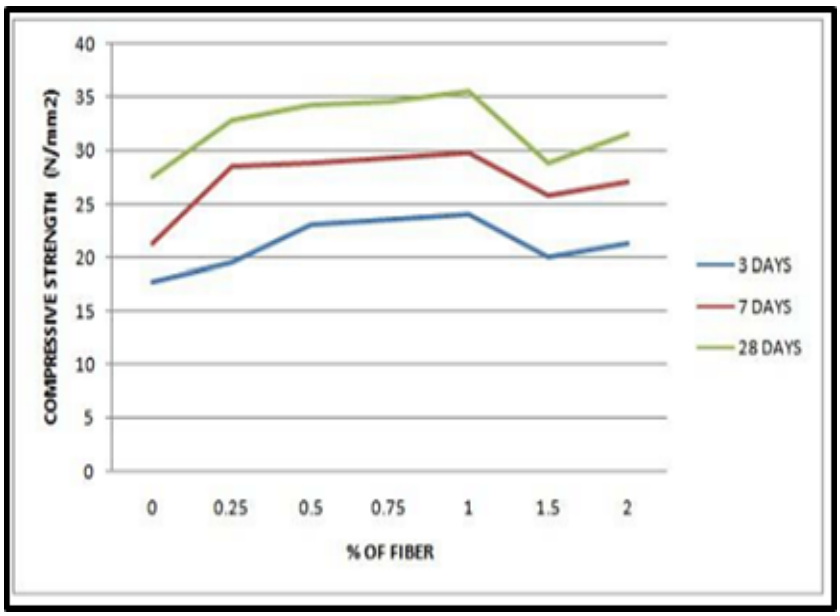

Figure 2.9 Compressive strength variation with respect to % of fiber content[52].

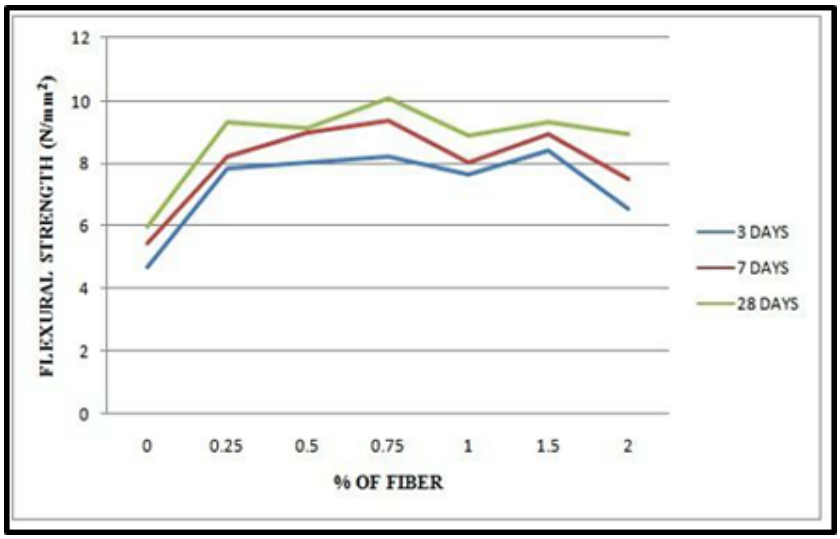

Figure 2.10 Flexural strength variation with respect to % of fiber content [52].

Rana (2013) [53] carried out test on steel fiber reinforced concrete to check the influence of fibers on flexural strength of concrete. It was interested in finding out the optimum quantity of steel fibers required to achieve the maximum flexural strength for M25 grade concrete. The mixing procedure which used in this study was dry ingredients (aggregates and cement) would be mixed be mixed in the mixer for (30 seconds). After that, steel fibers would be added (30 seconds). Then water (with superplasticizer) would be added gradually in 15 seconds and the mixing would be continued for (2 minutes). Extensive experimental work revealed that even at 1% steel fiber content, flexural strength of 6.46 ($N/mm2$) was observed compared to flexural strength of 5.36 ($N/mm2$) at 0%, resulting in an increase of 1.1 % in flexural strength.

Sabariman et al. (2018) [54] presented a study on the stress-strain behavior of SFRC by using the standard concrete cylinders were spirally confined with steel bars and with/without hooked-end steel fibers. The influence of the use of hooked-end steel fiber in spirally confined concrete with various pitches was investigated. The compressive test was carried out until the concrete specimens failed in the compressive crushing mode. It can be seen that the use of hooked-end steel fiber

contributes significantly in improving both compressive strength and ductility of concrete. The results indicated that both the stress and the strain of concrete increases, and thus, it becomes more ductile. The test system used by Sabariman et al was similar to the system which used by **Gilani (2007)** [55] to investigate various durability aspect of slurry infiltrated fiber concrete.

Zheng et al. (2018)[56] manufactured two types of steel fiber-reinforced (C50 and C60) by traditional mixing and vibratory mixing methods, respectively, and then, the cube compression test, flexural test, splitting tensile test, and the bending test were carried out. The reinforcement effects of mechanical properties were analyzed by comparing the traditional mixing and vibratory mixing methods. To ensure uniform distribution of basalt fibers in the mix, sand and macadam were mixed firstly, and then, cement and fiber were added. After the mixtures were mixed for 30 seconds, the water and additives were added during the course of stirring. The results show that vibratory mixing can effectively improve the distribution of steel fibers in concrete and can increase the density of steel fiber concrete.

Suksawang et al. (2018) [57] provided an in-depth examination study of elastic modulus of concrete with discrete fibers, including steel, polypropylene, macro-polyolefin, poly- vinyl alcohol, and basalt fibers. A new elastic modulus equation is proposed to better estimate of the elastic modulus of FRC with a maximum fiber volume fraction of 10%, in the data were observed, when the ratio of coarse to fine aggregate (C/S) $>$ 1, the fibers did not influence its elastic properties. However, when there was no coarse aggregate or when (C/S) $\leqslant$ 1, the elastic modulus decreased with an average reduction of 20%. This could be attributed to extra voids brought on by the addition of fiber as revealed in the results. The proposed equation was compared with existing equations from other codes, and equations proposed by other researchers. Using more than 400 data points obtained from the experimental program and 24 other literatures, the

accuracy of existing elastic modulus equations was evaluated. It was determined that existing equations do not provide a good prediction of elastic modulus of concrete with discrete fibers. The proposed equation provides the most accurate prediction for the elastic modulus of (FRC) and fiber reinforced cement composites (FRCC) with a coefficient of variation of 15% as compared to 32% using (ACI 318-14) equation for (C/S) $\leqslant$ 1. It is recommended that the proposed equation can be used for computing the elastic modulus of FRC. The proposed equation is applicable to a wide range of concrete with variety of fiber types, C/S, concrete strengths, and fiber volume fraction between 0.1% to 10%.

$$E_c = 4700\lambda_{Vf}\sqrt{f'_c} \quad (N/mm^2) \tag{2.1}$$

$$\lambda_{Vf} = 1 \quad for \quad \frac{C}{S} > 1 \tag{2.2}$$

$$\lambda_{Vf} = \frac{1 + 0.7^{V_f}}{2} \quad for \quad \frac{C}{S} \leqslant 1 \tag{2.3}$$

where:

V_f: Volume fraction of fiber, (%).

λ_{Vf}: Fiber effect factor.

In **(2019) Babaie et al.** [58] presented a study aimed to investigate the influence of a number of fiber parameters including fiber type, content and hybridization on strength and ductility of polymer fiber reinforced concrete (PFRC) and steel fiber reinforced concrete (SFRC) used mostly in tunnelling practices as the primary shotcrete lining. Many tests were performed on cylindrical and beam specimens to compare mechanical behavior (PFRC) and (SFRC). A variety of tests including uni-axial compressive strength test, direct uni-axial tensile strength test and tensile strength in bending were conducted. Among many conclusions from this research was that the compressive, tensile and flexural performance of SFRC was improved as the result of an increase in fiber amount, and this conclusion can be illustrate in the Figure 2.11.

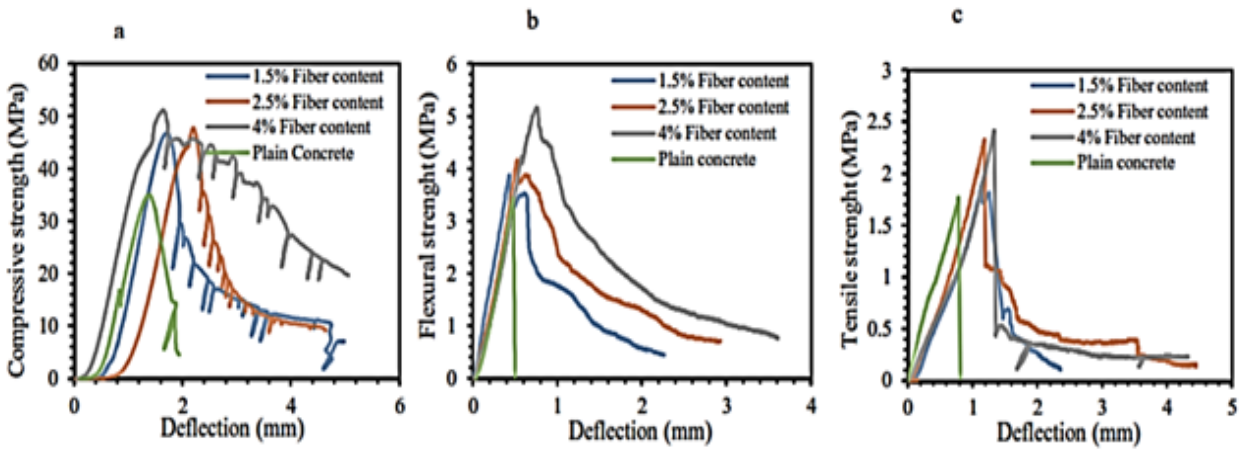

Figure 2.11 Results obtained from the tests at different proportions of steel fiber amount: (a) compressive test, (b) flexural test, (c) direct tensile test [58].

2.5 Review of Literature of Arc Welding E6013

Many research were be done to find the mechanical properties of welded joints using electrode E6013. In **(2014) Assi** [59] performed tests the suitable filler metal to weld the similar and dissimilar metals (Low carbon steel type A516 Austenitic stainless steel type 316L) under constant conditions such as, plate thickness (6 mm), voltage (78 V), current (120 A), straight polarity. This research deals with three major parts. The first parts: four types of electrodes were used for welding of dissimilar metals; two from mild steel (E7018, E6013) and other two from austenitic stainless steel (E309L, E308L). Various inspection were carried out include visual , X-ray , δ- ferrite phase , and micro-structures test. While the mechanical testing included tensile , bending and micro hardness test. The second parts done by used the same parameters to welding similar metals . The third parts deals with welding of dissimilar weldments by two processes, gas tungsten are welding (GTAW) and shielded metal are welding (SMAW).

The tensile test results of similar stainless steel welded joints showed that when welded with an electrode (E6013) it achieves tensile strength of (407 MPa) and yield strength of (273 MPa) which was less compared to use the electrode (E309L). But when the joint was welded from similar metals of low carbon steel,

the tensile test results were close to all electrodes used, whether they were stainless steel (E308l E309L) or carbon steel welding electrodes (E6013 E7018). As for the dissimilar welding metal, the results were similar with a slight increase in tensile strength and yield strength when using the welding electrode (E7018).

Ogbunnaoffor et al. (2016) [60] presented an study on the effect of welding current on the structure, tensile properties and performance of mild steel weld joints was studied. Mild steel plate (AISI 1018), 4mm thick, was used as base metal for preparing butt weld joints using shielded metal arc welding (SMAW) process. Welding currents of 65A, 70A, 75A, and 80A were applied using 2.5mm diameter welding electrodes (E6011 and E6013). The tensile properties of the butt weld joints were determined using a universal tensile testing machine model S/N 8889 in accordance with ASTM procedures. Macro structural investigations showed good penetration in all the weld joints. Table 2.2 show the tensile properties of welded joints.

Table 2.2 Tensile properties of welded joints [60].

Electrode type	Current (A)	UTS (MPa)	YS (MPa)	(%)Elongation
E6013	65	320.10	283.13	17.50
	70	365.15	292.12	24.30
	75	354.63	285.10	22.59
	80	383.20	319.37	23.64
E6011	65	382.10	310.52	18.50
	70	412.67	346.30	21.98
	75	421.70	358.50	20.10
	80	400.75	332.6	23.65
Base metal		458.39	365.29	14.28

It was observed from the above results that the ultimate tensile strength and yield strength values of weld joints produced with E6011 increased with increase in welding current till it reaches an optimal value which was at a welding current of 75A before decreasing on further increase in welding current. However, weldments

produced with E6013 gave none linear pattern. Maximum ultimate tensile strength and yield strength values were obtained at a welding current of 80A, the yield strength and ultimate tensile strength values of weld joints were lower than those of the base metal. Also it has been concluded that the depth of weld penetration and weld bead width remained unaffected by the welding current, even though both electrode types used gave different weld bead width values. The percentage elongation of the base metal is lower than that of the weld joints.

Nassar et al. (2018) [61] discussed the effect of welding variables on the heat-affected zone (HAZ) by using a tensile test of welded 10 mm thick low carbon steel AISI1010 commercial plate, which was welded using the Shielded Metal Arc Welding (SMAW) method. Different welding electrodes E6013 and E7018 were considered as welding parameters investigated. Tensile test specimens were prepared according to **ASTM standard (E8/E8M-09)** [62]. Single –V-groove butt joint with 3 mm root face and angle of 75^o with 2 mm opening was prepared to fabricate the SMAW welded joints. The specimens were linked by double pass arc welding with SMAW electrode type E7018 and E6013 with diameters equals to 3.25 mm. One run in a flat welding position was used to produce a butt weld joint. The welding conditions and process parameters such as welding currents of 90A for E6013 and 180A for E7018. The specimens welding processes and cooled specimens by the air at room temperature. The welded specimens were tested for tensile strength using the Instron tensile machine having 600 kN capacities. The results showed that the ultimate tensile strength of the specimen welded by E6013 was (432 MPa) and the yield strength was (327) MPa as shown in the Figure 2.12. The yield strength and ultimate tensile strength values of weld joints were lower than those of the base metal. Ultimate tensile strength of the weld joints has been improved in the specimens welded with E6013. The fracture toughness of welded specimen in E6013 joint was found better than welded specimen in E7018 butt

joint. The percentage elongation of the base metal was higher than that of the weld joints.

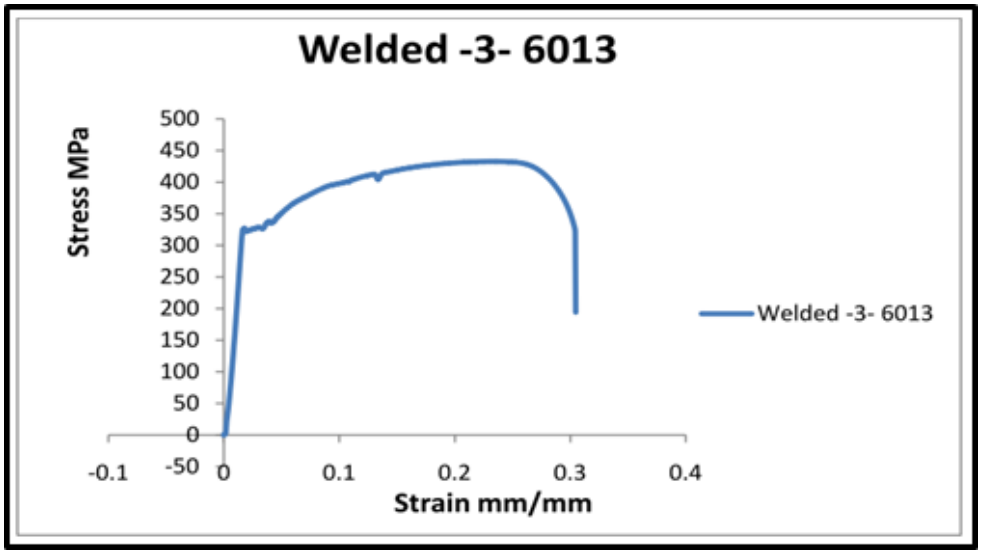

Figure 2.12 Stress-strain curve of weld specimens by E6013 [61].

Rezaeian et al. (2020) [63] presented results from an experimental investigation on high-temperature mechanical characteristic of steel welds made using shield metal arc welding (SMAW) process with E6013 and E7018 electrodes. Steady-state tension tests were conducted on weld metal specimens at $(20-800)^oC$ temperature range. Results from these experiments were utilized to evaluate stress-strain response, tensile strength, ultimate strength and the modulus of elasticity as a function of temperature for steel welds. Furthermore, the influence of electrode type in welding process and test temperature on the failure mode and microstructure of steel welds was investigated. Data from the experiments indicate rapid reduction in strength of steel welds at temperatures greater than 400^oC reaching to 50% and 80% of its original ultimate strength at 600 and 800 ^oC, respectively. Test data also indicate that the yield stress of steel welds decreases faster than that of structural steel at $(450-800)^oC$. The tensile fracture surface in welds was influenced by temperature level. The proposed reduction factors for high-temperature strength

properties of steel welds can be used to assess the fire performance of welded members and connections in steel-framed constructions.

Al-Obaidi et al. (2020) [64] investigated the effects of adding titanium dioxide nanoparticles (TiO_2NPs) to the welding joints in order to improve the mechanical properties of such welding joints of a 20 mm thickness (St-37) low carbon steel base plate by means of electric arc welding. The wire electrode AWS E6013 (4mm diameter) has been used to weld specimens. The cold spray coating method of the TiO_2NPs was used for the welding joints during the welding process. The selected samples from the tensile strength, hardness, and microstructure tests were examined by Scanning Electron Microscope (SEM). Improvements in tensile strength and hardness values of the welded joints with an increase in TiO_2NPs concentrations are observed. It was found that the average value of ultimate tensile strength of the welded sample without TiO_2NPs was (435.457) MPa, while the average ultimate tensile strength of the welded sample with 2% TiO_2NPs was (576.773) MPa with an improvement ratio of (32.45)%.

2.6 Push Out Test

Composite steel-concrete beams have been used for a considerable time in bridge and building construction. An essential element of a composite beam is the shear connection between the concrete slab and steel section. Presently, the headed stud is the most widely used shear connector in composite construction. Many types of devices have been used as shear connectors and economic considerations continue to encourage the development of new products of shear connectors. An experimental investigation of shear stud behavior is usually carried out by performing push-out tests.

In a typical push-out test specimen, studs are welded to both flanges of a W-shape. Later, a slab is poured on each side of the W-shape so that the studs will be embedded in concrete. The specimens are tested by applying an axial force

to the W-shape. A conventional push-out test specimen is shown in Figure 2.13. During the test, vertical slip between the slab and beam are measured [65].

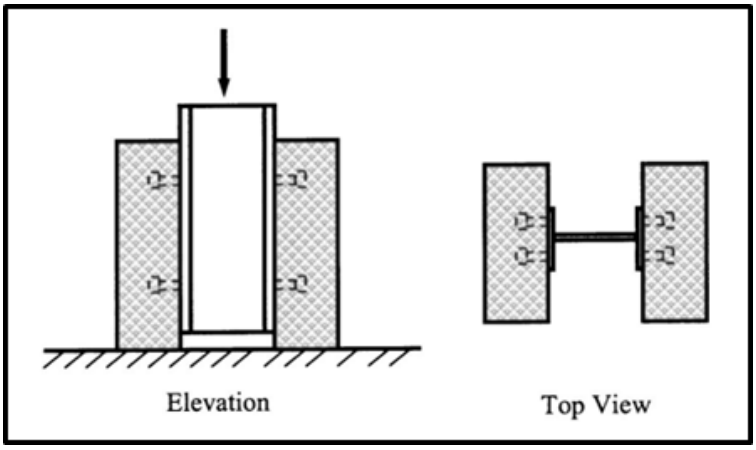

Figure 2.13 Conventional push-out test setup [65].

In the period between 1935 and 1951, after the early studies on helical connectors, European investigators turned their attention to other forms of mechanical connection devices, such as Bar and Tee connectors , Figure 2.14 (b) and (d)) [66]. These types of mechanical devices, primarily used in British bridge construction, were denoted as stiff connectors since they provided almost complete interaction by preventing slip at the steel flange/concrete slab interface by transferring the shear forces primarily by bearing on the concrete due to their relative stiffness, **Hicks et al.(2016)** [67].

In North America between 1939 and 1958, engineers turned towards shear connectors which required less fabrication, for example, the channel connector shown in Figure 2.14(c). These types of mechanical connecting devices were termed flexible connectors due to the fact they allowed a certain amount of slip at the steel flange/concrete slab interface and, for design purposes were idealised as a flexible dowel in an elastic medium. This assumption led to semi-empirical formulae relating the maximum stress to the concrete strength and the connector width, in addition to the flange and web thickness. In **(1952)** a study was carried

out by **Siess et al.** [68] to compare the performance of so-called stiff connectors with that of flexible connectors. From these investigations it was found that, when considering the load-slip performance obtained from push-out tests, the stiff connectors were superior to the flexible types. However, the differences were much smaller than had been expected by the investigators and from beam tests it was found flexible connectors could, in fact, provide adequate shear connection to develop full composite action [67].

The development of the electric drawn arc stud welding apparatus in 1954 allowed another type of flexible connector known as the headed stud connector Figure 2.14(a), to be rapidly fastened to the top flange of steel beams. This development was accompanied by extensive investigations in the USA between 1956 and 1959 at the University of Illinois **(Viest (1955)** [69]; **(1956)** [70]) and Lehigh University **Thürlimann (1959)** [71]) using push-out tests. From these research programmers it was found that the behavior of the headed stud connector was virtually identical to that of the channel connector. Although there is not a standardized procedure for fabricating and testing push-out test specimens, most researchers have used similar, though slightly different procedures **Viest et al. (1997)** [72]

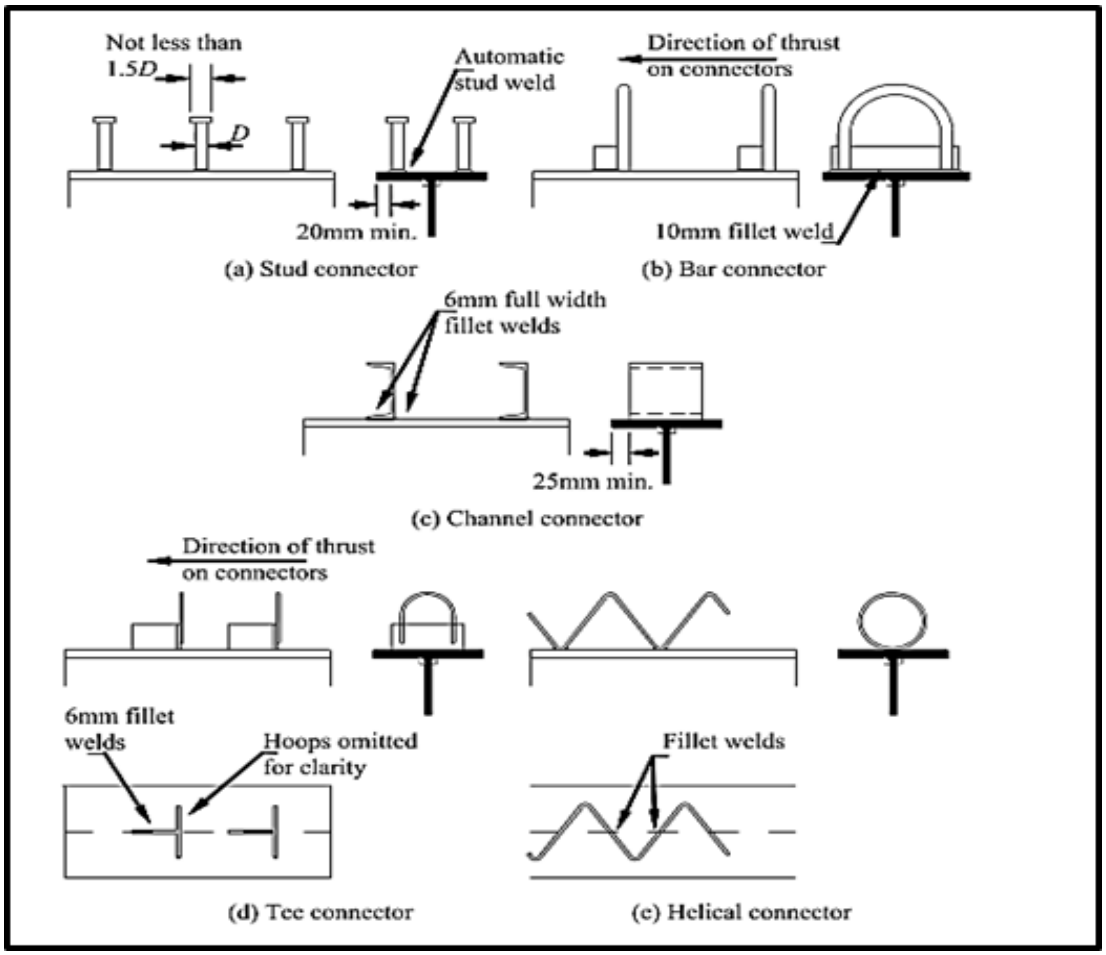

Figure 2.14 Typical shear connectors according to CP 117-1: 1965 [66].

Pashan (2006) [2] investigated seventy-eight specimens by used the push-out test. A chanal was used as a shear connector. Also, an experimental model was proposed to calculate the capacity of the shear connector. The behavior of mode of failure and shear strength were revealed effects when change some parameters such as; length, height, and thickness of the channel, and then, the geometry of the deck slab, and finally, the compressive strength of the concrete. The results show the increment of compressive strength effects on the behavior of the slipping and increase the shear strength. The length of the channel also increases the shear strength and slip.

Hosain and Pashan (2006) [73] summarized the results of an experimental research program involving the testing of push-out specimens with channel shear

connectors. The test program consisted of thirty six push-out specimens each twelve these specimens divided into three series. In each series, six specimens had solid concrete slabs and the other six specimens had concrete slabs incorporating wide-rib profiled metal deck with ribs parallel to the beam. The compressive strength of concrete, length and web thickness of the channel shear connector represented the test parameters. The test results showed that the load carrying capacity of the channel connector increases almost linearly with the increase in the channel length. Also the influence of web thickness of the channel connector was significant when failure occurred due to channel web fracture but minimal for concrete crushing type failure.

Wang et al. (2011) [74] conducted twelve push-out test specimens of stud shear connectors with large diameter and high strength. It were noticed that the use of studs with large diameter and high strength can simplify the composite structure, save construction time and make the steel and the concrete work together better. In addition, the shear resistance and shear rigidity were higher than the normal studs used in composite structures and can be better used in bridge structures. Twelve specimens were conducted by considering different diameters and different strengths of studs, and were divided into 4 groups. The length of each stud was 200 mm, and the diameters were (22, 25, and 30) mm. The tested average compressive strength was 70.3 MPa after 28 days. Two specimens in each group were tested under monotonic load, and the other one was tested under cycle load. The shear resistance and shear rigidity of studs with large diameter and high strength are all-higher than the normal studs used in composite structures and can be better used in bridge structures.

Prakash et al. (2012) [75] modified a push-out test by estimated the shear strength connectors. A high strength stud, (HSS), was used. A novelty technique was adopted, which confined concrete to avoid splitting through the loading. Four push-out specimens were tested to determine the strength and stiffness of the shear

connectors. The specimens were loaded till failure and slip had happened in the interface of steel and concrete. The results were remarked that the average ultimate failure load reached to (528 kN). The design shear strength, which equalized to the quarter of ultimate was (132 kN). The mean stiffness value was (53.3 kN/mm^2), which close to the empirical equations. From this experimental study it can be concluded that the confinement concrete enhances the compressive strength as well as splitting resistance of concrete, also due to the confinement effect it is found that even narrow width of concrete slab can be used for push-out test with HSS stud connectors . Therefore the confinement effect must be considered while designing concrete slab for push out specimens.

Titoum et al. (2016) [76] presented the results of experimental study and finite element modeling of twenty four push-out test specimens on a new shear connector of I-shape were tested under a static loading. The effect of the height of I-shape connector, the length of I-shape connector, the compressive strength of concrete and the number of transverse reinforcing bars were represented the parameters study on the ultimate load capacity. Also an equation was suggested for the prediction of the ultimate load capacity of I-shape shear connectors. The comparison between the I-shape connector and the channel connector by the finite element analysis confirmed the similarity of their behavior. The results showed that in specimens with I-shape connectors of higher steel grade and concrete slabs of low and moderate strength, failure was caused by cracking and crushing of the concrete surrounding the connector.

Yanez et al. (2017) [77] proposed a modified version of push-out test to determine the stiffness coefficient of the shear studs, which it is essential to compute the deflection of composite open web joists. The stud stiffness coefficient depends on the location of the shear studs either in strong or weak position with respect to steel deck stiffener. Furthermore, in order to investigate lower capacities of shear connectors in comparison with 19 mm, 13 mm and 16 mm diameter connectors

were used. The results showed that the studs placed in the strong position enhanced deflection values by 5% average.

De Seixas and De Miranda (2020) [33] performed a series of experimental tests in order to provide reliable information in terms of shear strength, deformation capacity and mechanisms of collapse associated with eight push-out test specimens in order to evaluate the behavior of three types of shear connectors (TWP, TWC and TWVP) which their details were shown in Figure 2.15. The experimental results indicated the type of failure associated with the shear connectors, revealed after demolition of the concrete slabs. Two types of failures were observed; the TWP failure was related to large plastic deformation of the thin-walled plate (double Z section), followed by the rupture of the steel around the self-drilling screws. While TWC failure was associated with the rupture of the bottom flange of the connector (tearing between the self-drilling screws and the stiffener of the lipped channel).Regarding the TWVP shear connectors could not be investigated by push-out tests because of the early truss collapse, occurring prior to the rupture of the TWVP itself. Actually, the squash collapse of the CFS steel truss could not have been prevented, even with additional reinforcements, Figure 2.16.

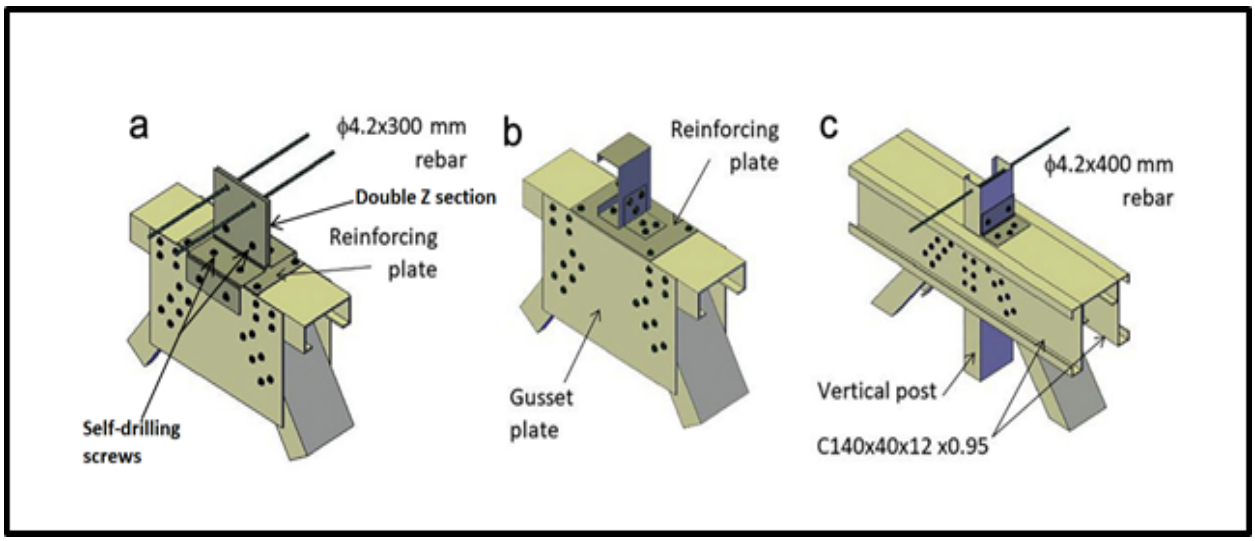

Figure 2.15 Innovative thin-walled CFS shear connectors: (a) thin-walled perfobond TWP, (b) thin-walled channel TWC, and (c) thin-walled vertical post TWVP [33].

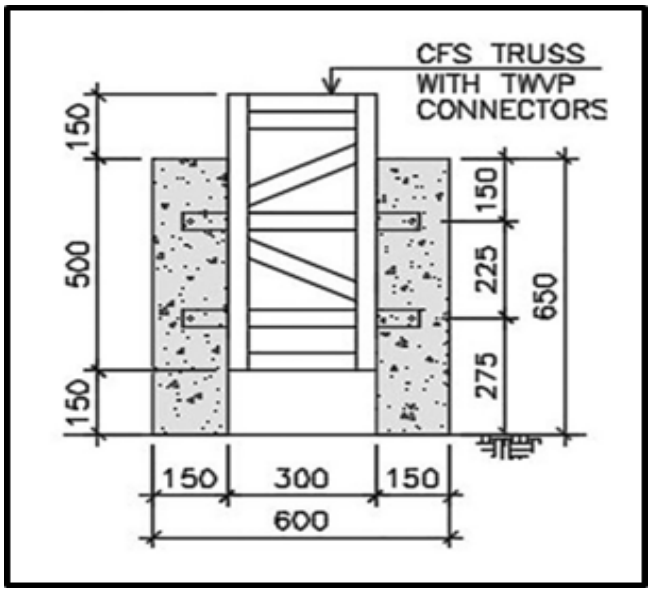

Figure 2.16 Set up of the push-out TWVP [33].

2.7 Conclusion Remarks

Based on the review of the literature, it is clear that, despite the fact that many studies have been conducted on the behavior of traditional HOWSJs and COWSJs, the majority of which used steel angles for interior web members, it was useful to extend previous works to prefabricate a new type of HOWSJ based on replacing these members by the waste of rebars, so it is a type of waste material management. Furthermore, there have been very few studies on the lateral buckling of HOWSJs.

Thus, the primary goal of this study is to investigate the performance of these new prefabricated HOWSJs that use less material by using rebar wastes as an interior web member and have a higher yield strength when compared to angles interior web members. These HOWSJs were then used to manufacture COWSJs using NC and SFC slabs, and their behavior was investigated across a number of variables. The second goal of this study was to conduct experiments in order to fully comprehend the lateral torsional buckling behavior of the prefabricated HOWSJs proposed in this study. Push-out tests were also performed in the current study to assess the shear resistance of a novel shear connector made from recycled rebars.

CHAPTER 3

EXPERIMENTAL INVESTIGATION

3.1 Experimental Program

The main target behind executing experimental tests was to investigate the behavior of new prefabricated hybrid steel joist girders supporting SFRC slabs that have been performed in this study and using the conducted results to compare and validate the theoretical results obtained in this research. Seventeen girders were tested under monotonic load, which were divided into two groups. Therefore, the experimental program was classified into two parts, the first part consisted of testing the first group of ten open web steel joist girders and the second part consisted of testing the second group of seven composite girders.

Two types of concrete used in the deck slab of composite specimens which was non fibrous concrete and steel fiber reinforced concrete. The composite girders consisted of open web steel joist and concrete deck slab, which were connected by a new type of mechanical shear connectors proposed in this study, thus the behavior of this type of connector was studied by achieving six specimens of push-out test to explain the load-slip relationship and the strength of the shear connectors used in this work.

Additionally, this chapter presents the fabrication procedure to produce specimens. Also the materials properties of steel and concrete which used in this work, instruments, and testing setup , are explained in this chapter.

3.2 First Group: Hybrid Open Web Steel Joists

3.2.1 Fabrication of Hybrid Open Web Joists

Ten prefabricated hybrid open web steel joists (PHOWSJs) specimens were tested in this study, which were divided into five pairs each pair consisted of two specimens according to the cross section shape models, plate 3-1. Since the study relied on the

manufacture of new types of steel joist, two specimens with the same geometry and material properties were manufactured for each model to know the real behavior of two specimens of the same model. All steel joists have the same span and were tested under the same boundary conditions. The program included investigating load-deflection behavior, failure mode, the lateral torsional buckling, and strain distribution along with the depth of steel joist. The variables adopted in this part of the study are:

1. The shape of the cross section of the joist.
2. The span to depth ratio of steel joists.
3. The effect of the diameter of interior web members.

Plate 3-1 Prefabricated hybrid open web Steel Joists specimens.

To fabricate the hybrid open web steel joist (HOWSJ) types used in this experiment a double angles (2L50×50×4mm) for both the top and bottom chord are connected by welding them together. The interior web members of different diameters of steel reinforcing bars were used to supply the required gap between the double angles of the top and bottom chords. After that, the joist seats were placed in their locations. Each open web steel joist was simply supported with a design length of (1800 mm) and overall span of (1900 mm). Initially, all the

individual components of steel joist were tack welding in their proper locations, then they were welded together using E6013 electrodes. Five models of (HOWSJs) were be fabricated in this study according to the shape of the cross sections, the diameter of reinforcing steel bars, and the height of specimens. The designation of the HOWSJ specimens was defined in Figure 3.1.

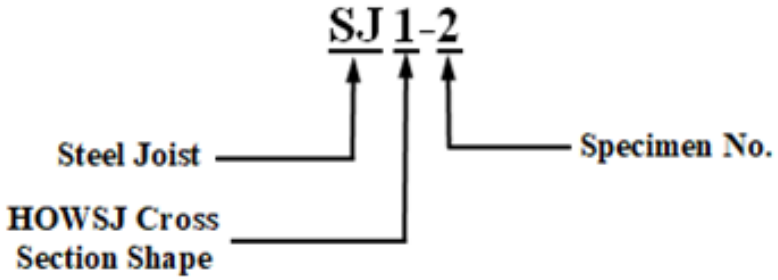

Figure 3.1 Designation of hybrid open web steel joist specimen.

Figure 3.2 illustrates the details of (HOWSJs) and the shape of cross section. The nominal cross section dimensions and properties of these sections are shown in Table 3.1 were the moments of inertia of (PHOWSJs) was calculated as a built up section, the overall depth of the joist is (h), and (d) is the depth between the centre-lines of the top and bottom angles. $d = h - (2y')$, where y' is the centerline of the angle (50×50×4) =13.6 mm. The details of each group can be simplified as illstrate in the next subsections:

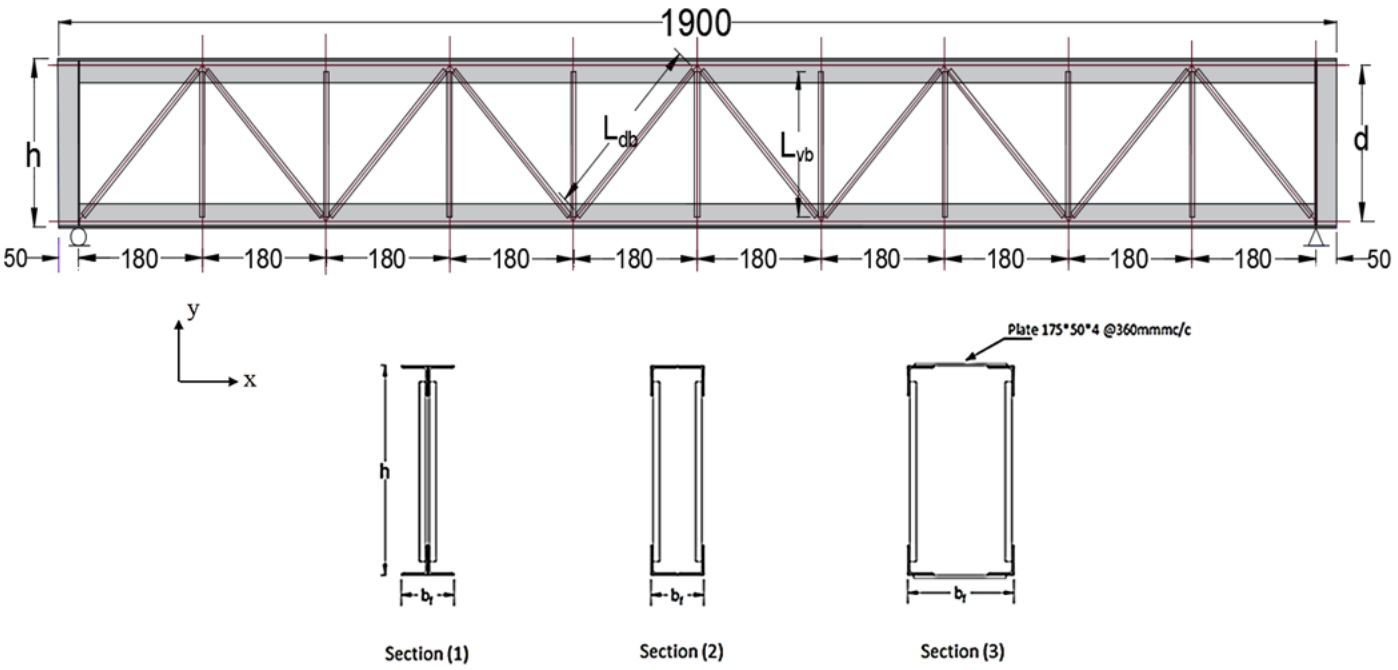

Figure 3.2 Prefabricated hybrid open web steel joists (all dimensions are in mm).

Table 3.1 Nominal cross section dimensions and sections properties of (PHOWSJs).

Models	Specimen No.	Cross Section Shape	Dimensions (mm)						Moment of Inertia (mm^4)	
			b_f	d	h	L_{db}	L_{vb}	d_b	I_x	I_y
Model A	SJ 1-1 SJ 1-2	Section-1	100	322.8	350	357	305	11.97	40892537.76	646597.76
Model B	SJ 2-1 SJ 2-2	Section-2	100	322.8	350	357	305	11.97	40892537.76	2420437.76
Model C	SJ 3-1 SJ 3-2	Section-3	200	322.8	350	357	305	11.97	40892537.76	11974277.76
Model D	SJ 4-1 SJ 4-2	Section-1	100	472.8	500	495	455	11.97	87315797.76	646597.76
Model E	SJ 5-1 SJ 5-2	Section-1	100	472.8	500	495	450	15.85	87315797.76	646597.76

3.2.1.1 Details of Steel Joists of Model A (SJ1-1 and SJ1-2)

The steel joists had an overall depth of (350 mm). The joists were fabricated by welding the both vertical and horizontal legs of angles of top and bottom chords back to back every (100) mm space. Then for web members a reinforcing steel bars with diameter of (11.97 mm) were used for the diagonal and vertical members on both sides of the joist with length (357 mm) and (305mm) respectively were welded at distance (13.6 mm) from top and bottom chords. At the ends of the model a double vertical angles were be welded, Plate 3-2.

Plate 3-2 welding between angles of top and bottom chords and the shape of cross section of Models A, D, and E.

3.2.1.2 Details of Steel Joists of Model B (SJ2-1 and SJ2-2)

The steel joists had an overall depth of (350 mm). The joists were fabricated by welding the web members of reinforcing steel bars with diameter of (11.97 mm) for the diagonal and vertical members with length (357 mm) and (305mm) respectively at distance (13.6 mm) from top and bottom chords at the first and second faces of the steel joist were prepared at first separately. Then, the two parts of steel joist faces were connected by welding the horizontal legs of the top and bottom chords

face to face every (100) mm space. At the ends of the model a double vertical angles were be welded, Plate 3-3.

Plate 3-3 Welding between angles of top and bottom chords and the shape of cross section of Model B.

3.2.1.3 Details of Steel Joists of Model C (SJ3-1 and SJ3-2)

The steel joists had an overall depth of (350 mm). The joists were fabricated by welding the web members of reinforcing steel bars with diameter of (11.97 mm) for the diagonal and vertical members with length (357 mm) and (305mm) respectively at distance (13.6 mm) from top and bottom chords at the first and second faces of the steel joist were prepared at first separately. Then, the two parts of steel joist faces in this model which is face to face with gap , the connecting of the horizontal legs of the two angles of top and bottom chords was made by welding a plate of dimensions (175×50×3.8) mm @ 360 mm centre to centre between them, five plates for top chord and six plates for bottom chord. Also a double vertical angles at the ends of (OWSJ) were be welded, Plate 3-4.

Plate 3-4 Welding between angles of top and bottom chords and the shape of cross section of Model C.

3.2.1.4 Details of Steel Joists of Model D (SJ4-1 and SJ4-2)

The steel joists had an overall depth of (500 mm). The joists were fabricated as same as the method of the model A but the differences are the length of web members of the diagonal and vertical members which are (495 mm) and (455 mm) respectively with diameter of (11.97 mm) reinforcing steel bars, Plate 3-2.

3.2.1.5 Details of Steel Joists of Model E (SJ5-1 and SJ5-2)

The steel joists had an overall depth of (500 mm). The joists were fabricated as same as the method of the model A but the differences are the length of web members of the diagonal and vertical members which are (495 mm) and (450 mm) respectively and the diameter of reinforcing steel bars was (15.85 mm), Plate 3-2.

3.2.2 Materials Properties of Hybrid Open Web Steel Joist Girders

The term Hybrid Steel Joist Girder means that more than one type of steel section has been used in the manufacture of this girder, or in other words, the hybrid steel girder does not consist of one homogeneous material, so it was necessary to test the material properties of each of these types of steel to study the behavior

of prefabricated hybrid steel joist accurately. These material properties are determined by conducting a tensile test for each type of steel section used in this study.

3.2.3 Properties of Steel Sections Used in Steel Joist Fabrication

Tensile tests were performed in a universal testing machine according to the requirements of ASTM A370-15 [78] to tested the mechanical properties of all steel sections which are used in this study. Curves of all tests included a negative elongation that refers to the slip occurs in the initial loading stage. All samples were tested in the state Company for Inspection and Engineering Rehabilitation/ministry of industrial and minerals of Iraq in Baghdad, Plate 3-5.

Plate 3-5 Universal testing machine and specimen during tensile testing.

The results of tests of the steel materials which were used to fabricate the steel joists specimens are listed as follows:

3.2.3.1 Properties of Steel Angles of Top and Bottom Chords, and Plate of 3.8 mm

Three tension coupons were cut from the two legs of angle (50×50×4)mm, also three coupons from plate with thickness (3.8 mm) which used in model C by Computer Numerical Control (CNC) machine. The shape and dimensions of the standard testing coupon were depicted in Figure 3.3.The tensile test results are presented in Table 3.2 which conform to the requirements of ASTM A36/A36M specifications [79],Table 3.3. Also Figure 3.4 and Figure 3.5 observed stress-strain curves of these coupons resulted from the computer of the Universal Testing Machine.

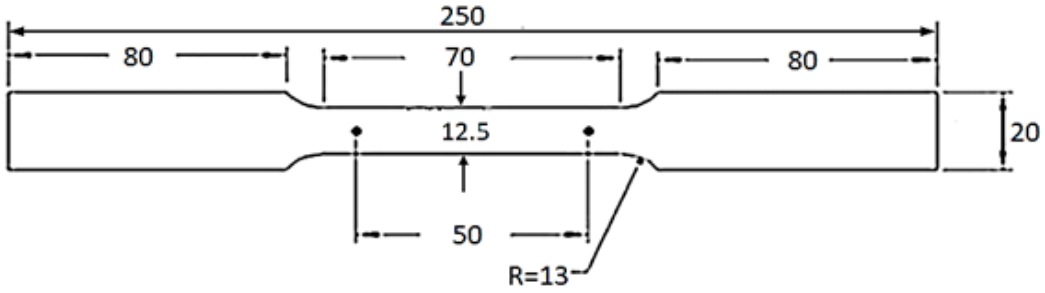

Figure 3.3 Dimensions of standard test specimens (all dimensions in mm).

Table 3.2 Tensile test results of the angle and plate coupons.

Specimen		Yield Strength (F_y) (MPa)	Ultimate Tensile Strength (F_u) (MPa)	Modulus of Elasticity (MPa)	Elong. (%)
Angles (50×50×4)	1	331.86	428.53	207115	43.58
	2	350.56	478.89	208820	41.24
	3	322.35	439.31	208023	43.37
	Ave.	334.92	448.91	207986	42.73
Plate (3.8 mm)	1	324.67	429.16	208730	47.88
	2	313.43	424.87	208260	47.86
	3	327.57	425.96	209650	47.98
	Ave.	321.89	426.66	208880	47.91

Table 3.3 ASTM A36/A36M specifications requirements for steel plate.

Min. Yield Strength, F_y (MPa)	250
Min. Ultimate Tensile Strength, F_u (MPa)	400-550
Min. Elongation % at Break	20% in (200mm) and (23%) in 50 mm

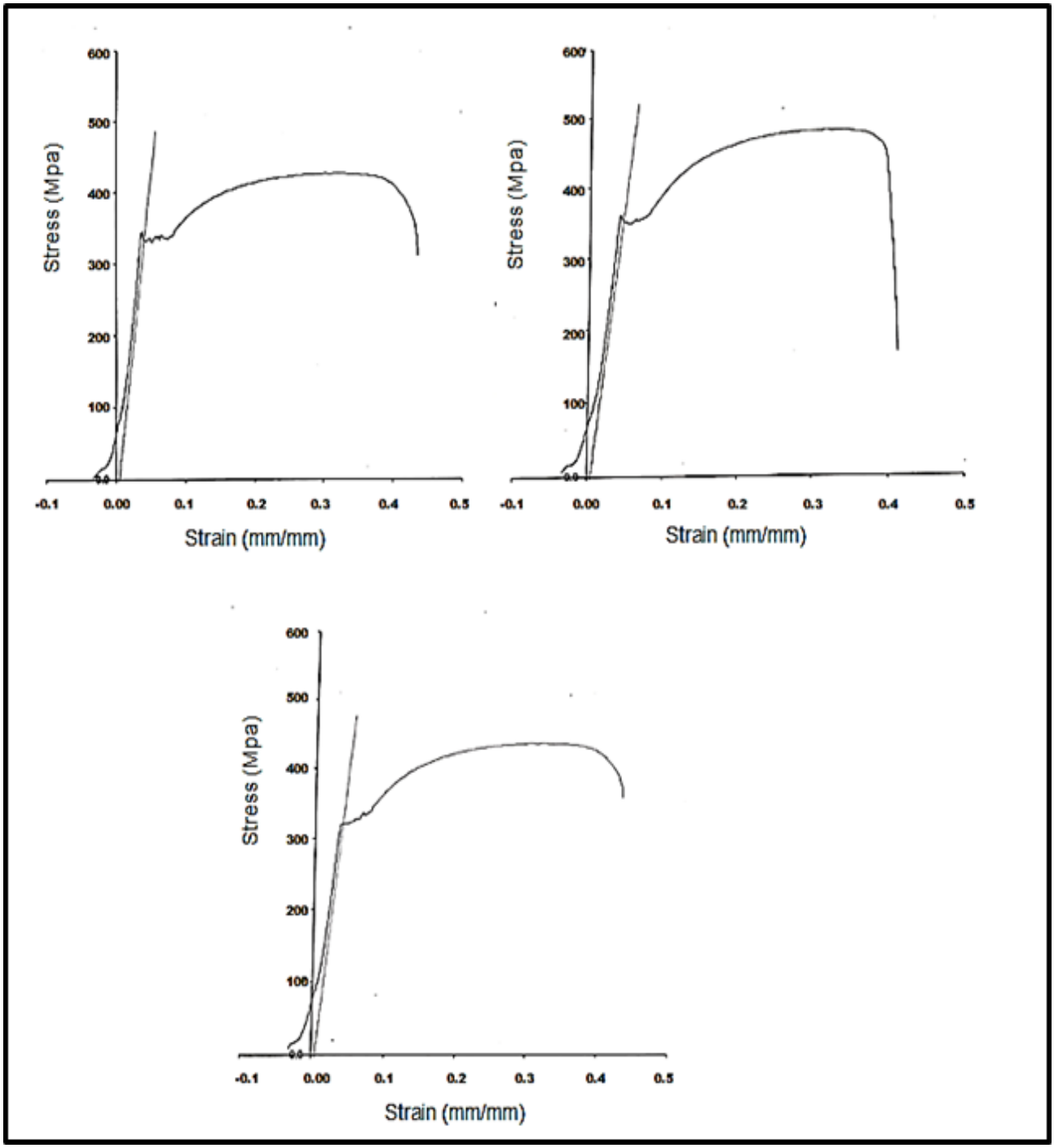

Figure 3.4 Stress- strain curves of angles of top and bottom chords.

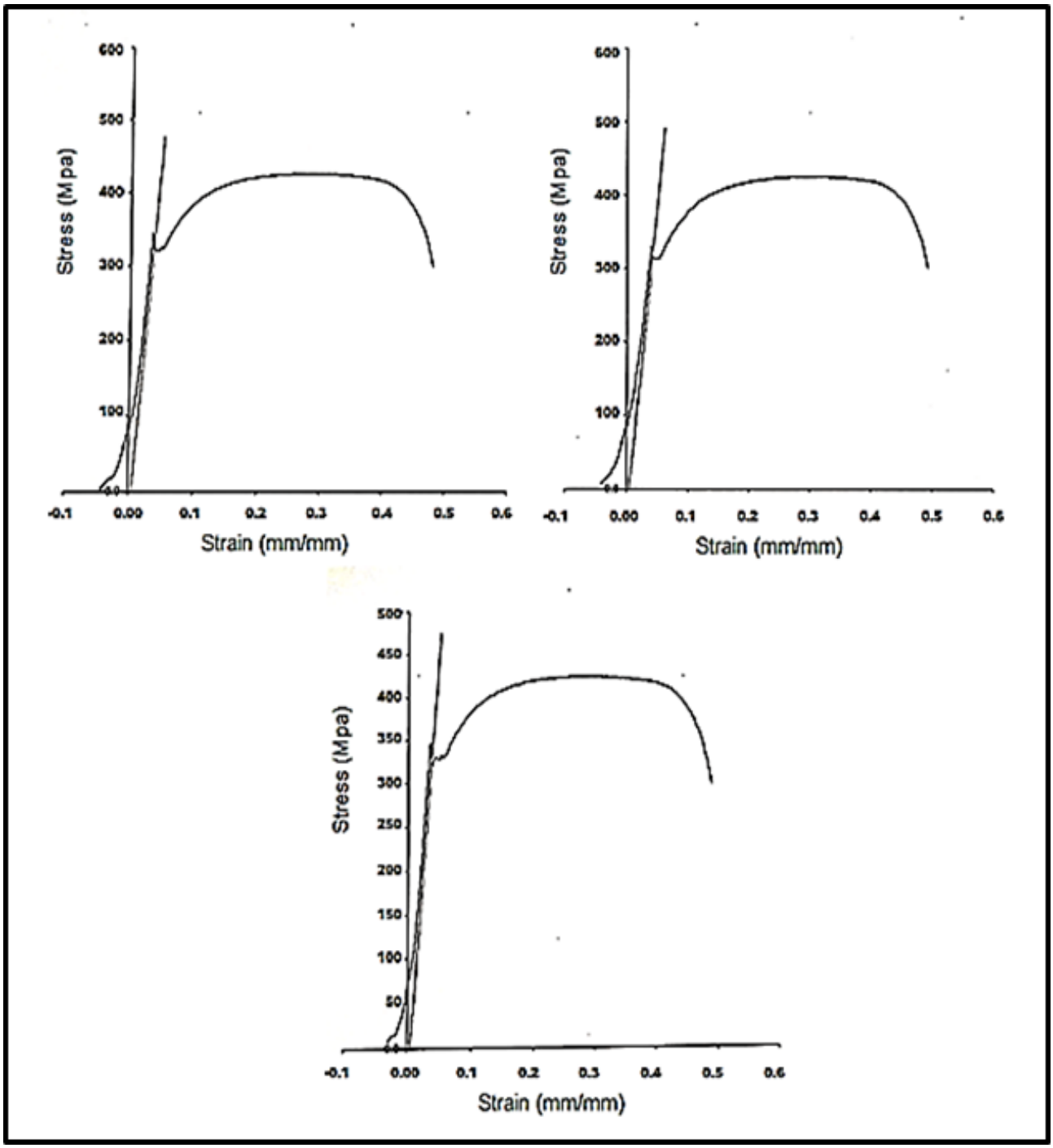

Figure 3.5 Stress- strain curves of plate (3.8mm).

3.2.3.2 Properties of Reinforcing Steel Bars

Deformed reinforcing steel bars were used in the experimental work with diameters (12 mm and 16 mm) as an interior web members. All the reinforcing bars utilized with different diameters have been subjected to a tensile test in the laboratory. The length of specimens was (500 mm) and the gage length was (203mm). The actual

diameter for reinforcement bars was computed by the weight method as shown in Table 3.4 which also show that the results of tensile test for reinforcing bars was conformed to the properties prescribed by the specification according to ASTM A615/A615M-08a [80] as shown in Table 3.5. Also the stress- strain curves of each specimen is represented in Figures 3.6 and 3.7.

Table 3.4 Tensile test results of the reinforcing steel bars .

Reinforcing steel bar		Specimen No.	Yield Strength, F_y (MPa)	Ultimate Tensile Strength, F_u (MPa)	Modulus of Elasticity (MPa)	Elongation%
Nominal Diameter (mm)	Measured Diameter (mm)					
Rebar 12	11.97	1	556.24	651.11	200957	16.72
		2	559.08	659.50	208333	17.37
		3	547.01	658.05	204300	16.59
		Ave.	554.11	656.22	204530	16.89
Rebar 16	15.85	1	544.45	677.47	205056	19.31
		2	607.31	670.79	208531	16.80
		3	552.73	677.39	201755	18.13
		Ave.	568.16	675.22	205114	18.02

Table 3.5 ASTM A615/A615M-05a specifications requirements for reinforcing bar.

Min. Yield Strength, F_y (MPa)	420
Min. Ultimate Tensile Strength, F_u (MPa)	550
Min. Elongation% at Break	9 % in (200 mm)

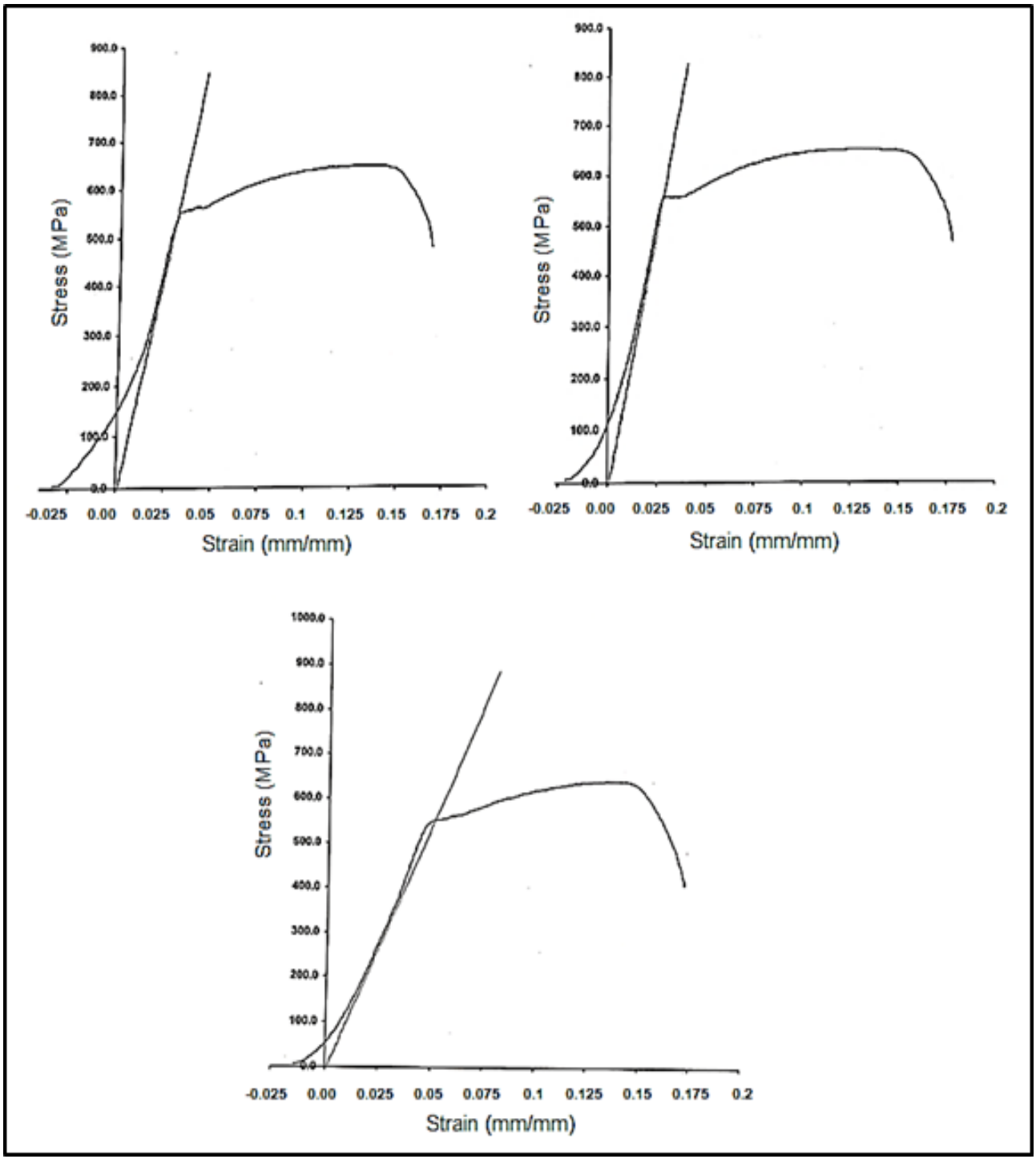

Figure 3.6 Stress- strain curves of reinforcing Bar (12 mm).

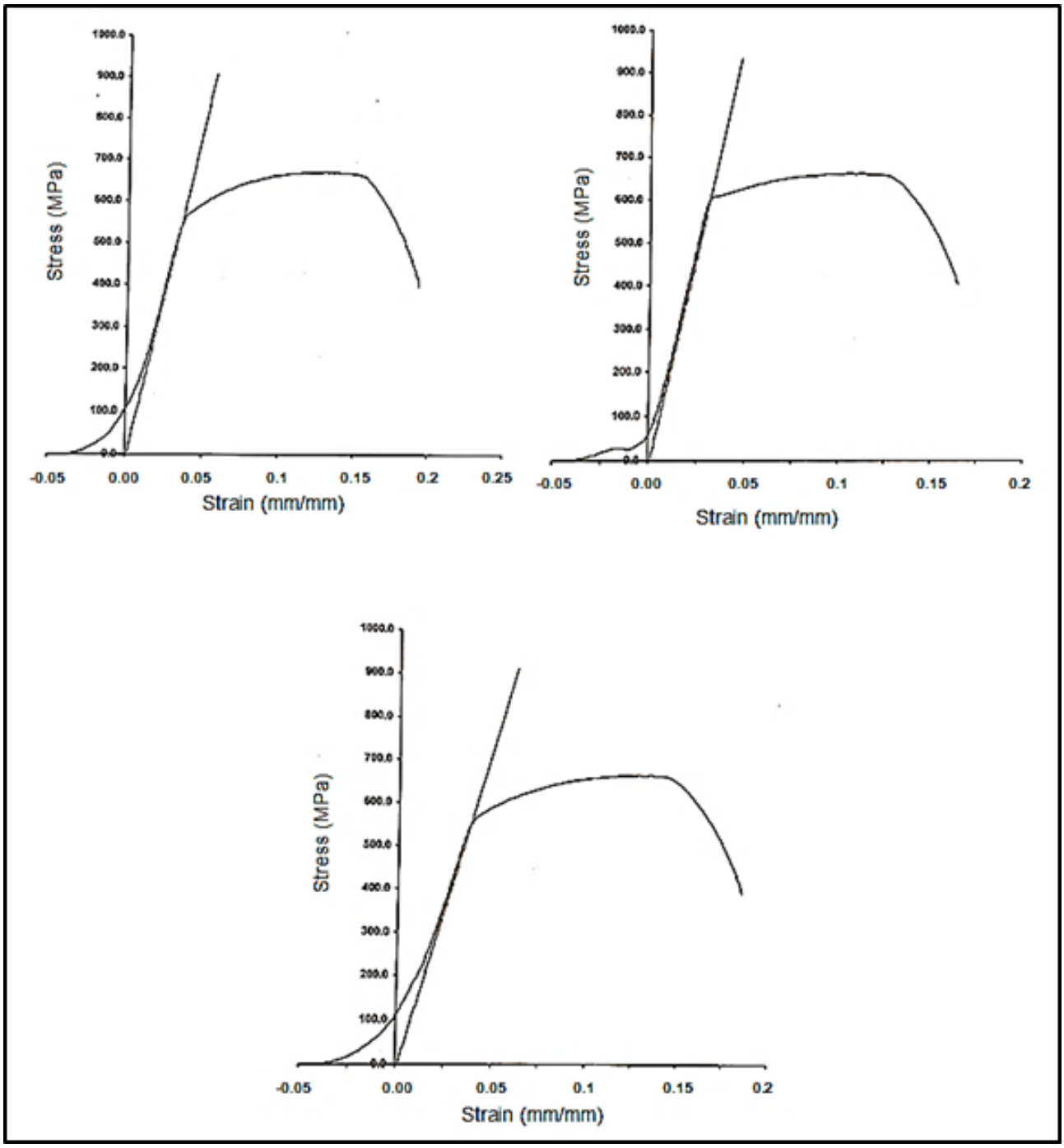

Figure 3.7 Stress- strain curves of reinforcing bar (16 mm).

3.3 Welding Electrode

The type of welding which used to welded all specimens in this study was E6013 welding electrode using (SMAW) arc welding, plate 3.6. Welding Electrode AWS E6013 is a low carbon steel electrode with high titanium-potassium type coating, and suitable for both AC and DC. It is able to provide excellent welding

technological performance, because the arc is extremely stable, and spatter loss is negligible. The slag has good fluid, and solidified slag is very easy to remove. The manipulate is free, and restrike is easy. It can give smooth and beautiful ripples. The welding by using E6013 can be done in flat, overhead, horizontal and vertical (upwards). The chemical composition of E6013 electrode is shown in Table 3.6.

Plate 3-6 Welding electrode type.

Table 3.6 Welding electrode AWS E6013 chemical composition.

Chemical Composition	C	Mn	Si	S	P	Ni	Cr	Mo	V
Guarantee Value	$\leqslant 0.2$	$\leqslant 1.2$	$\leqslant 1.00$	$\leqslant$ 0.035	$\leqslant 0.04$	$\leqslant 0.3$	$\leqslant 0.2$	$\leqslant 0.3$	$\leqslant 0.08$
General Result	0.079	0.380	0.210	0.018	0.024	0.020	0.032	0.005	0.010

Many researches were be done to find the mechanical properties of welded joints using electrode E6013, in this study the results were obtained by Nasser et al.[61] which were very closely to the AWS A5.1 requirements [81] as shown in Table 3.7, and which will be used in representation of welding in the numerical analysis.As mentioned previously in Section (2.5), Nasser et al. research adopted different welding electrodes E6013 and E7018 were considered as welding parameters investigated. Tensile test specimens were prepared according to ASTM standard E8/E8M-09 [62].

Table 3.7 Tensile test results of welding electrode AWS E6013 [61].

Test results			AWS A5.1			
F_y (MPa)	F_u (MPa)	Elong. (%)	Min. F_y (MPa)	Min. F_u (MPa)	Min. Elong. (%)	
327	432	30	330	430	17	

3.4 Steel Joists Testing and Instruments

Different instruments were used in the test program of steel joists were prefabricated in the present study, such as the hydraulic testing machine, linear variable displacement transducers, digital dial gauge and strain gauges.

3.4.1 Testing Machine

Ten prefabricated steel joists were be tested by using a hydraulic testing machine with capacity 1000 kN available at Structures Laboratory of Civil Engineering at Kufa University as shown in Figure (3.8). The loading process was monitored by a load was applied between the Hydraulic jack and top chord of steel joists.

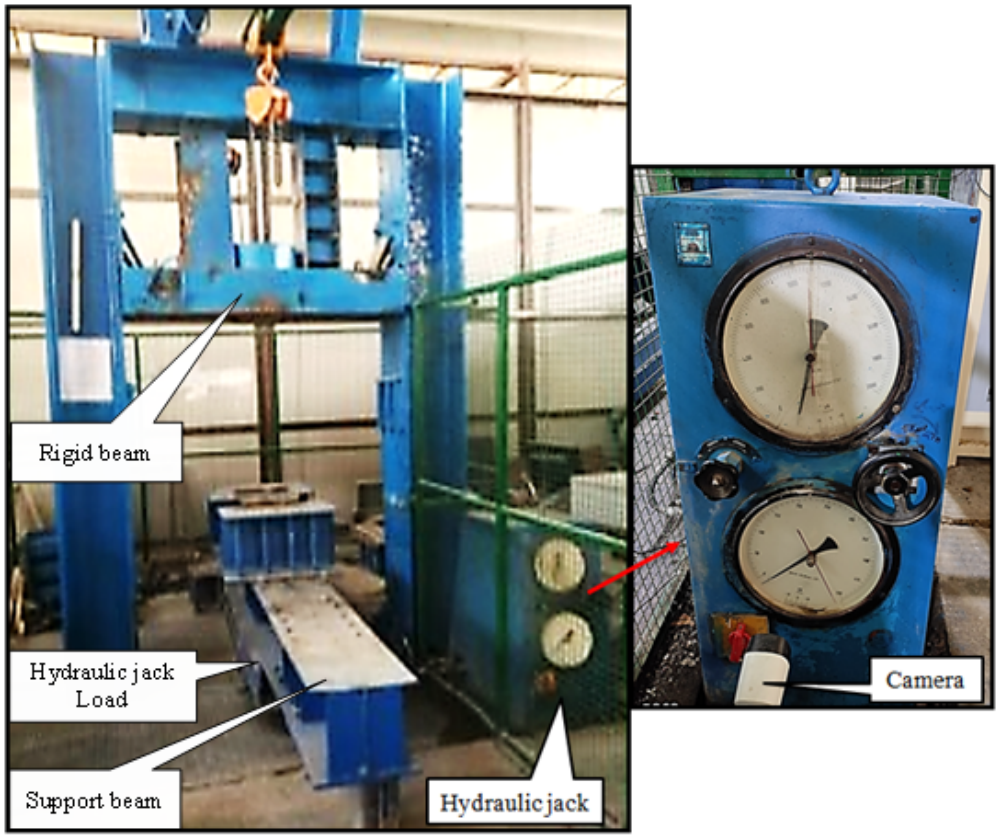

Figure 3.8 Universal testing machine.

3.4.2 Loading and Supporting Conditions

All steel joist specimens were tested under the effect of monotonic load. A central single concentrate load was applied on the top chord up to failure by using steel shaft with diameter (25 mm) and the deflection was recorded by using two digital dial gages one put at quadrature of span and the other put at third point of this simply supported joists which has been watched by using cameras. While the mid span deflection was recorded by using Linear Variable Displacement Transducer (LVDT). Also the lateral displacements at the centerline of all joist specimens were recorded by using (LVDT) for the top chord and a digital dial gauge for the bottom chord of the joist specimens which also watched by another camera. The specimens were prepared and plotted to locate the position of supports, application of load, the positions of the (LVDT), digital dial gauges, and strain gauges. Details of steel joist setup, and lateral displacement gauges are shown in Figure 3.9.

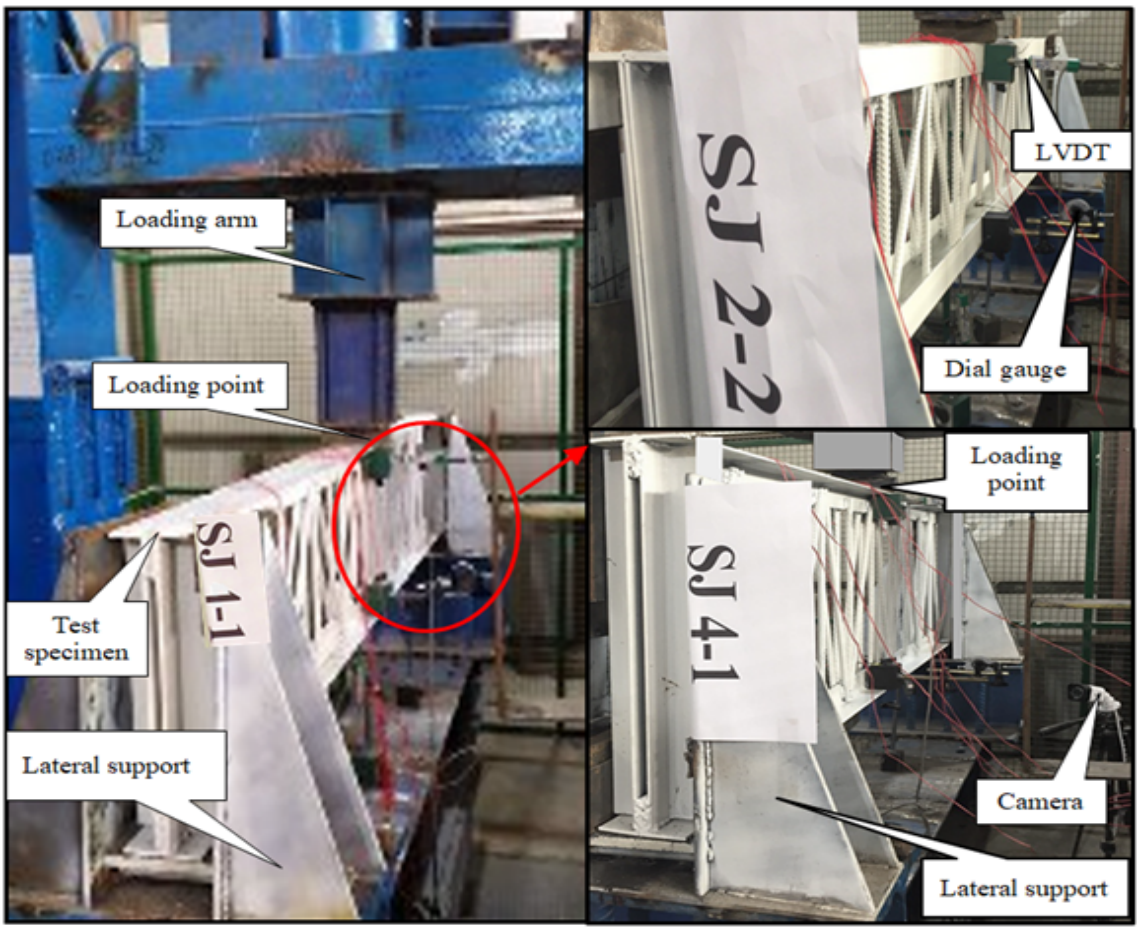

Figure 3.9 Typical instruments arrangement of OWSJ girders surfaces.

Four sizes supports have been used in this work which were manufactured by using steel plate with thickness of (6 mm) to represent the simply supported case (roller and hinge) were used with stainless steel shafts with diameter (50 mm) welded to the support at the ends of beam. The beam supports restrained for lateral torsional buckling that prevent the lateral deflection and twist rotation as possible in the ends of the steel joist specimen during the test, this shape of support called fork support. Thereby, the length between lateral support points that were braced against lateral deformation of compression flange and braced against twist. The details of cutted plates used to manufacture the fork end supports and their final details and shapes were illstrate in Figure 3.10.

Figure 3.10 Details of fork end supports.

3.4.3 Linear Variable Displacement Transducers (LVDT)

Two Linear Variable Displacement Transducers (LVDT) were used, Plate 3.7. One of them was measured a vertical deflection at the bottom of the mid-span of the joist, Figure 3.11 , and the other one was located laterally at the top chord at the middle span of the steel joist to measure the top lateral displacement (out of plain deformation) as shown in Figure 3.9. The minimum division could be measured by about 0.01mm with a slight effect of electrical noises.

3.4.4 Digital Dial Gauges

Three digital dial gauges as shown in Plate 3.8 were used in the present test. Two of them was put in two different positions to measure the vertical deflection at quarter and third span, as shown in Figure 3.11. Whereas the third dial gauge was set at bottom chord to measure the bottom lateral displacement in the middle span of the steel joist, as shown in Figure 3.9.

The maximum capacity of digital dial gauges used is 50 mm with resolution 0.01 mm. Four cameras were used in the test. Each dial gauge was coupled with a camera to monitor the dial gauge readings, other camera used to monitor the load from hydraulic jack, and an additional camera to monitor the screen that shows the results of data logger and all these cameras were connected to a computer.

Plate 3-7 Photograph for linear variable displacement transducers(LVDT).

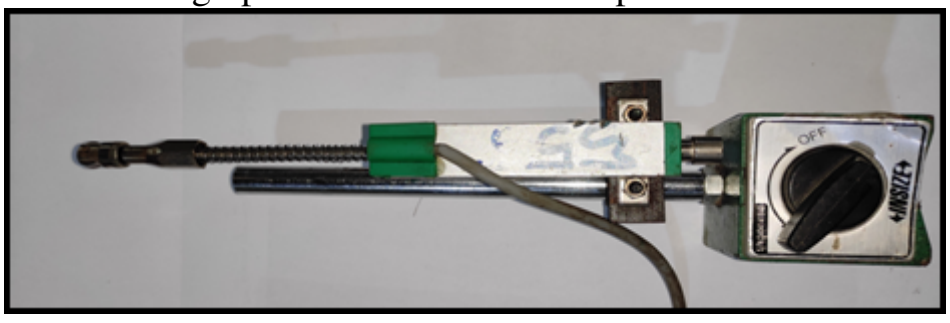

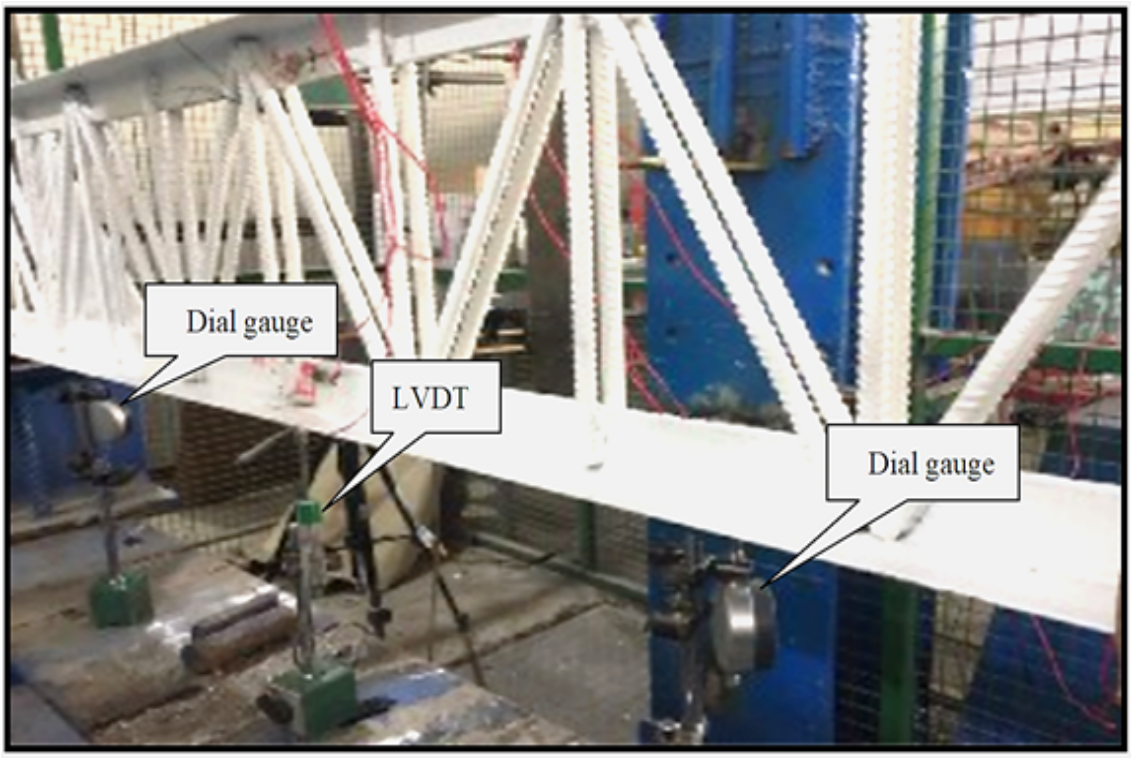

Figure 3.11 Positions of the (LVDT) and dial gauges for measuring the deflection of the steel joist.

Plate 3-8 Photograph for digital dial gauges.

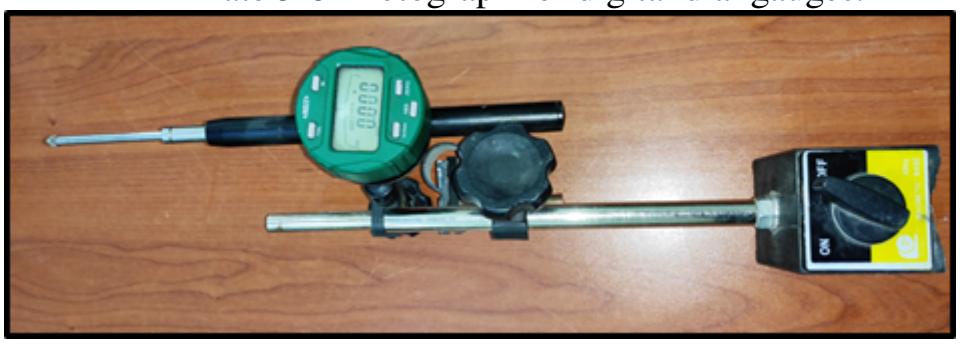

3.4.5 Strain Gauges

A set of an electrical strain gauge sensors for steel were used at a different locations in this study to investigate suitable information of strains in the PHOWSJ models. For each steel joist specimen six (KFGS-5-120-C1-11L5M2R) strain gauges were attached on the joists which was imported with its own adhesive material from (Kyowa Electronic Instruments Co., Ltd, Japan). The strain gauge factor at (23 °C, 50% R.H.) is 2.06 ± 1%, its length is 5 mm and the gauge electric resistance is 120.4 ± 0.4% with transverse sensitivity ratio of 0.3 ± 0.2%, Plate 3.9. The

surfaces of the places where the strain gauges sensors were placed must be cleaned with special paper with acetone before applying its special adhesive. They were fixed at the top and bottom chords of the steel joists, as well as on the interior web members, so that their locations were in the places where the maximum axial tension and compression stresses were expected to occur. Also Plate 3.10 shows their locations for different models.

The strain gauges of top chord were at a certain distance from the centreline of the steel joists to avoid error data, which could be produced due to direct stress of applied vertical load, and depending to manufacturing instructions, also for bottom chord. Figure 3.12a shows the locations of all strain gauges, LVDT, and dial gauges for the steel joists and the position of strain gauges for all cross sections of models were shown in Figure 3.12b.

Plate 3-9 Strain Gauges for the Steel surfaces.

Plate 3-10 Locations of strain gauges for different models.

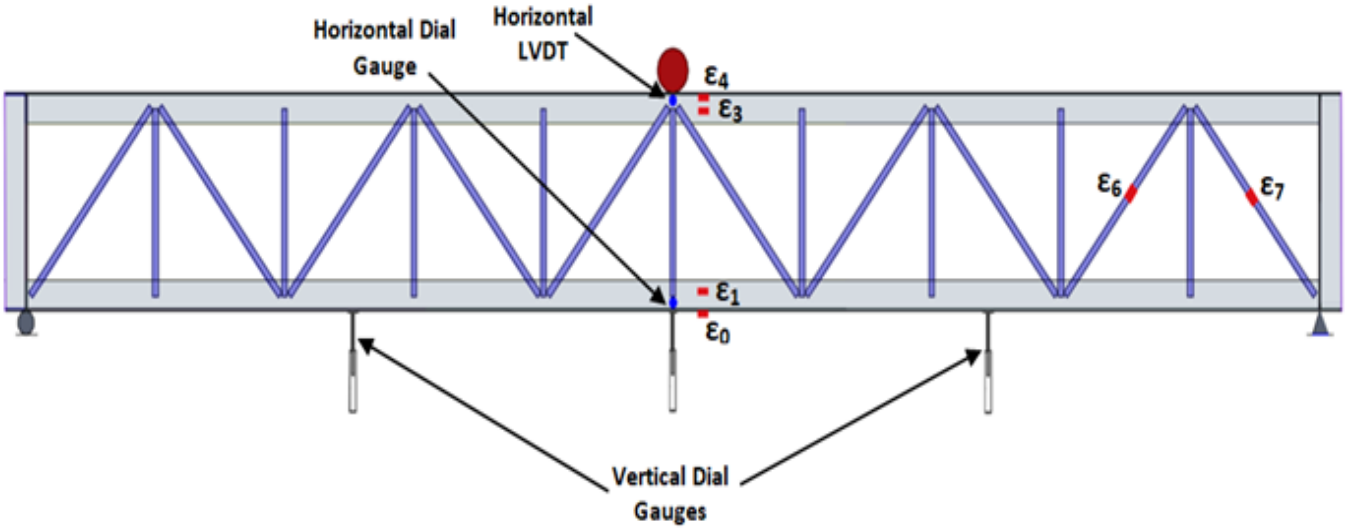

(a): Strain Gauges, LVDT Sensors, and Dial Gauges Arrangement for the OWSJ Girder surfaces.

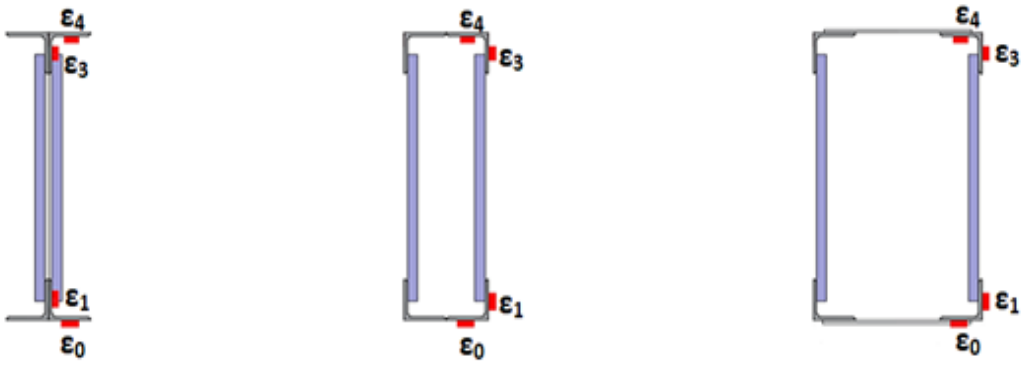

(b): Strain Gauges at Top and Bottom chords of OWSJ Girders surfaces.

Figure 3.12 Typical instruments arrangement of OWSJ girders surfaces.

3.4.6 Data Logger System

All the strain gauges and LVDTs were connected to data acquisition system to record the readings of them. The output results were then converted to data using LabVIEW software package. Plate 3.11 shows the data acquisition used.

Plate 3-11 Photograph for the data logger and the screen of cameras.

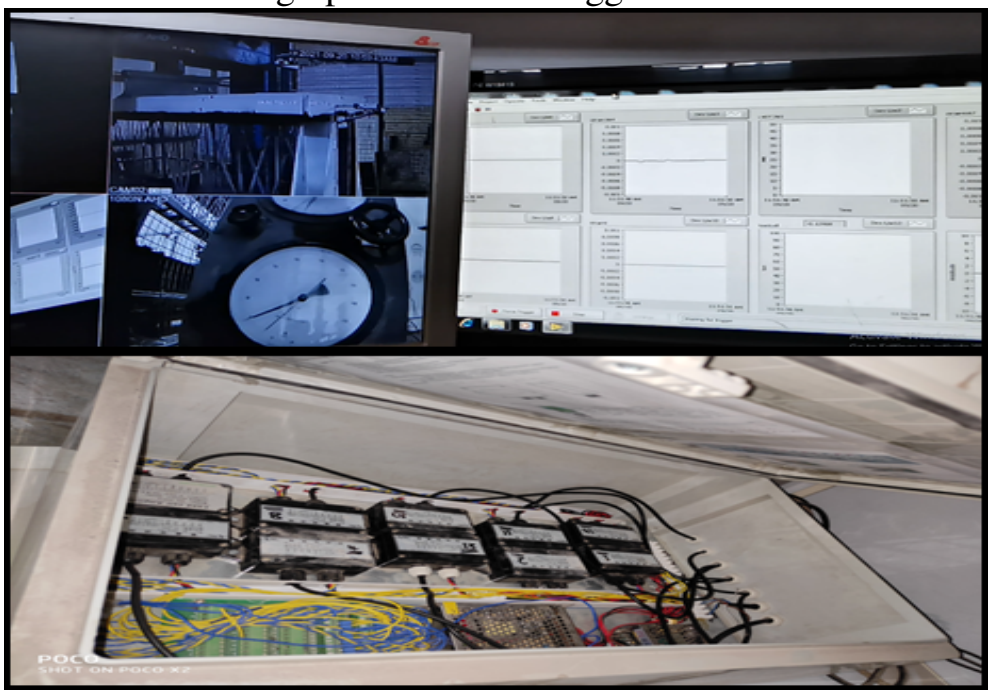

3.5 Second Group: Composite Open Web Steel Joist Girders

3.5.1 The Geometry and Construction of COWSJ Girders

Seven composite open web steel joists (COWSJs) specimens were adopted in this study, each (COWSJ) was simply supported with a design length of 1800 mm and overall span of 1900 mm. The (COWSJs) were fabricated by using either steel fiber reinforced concrete or non fibrous concrete cast placed over the same three section of (HOWSJs) which they were investigated in the first group of the experimental work. The material and geometrical properties of open steel joist girders were similar to steel joist girders models A, B, and C. These Steel girders have been explained in sections (3.2.1.1), (3.2.1.2) and (3.2.1.3).

Four variables were investigated on these specimens, which are:

1. The shape of the cross section of steel open web joist.
2. The span to depth ratio of HOWSJs, whether 5.1 or 3.6.
3. Type of the concrete slab, five of the total specimens were cast with steel fiber reinforced concrete (SFRC), while the other two were cast with non fibrous concrete (NC).
4. The effective width of the concrete slab deck.

The designation details of the composite open web steel joist specimens was defined in Figure 3.13. Table 3.8 summarizes the details of the composite open web steel joist specimens. Figure 3.14 show the details and dimensions of composite girders specimens fabricated in the present work subjected to monotonic load at the mid-span.

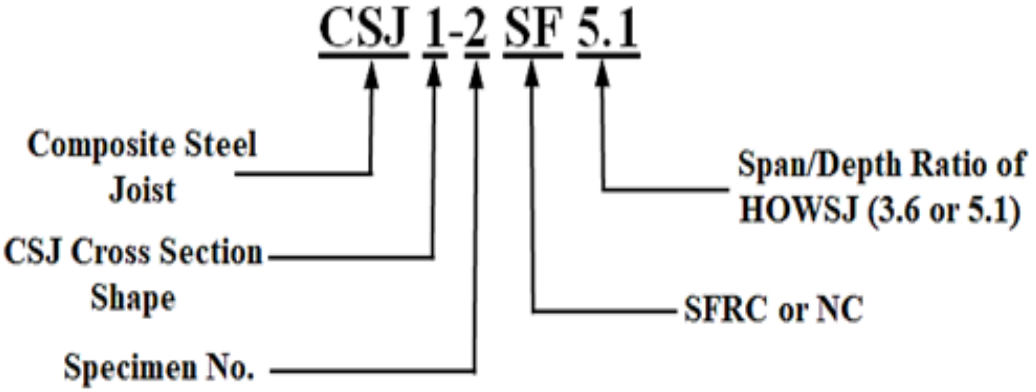

Figure 3.13 Designation of the COWSJ specimen.

Table 3.8 Details and dimensions of the COWS joist specimens.

Specimen No.	HOWSJ Cross Section Shape	Depth of HOWS, $h_j (mm)$	Chord Width of HOWSJ, (mm)	Span/Depth Ratio of HOWSJ, (L/D)	Effective Width of Concrete Slab, $b_e (mm)$
CSJ 1-1 SF 5.1	Section (1)	350	100	5.1	400
CSJ 2-2 SF 5.1	Section (2)	350	100	5.1	400
CSJ 3-3 SF 5.1	Section (3)	350	200	5.1	400
CSJ 3-4 SF 5.1	Section (3)	350	200	5.1	500
CSJ 3-5 N 5.1	Section (3)	350	200	5.1	500
CSJ 3-6 SF 3.6	Section (3)	500	200	3.6	500
CSJ 3-7 N 3.6	Section (3)	500	200	3.6	500

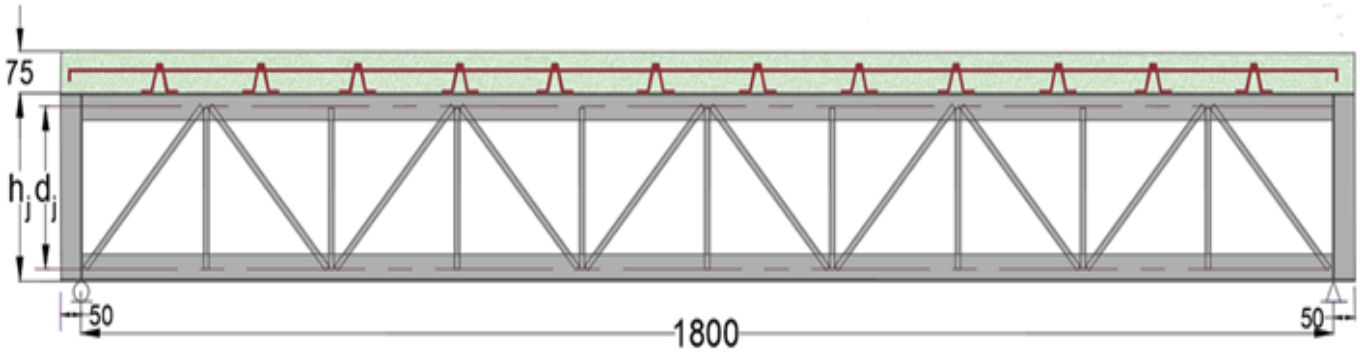

(A) Longitudinal schematic drawing of COWSJ.

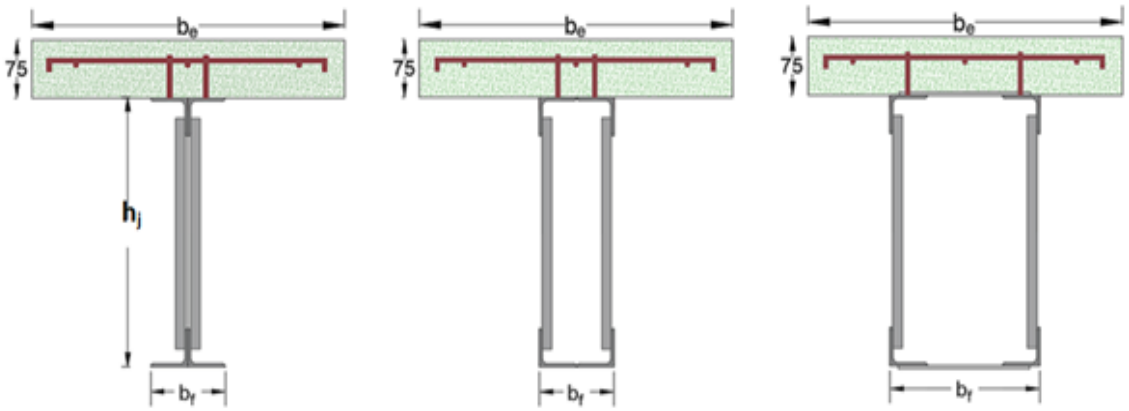

(B) Cross sections shapes of the COWSJ.

Figure 3.14 Details of the COWSJ specimens.

3.6 Materials of the Concrete Deck Slab

The materials which were used to produce a non fibrous and fiber reinforced concrete were be tested according to American Society for Testing and Materials (ASTM) and Iraqi Standards (IQS) to determine the properties of materials.

3.6.1 Cement

Among the many types of Ordinary Portland cement available in the local market, most of the researchers used three types of cement, and these types are AL-JESSER, KARASTA and Al-MASS Portland cement. In order to use the best types of cement in the manufacture of concrete used in this study, some results of the researchers' tests for the compressive strength of some of these types were reviewed, the test was at the age of three and seven days according to the Iraqi Standard Specification, and the results of the compressive strength of the cube of their tests were listed in Table 3.9.

Table 3.9 Compressive strength of some types of ordinary cement [82],[83],[84].

Cement Type	Compressive strength, (f_{cu}) MPa.	
	3 Days	7 Days
AL-JESSER, Ordinary	19.43	26.2
KARASTA, Ordinary	21.05	34.5
Al-MASS, Ordinary	24.4	32.3

The results of the researchers test shown in the Table 3.9 above proven that the ordinary cement type KARASTA as Portland-limestone cement type CEM II/A-LL the gave the highest compressive strength at age of seven days, so this type was used in this study. This type of cement is produced by LAFARGEHOLCIM, Karbala Cement Manufacturing Limited, KCML. The chemical and physical properties of that cement are listed in Table 3.10 which was conformed with the requirements of the Iraqi Standard Specification No.5/1984 [85], these results were obtained by the

laboratories of Engineering Consulting Bureau at the University of Kufa/ Faculty of Engineering.

Table 3.10 Chemical and physical properties of KARASTA, ordinary cement.

Chemical Properties of Cement			
Chemical Composition		Test Results,% by weight	Allowable Limits According to IQS No.5:1984
CaO %		61.25	Not limited
SiO_2%		19.86	Not limited
Al_2O_3%		3.38	$\leqslant 6$
Fe_2O_3%		4.72	$\leqslant 6$
MgO %		1.87	¡ 5
SO_3%		2.28	¡ 2.8
Free Lime Free CaO		1.56	4
Lime saturation factor		0.97	(0.66 -1.02) %
Loss on Ignition		2.44	$\leqslant 4$
Insoluble Residue		0.85	$\leqslant 1.5$
C_3S%		62.80	Not limited
C_2S%		8.35	Not limited
C_3A%		5.04	$\leqslant 8$
C_4AF%		11.19	Not limited
Physical Properties of Cement			
Setting Time	Initial(min.)	70	$\geqslant 45min$
	Final(min.)	250	$\leqslant 600min$
Fineness (Blaine Method)(cm^2/g)		3080	$\geqslant 2500$
Compressive Strength, (MPa)	3 Days	18.39	¿15
	7 Days	29.52	¿23

3.6.2 Fine Aggregate

The natural fine aggregate passed 4.75 mm sieve with fineness modulus of 2.73 used in this work was brought from (Al-Nawafith Company for producing sand and gravel filters) in Al-Najaf, which comply with the Iraqi specifications (IQ.S

45/1984) Zone (2) [86] and ASTM C33/C33M specifications [87]. Table 3.11 shows the grading of the used sand.

Table 3.11 Grading of fine aggregate.

Sieve No.	Sieve size, (mm)	% Passing		
		Fine Aggregate	IQS No. 45 Zone (2)	ASTM C33/C33M
No.4	4.75	96	90-100	95-100
No.8	2.36	88	75-100	80-100
No.16	1.18	82	55-100	50-85
No.30	0.6	43	35-59	25-60
No.50	0.3	14	8-30	5-30
No.100	0.15	4	0-10	0-10
Sulphate Content SO_3%		0. 2	$\leqslant$ 0.5	***

3.6.3 Coarse Aggregate

Locally available normal weight, rounded aggregate of maximum size 9.5mm was utilized in this work, which was brought from (Al-Nawafith Company for producing sand and gravel filters) in Al-Najaf. The grading of this type of coarse aggregate were shown in Table 3.12 which comply with the requirements of Iraqi specification (IQS- No. 45/1984) [86] and ASTM C33/C33M specifications [87].

Table 3.12 Grading of coarse aggregate.

Sieve No.	Sieve size, (mm)	% Passing		
		Coarse Aggregate	IQS No. 45/1984	ASTM C33/C33M
(1 /2 in.)	12.5	100	100	100
(3 /8 in.)	9.5	96	85-100	85-100
No.4	4.75	19	0-25	10-30
No.8	2.36	3.4	0-5	0-10
Sulphate Content SO_3%		0.03	$\leqslant$ 0.1	***

3.6.4 Steel Fibers

Straight steel fibers were used in this research, manufactured by JINGJIANG HONGTU STEEL FIBER FACTORY in China, as shown in Plate 3.12; with a nominal length of (13 mm), diameter of (0.2 mm), and aspect ratio (length of the fiber to the diameter of the fiber) was about (65). The properties of the steel fibers are introduced in Table 3.13. Two fraction volumes were adopted in this study of 0% and 1%, where the plain concrete was used as a reference for comparison to produce ductile concrete.

Plate 3-12 Steel fibers used in this research work.

Table 3.13 Properties of steel fibers*.

Material	Property	Specifications
Copper Coated Steel Fiber	Shape	Straight
	Tensile strength	$\geqslant 2850MPa$
	Density	7850 kg/m^3
	Appearance	Golden and Bright
	Length	12-14 mm
	Diameter	0.2-0.25 mm
	Aspect ratio (L_f/D_f)	65

* Supplied by the manufacturer.

3.6.5 Water

Tap water which conformed to IQS1703/1992 [88] was used for mixing concrete materials and curing all specimens.

3.6.6 Superplasticizer

Third generation admixture Sika ViscoCrete- F180G was used in this study as a high range water reducer agent HWRA that provides long workability times. This product is a high performance super plasticizer based on modified poly carboxylates based polymer. It is conformed to the requirements of ASTM C494-types F and G, C1017 Types I and II [89] . The typical properties of the plasticizer as reported by the manufacturer were attached in Appendix (C).

3.6.7 Shear Connectors

A new type of the shear connectors which have been used in this work were prefabricated from a deformed rebar of 6 mm diameter as a hoke inside concrete which can be used to recycle the remaining pieces of rebar, providing environmental benefits. The deformed rebar were prepared by cutting into a specified length and bend from the middle with a plate cutter machine, then the legs were bend manually, Figure 3.15 shown the final shape and dimensions of the shear connector used in this work.

The shear connectors were welded at the centre-line of each of the top chord as shown in Figure 3.16. The mechanical properties and the actual measured diameter for the steel bars were depicted in Table 3.14, which also show that the results of tensile test for reinforcing bars was conformed to the properties prescribed by the specification according to (ASTM A615/A615M-08a) [80]. The actual measured diameter for the steel bars was (5.95 mm). Plate 3.13 show the tensile coupon specimen of rebar during test. The mechanical properties of deformed rebar should be also conformed to the AASHTO requirements [90] for the materials of stud shear connectors, which also illustrated in Table 3.14.

This test was obtained by tensile test using a universal testing machine in the laboratories of Engineering Consulting Bureau at the University of Kufa/ Faculty of Engineering. The numbers of shear connectors were be estimated according to Standard specification for CJ-series composite steel joists [6].

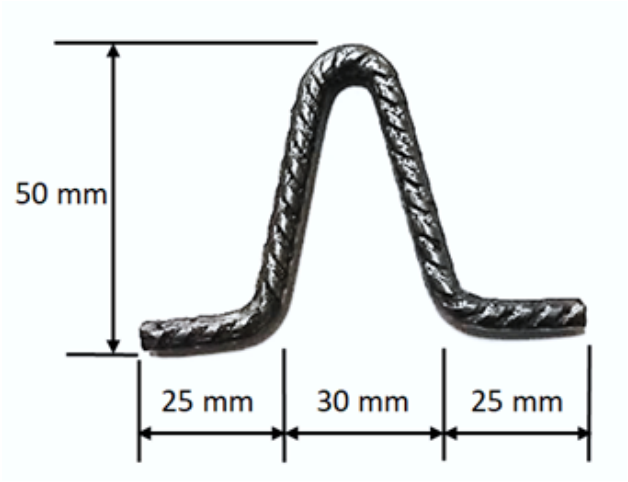

Figure 3.15 Shape of shear connector used in this study.

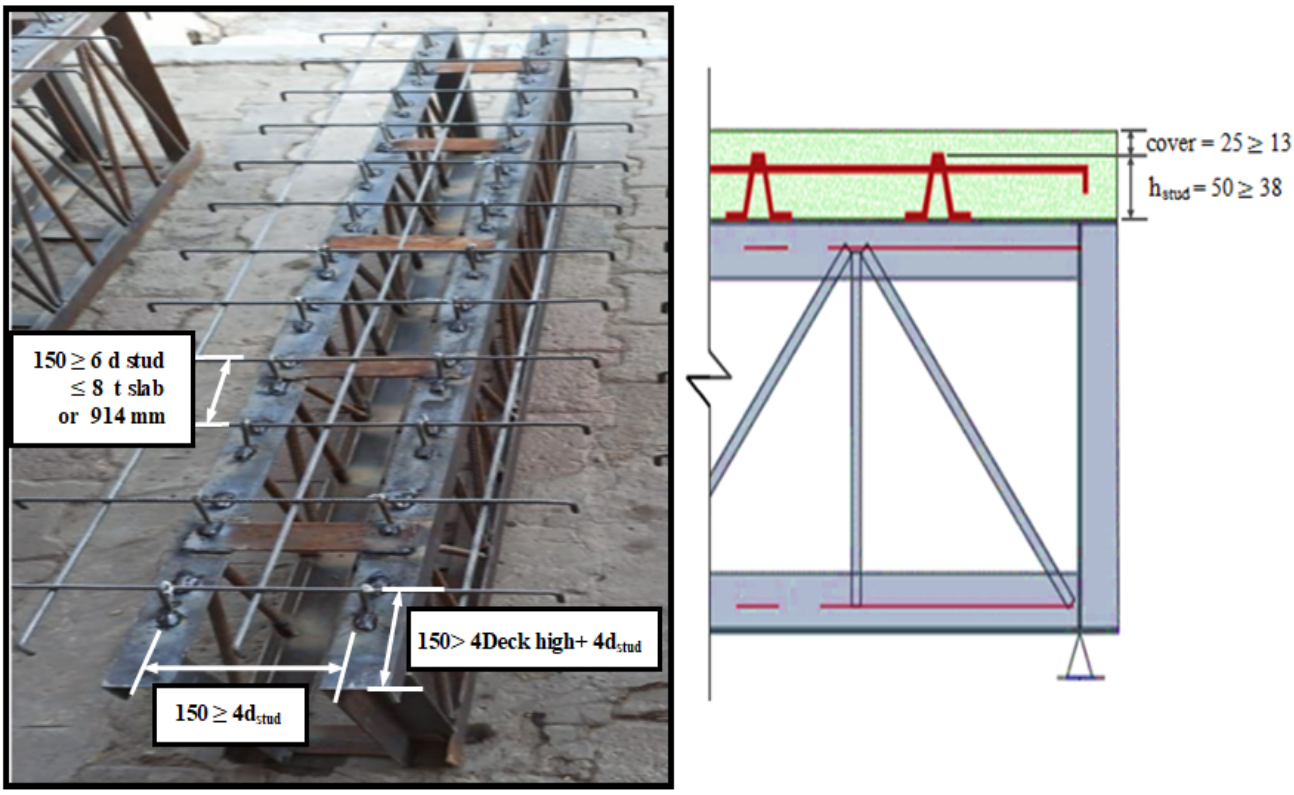

Figure 3.16 Distributions of the shear connectors according to SJI requirements. (all dimensions in mm)

Table 3.14 Tensile test results of the deformed reinforcing steel bar (6 mm dia.).

Specimen No.	Yield Strength, F_y (MPa)	Ultimate Tensile Strength, F_u (MPa)	Elongation. %
1	353.58	468.04	24.25
2	357.46	475.53	26.58
3	351.93	463.29	25.25
Average	354.32	468.95	25.36
ASTM Requirements for Steel Bar (Min.)	280	420	—
AASHTO Requirements for Stud Material (Min.)	345	415	20% in 50 mm

Plate 3-13 Reinforcing bar (6 mm dia.) coupon specimen during tensile test.

The horizontal shear at the interface between the steel beam and the concrete slab is assumed to be transferred by shear connectors. For composite action in positive moment regions (concrete in flexural compression), the total horizontal shear force V' between the point of maximum positive moment and the point of zero moment is the least of the following three limit states [91]:

$$\text{Concrete crushing} \qquad V' = 0.85 f'_c A_c \tag{3.1}$$

$$\text{Tensile yielding of steel section} \qquad V' = A_s F_y \tag{3.2}$$

$$\text{Strength of shear connectors} \qquad V' = \sum Q_n \tag{3.3}$$

where:

A_c:area of concrete slab within effective width, (mm^2).

A_s :area of steel cross section, (mm^2).

$\sum Q_n$:sum of nominal strengths of shear connectors between point of maximum positive moment and point of zero moment, (N).

The number of shear connectors (N) required between the section of maximum bending moment, positive or negative, and the adjacent section of zero moment is equal to the horizontal shear force (V') divided by the nominal strength of one shear connector. The nominal strength, (Q_n) , of one stud shear connector embedded in solid concrete or in a composite slab is:

$$Q_n = 0.5 A_{stud} \sqrt{f'_c E_c} \leqslant (R_p R_g A_{stud} F_{ustud}) \tag{3.4}$$

where the diameter of stud shear connector (d_{stud}) adopted in this study was: $d_{stud} = 2 \times diameter\ of (6mm) rebar$

Hence, the number of studs provided between mid-span and each support must be at least:

$$N = \frac{P}{0.85 Q_n} \tag{3.5}$$

where P: whichever is smaller of Equations 3.1 and 3.2.

In the experimental of this study Equation 3.5 was used for estimating the required number of shear connectors for all composite steel joists specimen. After calculating the number of shear connectors for each of the specimens used in this

study, the lowest number that was calculated was adopted for all other specimens in order for the comparison to be fair between the load -slip relationship between the specimens for the same number of shear connectors, but using different shapes of sections and different heights of steel joist. Also, according to the type of concrete used in the casting of the slab, as detailed in Section (3.5.1).

The least number of studs obtained in this work between mid-span and each support was about 12 shear stud, the studs placed in two groups, Figure 3.16, therefore, there should be at least 6 groups on each half OWS joist, thus 24 stud shear connectors were be used in each COWSJ in this work. This number of shear studs provided a total stud strength greater than the yield capacity of the bottom chord, approximately 255.02 % , and 234.95 % composite action for SFRC and NC respectively, which conformed to the standard specification for CJ-series composite steel joists [6] which recommended that the strength of shear connection, NQ_n , shall be no less than 50 percent of the bottom chord yield strength. The distributions of the shear studs shown in Figure 3.16 were also conformed to the specifications of SJI [8], as illustrated previously in Figure 1.7.

3.6.8 Deformed welded wire fabric (wire mesh)

Deformed welded wire fabric (WWF) of 6 mm diameter and spaced at 150mm c/c in both directions was used in the experimental work to reduce shrinkage cracks (minimum ratio) according to ACI 318R-19 [92]. The mechanical properties of the WWF were depicted in Table 3.15 which conformed to the requirements of ASTM A1064 specifications [93], ASTM A1064 specified that no fewer than 50% of tests shall be carried out across welds. The transverse wire forming the welded intersection was also extended approximately 25 mm beyond each side of the intersection, Plate 3.14 show the WWF reinforcement tensile coupon specimen during test. The test was done using the tensile testing machine, which was available at the laboratories of Engineering Consulting Bureau at the University of Kufa/ Faculty of Engineering. Nineteen pieces of WWF reinforcement were used

in this study, seven for the COWSJs specimens and twelve for push out specimens. They prepared by cutting into the designation dimensions and bend the ends from the two directions using the plate cutter machine, as shown in Plate 3.15.

Table 3.15 Tensile test results of the deformed welded wire fabric.

Specimen No.	Yield Strength, F_y (MPa)	Ultimate Tensile Strength, F_u (MPa)	Elongation (%)
1	548.25	591.21	24.63
2	532.36	572.43	25.74
3	544.72	633.39	20.56
Average	541.76	599.01	23.64
ASTM A1064 Requirements (Min.)	480	550	—

Plate 3-14 WWF reinforcement coupon specimen during tensile test.

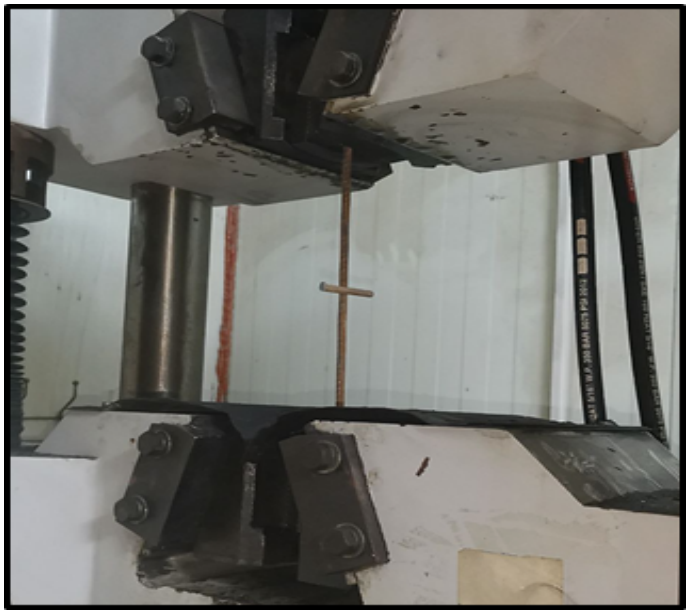

Plate 3-15: Cutter machine used to cut and bend the ends of WWF reinforcement.

3.7 Trail Mixes

To find the best mix proportion of ingredients to produce non fibrous and steel fiber concrete, thus primarily three trail mixes for non fibrous concrete were carried out according to (ACI-211.1R) [15] to get a nominal compressive strength of concrete about (28- 30) MPa after age 28-days, as shown in Table 3.16.

Table 3.16 Non fibrous concrete mix proportioning for trail mixes.

Trial NO.	Cement (kg/m^3)	Coarse Aggregate (kg/m^3)	Fine Aggregate (kg/m^3)	(w/c) ratio	S.P. (l/m^3)	Slump (mm)	7 days	
							f_{cu} (MPa)	f'_c (MPa)
1	441	739	893	0.49	0.6	51	27.38	18.44
2	384	760	929	0.54	0.8	67	23.64	15.72
3	420	748	905	0.47	1	¿ 100	29.53	19.27

From the results of tests showed in the above table it can be mentioned that the best proportion of ingredients which have been gotten in the present study was for trail No.3 are listed in Table 3.17, which was used to produce SFRC for the deck slab.

Table 3.17 The final best proportion of ingredients of concrete.

Concrete Type	Cement (kg/m^3)	Coarse Aggregate (kg/m^3)	Fine Aggregate (kg/m^3)	(w/c) ratio	S.P. (l/m^3)	Steel Fiber	
						Volume (%)	Weight (Kg)
Non fibrous Concrete	420	748	905	0.47	1	0	0
Steel Fiber Concrete	420	748	905	0.47	1	1	78.5

3.8 Preparation for Specimens Casting

3.8.1 Concrete Mix Procedure

3.8.1.1 Non fibrous Concrete (NC)

Firstly, the fine and coarse aggregate were washed and dried to remove any mud particles before mixing process. Then all ingredients are weighed separately as per the mix details. A rotary mixer was used to mix the concrete. After moistened the mixer, the fine, coarse aggregate, and cement were blended, then third amount of the providing water is added and mixed for 2 minutes, after that the second third amount of the providing water was fed and mixed for 2 minutes, finally The last third of the water amount was added after mixing it with the (Sika Viscocrete-F180G) superplasticizer. Approximately 10 minutes were the overall time for mixing from adding water to the mix.

3.8.1.2 Steel Fiber Reinforced Concrete (SFRC)

Primarily, all quantities of ingredients were weighed and packed in clean containers prior mixing. The interior surface of the mixer was cleaned and moistened before placing the materials. The mixing process was started by setting dry materials (cement, fine and coarse aggregate) in the rotational blender and mixed for 4 to 5 minutes. Then (2/3) of mixing water was added gradually to the mix and all components were remixed for 2 minutes. While, (1/3) of mixing water was mixed with the whole amount of the superplasticizer before added it into the mixer. The

required quantity of steel fiber was added uniformly to the mix by hand spraying during the rotation of mixer to ensure uniformly distribution of steel fibers and avoid balling of them. The mixing operation was continued until homogeneous concrete was obtained.

From the two types of concrete mixtures, groups of cubes, prisms and cylinders were prepared and oiled before the casting process, they were cast simultaneously with the specimens to determine the mechanical properties for each specimen. The molds were removed after 24 hours maintenance, and then specimens were cured by the same way of curing the slabs of composite open web steel joist by covering them with burlap sacks and remained moist for up to 28 days .

3.8.2 Tests of Fresh Concrete (Slump Test)

The slump test for NC which was done depending on ASTM C143/C143M [94]. It is found that the value of slump was about (100 mm), while for SFRC the slump was (86 mm), and from these results it can observed that the workability of steel fibre reinforced concrete gets less than of NC.

3.8.3 Forms Preparation

Two types of forms which were fabricated from plywood with thickness of (16.5 mm) were used in this experimental work according to the required dimensions as follows:

• Seven plywood molds were made for casting five composite open web steel joists with steel fiber reinforced concrete, and two with non fibrous concrete.

• Six plywood molds were made for casting three push out specimens with SFRC and three push out specimens with NC., Plate 3.16 show the plywood molds used in the experimental work. All the molds were cleaned and oiled before casting concrete.

Plate 3-16: Plywood forms used in the experimental work.

3.9 Casting of Specimens and Curing

3.9.1 Push-out Test Specimens

The steel-concrete composite beams have been widely used in bridge and high rise building structures. The shear connection between the steel section and the concrete slab is an essential component of a composite beam, thus the shear connector represent an important component of the composite beam. The shear connectors are commonly used to ensure composite action in a steel-concrete composite beam. Their main function is to transfers the longitudinal shear forces at the steel joist-concrete interface, and to prevent vertical separation between the concrete slab and the supporting steel beam. Push-out test has been proven to be an effective method for determining the nominal shear strength and ultimate slip of shear stud connectors.

Many types of shear connectors have been developed and used as showed previously in Figure 2.14. Welded studs are the most practical connectors for achieving the composite action between steel girders and concrete slabs owing to their rapid welding technique and out-standing mechanical performance.

In this study, a new type of shear connectors were be fabricated using a deformed bar used as a hoke inside concrete, and then welded that bar on the

steel section, as explained before in Section (3.6.7), thus it was very important to evaluate the shear capacity of the shear connectors and their behavior in COWSJs which have been used in this work by using the push out test according to BS 5400-5:2005 [95].

The slab thickness, details of reinforcement, and distribution of shear connectors of push out test specimens were as the same as the real composite joist used in this work, as shown in Figure 3.17. A rolled steel Section W10×30 was used in the test with length was equal to (600 mm).

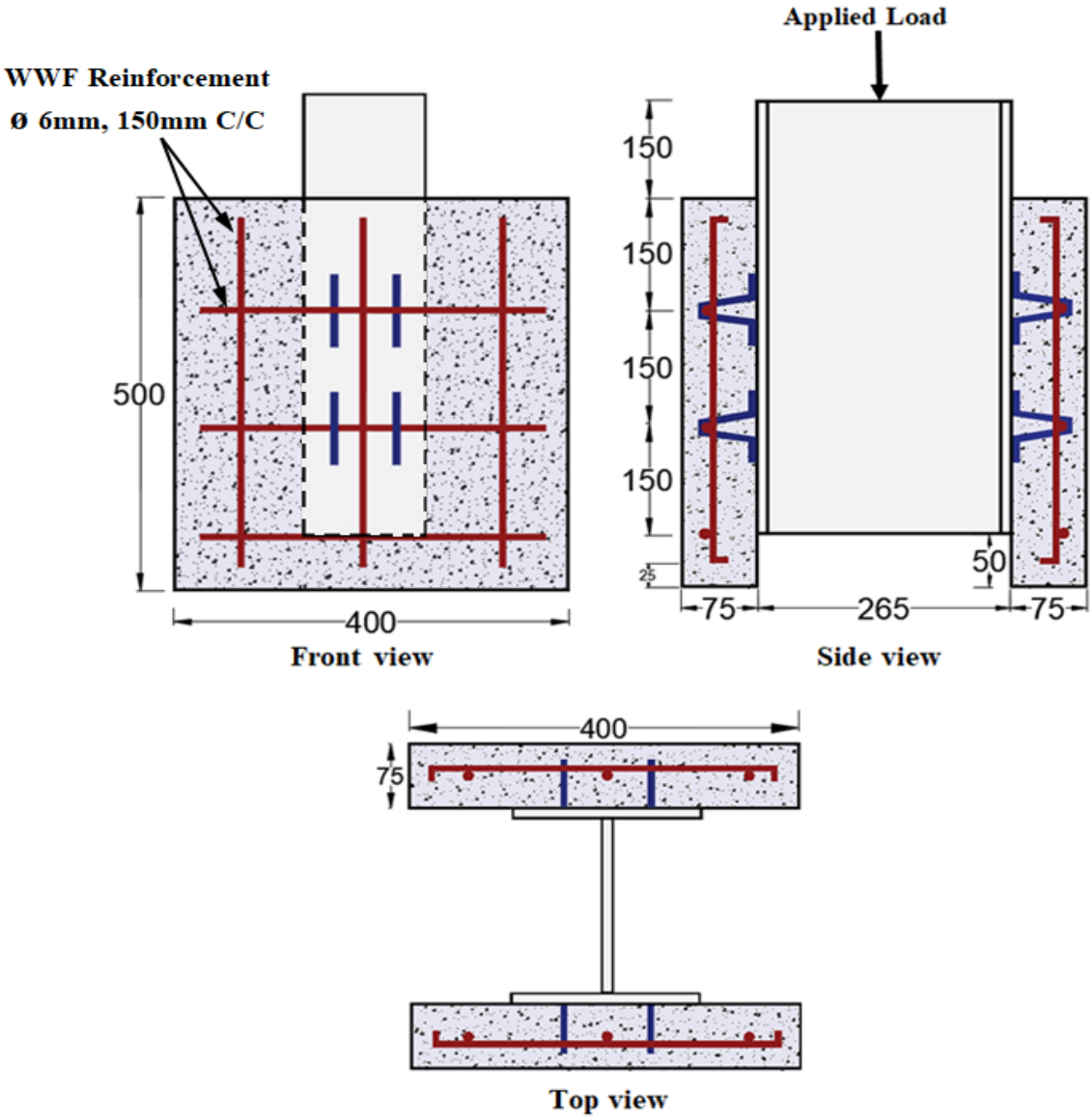

Figure 3.17 Details of push out specimens.

Six push-out specimens were tested in total, three of which were cast of non fibrous concrete and the other three of which were cast of steel fiber reinforced concrete. The push out specimens were cast vertically; rather than horizontally, so that both slabs could be cast from the same concrete batch, eliminating any variation in concrete strength between the slabs. Six forms were fabricated so that all specimens could be cast simultaneously. Before casting concrete, all of the molds were cleaned and oiled. After (24 hours), the specimens were demolded, marked, and the concrete slabs of all specimens were covered with gunny bags, and water was sprinkled frequently to maintain the wetness in concrete slabs for 28 days until test time, Plate 3.17 shown the curing of push-out specimens.

Plate 3-17: Curing of push-out specimens.

3.9.2 Composite open web steel joist specimens(COWSJs)

Seven composite open web specimens were fabricated by using the three models (A, B, and C) of open web steel joists which were tested in the first group of this work, Plate 3.18. Each composite steel joist was simply supported with a design length of (1800 mm) and overall span of (1900 mm). The overall thickness of the composite concrete slab was 75 mm for all specimens. Then to achieved an adequate interaction at the interface between the steel joist top chord and the

concrete slab, the shear studs which were prefabricated as illustrated previously in Section (3.6.7) were welded from one leg at the centerlines of the top chords of steel joists using $E6013$ electro-rods according to $AWSD1.1/D1.1M$ requirements [96], and left the other leg without welding in order for the reinforcement to be inserted at the bottom of all connectors at the same time, then the other leg of the connector was welded, Plate 3.19. After that, the WWF reinforcement was raised to the top and connected to the tops of the connectors by a metal wires, Plate 3.20. Working with this mechanism will add to the work two benefits:

• The first is to ensure the stability of the WWF reinforcement in its designated place, especially during the casting process.

• The second is that perhaps the WWF reinforcement will contribute to the transfer of the shear force at the steel joist -concrete interface because they will almost work as one unit inside the concrete, and the WWF reinforcement provided confinement of concrete in the vicinity of the shear stud and that may be significantly enhanced the compressive strength as well as splitting resistance of concrete.

Then the necessary materials for casting specimens were prepared and weighted according to the trial mix percentages. The forms were cleaned and greased. The specimens were placed on the forms with 25mm top cover. Both NC, and SFRC the concrete mix was cast in the form and electrical vibrator was used to be sure that enough amount of concrete gets into all smalls and eliminate the voids. Cylinders and cubes which were used for different concrete tests were taken from each batch cast. After (24 hours) the specimens demolded, marked and then the concrete slab of all specimens were covered with gunny bags and water was sprinkled frequently to maintain the wetness in concrete slabs for 28 days until test time, Plat 3.21.

Plate 3-18 Open web steel joists used to COWSJs fabrication.

Plate 3-19 Welding of one leg of shear stud process.

Plate 3-20 Connection between the shear connectors and WWF reinforcement.

Plate 3-21: Curing of the concrete slab of COWSJ specimens.

3.10 Mechanical Properties of Hardened Concrete

After 28 days, all samples of cylinders and cubes were tested in the laboratories of civil engineering department at the University of Kufa/ Faculty of Engineering to fined the compressive strength of cylinders and cubes, modulus of rupture, splitting tensile strength, modulus of elasticity and stress-strain curve for both of NC and SFRC. Plate 3.22 show some concrete samples prepared for testing.

Plate 3-22 Concrete samples prepared for testing.

3.10.1 Compressive Strength Test

The compressive strength test was determined according to ASTM C39/C39M,2018 [97] for both NC and SFRC. Two type of samples were used, cylindrical (100 × 200) mm, as well as a cubic sample were used with dimensions of (100 × 100× 100) mm. Each type of mold had three specimens to calculate the average value. Experimental tests were conducted by a digital hydraulic testing machine has ultimate capacity 1900 kN, as shown in Plate 3.23.

Plate 3-23 Compressive strength test.

3.10.2 Flexural Strength Test (Modulus of Rupture)

Flexure test was done by using a prisms of size (100x100x400) mm which tested under two pointed load at third distance of the length, according to ASTM C78, 2002 [98]. Three prisms for each type of concrete were tested as simple beam, and the average of three samples were calculated. Plate 3.24 show the machine, specimens at testing, and some of testing results.

Plate 3-24 Flexural strength test.

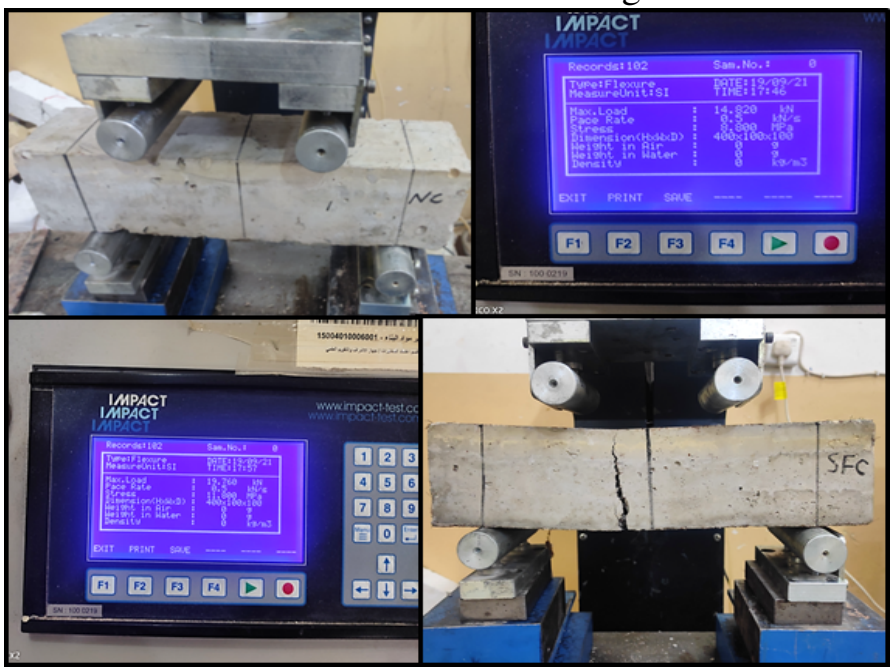

3.10.3 Splitting Tensile Strength Test

The splitting test was achieved according to ASTM standard C496/C496M, 2004 [99]. Six cylindrical samples of (100×200) mm were used to determine the splitting tensile test for both NC and SFRC. Some specimens testing and their results were illstrate in Plate 3.25.

Plate 3-25 Splitting tensile strength test.

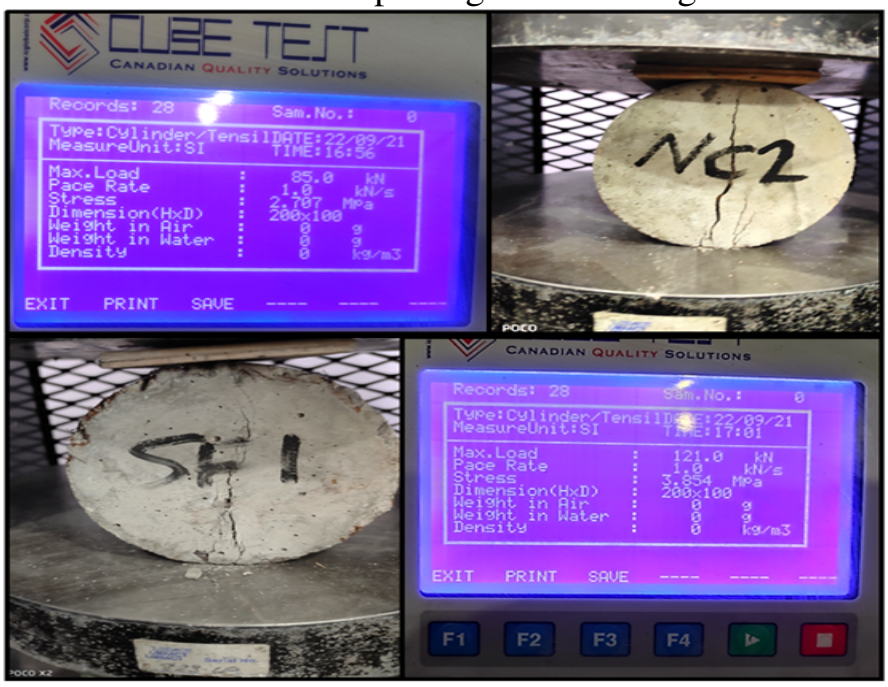

3.10.4 Modulus of Elasticity

Modulus of elasticity is one of the most significant properties of a solid material that describes the stiffness of materials. To determine monotonic modulus of elasticity, cylinder molds of (150x300) mm dimensions were used under compression testing machine with a capacity of 2000 kN. The static modulus of elasticity for NC only was performed based on ASTM C469, 2002 [100] as shown in Plate 3.26. Equation 3.6 was applied to calculate the modulus of elasticity. While the modulus of elasticity of SFRC was calculated through the slope of stress strain relationship between zero stress and (20 %) of the ultimate compressive capacity [55].

$$E = \frac{S_2 - S_1}{\epsilon_2 - 0.00005} \tag{3.6}$$

where

S_2 = Stress corresponding to 40 % of ultimate load, MPa.

S_1 = Stress corresponding to a longitudinal strain ϵ_1 of 0.00005, MPa.

ϵ_2 = Longitudinal strain produced by stress S_2.

Plate 3-26 Testing of static modulus of elasticity for NC.

3.10.5 Stress-Strain Behavior in Compression

Stress-strain curves in compression for NC and SFRC types were plotted depending on the experimental tests after 28 days by using cylinder specimens of (150×300)mm. The test was conducted in a 1000 kN compression universal testing machine with a rate of loading controller. Before testing, the cylinder was grinded and capped with a hard plaster on the cast face to ensure parallel loading faces of the test specimens and constant height for all cylinders. The load was applied at a very slow to perform the compressive test is shown in Figure 3.18, the test was carried out until the concrete specimens failed in the compressive crushing mode.

The data collected during the tests were the compressive load and shortening until the failure of the specimens. For measuring the shortening displacements, LVDTs was installed in addition to dial gage of 50 mm capacity at the two opposite sides of the specimen to average the values. All the measurements were transferred to the data logger , and the data were recorded and displayed in the computer. Strain calculations was found through the average deformation ,for LVDT and the dial gage readings , on the original length for the specimen. The test system which is used in present study was similar to the system that used by Sabariman et al, (2018) [54] and by Flayyih (2020) [101] .

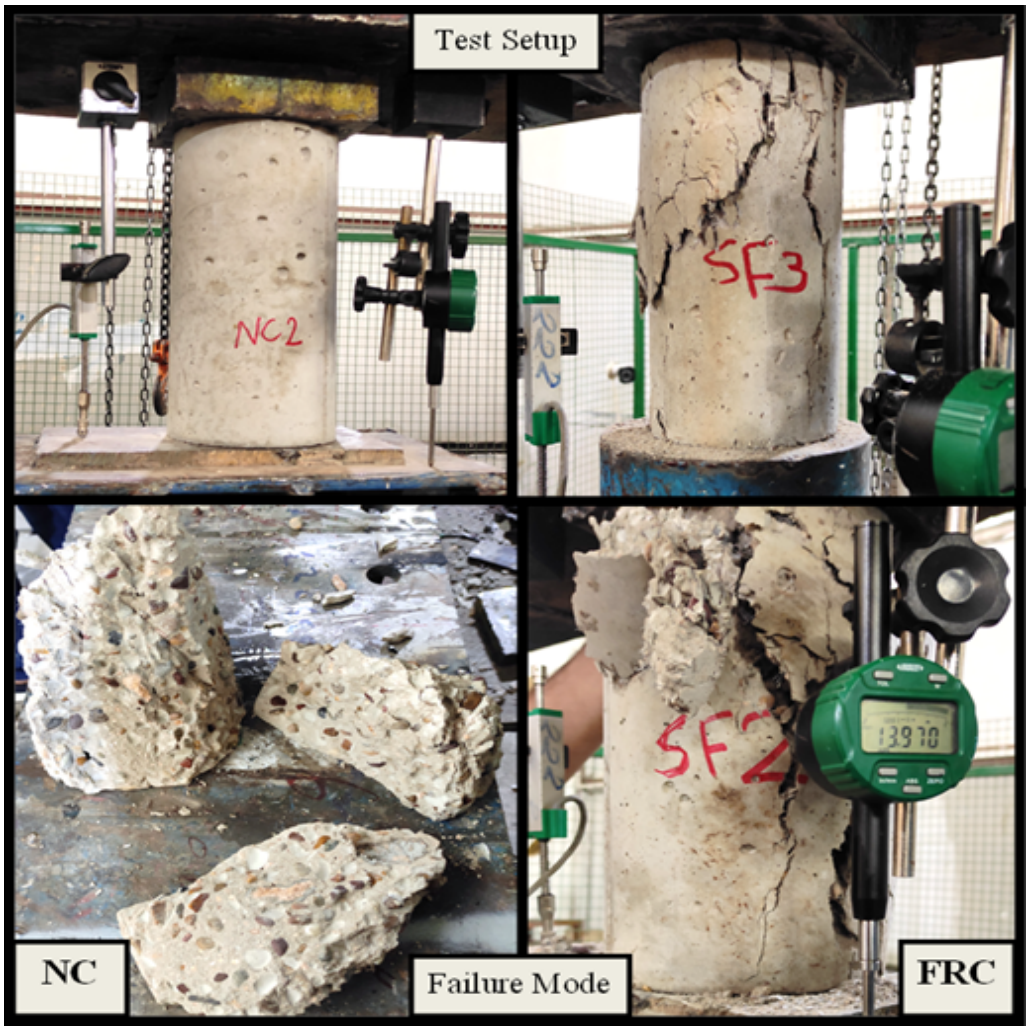

Figure 3.18 Compression stress-strain test for NC and SRC.

3.11 Test Setup and Instruments

After 28 days The test was conducted at the Structural Civil Engineering Laboratory of University of Kufa for all specimens. The push out and composite joist specimens were painted with white color prior to test to provide a better surface for crack marking, as shown in Plate 3.27. All the devices and Instruments, such as compression machine, linear variation displacement transducer (LVDT), strain gauges, and the digital dial gauges were used to test the second group of this work. All devices and Instruments previously explained in details in the Section (3.4). Only one device was added in this part of the work and it was the Crack meter.

A crack meter was used to measure the crack width which occur in the concrete related to the composite beams which will be tested. This type is used manually, where it is capable of amplifying the view 40 times with self-internal bulb and accuracy of 0.05 mm, see Plate 3.28.

Plate 3-27 Preparation and painting of all specimens in the laboratory.

Plate 3-28 Microscope used to measure the crack width.

3.11.1 Push-Out Specimens

Push-out specimens comprise three major components: a steel beam, a stud connector, and a reinforced concrete slab. For each type of concrete, three specimens were tested. Figure 3.19 show the compression machine used for the test, with capacity of 1000 kN in Structures Laboratory of Civil Engineering at Kufa University.

The relative slip between the steel and the concrete was measured using two linear variation displacement transducers (LVDTs). At each loading increment, the data logger measured the magnitude of the load as well as the relative slip of the shear stud. All specimen's exposure to load up to failure. Furthermore, all specimens were bonded at the bottom and top to prevent the concrete slab from overturning. This technique was implemented in response to the recommendations made by Prakash et al.,2012 [75], which was mentioned in the chapter two, Section (2.6).

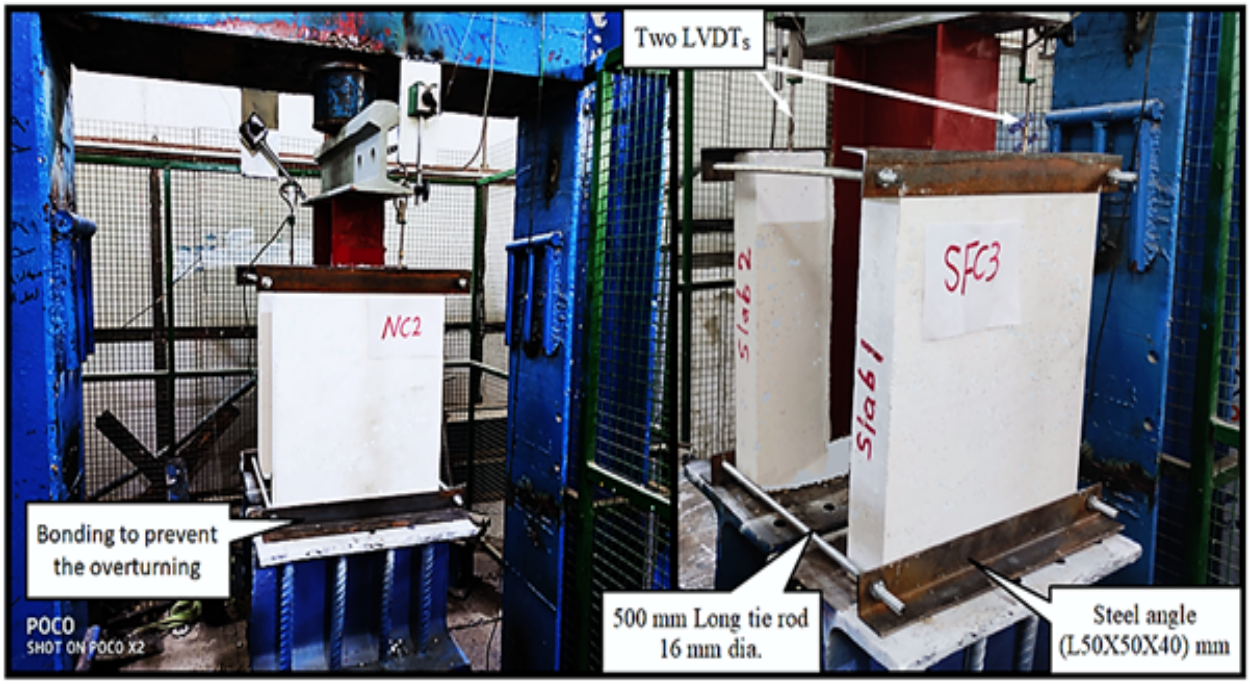

Figure 3.19 Push out test of specimens.

3.11.2 Composite Open Web Steel Joist Specimens

Seven simply supported COWSJS were tested under the effect of monotonic load. Five COWSJS consisted of steel fiber reinforced concrete, while the other two specimens have composite beams consist of non fibrous concrete.

The load was subjected on COWSJ up to failure by using hydraulic testing machine has load capacity 1000 kN. The specimens were loaded using rigid steel I- beam which used to distribute the pressure force on the tested specimen as one point load and it was applied incrementally 5 kN/ min. Figure 3.20 displayed the test setup of the COWS joist specimen on the compression testing machine.

The deflection under the mid span of COWSJ specimens was measured by using LVDT, the deflections were also measured in one quarter and three quarters of the span by using two digital dial gauges which their readings were monitored using two cameras. Another LVDT was set to measure the relative movement (slip) which occurred between the concrete slab and the top chord of the steel joist, Figure 3.21.

A total of six electrical strain gauges were fixed on top and bottom chords as well as interior web members of open web steel joist, Figure 3.22. They were installed prior to testing at the same critical locations of maximum axial tension and compression forces of the steel joists which were tested in the first group to make a comparison on the behaviour of steel joists used in the two groups. In the experimental tests of the COWSJS group, the same type of electrical strain gauges was used in the first steel joists group were adopted, whose their properties were previously explained in Section (3.4.5).

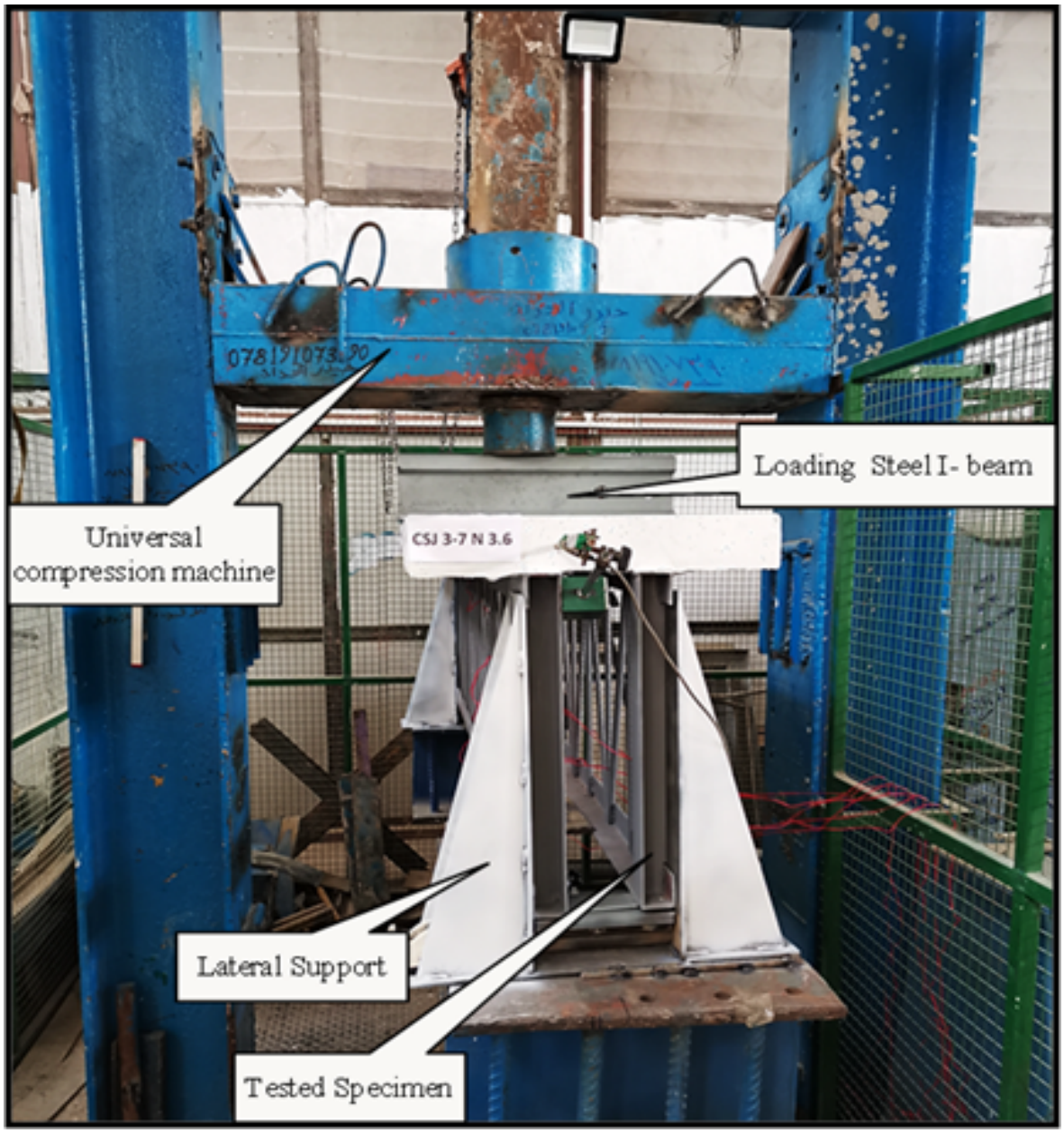

Figure 3.20 COWSJ specimens setup on the testing machine.

Figure 3.21 Locations of instruments for COWSJ testing.

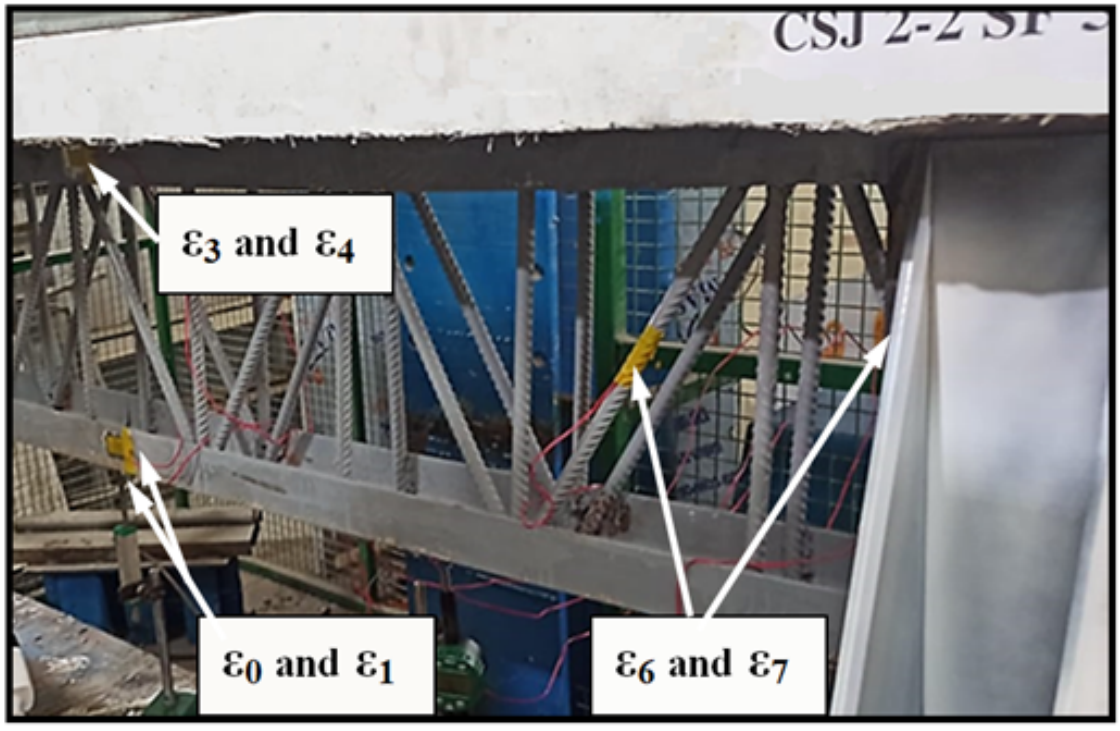

Figure 3.22 Strain gages locations of COWSJ specimen.

CHAPTER 4

RESULTS OF EXPERIMENTAL WORK

4.1 General

All the results of the experimental test were presented and discussed in this chapter. The experimental program is divided into three main groups: The first group deals with the results of HOWSJ tests, the second one deals with the push-out tests, and the third with the results obtained from the composite open web joists tests.

Generally, this study investigated the behavior of the HOWS joists when using as a new pattern of open web steel joist technique. Whereas, this new technique used in the plate girders and composite girders. Therefore, the HOWSJs and composite steel joist girders tested under monotonic load to study the behavior of them.

4.2 HOWS Joists Results

The results of HOWS joists were presented in this section, as well as the comparisons were achieved between their results according to the shape of the cross section of the joist, the span to depth ratio of steel joists, and the effect of the diameter of interior web members.

4.2.1 Results of HOWS Joists of Models A, D, and E

This section presents The failure mode, load- mid span deflection curves , and load – strain curves for the models A, D, and E specimens, which they had the same cross section where the top and bottom chords which were prefabricated by welding the angles back to back but they were different in their depth and in the diameter of bars of the interior web members.

This study aims to use the HOWS joists that were suggested in this work as an alternative technique instead of traditional OWS joists in steel girders, therefore,

the results must be compared between the different shapes of these HOWSJs. Two factors were studied for these models of HOWSJs under concentrated load at mid-span. The first factor was the length to the depth ratio L/D of the OWSJ, which were 5.1 for Model A specimens, and 3.6 for both Model D and Model E specimens. The second variable was slenderness ratio of the diagonal interior web members (kL/r) which were 119.29, 165.41, and 124.92 for Models A, D, and E respectively, because the specimens of Model D were had interior web member with rebar diameter of 11.97 mm while 15.85 mm diameter of rebar was used for fabricating Model E specimens.

4.2.1.1 Failure Mode of Model A,D, and E Specimens

From the experimental results it can be observed that the modes of failure of each two specimens for the three models were the same. The failure occurred due to the local buckling of the diagonal interior web members near the supports, this failure mode for open web steel joists called a crimped-end web members, as mentioned by Buckley, et al. (2007) [102] in their research, so a special attention must be given to a "critical panel zone". This segment, under the uniform loading condition and an effect at the crimp transition zone, will cause buckling on the diagonal interior web member near the support before mid-span, thus the buckling of the web member in mid span was very little comparing with the end web members. Also it can be mentioned that local buckling of the diagonal interior web members decreased when the slenderness ratio decreased as for Model E specimens when compared them with Model D specimens.

Another failure mode was happened due to the top and bottom chords buckling due to the deflection of the joist, in addition to the local buckling of the vertical leg of the top and bottom chord near the supports in the regions which was not welded, this buckling occurred because they behave as a vertical web connected with the web members. Finally there was welding joint fracture failures between the web members (vertical and diagonal) and the chords at top and bottom

of the two HOWSJ specimens were tested in this study. Plates (4-1) to (4-3), show the mode of failures on the two joist specimens tested for each model.

Plate 4.1 Mode of failures of Model A HOWSJ specimens.

Plate 4.2 Mode of failures of Model D HOWSJ specimens.

Plate 4.3 Mode of failures of Model E HOWSJ specimens.

4.2.1.2 Load-Mid Span Deflection Curves of Models A, D, and E

HOWS joist specimens of Models A, D, and E had the same shape of the cross section, but these three models had two combination variables were adopted in this study , the first was the effects of the length to the depth ratio L/D. The second was the effect of the diameter bar of the interior web members used to fabricate the models. Table (4-1) presented the yield strength, deflection at yield strength,

ultimate load, and the deflection at the ultimate load for each specimens of these three models. Where the elastic buckling had occurred when the compressive diagonal interior webs strength vanished, and then the tensile diagonal interior webs will be resisted all stresses, until the interior webs yielded or buckled. Also the results test for the three models specimens of load versus vertical deflection are illustrate in Figure (4-1) to (4-3).

By observing the results shown in Table (4-1), it can be noted that every two specimens of the same model had very close values of ultimate load, yield strength, deflection at the ultimate load, and yield deflection. Also Figures from (4-1) to (4-3) show that the two specimens for each model have to a large extent the same behavior, and from this it is concluded that the model-prefabricated process was accurate and used materials that have the same properties, so the experimental results were very close for each two specimens.

Therefore, the mean for each two specimens was calculated in order to make a comparison between the experimental results for the different models as shown in Table (4-2). From this Table it can be recognized that ultimate load capacity of the HOWSJS increased when the depth of the joist increased as for Model D specimens which had a depth of (500 mm) and interior web of diameter (11.97 mm) by about (1.81%) compared with Model A specimens which their depth were (350 mm) with same interior web diameter, but for the depth (500 mm) for Model E specimens with diameter for interior web of (15.85 mm) the enhancement was about (27%) compared with model A and (25.7%) compared with model D specimens . From these results, it is concluded that the increasing of the depth of the joist led to a very small increase in the ultimate load capacity of the HOWS joist in case of using the same diameter of the rebar, but this increasing of depth may led to enhanced the ultimate load capacity reach up to (25.7%) in the case of increasing the diameter of the interior web members by (24.48%). Also it can be concluded that for Models D and E which they had the same L/D ratio of 3.6, when the slenderness ratio

of the diagonal interior web member for Model E decreased about (24.48%) the deflection of the HOWSJ decreased by about (11.32%).

The Normalized load-mid span deflection curve, Figure (4-4) was adopted to make a comparison between the three models, the testing results illustrated that the yield strengths decrease when the L/D ratio increased. Also it can be recognized that the Model A was had a maximum deflection more than of models D and E. Also Model D was had a maximum deflection more than of Model E, that was because when reduced the slenderness ratio of the diagonal interior web members for Model E made them more stable.

Table 4.1 Experimental results of Models A, D, and E HOWSJ specimens.

Models	Specimen No.	Yield strength, P_y (kN)	Ultimate load, P_u (kN)	Def. at yield strength (mm)	Def. at ultimate load, (mm)
Model A	SJ 1-1	65.68	101.34	4.296	8.056
	SJ 1-2	63.41	100.65	3.848	7.544
Model D	SJ 4-1	51.34	103.16	3.915	10.311
	SJ 4-2	49.87	102.54	3.395	9.642
Model E	SJ 5-1	54.43	136.59	2.374	8.626
	SJ 5-2	58.65	140.23	2.908	9.075

Table 4.2 Mean experimental results of Models A, D, and E HOWSJ specimens.

Models	Specimens No.	Mean Yield strength, P_y (kN)	Mean Ultimate load, P_u (kN)	Mean Def. at yield strength $\delta_y(mm)$	Mean Def. at ultimate load, $\delta_u(mm)$
Model A	SJ 1-1 SJ 1-2	64.55	100.99	4.07	7.80
Model D	SJ 4-1 SJ 4-2	50.61	102.85	3.66	9.98
Model E	SJ 5-1 SJ 5-2	56.54	138.41	2.64	8.85

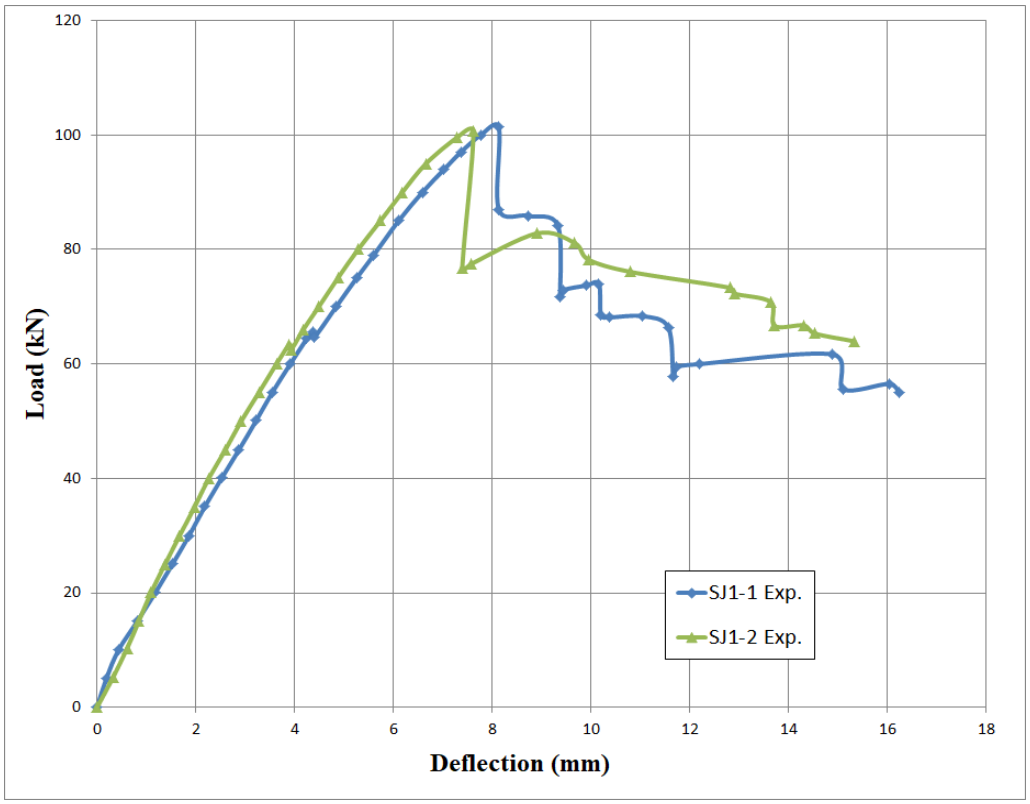

Figure 4.1 Experimental load-mid span deflection curves for model A specimens.

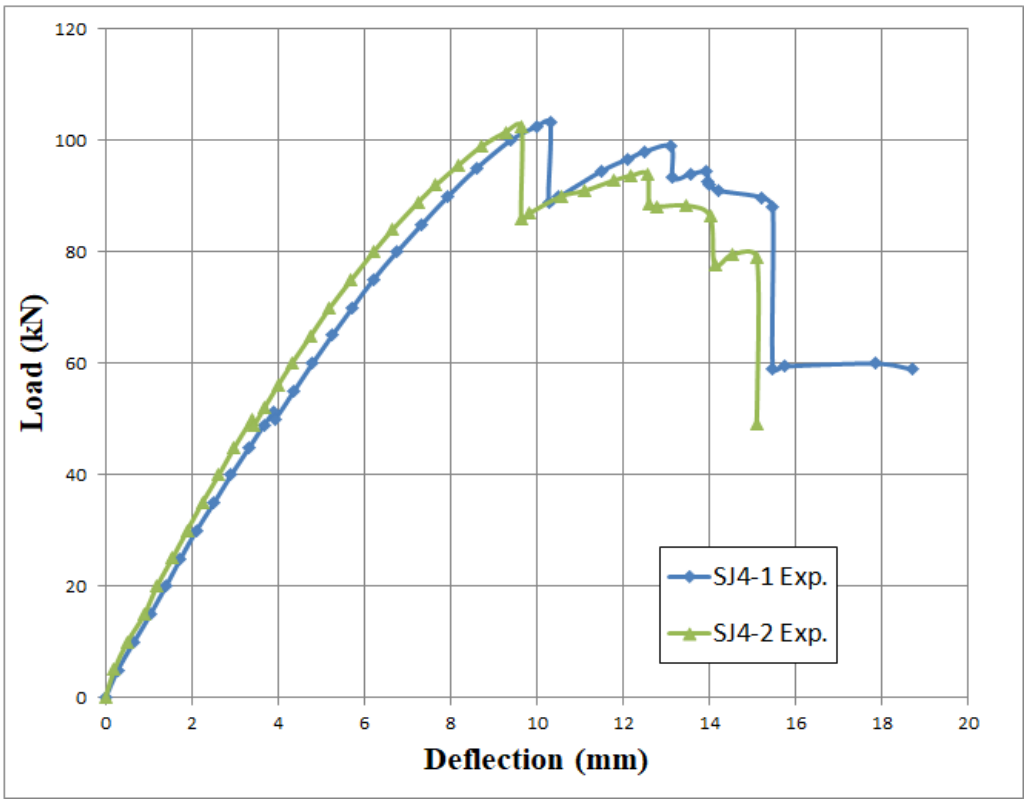

Figure 4.2 Experimental load-mid span deflection curves for model D specimens.

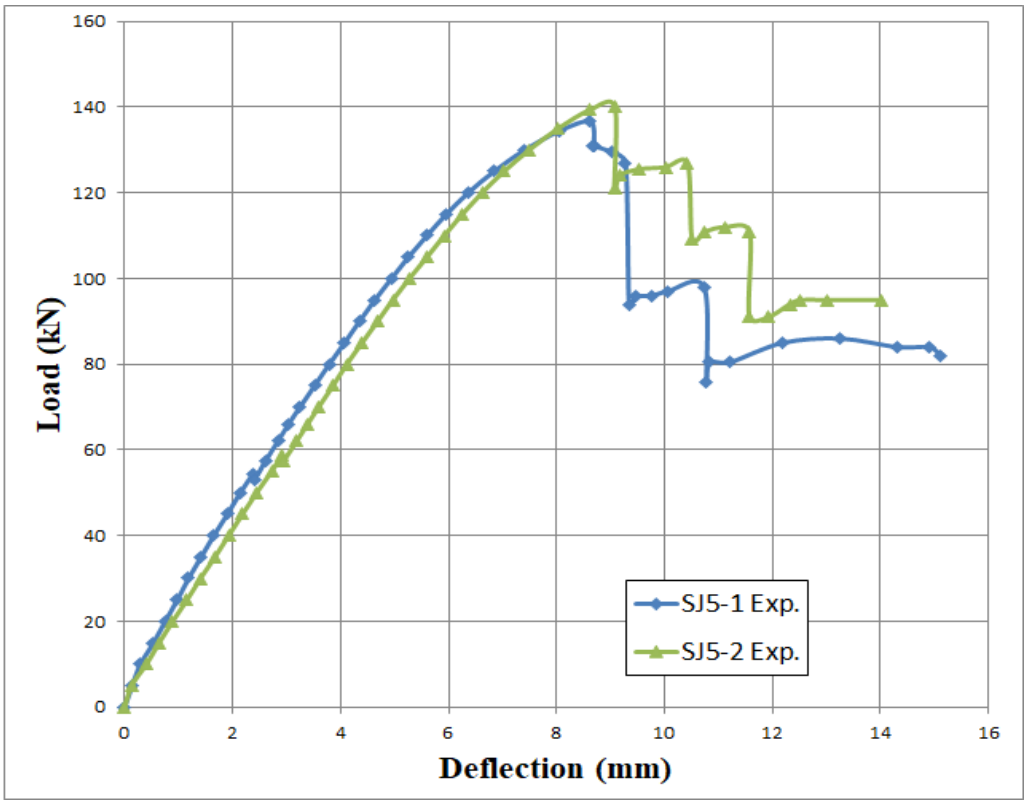

Figure 4.3 Experimental load-mid span deflection curves for model E specimens.

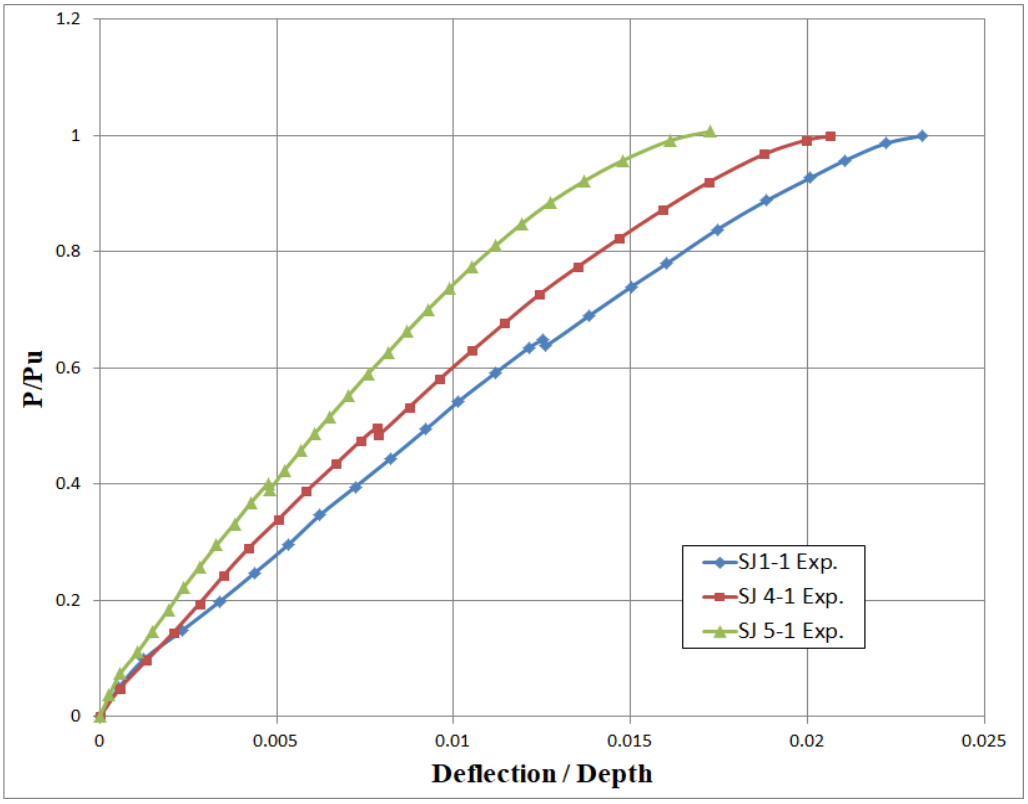

Figure 4.4 Normalized load-mid span deflection curves for SJ1-1, SJ4-1, and SJ5-1 specimens.

The vertical deflection along the span of the joist was plotted for the models A, D, and E specimens so as to represent the final geometry of the HOWSJ at ultimate load capacity, as shown in Figures from (A-1) to (A-3) in Appendix A .

4.2.1.3 Stiffness, Hardness , and Ductility Index Comparison for Models A, D, and E Specimens.

Stiffness, Hardness, and Ductility Index are an important structural performance indices which account degree of deformability in structures. Table (4-3) show a comparison between these indices for the mean values of each two specimens for the same model. Also Figure (4-5) show the comparison between the three specimens SJ1-2, SJ4-2 and SJ5-2 load-deflection behavior. In general, the results in Table(4-3) and Figure(4-5) indicated that the enhancement in the stiffness of Model E specimens was significantly higher than Model D specimens by about (35.4%), and about (26%) comparing with Model A specimens, and the Model A had a stiffness value higher than Model D by (12.7%), although the Model D had an span/ depth ratio (L/D) less than Model A and the reason was because the slenderness ratio of the diagonal interior web members for Model D more than the slenderness of the diagonal interior web members for Model A.

Regarding the index of the hardness, the results of tests show that the Model E specimens also had a highest hardness value among other Model specimens, which was higher about (34.1%) than for Model D, in spite of the less increase in the hardness compared with Model A by about (17.2%).

Finally for the ductility index it can be noticed that the Model E had a higher ductility about 1.23 and 1.74 times the ductility of Model D and Model A, respectively. But the Model D had a ductility about 1.42 times the ductility of Model A specimens. The highest ductility value of Model E means that model had the best system performance among other model specimens, since such value reflects the system ability to deform and clearly observed under visual inspection

before structure collapsing. Hence, such ratio reflects an indication to yielding failure rather that its occurrence suddenly.

Table 4.3 Stiffness, hardness , and ductility index results of Models A, D, and E specimens.

Models	Model A	Model D	Model E
Mean Yield strength, $P_y(kN)$	64.55	50.61	56.54
Mean Ultimate load, $P_u(kN)$	100.99	102.85	138.41
Mean Def. at yield strength, $\delta_y(mm)$	4.07	3.66	2.64
Mean Def. at ultimate load, $\delta_u(mm)$	7.80	9.98	8.85
Stiffness, $P_y/\delta_y(kN/mm)$	15.85	13.83	21.42
hardness, $P_u/\delta_u(kN/mm)$	12.95	10.31	15.64
Ductility index, δ_u/δ_y	1.92	2.73	3.35

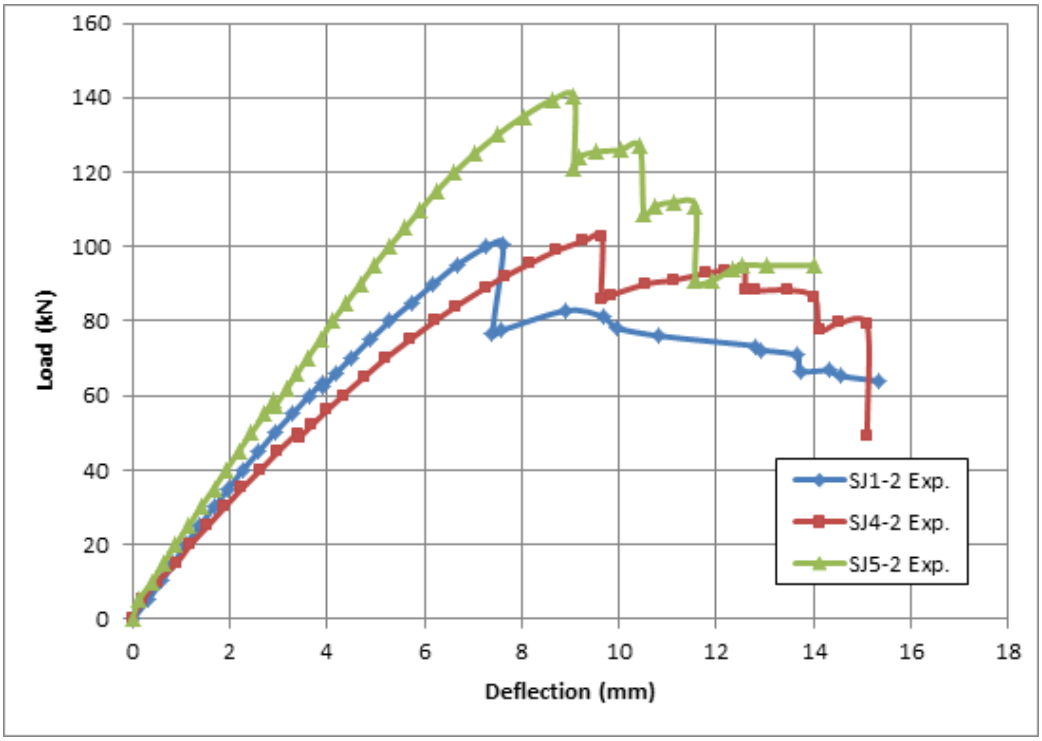

Figure 4.5 Load-mid span deflection curve for SJ1-2, SJ4-2, and SJ5-2 specimens.

4.2.1.4 Strain Results of Models A, D, and E

The strain gauges' sensors were used in this study for all specimens of models to measure the uniaxial strain at six critical points of the HOWSJs, two at the horizontal leg of angles of the top and bottom chords, two at the vertical leg of angles of the top and bottom chords at a section distance of (50mm), and two at the center of the length of interior web members near the support, as shown previously in Figure (3-12).

The strain gauges readings, show the mean behavior of the HOWSJ Model A, specimens during the test as explained in Figures (4-6) to (4-8). Figure (4-6) illustrate that the strain gauge (ϵ_1) on vertical leg of angle bottom chord exhibited a compression strain up to failure load, indicating that the bottom chord's vertical leg behaves as a web member with the interior web members to which they were welded and this is a type of stress concentrations at the members' connection, while the behavior of the strain gauge (ϵ_0) on the horizontal angle leg of the bottom chord was in tension. It can also be seen that the strain at the horizontal leg of the angle of the top chord became very close to the yield limit of the angle, as shown in Figure (4-7). The failure of the HOWSJ Model A specimens was due to the interior web members buckling because the strain reached the yield limit before reaching the top chord to the yield limit, as shown in Figure (4-8).

Figures (4-9) to (4-11) show the strain behavior of the HOWSJ Model D specimens. Figure (4-9) shows that the behavior of the vertical and horizontal legs of the bottom chord of Model D which is very similar to their behavior on the Model A, but the strain in the horizontal (ϵ_0), and vertical legs (ϵ_1) of bottom flange was more than of these in Model A by about (5.2%), and (67%), respectively. The failure of the HOWSJ Model D, specimens was due to the buckling of the top chord, Figure (4-10) just before the interior web members reached the limit of the yield, Figure (4-11).

Regarding, Figures (4-12) to (4-14) explained the behavior of strains gauge for the HOWSJ Model E specimens. It can be recognized that these specimens also had the same behavior of strain gauges readings for the Models A, and D specimens. But the different was the reading of the strain gauge (ϵ_0) on the bottom tension chord which had a value more than for Model A, and D by about (24.6%), and (20.4%), respectively. These results proved that the Model E specimens had a high stiffness and also had high ductility compared to other models, this was because they was had an interior web members of diameter (15.85 mm) which made their more stable from the others two model specimens.

Finally, the readings of the compressive strain gauges on the end web members (ϵ_7), show that the strain in Model D was more than of Model A and E by about (13.5%), and (63%), respectively. And from these results it can be concluded that when the diameter of rebar of the interior webs increased by (24.5%) led to decrease the strain on the interior webs by about (63%).

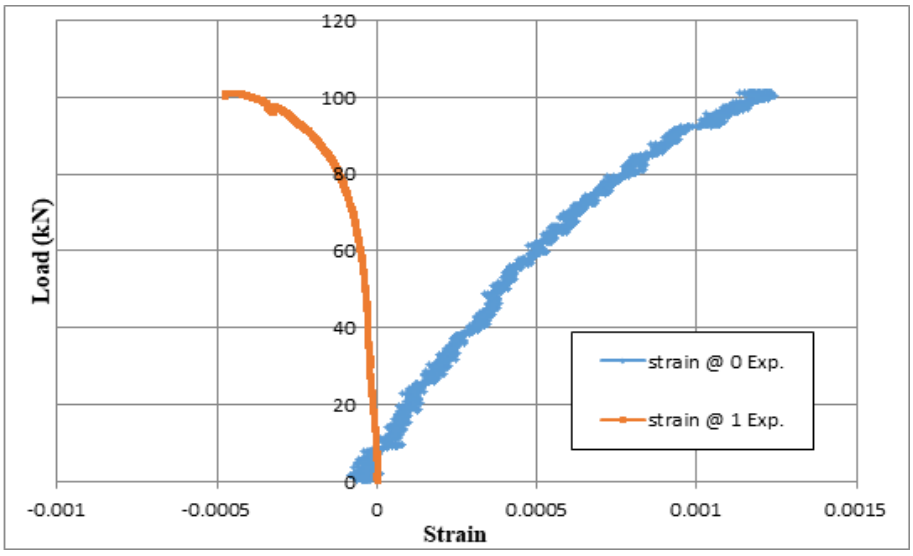

Figure 4.6 Load – strain curve of bottom chord of Model A HOWSJ specimens.

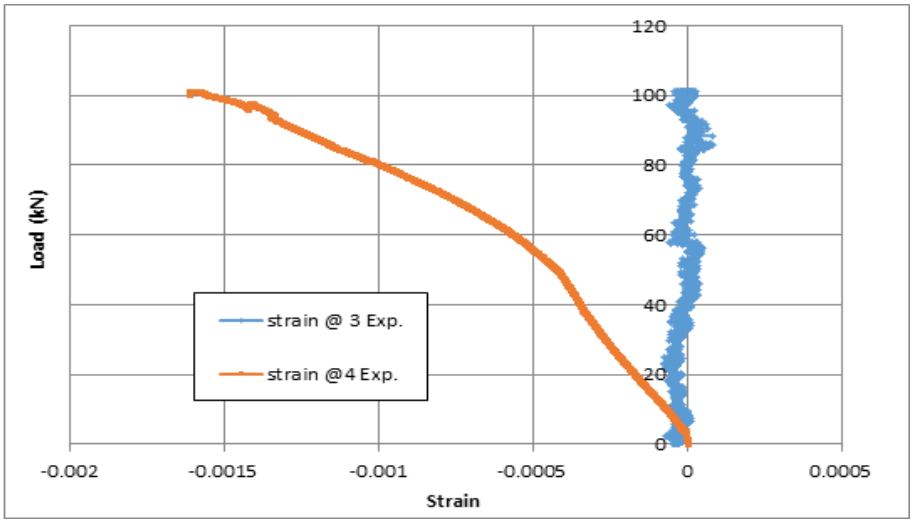

Figure 4.7 Load – strain curve of top chord of Model A HOWSJ specimens.

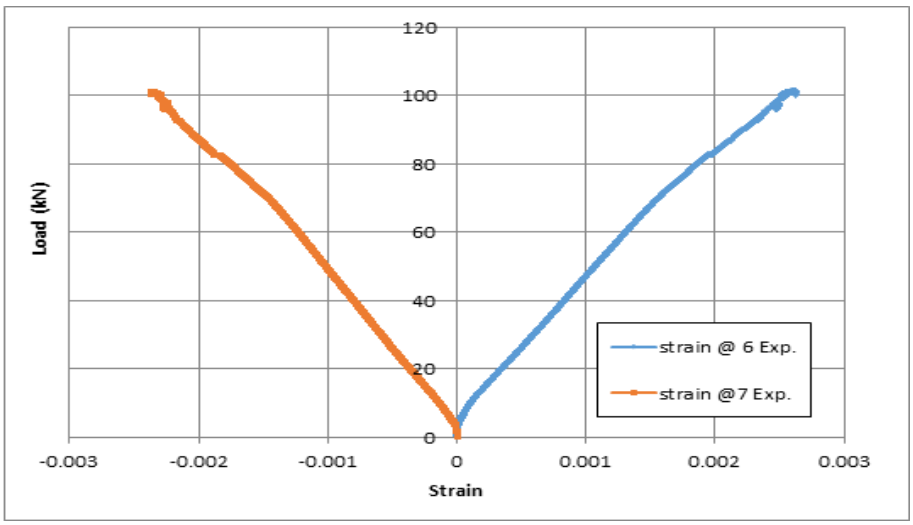

Figure 4.8 Load – strain curve of interior diagonal webs near the support of Model A HOWSJ specimens.

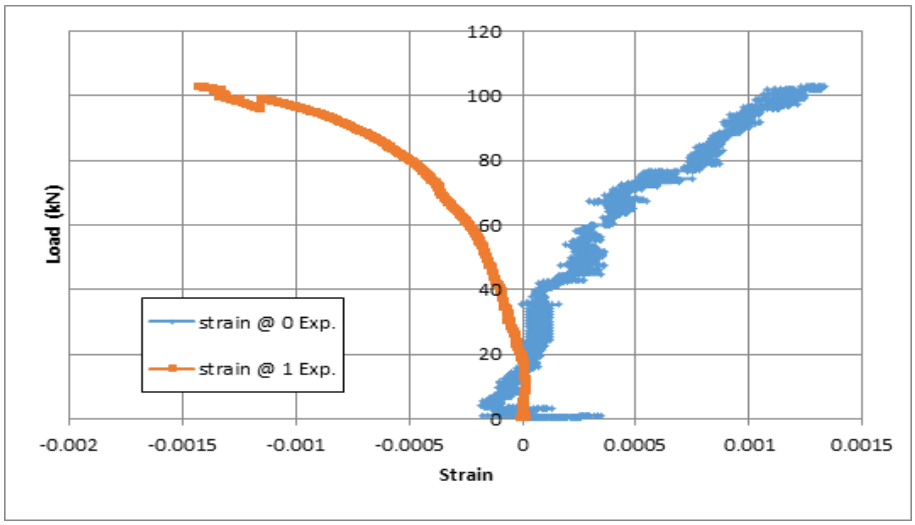

Figure 4.9 Load – strain curve of bottom chord of Model D HOWSJ specimens.

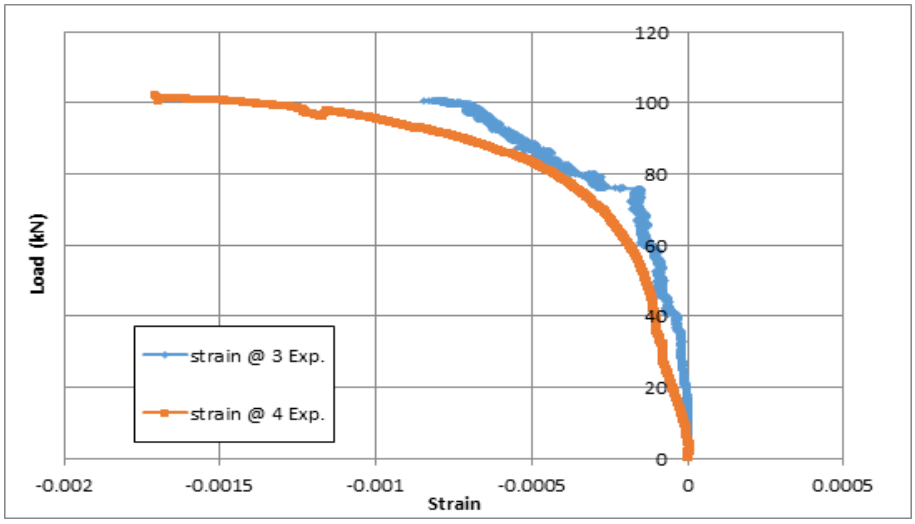

Figure 4.10 Load – strain curve of top chord of Model D HOWSJ specimens.

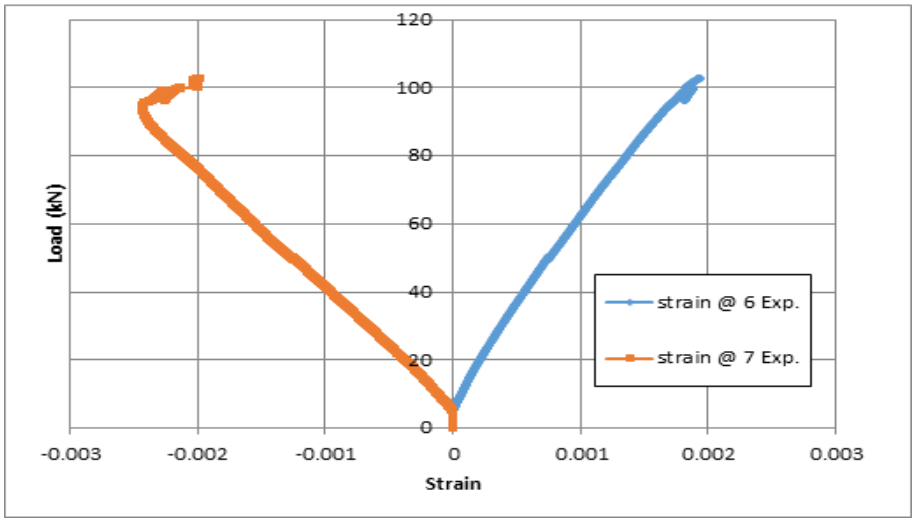

Figure 4.11 Load–strain curve of interior diagonal webs near the support of Model D HOWSJ specimens.

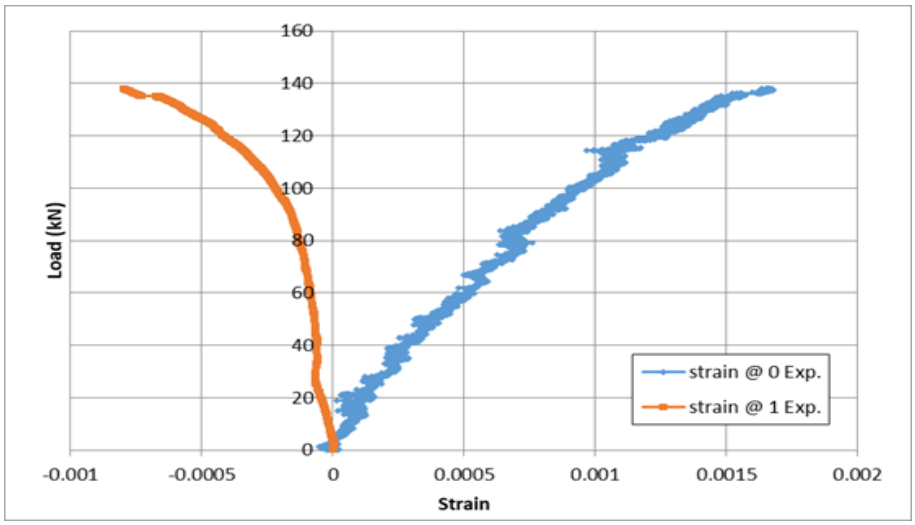

Figure 4.12 Load – strain curve of bottom chord of Model E HOWSJ specimens.

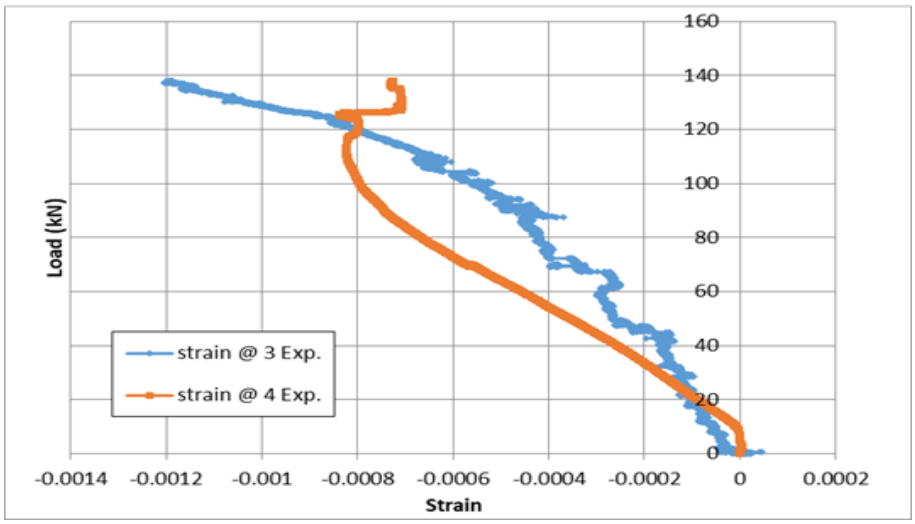

Figure 4.13 Load – strain curve of top chord of Model E HOWSJ specimens.

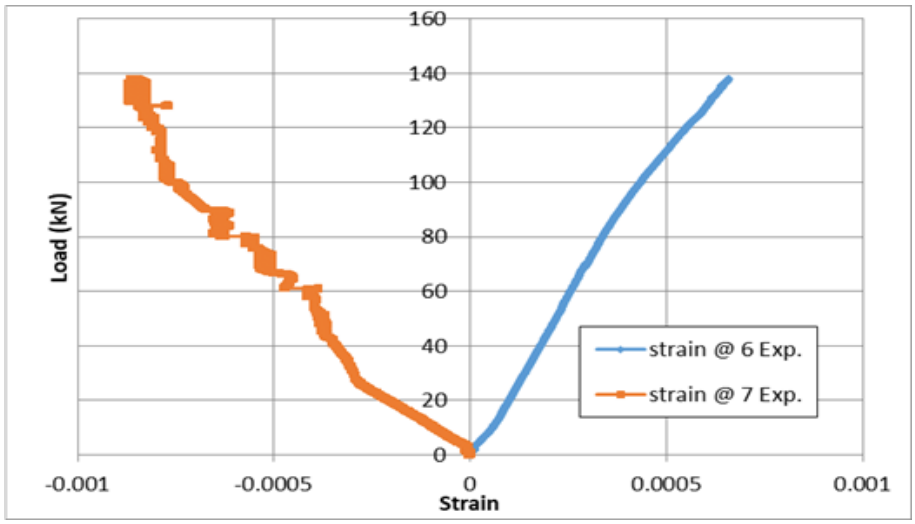

Figure 4.14 Load–strain curve of interior diagonal webs near the support of Model E HOWSJ specimens.

4.2.2 Results Summary of Model A, D, and E

From above comparisons between the Model A, D, and E HOWSJ six specimens it can be conclude that the behavior of HOWS joists which had the same cross section changed due to many parameters. The length to depth ratio affected the analysis behavior of the joists. Therefore, when the L/D decreased the enhancement of the ultimate capacity was very little, about just (1.81%). This slight increase was in the case of using the same bar diameter for the interior web used in prefabricated joists with L/D of 5.1 and joist with L/D of 3.6, but when the bar diameter of the

interior web was increased by about (24.48%) the enhancement of the ultimate load capacity was increased about (27%). Based on the location and direction of buckling for each specimen, it appears, that slenderness ratio of the diagonal interior web members effects were more critical for deeper members, where for Model E specimens when the slenderness ration of the diagonal interior web decreased about (24.48%) the deflection decreased by about (11.3%) and the ultimate load capacity increased about (25.7%) compared with Model D specimens.

For these three models a crimped-end web members failure occurred due to the local buckling of the diagonal interior web members near the supports before mid-span, thus the buckling of the web member in mid span was very little comparing with the end web members, so a special attention must be given to the crimp transition zone, because this failure mode may cause a reduction in stiffness of this type of HOWS joist.

4.2.3 Results of HOWS Joists of Models B and C

One of the main variables were adopted in this study was the effect of the shape of cross section on the behavior of the HOWSJ models, so in this section a comparison between three different cross section shape was made due to the failure mode, load- mid deflection curves , and load – strain curves for the models A, B and C specimens, which they had a different cross section but they had a same length/depth ratio and the same rebar diameter of the interior web members , where their cross section details were explained previously in Section (3.2.1) and also illustrated in Figure (3-2).

4.2.3.1 Failure Mode of Models B and C Specimens

A failure mode occurred due to the top and bottom chords buckling due to the deflection for all the HOWSJ specimens.

For Model B specimens, the local buckling was occurred in the vertical legs of the angles of top chord. Regarding Model C specimens, the failure happened

due to local buckling on the vertical and horizontal legs of the angles of top chord because those joists had unrestrained chord (weak stiffened chord) compared with Model B, because of them manufacturing shapes. Also the test results show that the failure had occurred due to the instability of the interior web members for these two models, where a local buckling of the diagonal interior web members was occurred at the mid-span of the joist and near the supports, but for Model B specimens the buckling of the diagonal interior webs near the support was greater than that of the diagonal interior webs at mid-span of the joist, and for Model C specimens the buckling of the diagonal interior webs at mid-span was greater than that which occurred for them near the supports.

There were also welding joint fracture failures between the web members (vertical and diagonal) and the chords at the top and bottom of the all models of HOWSJ specimens.

As mentioned from the modes of failure for all models of HOWS joists tested in this research that they had a failure mode of interior web members buckling near the supports called crimped-end web members and extended to the corner of the vertical legs of the top and bottom chord, but Model C specimens they were had less buckling deformation in these interior webs than the other models because this model had a width of cross section of 200 mm compared with the (100 mm) width for Model A and B. Plates (4.4) and (4.5), show the mode of failures of the two joist specimens tested for each model.

Plate 4.4 Mode of failures of Model B HOWSJ specimens.

Plate 4.5 Mode of failures of Model C HOWSJ specimens.

4.2.3.2 Load-Mid Span Deflection Curves of Models B and C Specimens

HOWS joists specimens of Model B and Model C, also Model A had the same depth but they had a different shape of the cross section. Table (4-4) presented the yield strength, deflection at yield strength, ultimate load, and the deflection at the ultimate load for each specimens of these two models. Also the results test for these models specimens of load versus vertical mid span deflection are illustrate in Figure (4-15) and (4-16).

From the results shown in Table (4-4), it can noted that every two specimens of the same model had very close values of ultimate load, yield strength, the deflection at the ultimate load, and yield deflection. Also Figures from (4-15) and (4-16) show that the two specimens for each model have to a large extent the same behavior, as for the previous models. Therefore, the mean for each two specimens was calculated in order to make a comparison between the experimental results for the different models.

Generally, the mean values of the test results of ultimate load capacity of the HOWSJ Model A specimens, which their top chord welded back to back were more than for the Models B and C by about (7.4%) and (14.5%), respectively. Whereas the load capacity of Model B specimens were more than for Model C specimens by (7.7%), but at the same time Model A and Model B specimens were had a maximum deflection less than for Model C by about (25.1%) and (12.8%), respectively. From these results, it can be concluded that the increasing of the width of the joist led to decrease in the ultimate load capacity of the HOWS joist, but the deflection at ultimate load capacity had a significantly large increasing.

Table 4.4 Experimental results of Models B, and C HOWSJ specimens.

Models	Specimens No.	Yield strength, P_y (kN)	Ultimate load, P_u (kN)	Def. at yield strength, δ_y (mm)	Def. at ultimate load, δ_u (mm)
Model A	SJ 1-1	64.55	100.99	4.07	7.80
	SJ 1-2				
Model B	SJ 2-1	59.72	94.24	4.483	9.369
	SJ 2-2	57.25	92.81	3.866	8.782
Model C	SJ 3-1	47.23	84.97	3.233	10.251
	SJ 3-2	49.31	87.65	3.898	10.562

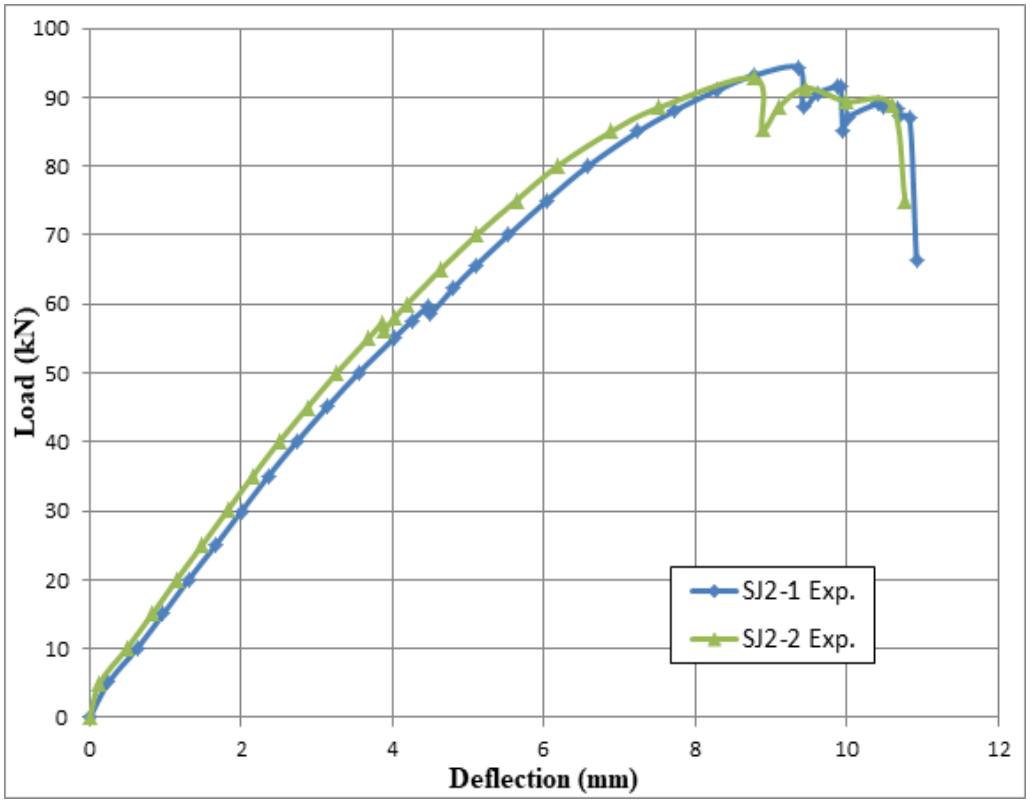

Figure 4.15 Experimental load-mid span deflection curve for model B specimens.

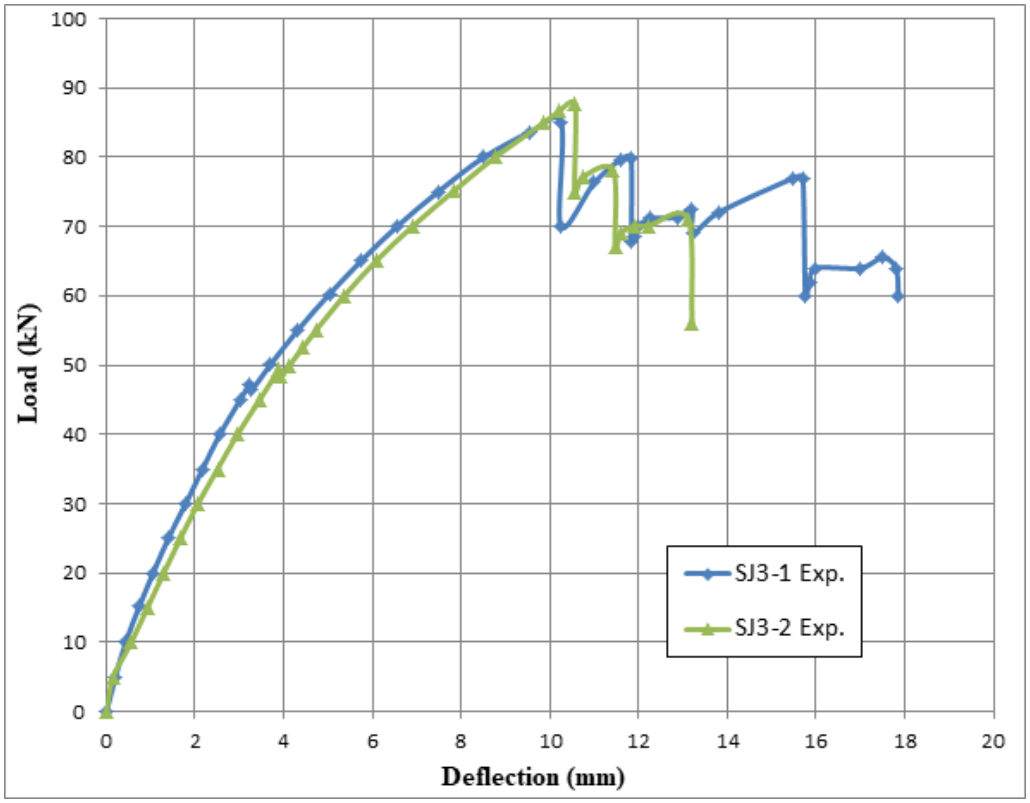

Figure 4.16 Experimental load-mid span deflection curve for model C specimens.

Also Figures from (A-4) and (A-5) in Appendix A show the vertical deflection a long the span of Model B, and C specimens so as to represent the final geometry of the steel joist at the ultimate load capacity.

4.2.3.3 Stiffness, Hardness , and Ductility Index comparison for Models B, and C Specimens.

This subsection concerned with the comparison between the specimens results of Model A, B, and C by using the stiffness, hardness , and ductility Index of each model. Table (4-5) show a comparison between these indices for the mean values of each two specimens for the same model. Also Figures (4-17) and (4-18) show a comparison between the load-mid span deflection behavior for the specimens of each model.

Generally, the results in Table(4-5), Figures (4-17) and (4-18) indicated that the flexural stiffness of Model A specimens was significantly higher than Model B, and C specimens by about (11.7%), and about (14.7%) respectively, and the Model B had a flexural stiffness value higher than Model C by (3.4%).

Regarding the index of the hardness, the results of tests show that the Model A specimens had a highest hardness value among other Model specimens, which was higher about (20.4%) and (35.98%) than of models B and C, respectively.

Finally for the ductility index it can be noticed that the Model C had a higher ductility about 1.52 and 1.35 times the ductility of Model A and Model B specimens, respectively. But the Model B had a ductility about 1.13 times the ductility of Model A specimens. The highest ductility value of Model C means that this model had the best system performance among other model specimens, since such value reflects the system ability to deform and clearly observed under visual inspection before structure collapsing. Hence, this ratio gives an indication to yielding failure rather that its occurrence suddenly.

Table 4.5 Stiffness, hardness, and ductility index results of Models A, B, and C HOWSJ specimens.

Models	Model A	Model B	Model C
Mean Yield strength, P_y (kN)	64.55	58.49	48.27
Mean Ultimate load, P_u (kN)	100.99	93.53	86.31
Mean Def. At yield strength, $\delta_y(mm)$	4.07	4.18	3.57
Mean Def. At ultimate load, $\delta_u(mm)$	7.80	9.08	10.41
Stiffness, $P_y/\delta_y(kN/mm)$	15.85	13.99	13.52
hardness, $P_u/\delta_u(kN/mm)$	12.95	10.31	8.29
Ductility index, δ_u/δ_y	1.92	2.17	2.92

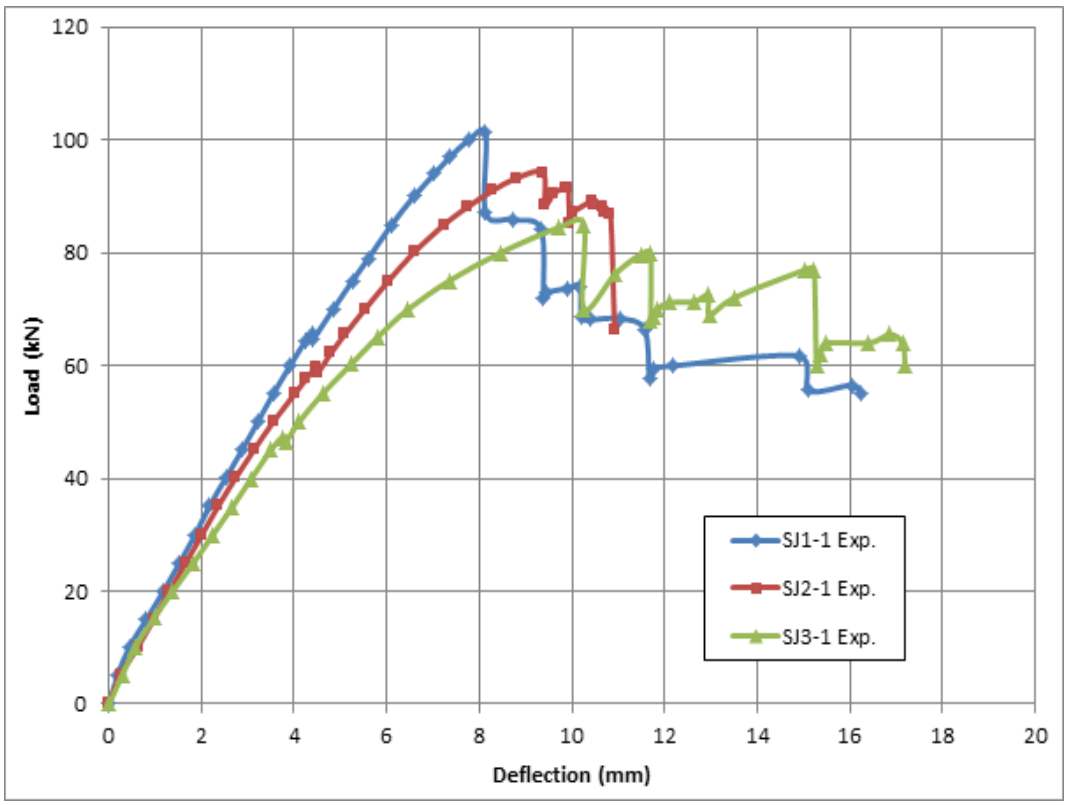

Figure 4.17 Load-mid span deflection curve for SJ1-1, SJ2-1, and SJ3-1 specimens.

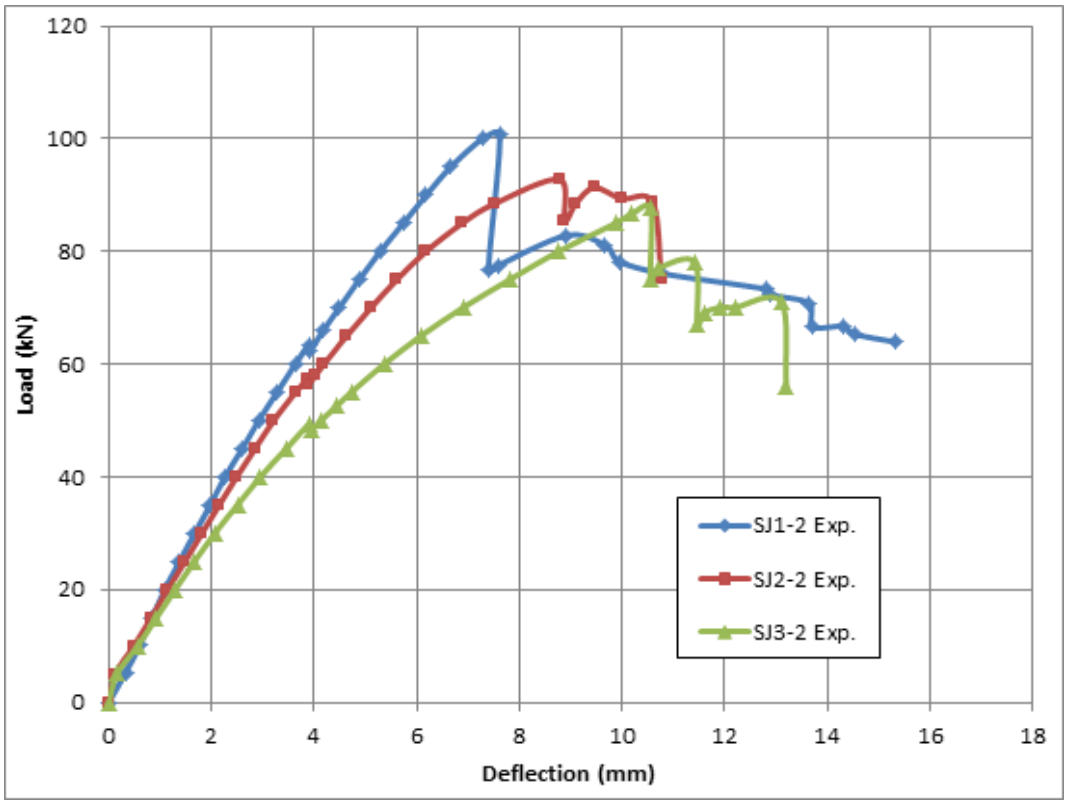

Figure 4.18 Load-mid span deflection curve for SJ1-2, SJ2-2, and SJ3-2 specimens.

4.2.3.4 Strain Results of Models B, and C

The strain gauges readings, show the mean behavior of the HOWSJ of models B and C specimens during the test as explained in Figures from (4-19) to (4-24). Figures (4-19) and (4-22) illustrate that the strain gauge (ϵ_1) on vertical leg of angle of the bottom chord exhibited a tension strain up to failure load in both Models B and C, but it exhibited as a compression strain for Model A. And the maximum value for (ϵ_1) for Model C was higher than for models A and B by about (14.52%) and (22.89%), respectively. While the behavior of the strain gauge (ϵ_0) on the horizontal angle leg of the bottom chord was in tension for all models' specimens and its maximum value for Model C was higher than for models A and B by about (19.24%) and (63.95%), respectively. From Figures (4-7), (4-20), and (4-23) it can be recognized that the strain at the horizontal leg of the angle of top chord (ϵ_4) became very close to the yield limit of the steel angle for the three

model specimens, but it was in the Model C more than of the models A and B by (65.79‰) and (51.80‰), respectively. And from these figures it can be noted that the behavior of the strain gauge (ϵ_3) on the vertical angle leg of the top chord was in compression for all models' specimens, also it can be mentioned that (ϵ_3) for Model C was a very higher than from the one for Model B by (80.41‰), while (ϵ_3) of Model B was higher than from the one for Model A by (98.26‰).

Regarding the strain gauges (ϵ_6 and ϵ_7) were exhibited a tension and a compression strains, respectively up to failure load for all models specimens. Figures (4-21) and (4-24) they emphasized that the strain gauges on the diagonal interior web members (ϵ_6 and ϵ_7) for Model C specimens were more than from Model B specimens by about (4.94‰) and (28.65‰), respectively.

Finally, by comparing the above results with HOWSJ Model A specimens, it can be noted that the readings of the strain gauges at the top chord for Model C and B were very higher. Also the reading of the stain gauges on the interior web members (ϵ_6 and ϵ_7) in Model A was greater than from Model B by about (50.49‰) and (41.82‰), respectively. And the reading of the stain gauges on the interior web members (ϵ_6 and ϵ_7) of Model A was also more than of Model C by about (47.92‰) and (18.52‰), respectively. The reason of this was due to the fact that the distance between the interior webs in Model C was (200mm), and (100 mm) for Model B, while in Model A the distance was about (8mm), This made the stresses were more concentrated in the interior web members of the Model A than the other two models.

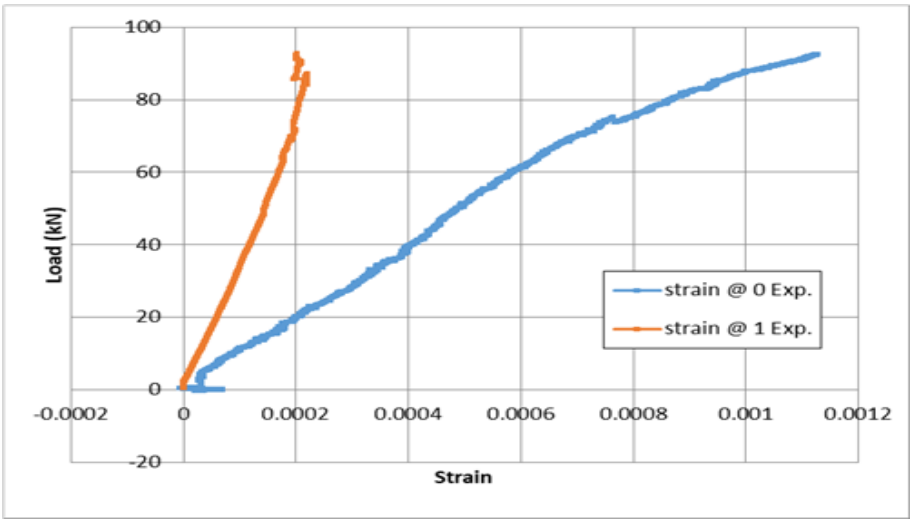

Figure 4.19 Load – strain curve of bottom chord of Model B HOWSJ specimens.

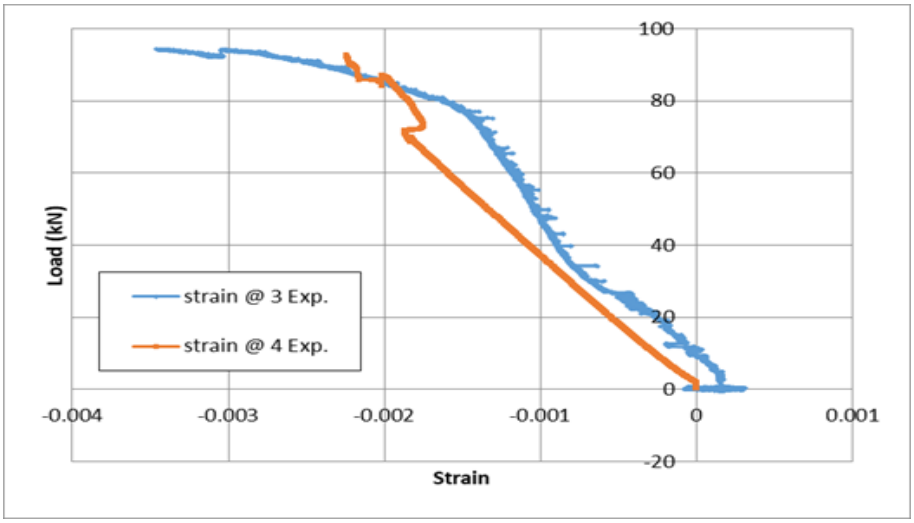

Figure 4.20 Load – strain curve of top chord of Model B HOWSJ specimens.

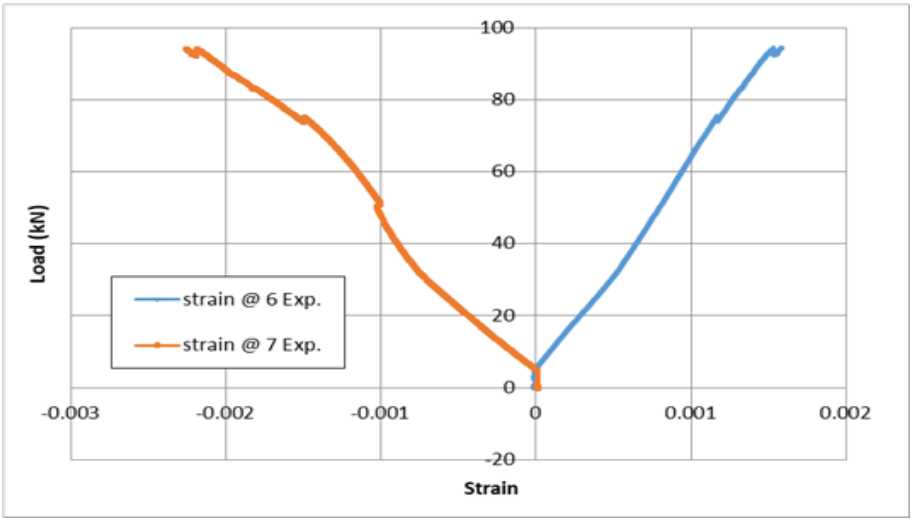

Figure 4.21 Load – strain curve of interior diagonal webs near supports of Model B HOWSJ specimens.

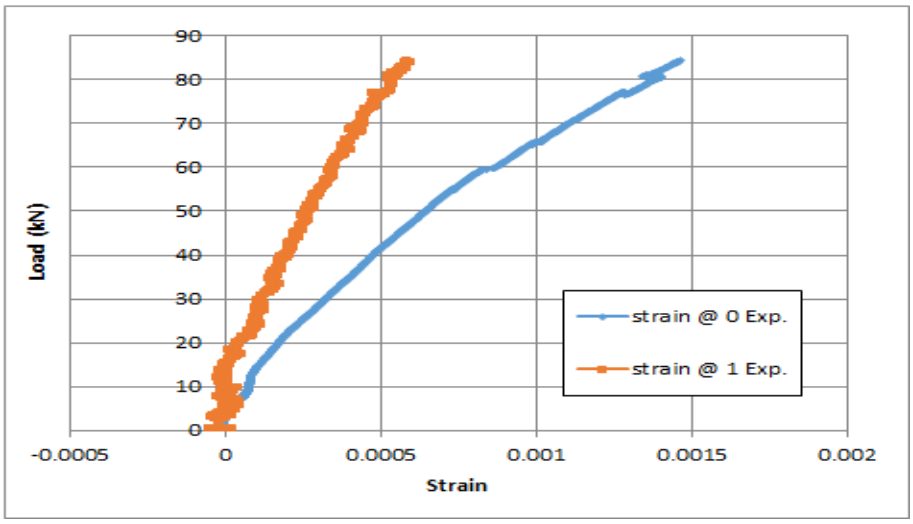

Figure 4.22 Load – strain curve of bottom chord of Model C HOWSJ specimens.

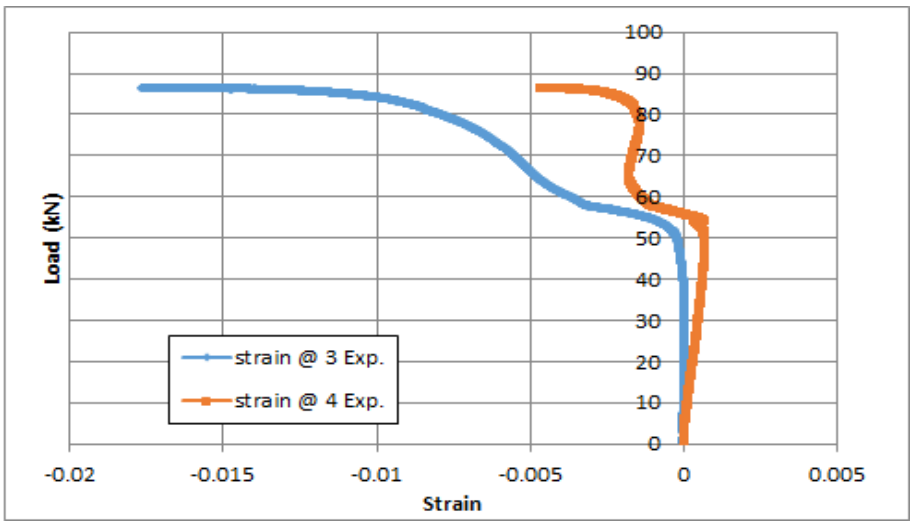

Figure 4.23 Load – strain curve of top chord of Model C HOWSJ specimens.

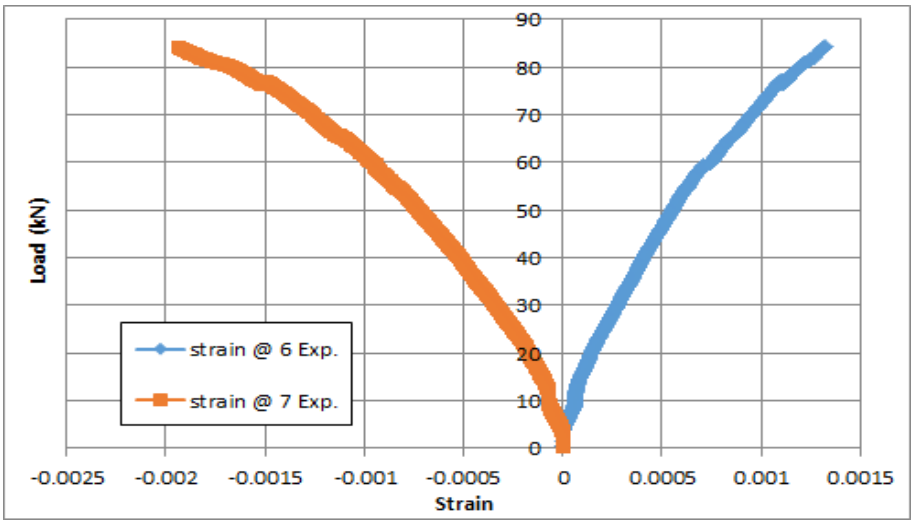

Figure 4.24 Load – strain curve of interior diagonal webs near support of Model C HOWSJ specimens.

4.2.4 Results Summary of Model A, B, and C

From pervious comparisons between the Model A, B, and C HOWSJ six specimens it can be conclude that the behavior of HOWS joists which had a different cross section changed due to many parameters. Therefore, when the width between the interior web members of the HOWS joist increased the ultimate capacity and the stiffness of the HOWS joist were decreased. Thus Model A was had ultimate capacity more than from Models B, and C, and it was more stable and more stiffened.

But on the other hand, it was found that the ductility of the HOWSJ increased when the flange width of the chords of HOWSJ increased which led to increase the distance between the interior web members in the cross section direction of the joist. As mentioned that for model C the value of the capacity has decreased almost(14.5%) , while the ductility index has increased by (34.3%) compared with Model A, and this was a significant increase for the ductility index, which is considered one of the important factors in structures design. Therefore, sections similar to Model C can be used, but at the same time, a way must be found to strengthen the top cord against local buckling to increase the stiffness of this model.

4.3 Properties of Hardened Concrete Tests Results

This section presented the test results of control specimens were casted from each mixture to determine the mechanical properties of NC and SFRC including compressive strength, splitting tensile strength, modulus of rupture and stress-strain relationship in compression. These tests were performed on the control specimens at the day of the composite open web steel joists test.

4.3.1 Results of Compressive Strength Test

The compressive strength of three cubic specimens of (100 × 100)mm and three cylindrical specimens of (100 × 200)mm for each of NC and SFRC were illustrate in Table (4-6) at ages 7 and 28 days. The results of tests showed that the ratio of compressive strength for cylindrical samples to cube samples was 0.81 and 0.85 for NC and SFRC, respectively. Also NC appeared a compressive strength lower than SFRC by about (9.47%), which proved that the compressive strength is less affected by the presence of (1.0%) volume fraction of steel fibers.From Plates (4-6) and (4-7) it can be noticed that in SFRC the pattern of the cracks at failure was more than from cracks in NC, this means that the steel fiber blocked the movement of particles and reduced crushing. Generally, the experimental results showed that compressive strength of the concrete type is less affected by the presence of fibers, but the mode of failure of SFRC specimens considerably changes from rupture to ductile. Due to bridging effect of the fibers, the tested cubic and cylinder specimens did not crush but held their integrity up to the end of the test.

Table 4.6 Results of compressive strength test of concrete.

Concrete Type	Age (days)	Cubic Comp. Strength, f_{cu} (MPa)		Cylinder Comp. Strength, f'_c (MPa)	
		Individual	Average	Individual	Average
(NC)	7	24.47	26.94	21.09	20.87
		25.24		20.76	
		31.1		19.95	
	28	38.43	38.68	32.13	31.37
		39.76		31.47	
		37.85		30.52	
(SFRC)	7	26.99	29.95	22.86	24.48
		32.08		25.64	
		30.79		24.94	
	28	40.76	40.68	34.64	34.65
		39.98		35.08	
		41.29		34.25	

Plate 4-6 Failure mode of NC samples due to compressive strength.

Plate 4-7 Failure mode of SFRC samples due to compressive strength.

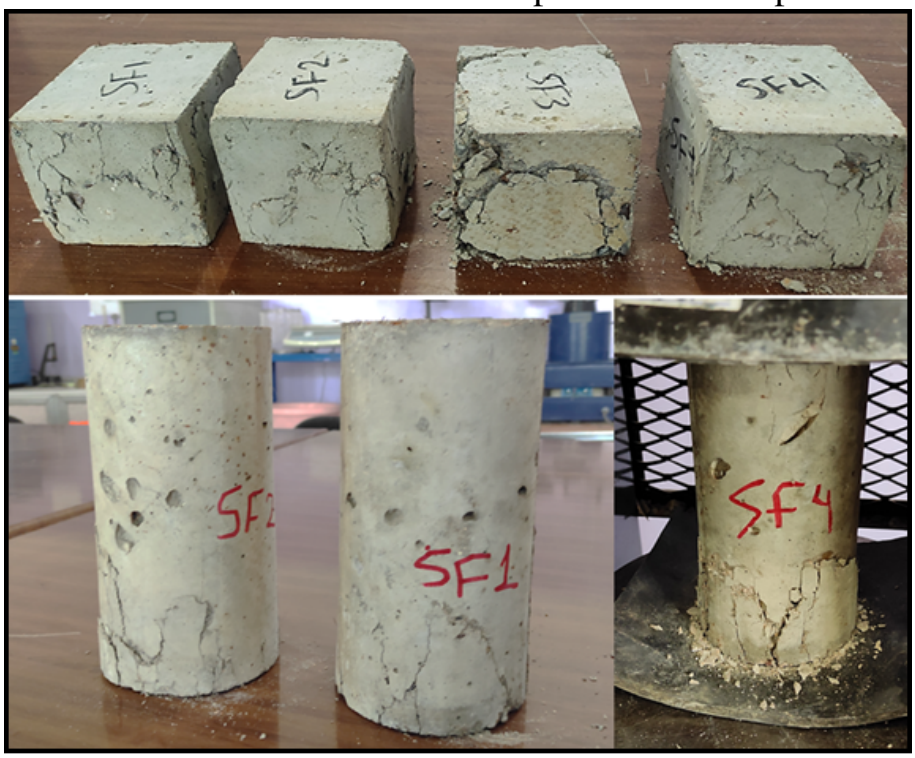

4.3.2 Results of Flexural Strength Test

Figure (4-25) show the crack pattern of NC and SFRC prisms after failure, from this figure it can be noticed that the specimens of NC had shown a typical crack propagation pattern which led into splitting of beam in two piece geometry. But due to addition of steel fibres in concrete cracks gets discontinued which results into the ductile behavior of SFRC. The experimental results of the modulus of rupture showed that the fraction volume 1% of steel fiber improved the flexural strength of concrete by (35.88%), as illustrate in Table (4-7). This enhancement in flexural capacity of SFRC may be attributed to the ability of steel fiber to arrest and disperse the developing of micro cracks in the sample under the applied load. In general it can be concluded that the effect of steel fiber content on increasing the flexural strength was more than the effect of increasing the compressive strength by about (73.6%).

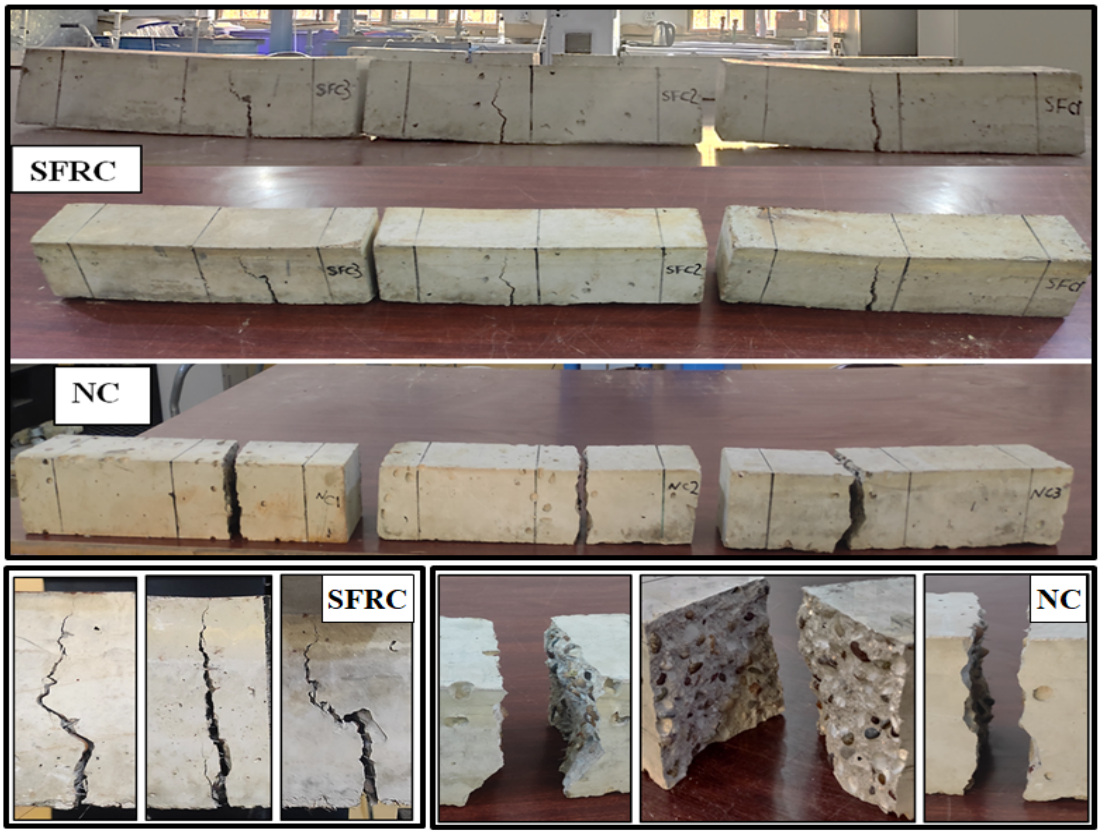

Figure 4.25 Modes of failure for SFRC and NC samples under flexural tensile test.

Table 4.7 Results of flexural strength test.

Specimen No.	Modulus of Rupture, $f_r(MPa)$			
	(NC)		(SFC)	
	Individual	Average	Individual	Average
1	4.72		7.90	
2	5.93	5.11	8.28	7.97
3	4.67		7.73	

4.3.3 Results of Splitting Tensile Strength Test

Splitting tensile test was carried out at age 28 days to investigate the tensile strength for NC and SFRC. The results of the test for cylindrical samples of (100×200)mm are presented in Table (4-8). Plate (4-8) show the failure mode of SFRC and NC under splitting tensile test.

The average results showed that the SFR had a more excellent tensile resistance than NC by about (24.35%),where the mechanism of bridging of fiber led to control the micro-cracks. The tensile strength increased inside the matrix of concrete because of the using of the steel fiber increased the bond between particles[11].

Table 4.8 Results of splitting tensile strength test.

Specimen No.	Splitting Tensile Strength, $f_{sp}(MPa)$			
	(NC)		(SFC)	
	Individual	Average	Individual	Average
1	2.71		3.85	
2	3.08	2.92	3.59	3.86
3	2.96		4.13	

Plate 4-8 Modes of failure for NC and SFRC samples under splitting tensile test.

4.3.4 Stress- Strain Curves for NC and SFRC in Compression

The stress-strain curve for NC and SFRC were plotted. All samples were tested under uniaxial compression pressure. From test results it can be concluded that the SFRC had a very high values of maximum strain which was about (74.51%) more than of NC, demonstrating a high ductility. As a result for that, toughness (energy absorption) of SFRC was enhanced as the area under the stress-strain curve grew. While the compressive strength of the SFRC was enhanced slightly by about (9.4%) compared with the compressive strength of NC, Figure (4-26).

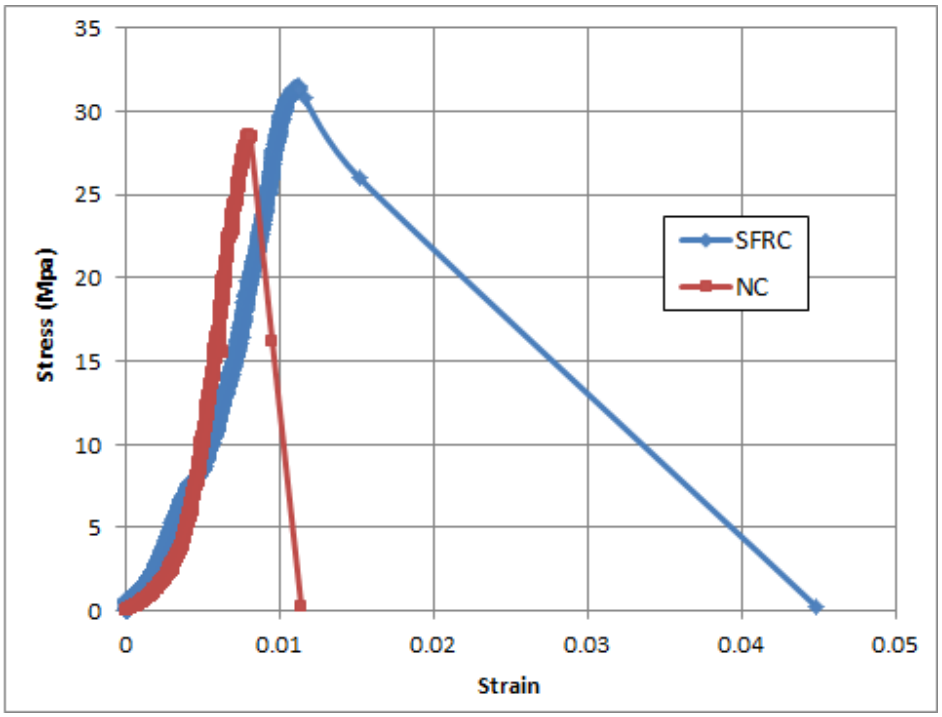

Figure 4.26 Stress-strain curves for NC and SFRC.

4.3.5 Results of Modulus of Elasticity Tests

The modulus of elasticity of NC was obtained according to ASTM C469-2002 [100]. While the modulus of elasticity of SFRC was calculated through the slope of stress strain relationship between zero stress and (20 %) of the ultimate compressive capacity [55]. The obtained results which illustrate in Table (4-9) show that the the experimental results of modulus of elasticity for NC were higher than the values calculated by using the ACI 318-19, Equation (3-6) [92]. And also were higher for SFRC compared with Equation (2-1) by (Suksawan et al,2018) [57], where ($C/S = 0.83 < 1$, and $V_f = 1\%$) which were used in this study.

Table 4.9 Results of modulus of elasticity of concrete.

Concrete Type	Exp. Modulus of Elasticity (MPa)	Theoretical Modulus of Elasticity (MPa)
NC	26731	26324 (Equation 3.6)
SFRC	28107	27616 (Equation 2.1)

4.4 Push-out Tests (POT) Results

Six specimens were investigated by push-out test, three specimens were with non fibrous concrete slabs, and three specimens were with steel fiber reinforced concrete slabs. The test was carried out by gradually applying a direct load to a steel section while the system was supported by concrete. The maximum shear resistance per connector was calculated by dividing the maximum applied load at failure by the total number of studs used in the specimen (four studs for each slab). Table (4-10) show the mean of the maximum shear resistance per connector results for the two slabs of one specimen , as well as the corresponding average slip at the maximum shear capacity evaluated from the two measured points of the push-out specimens. Furthermore Table (4.11) show a comparison between the shear stud resistance results from this experiments and the ultimate shear resistance calculated from some commonly used design codes such as AASHTO LRFD code [103], Eurocode code [104], the standard specification for CJ-series composite steel joists [6], and GB 50017 code [105], as shown in Appendix (B). For the experimental results, it can be observed that the calculated codes results based on Equations (B.1) to (B.4) were conservative for both NC and SFC.

Figures (4-27) and (4-28) show the results of the NC and SFRC slab specimens, respectively. According to these figures, the relative slip at peak load was approximately (3.02 mm) for NC specimens and (2.53 mm) for SFC specimens, which means that by using steel fiber with fraction volume of 1% caused to decrease the slip by about (16.23 %). From these figures it can be concluded that SFC enhanced the stiffness and the toughness (energy absorption) of the shear connector in the composite system, where the area under the load- slip curve was increased when using the SFC slab. It should be noted that there was a strong bond between the SFRC and the shear connectors, and this bond weakens with the specimens cast with non fibrous concrete of the same dimensions, whereas

the steel fiber reinforced concrete specimens show an increase in shear capacity of the connector of about (7.87%).

The load-slip curves for both types of concrete were had a nonlinear behavior because the failure was accrued by the steel shear connector and concrete simultaneously, where the failure occurred when the shear connector had fractured with smooth shear surface and obvious shear deformation. Plates (4-9) and (4-10) show the failure mode for NC and SFC specimens, respectively. There were no cracks or crushing in the vicinity of shear studs embedded in SFC slabs of push-out specimens in contrast to the specimens in which slabs were cast with NC, which was another advantage of adding steel fibers to the concrete. Also, it can be observed that the cracks for the slab cast with NC were more than from SFC slabs.

Table 4.10 Results of push-out test.

Concrete Type	specimen	Maximum shear resistance per connector, (kN)	Slip at Maximum shear capacity, (mm)
(NC)	POT-NC1	50.52	3.35
	POT-NC2	50.87	3.12
	POT-NC3	51.69	2.59
	Average	51.03	3.02
(SFRC)	POT-SFC1	55.36	2.65
	POT-SFC2	54.53	2.51
	POT-SFC3	56.27	2.42
	Average	55.39	2.53

Table 4.11 Comparison of experimental and theoretical shear stud resistance.

Type of concrete slab	non fibrous concrete (NC)	Steel fiber concrete (SFC)
Experimental results (kN)	51.03	55.39
Equation (B.1) results (kN)	Min. of (50.92,52.16)	Min. of (54.88, 52.16)
Equation (B.2) results (kN)	Min. of (41.73,41.76)	Min. of (41.73,43.91)
Equation (B.3) results (kN)	Min. of (50.92,39.12)	Min. of (54.88, 39.12)
Equation (B.4) results (kN)	Min. of (50.92,36.51)	Min. of (54.88,36.51)

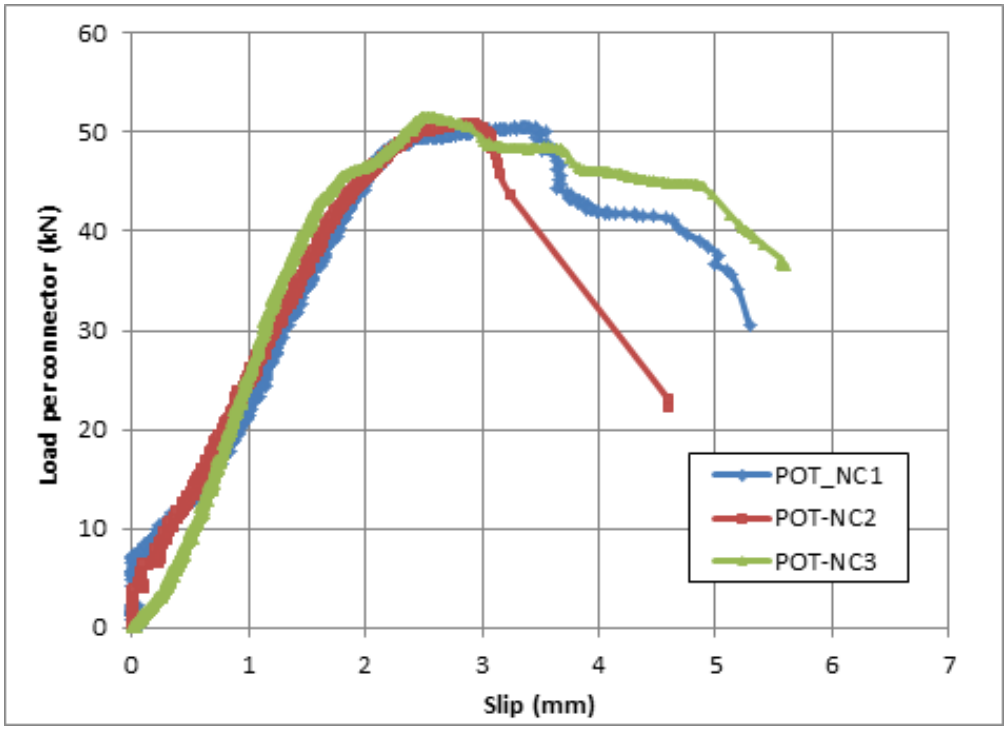

Figure 4.27 Load-slip curves of NC push-out specimens.

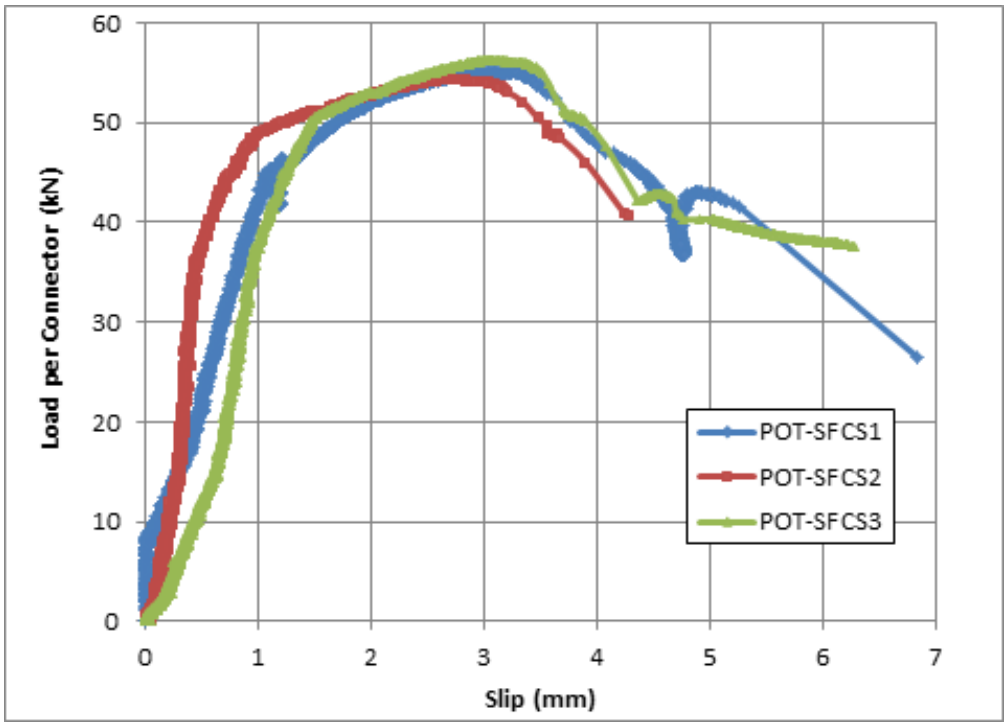

Figure 4.28 Load-slip curves of SFC push-out specimens.

Plate 4-9 Failure modes of NC push-out specimens.

Plate 4-10 Failure modes of SFC push-out specimens.

4.5 Composite Open Web Steel Joists Results

This section discussed the results of seven COWS joists , which were tested under monotonic load. These COWS joists were classified into two sets. The first set had three COWS joists with three different cross section shape of the steel joist, and the second set has three COWS joists with the same cross section shape but

with different type and width of concrete slab, the details of each specimen were be illustrated in Table (3-8) previously.

4.5.1 Failure Modes of Composite Open Web Steel Joist Specimens

The COWSJ specimens were all tested under monotonic load until failure occurred. All specimens failed due to bottom chord yielding, buckling of diagonal interior web members, failure at welded joints between the vertical legs of top and bottom chords and interior webs, and concrete cracks within midspan.

The failure modes in the concrete of composite specimens were observed after bottom chord yielding, and they began with small tensile cracks in the bottom surface beneath the region of subjecting load, because this region was subjected to tensile stresses because the neutral axis was within the concrete slab for all specimens, and it may have been caused by the presence of shear connectors in that region. These cracks were followed by small longitudinal or transverse cracks in the concrete slab's middle upper surface, which could be attributed to the weakness and caused by the use of longitudinal steel reinforcement. The spread of crack width and length was slower in steel fiber reinforced concrete specimens than in non-fibrous concrete specimens; these cracks increased in number with increasing applied loads until they reached the level of increasing crack width, at which point the concrete was considered failed. The failure mode in the concrete of the COWSJ Specimens CSJ1-1 SF5.1, CSJ2-2 SF5.1, and CSJ3-6 SF3.6 begins with small cracks in the bottom surface beneath the region of subjecting load, followed by longitudinal cracks in the middle upper surface of the concrete slab, which may be due to shear flow caused by the shear connectors in that region. While transverse cracks occurred instead of longitudinal cracks in the middle upper surface of the concrete slab for the specimens CSJ3-3 SF5.1, CSJ3-4 SF5.1, and CSJ3-5 N5.1, this could be due to flexural failure or the use of longitudinal steel reinforcement. Finally, both longitudinal cracks, transverse cracks, and crushing

beneath the applied load occurred in the middle upper surface of the concrete slab for the CSJ3-7 N3.6 specimen.

In general, the COWS joists were subjected to shear instability in the diagonal interior web members near the supports (crimped-end web members), which extended through the other web members along the joist. The local buckling of the diagonal interior web members was greater in specimens with a span to depth ratio (L/D) of (3.6) than in specimens with a (L/D) ratio of (3.6). (5.1).

Table (4.12) displayed the first visible crack loads, ultimate load capacity, percentage of load caused by the first crack to ultimate load, and first crack width for each specimen, and Figures (4-29) to (4-35) displayed the failure modes of each specimen. Plate (4-11) also included photos of the first crack width measured with a crack meter for some specimens.

Table 4.12 Experimental results of first crack load.

Specimen No.	First Crack Load, P_{crack} (kN)	Ultimate Load Capacity, P_u (kN)	(P_{crack}/P_u) (%)	Width of First Crack (mm)
CSJ 1-1 SF 5.1	70	160.153	43.71	0.04
CSJ 2-2 SF 5.1	70	155.495	45.02	0.05
CSJ 3-3 SF 5.1	60	137.892	43.51	0.03
CSJ 3-4 SF 5.1	65	139.684	46.53	0.05
CSJ 3-5 N 5.1	45	135.157	33.39	0.04
CSJ 3-6 SF 3.6	60	145.978	41.10	0.05
CSJ 3-7 N 3.6	45	140.286	32.08	0.05

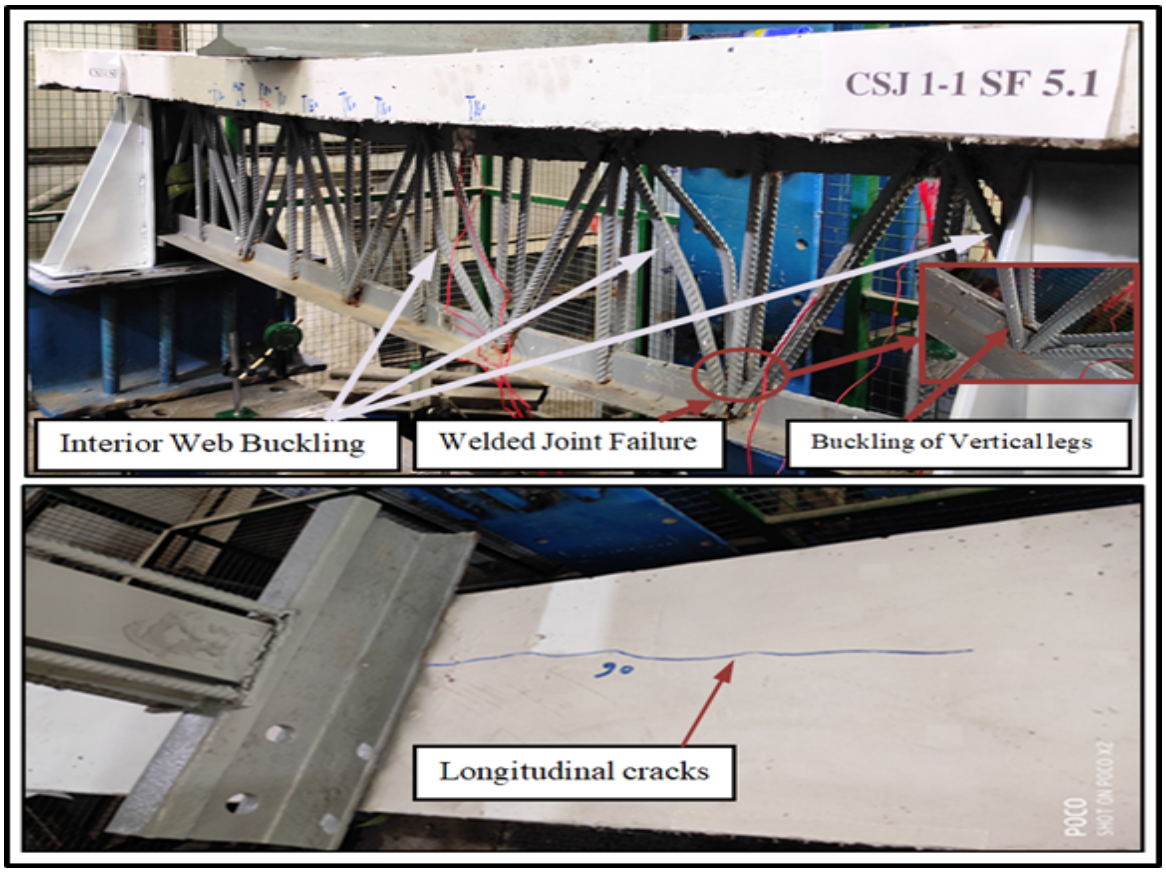

Figure 4.29 Mode failure of CSJ 1-1 SF 5.1 specimen.

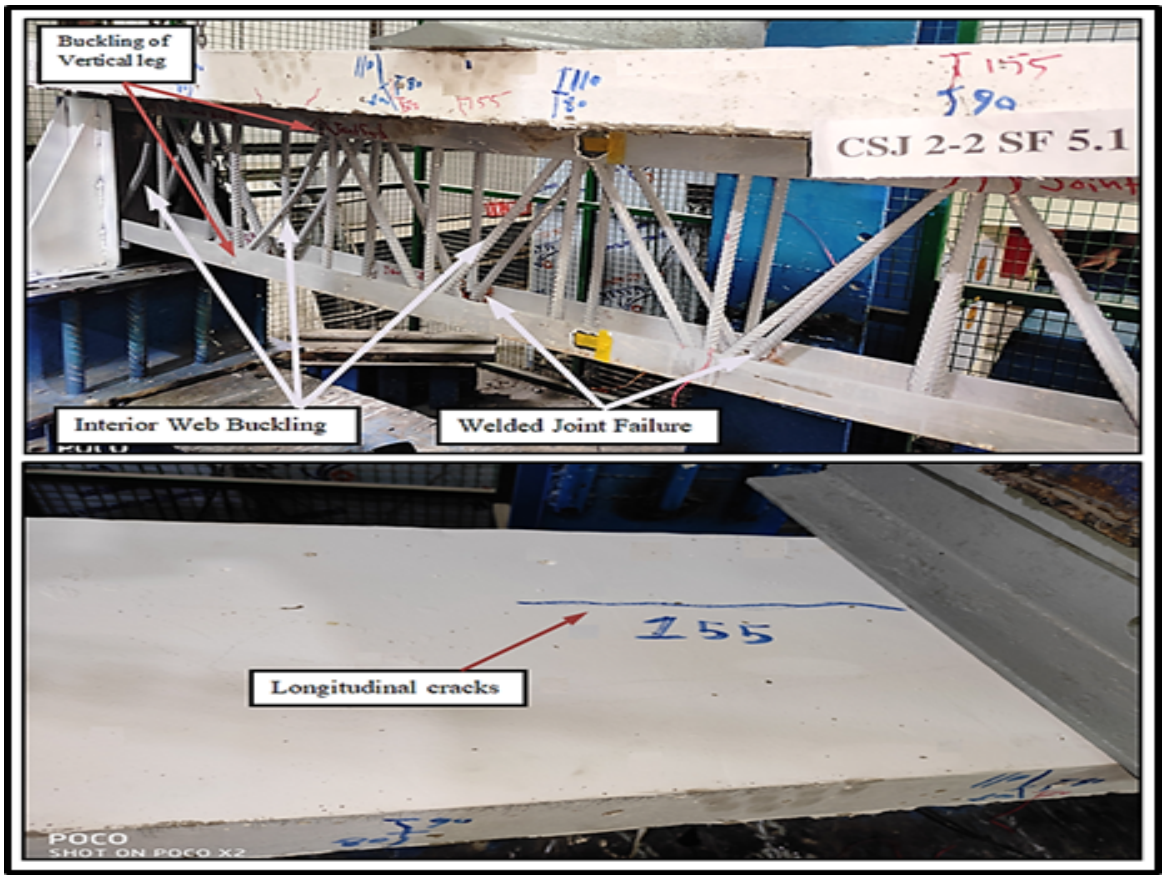

Figure 4.30 Mode failure of CSJ 2-2 SF 5.1 specimen.

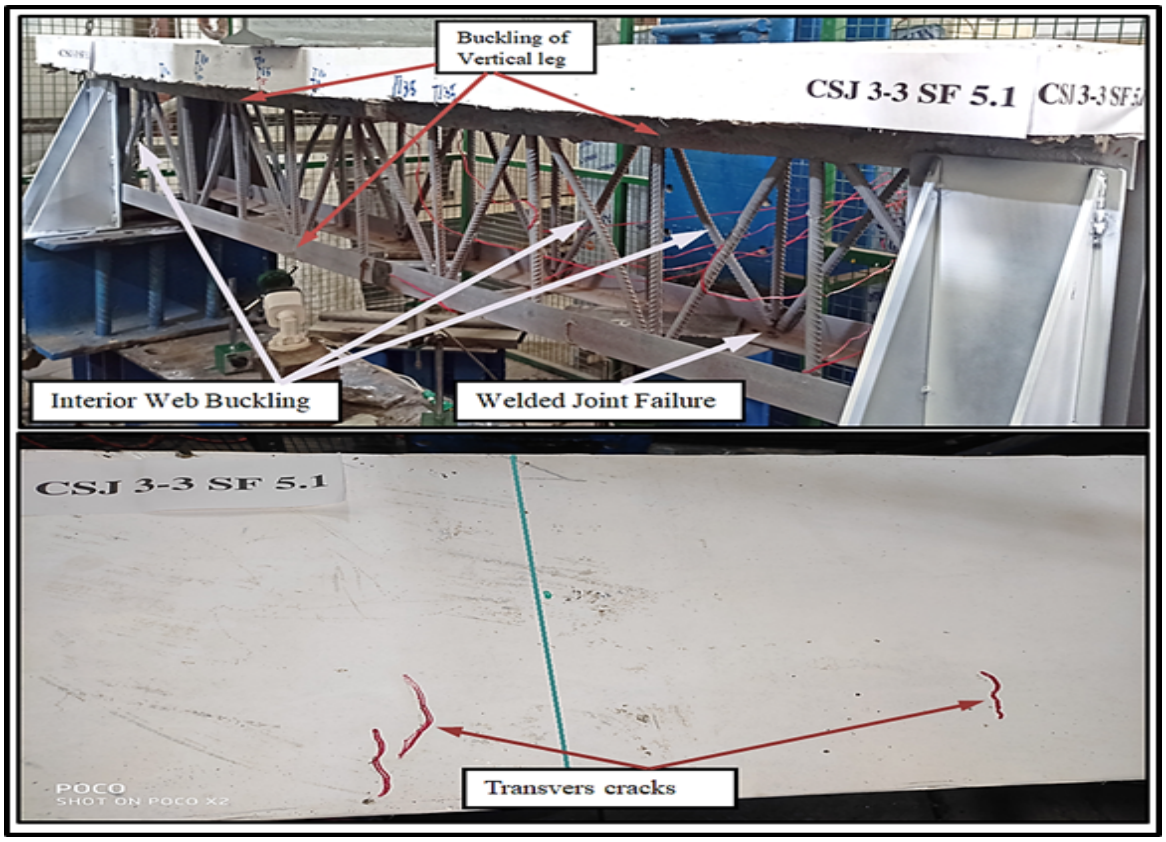

Figure 4.31 Mode failure of CSJ 3-3 SF 5.1 specimen.

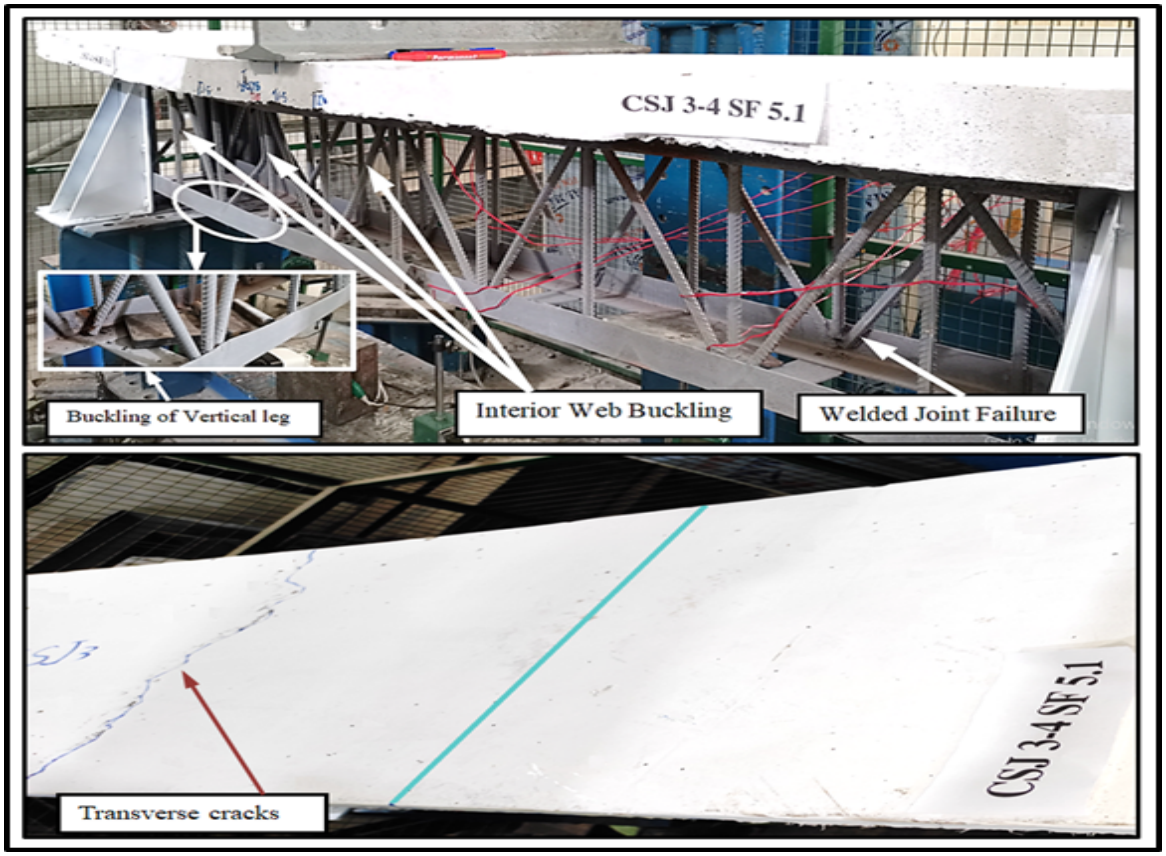

Figure 4.32 Mode failure of CSJ 3-4 SF 5.1 specimen.

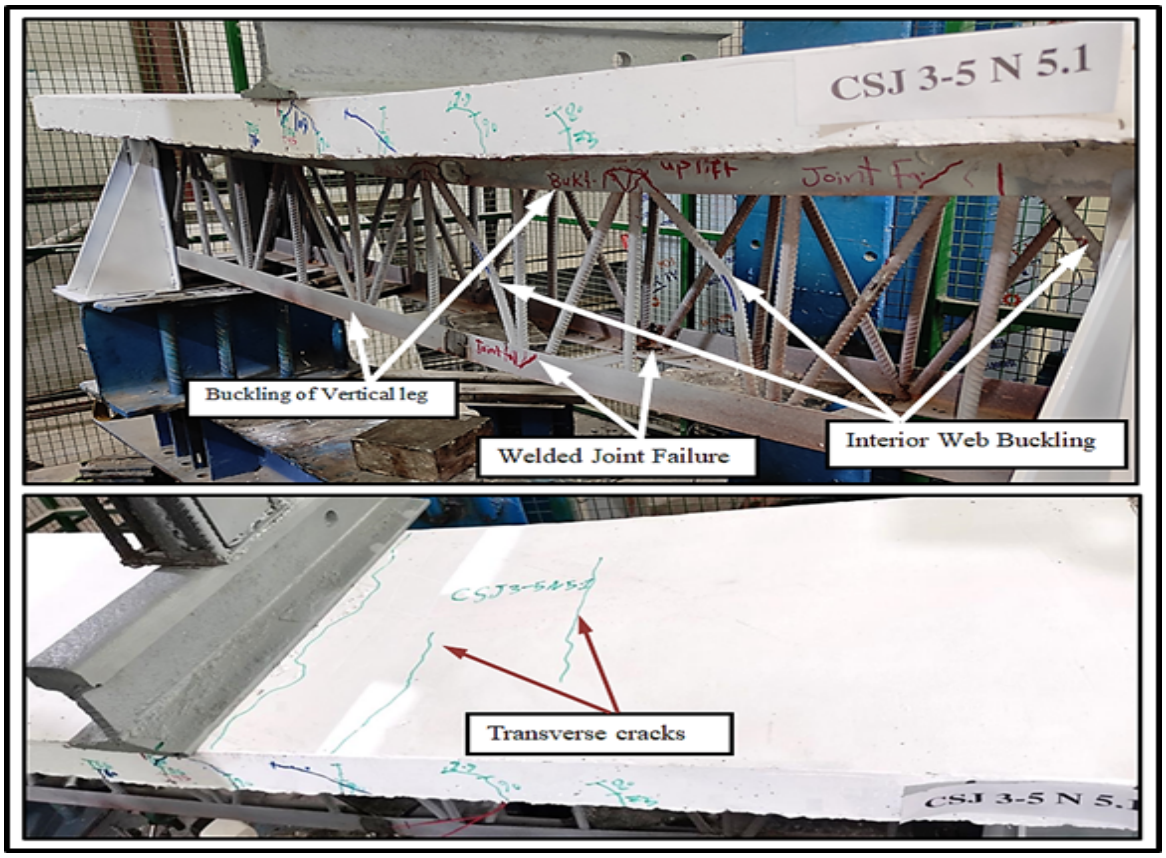

Figure 4.33 Mode failure of CSJ 3-5 N 5.1 specimen.

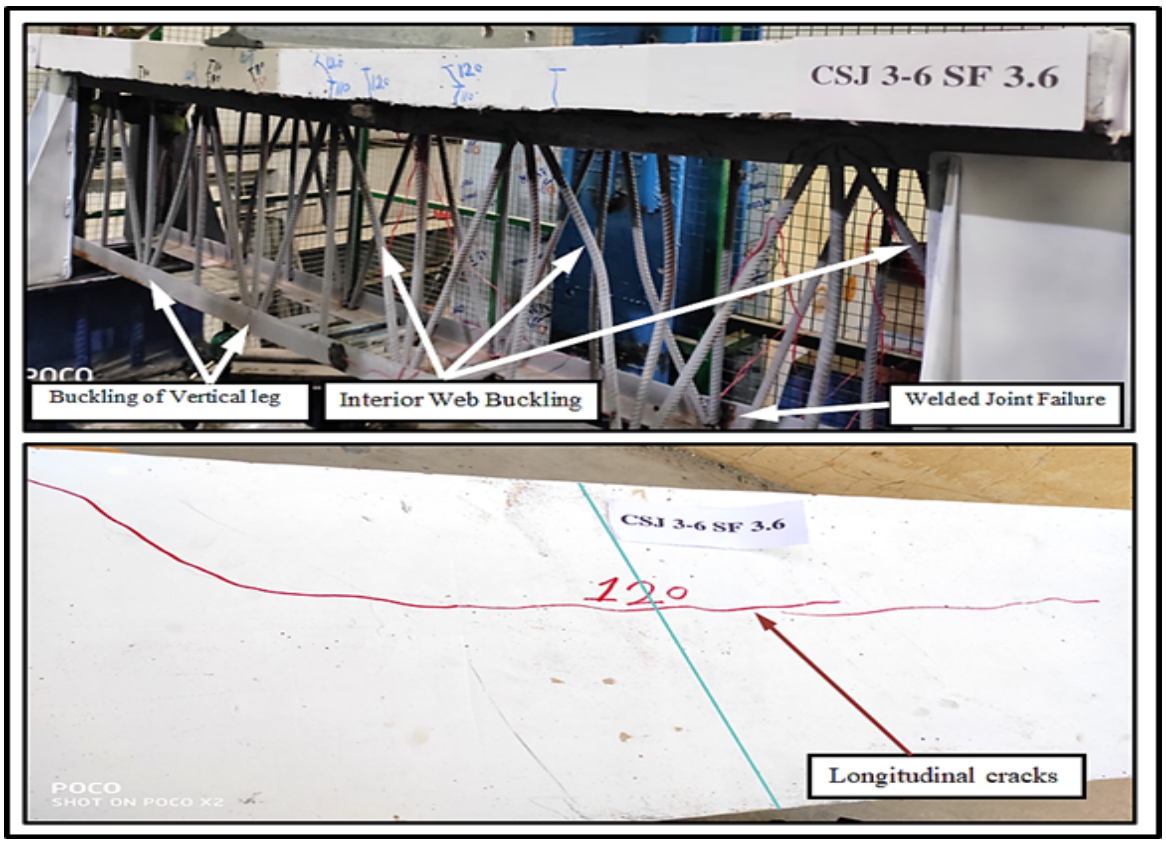

Figure 4.34 Mode failure of CSJ 3 -6N 3.6 specimen.

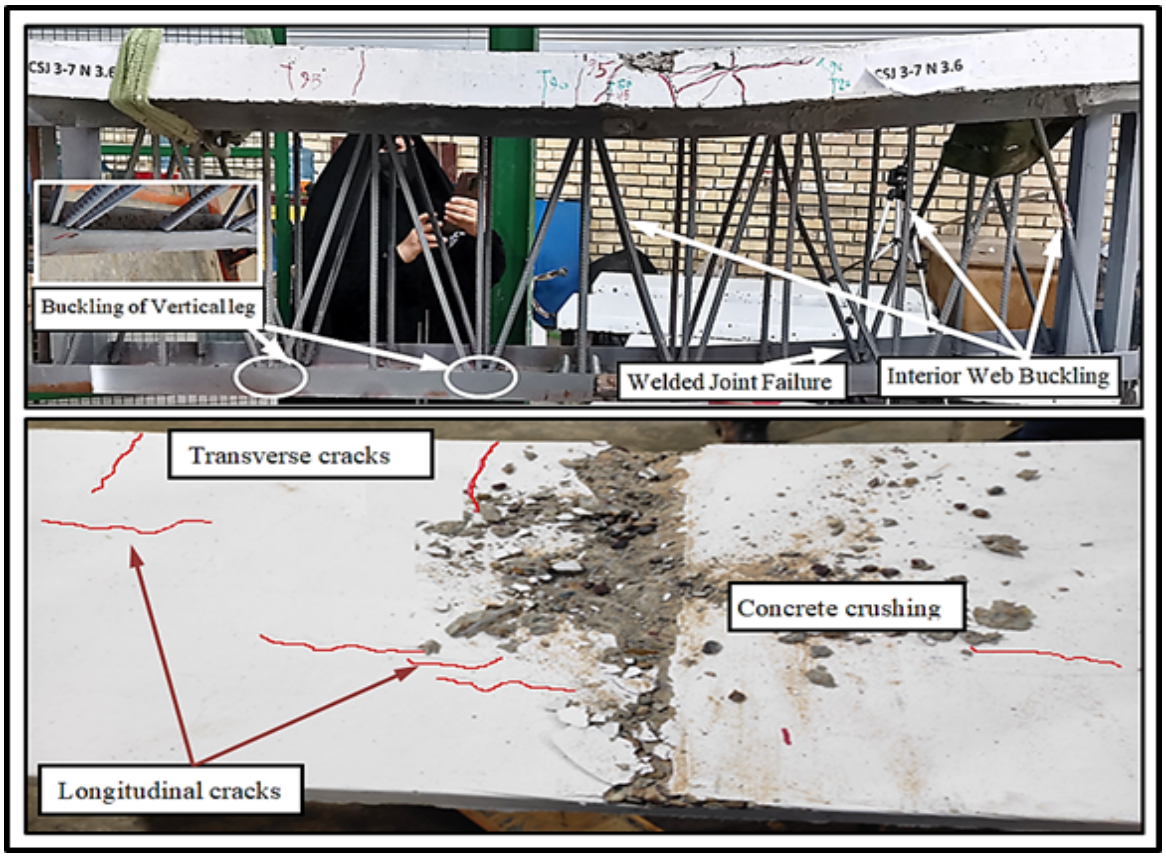

Figure 4.35 Mode failure of CSJ 3-7 N 3.6 specimen.

Plate 4-11 Photograph for crack width for some COWSJs specimens.

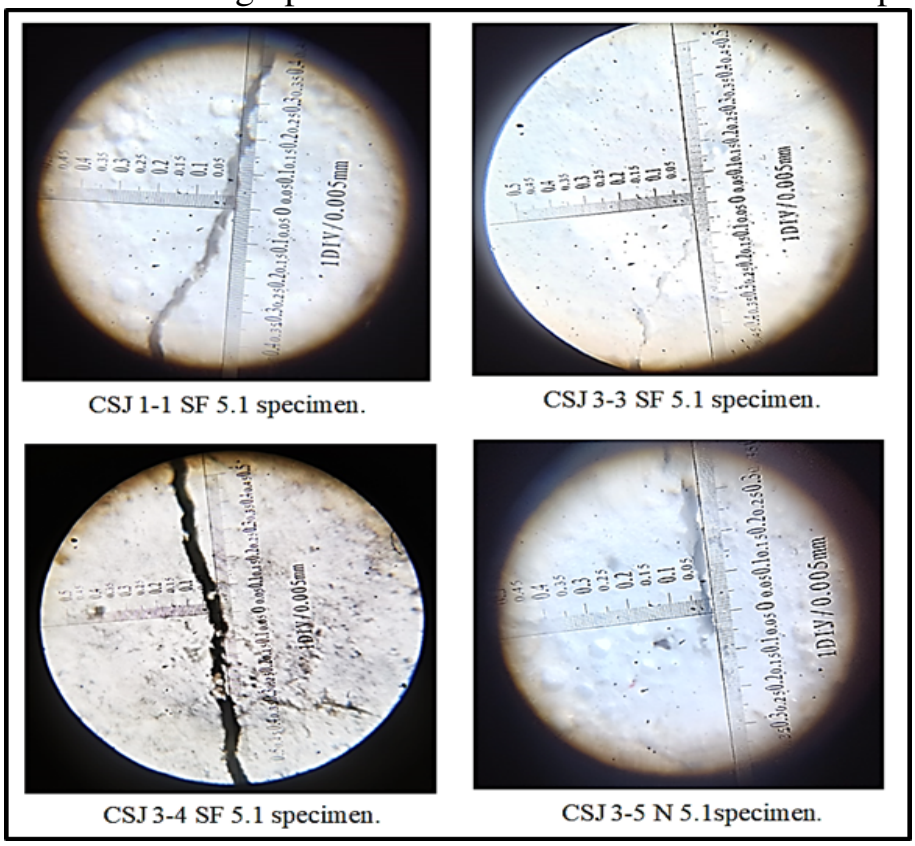

4.5.2 Load-Mid Span Deflection Curves of COWSJ Specimens

The ultimate load capacity and the mid span deflection at the ultimate load were illustrate in Table (4.13). The load versus deflections at the mid-span of all the seven specimens were recorded and introduced in Figures from (4-36) to (4-42). The following subsections show the comparison between the results of all specimens. Also Figures from (A-6) to (A-12) in Appendix A show the vertical deflection a long the span of all specimens to represent the final geometry of the COWSJ specimens at the ultimate load capacity.

Table 4.13 Experimental ultimate load capacity and mid-span deflection at ultimate load for COWSJ specimens.

Specimen No.	Ultimate Load Capacity, P_u (kN)	Experimental Deflection, (mm)
CSJ 1-1 SF 5.1	160.153	8.754
CSJ 2-2 SF 5.1	155.495	9.120
CSJ 3-3 SF 5.1	137.892	10.719
CSJ 3-4 SF 5.1	139.684	10.775
CSJ 3-5 N 5.1	135.157	10.387
CSJ 3-6 SF 3.6	145.978	10.631
CSJ 3-7 N 3.6	140.286	10.265

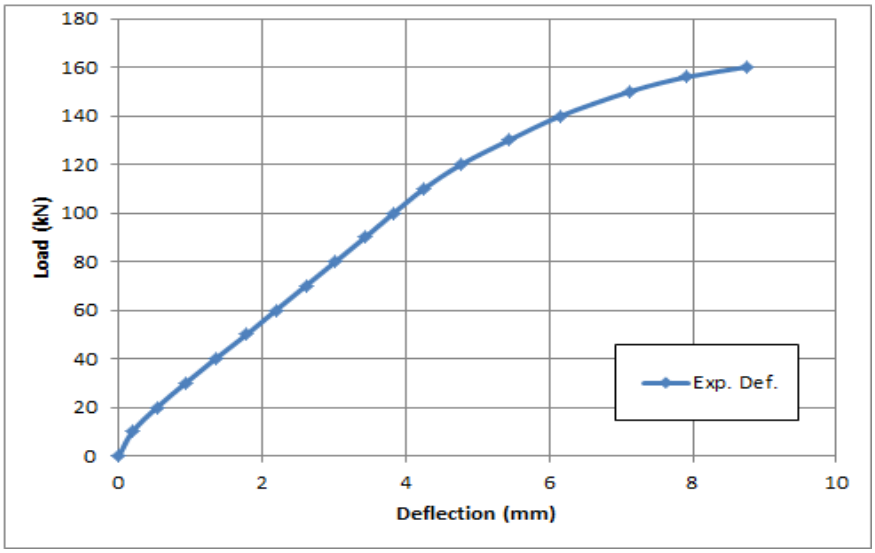

Figure 4.36 Load- mid span deflection curve of CSJ 1-1 SF 5.1 specimen.

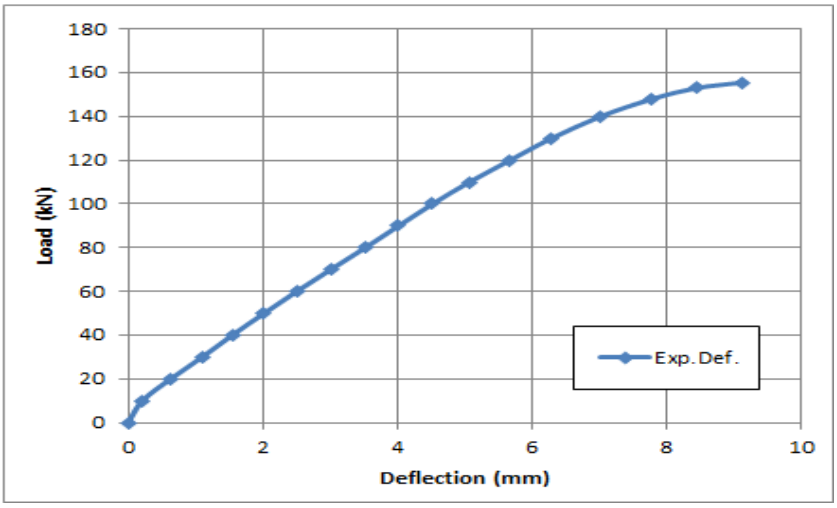

Figure 4.37 Load- mid span deflection curve of CSJ 2-2 SF 5.1 specimen.

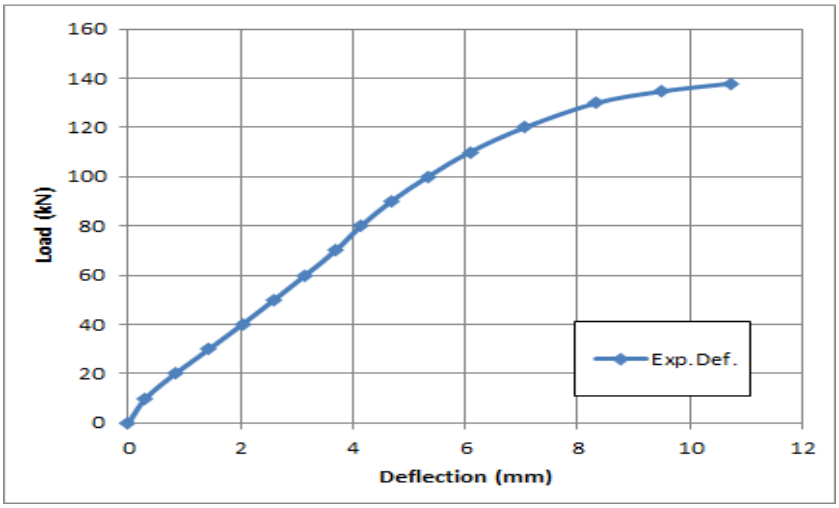

Figure 4.38 Load- mid span deflection curve of CSJ 3-3 SF 5.1 specimen.

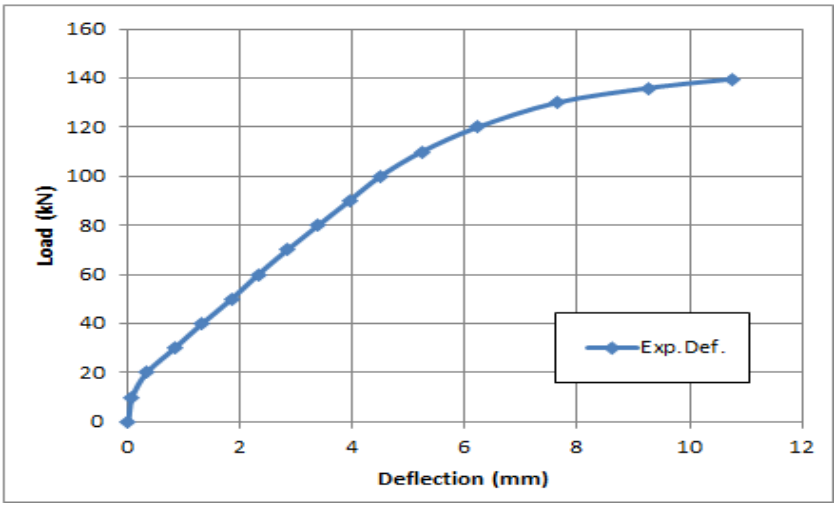

Figure 4.39 Load- mid span deflection curve of CSJ 3-4 SF 5.1 specimen.

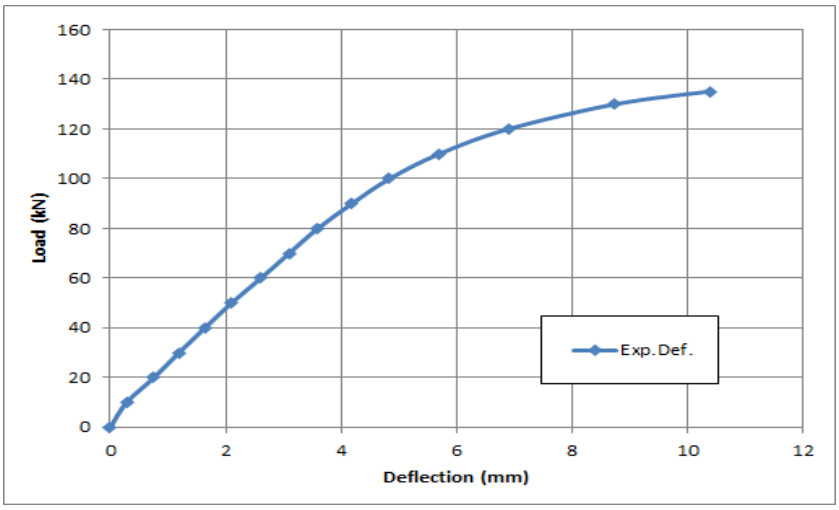

Figure 4.40 Load- mid span deflection curve of CSJ 3-5 N 5.1 specimen.

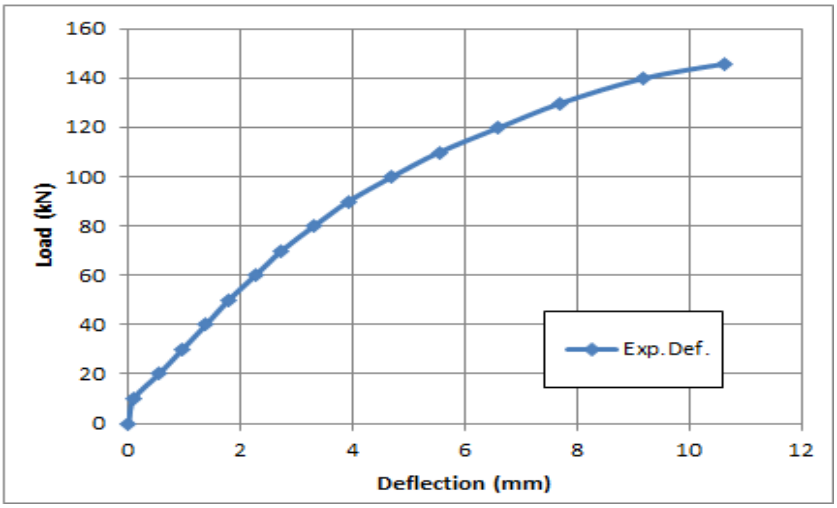

Figure 4.41 Load- mid span deflection curve of CSJ 3-6 SF 3.6 specimen.

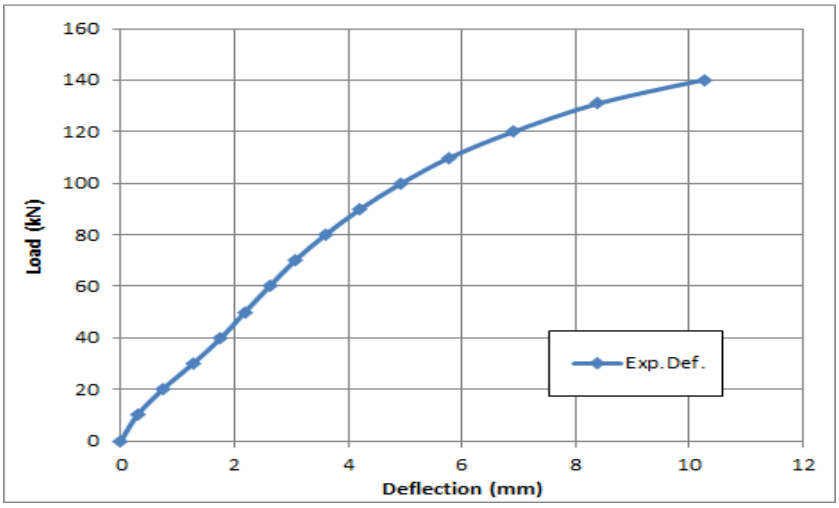

Figure 4.42 Load- mid span deflection curve of CSJ 3-7 N 3.6 specimen.

From the overall look of the experimental results of the load versus mid span deflection for all specimens it can be discussed the effects of the following variables on behavior of the specimens in the next sub sections:

4.5.2.1 Effect of the Shape of the Cross Section

Figure (4-43) show a comparison between the experimental results of the specimens CSJ 1-1 SF 5.1, CSJ 2-2 SF 5.1, and CSJ 3-3 SF 5.1,which they had the same L/D ratio of steel joist of (5.1), the same effective width of concrete slab, and the same type of concrete slab(SFRC),but they had a different steel joist cross section shape, it can be observed that the specimen CSJ 1-1 SF 5.1 had an ultimate load capacity greater than the specimens CSJ 2-2 SF 5.1 and CSJ 3-3 SF 5.1 by about (2.91%) and (13.89%),respectively, whereas the specimen CSJ 2-2 SF 5.1 had an ultimate load more than the ultimate load of specimen CSJ 3-3 SF 5.1 by about (11.32%). But at the same time, the specimen CSJ 1-1 SF 5.1 had a deflection at the ultimate load less than for specimens CSJ 2-2 SF 5.1, and CSJ 3-3 SF 5.1 by about (4.01%) and (18.33%), respectively; and the deflection of specimen CSJ 2-2 SF 5.1 was more than for specimen CSJ 3-3 SF 5.1 by about (14.92%). So from these comparison and from Figure (4-43) can be concluded that the stiffness of the specimens CSJ 1-1 SF 5.1 and CSJ 2-2 SF 5.1 were closed, while the stiffness of the specimen CSJ 3-3 SF 5.1 was less than the other two specimens. On the other hand from Figure (4-43) which was illustrate a comparison between the load- mid span deflection of specimens CSJ 1-1 SF 5.1, CSJ 2-2 SF 5.1, and CSJ 3-3 SF 5.1 can be noticed that the behaviour of the specimen CSJ 3-3 SF 5.1 was more ductile from CSJ 1-1 SF 5.1 and CSJ 2-2 SF 5.1 specimens, i.e. it's had longer load versus deflection curves.

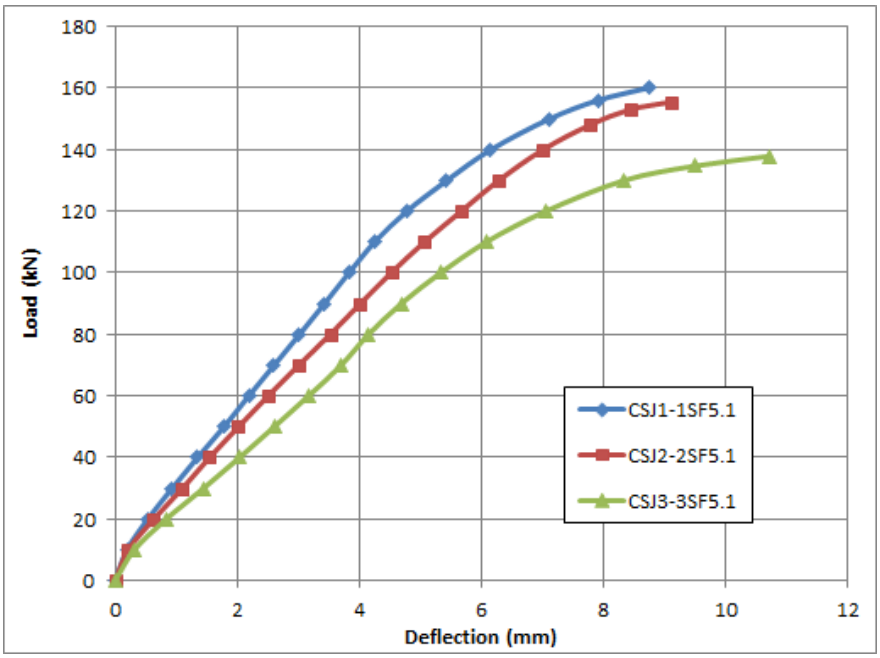

Figure 4.43 Load- mid Span deflection curve of specimens CSJ 1-1 SF 5.1, CSJ 2-2 SF 5.1, and CSJ 3-3 SF 5.1.

4.5.2.2 Effect of the Effective Width of the Concrete Slab Deck

The specimens CSJ 3-3 SF 5.1, and CSJ 3-4 SF 5.1 had the same steel joist cross-section, same L/D ratio of steel joist of (5.1), but they had a different effective width of concrete slab which were 400 mm and 500 mm, respectively. Thus they had different locations of a neutral axis, where for specimen CSJ 3-3 SF 5.1, (29.5%) of the concrete slab was under normal compressive stress, while (23.6%) of the concrete slab was under normal compressive stress in specimen CSJ 3-4 SF 5.1. It can be observed from table (4-10) that the failure load of the specimens CSJ 3-4 SF5.1 and CSJ3-3 SF5.1 were closed about of (139.684 kN) and (137.892 kN), respectively. But the stiffness of CSJ 3-4 SF5 specimen was slightly higher than from that for CSJ3-3 SF5.1 specimen, as shown in Figure (4-44).

A normalized load- mid span deflection curve for these two specimens was illustrate in Figure (4-45) to make a fair comparison between them, this figure emphasized that when the location of the neutral axis moved up, the behavior of the of COWS joists was affected and the stiffness of the COWS joists was increased

slightly. Also Figure (4-45) show that when the width of the deck slab increased by about (20%), the normalized deflection of CSJ 3-4 SF5.1 specimen became less than from that for specimen CSJ 3-3 SF 5.1 by (19.58 %).

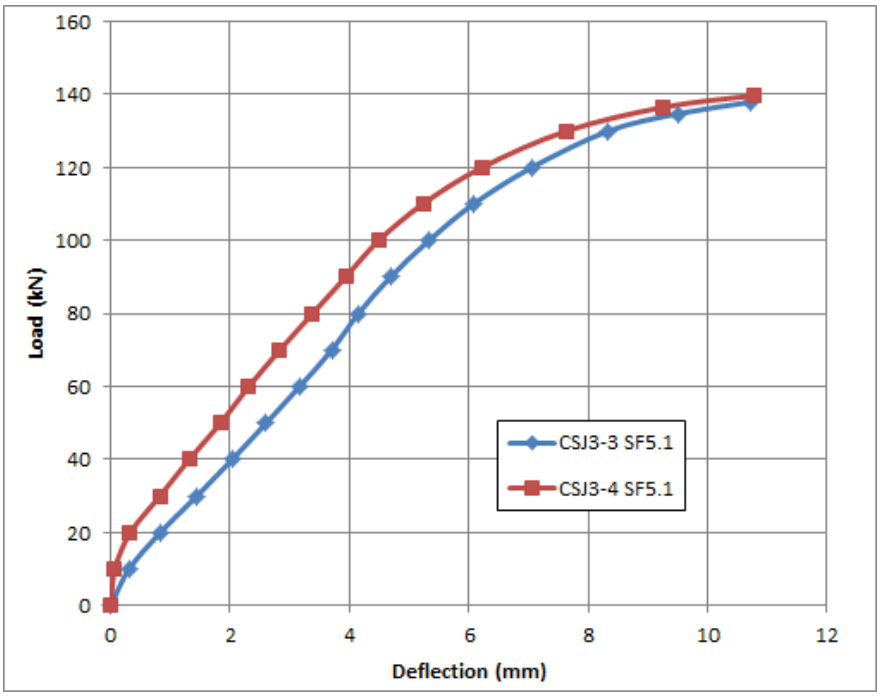

Figure 4.44 Load- mid span deflection curve of specimens CSJ 3-3 SF 5.1, and CSJ 3-4 SF 5.1.

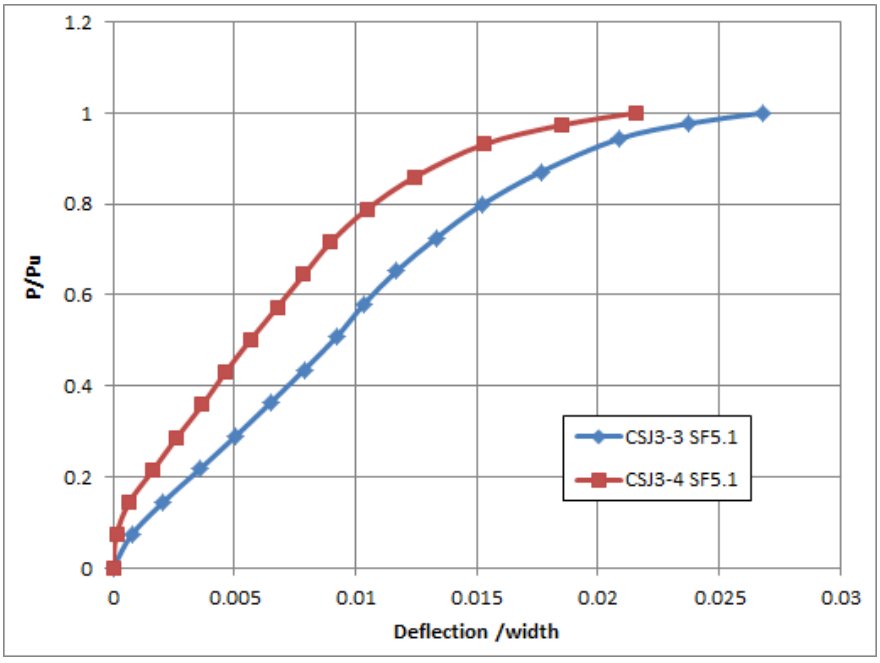

Figure 4.45 Normalized load- mid span deflection curve of specimens CSJ 3-3 SF 5.1, and CSJ 3-4 SF 5.1.

4.5.2.3 Effect of Type of the Concrete Slab

CSJ3-4 SF 5.1 and CSJ3-5 N5.1 specimens had a different type of concrete slab, where CSJ3-4 SF 5.1 was fabricated by using SFRC slab while NC was used to fabricate CSJ3-5 N5.1 specimen, but at the same time they had the same cross section shape of the steel joist, the same L/D ration of steel joist of (5.1), and the same effective width of concrete slab, Figure (4-46) show a comparison between load- mid span deflection of these two specimens.

Regarding CSJ3-6 SF 3.6 and CSJ3-7 N3.6 specimens also they had a different type of concrete slab, where CSJ3-6 SF 3.6 was fabricated by using SFRC slab while NC was used to fabricate CSJ3-7 N3.6 specimen, but at the same time they had the same cross section shape of the steel joist, the same L/D ration of steel joist of (3.6), and the same effective width of concrete slab, Figure (4-47) show a comparison between load- mid span deflection of these two specimens.

From the experimental results it can be concluded that the maximum load capacity of the COWS joists casted of SFRC was more than that for the specimens casted of NC. For the specimens CSJ3-4 SF 5.1 and CSJ3-5 N5.1 the percentage of increasing in the ultimate capacity was not exceed (3.24%), while for the specimens CSJ3-6 SF 3.6 and CSJ3-7 N3.6 the percentage of increasing in the ultimate capacity was not exceed (3.89%). From these comparisons it can be concluded that the using of SFRC on COWSJs ultimate strength enhancement was slight effect because on all COWSJs the failure mode was due to the steel joist failure before reached the concrete slab to its ultimate strength. And when compared the results of the mid span deflection it can be noticed that the deflection of CSJ3-4 SF 5.1 specimen was more than that for CSJ3-5 N5.1 specimen by (3.60%), and the mid span deflection of CSJ3-6 SF 3.6 specimen also was more than that for CSJ3-7 N3.6 by (3.44%). From these comparisons it can be concluded that the type of concrete which used to cast the concrete slab of COWSJ was enhanced slightly each

of the ultimate strength, the ductility, and the stiffness of the specimens, and these little in enhancement may be because of the difference between the compressive strength of NC and SFRC which used in this study was not exceed (9.47%). These slightly enhancement in the behavior of COWSJs can also be clearly seen in the Figures (4-46) and (4-47).

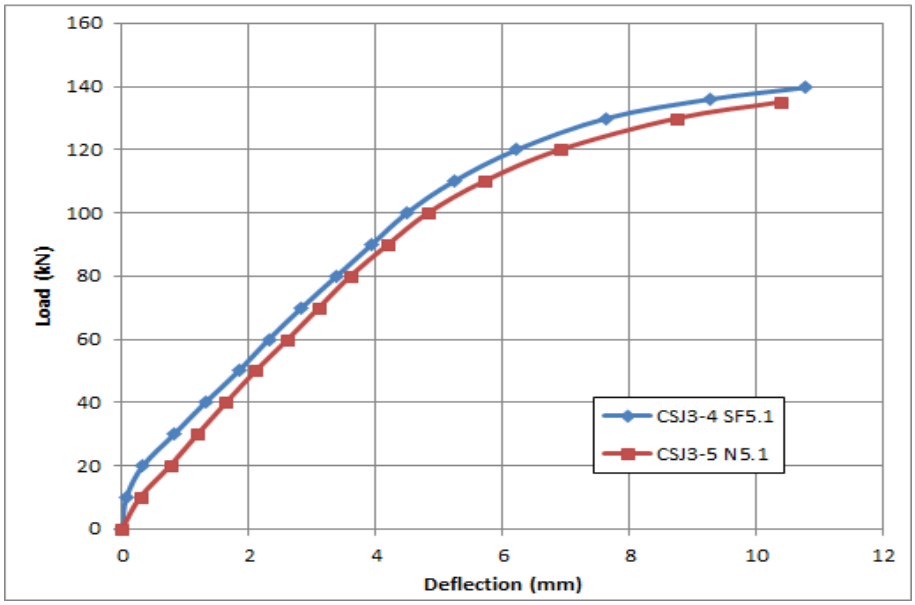

Figure 4.46 Load- mid span deflection curve of specimens CSJ3-4 SF 5.1 and CSJ3-5 N5.1.

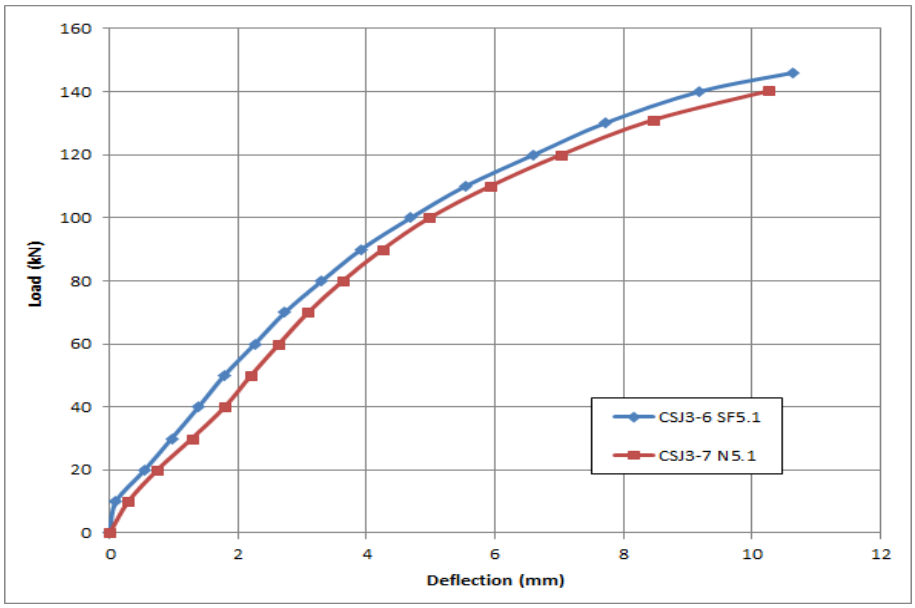

Figure 4.47 Load- mid span deflection curve of specimens CSJ3-6 SF 3.6 and CSJ3-7 N3.6.

4.5.2.4 Effect of the Span to the Depth Ratio of HOWSJ

The final parameter that has been conducted in this study was the length to depth ratio (L/D) of HOWSJ. So a comparison between specimens CSJ3-5 N5.1 and CSJ3-7 N3.6 has been discussed in this subsection, Figure (4-48) show a comparison between the load – mid span deflection of these two specimens. From the other hand the experimental results of CSJ3-4 SF 5.1 and CSJ3-6 SF3.6 specimens were compered to study the effect of the (L/D) ratio of HOWSJ on the behavior of the COWS joists, as shown in Figure (4-49). Each two compared specimens were had a different L/D ratio but they had the same cross section shape of the steel joist, the same effective width of concrete slab, and the same type of concrete slab. The testing results for specimens casted with NC were illustrated that the ultimate strength capacity was decreased when the L/D ratio increased, where the ultimate strength capacity for CSJ3-7 N3.6 was more than that for CSJ3-5 N5.1 specimen by about (3.66 %), see Figure (4-48). On the other hand it can be recognized that for specimens casted with SFRC, the ultimate strength capacity was also decreased when the L/D ratio increased, where the ultimate strength capacity for CSJ3-6 SF3.6 was more than that for CSJ3-4 SF 5.1 specimen by about (4.31 %), as shown in Figure (4-49).

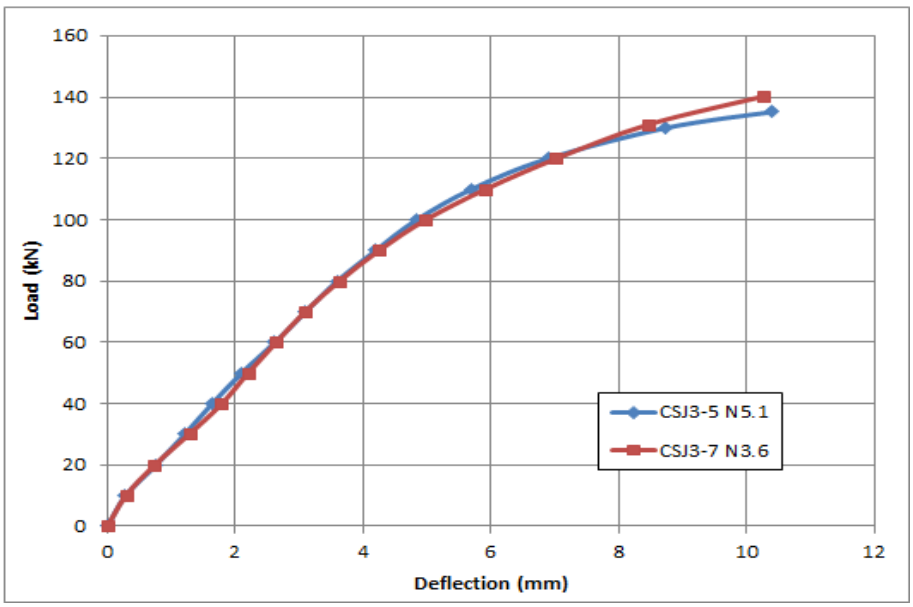

Figure 4.48 Load- mid span deflection curve of CSJ3-5 N5.1 and CSJ3-7 N3.6.

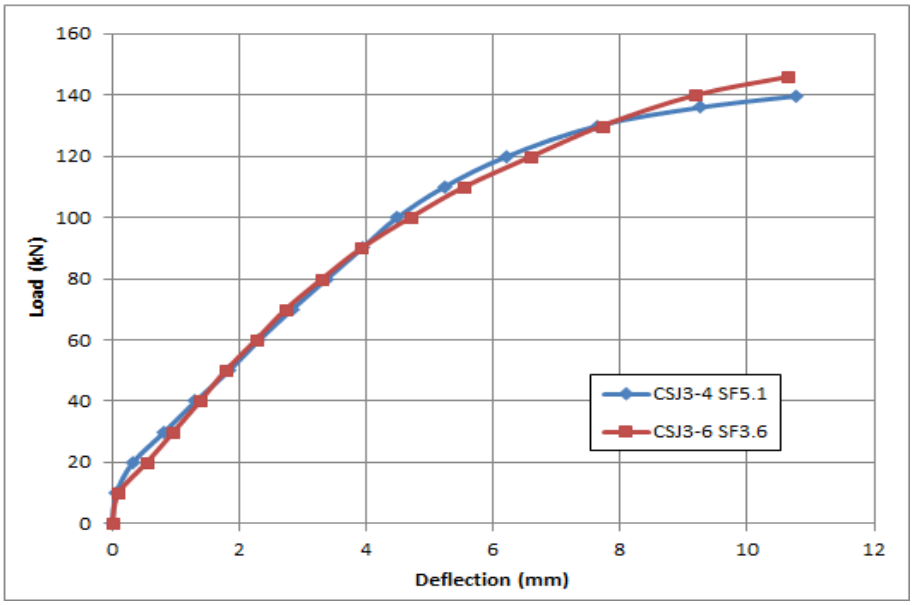

Figure 4.49 Load-mid span deflection curve of CSJ3-4 SF 5.1 and CSJ3-6 SF 3.6.

The Normalize load-mid span deflection curve, Figures (4-50) and (4-51) were adopted to make a fair comparison between each two specimen. From these figures it can be observed that the normalized mid span deflection for CSJ3-7 N3.6 decreased by (30.83 %) compared with CSJ3-5 N5.1, also the normalized mid span deflection for CSJ3-6 SF3.6 decreased by (30.94 %) compared with CSJ3-4 SF 5.1. From these figures, it was also clear that the stiffness of specimens with higher L/D ratios decreased for the two types of concrete slabs.

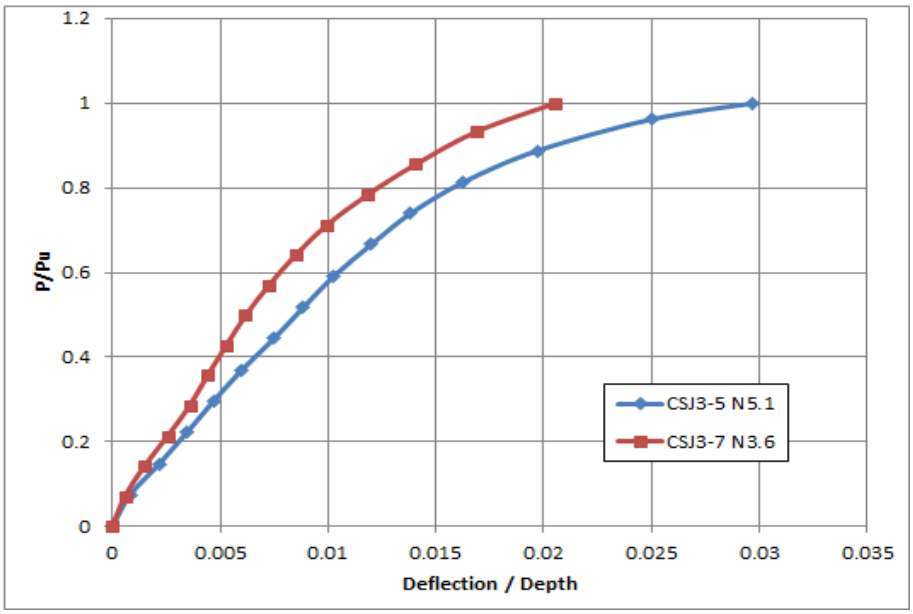

Figure 4.50 Normalized load- mid span deflection curve of CSJ3-5 N5.1 and CSJ3-7 N3.6.

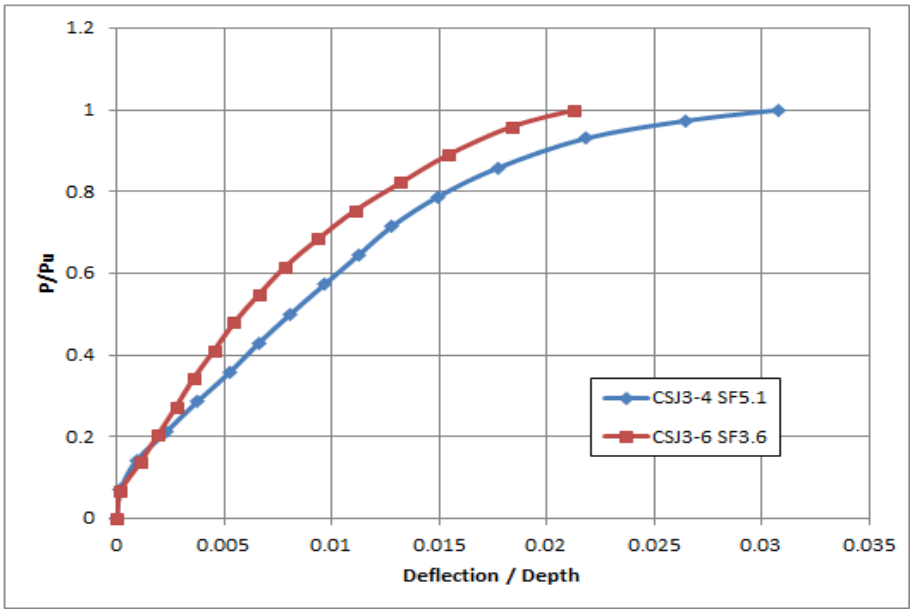

Figure 4.51 Normalized load- mid span deflection curve of CSJ3-4 SF 5.1 and CSJ3-6 SF 3.6.

4.5.3 Relative Slip between Concrete Slab and HOWSJ

The relationship between applied load and relative slip between the concrete slab and the top chord of the steel joist for all specimens was plotted in Figure (4-52), where each curve introduces the load versus slip for each specimen. Also, the experimental relative slip at the ultimate load was illustrate in Table (4.14)

From over all look of the experimental load slip results it can be concluded that the amount of the slip was less in the specimens which their concrete slab were casted with SFRC, this behaviour can explained by comparing between specimens CSJ3-4 SF5.1 and CSJ3-5 N5.1, it can be observed that the slip which occurred in CSJ3-4 SF5.1 specimen was less than the slip of CSJ3-5 N5.1 by about (3.45 %) and by about (4.98 %).

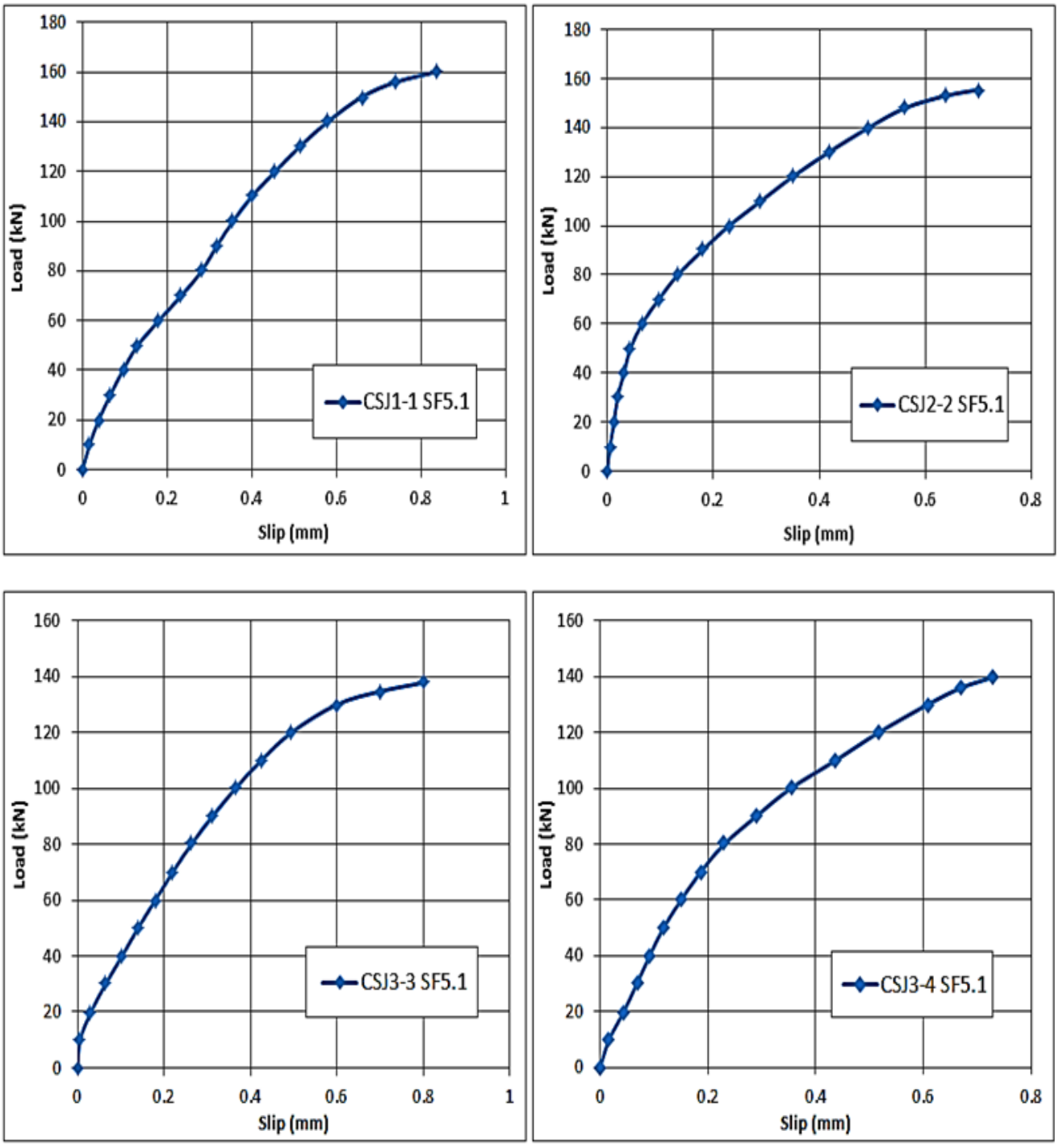

Figure 4.52 Load- slip curves of all COWSJ specimens.

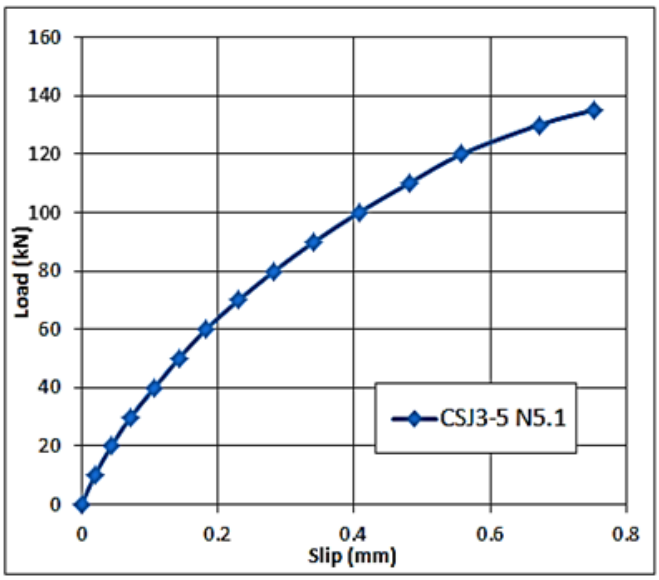

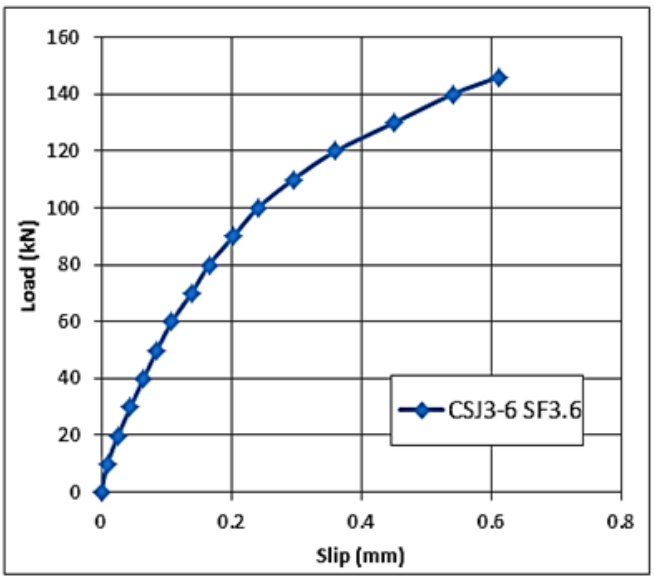

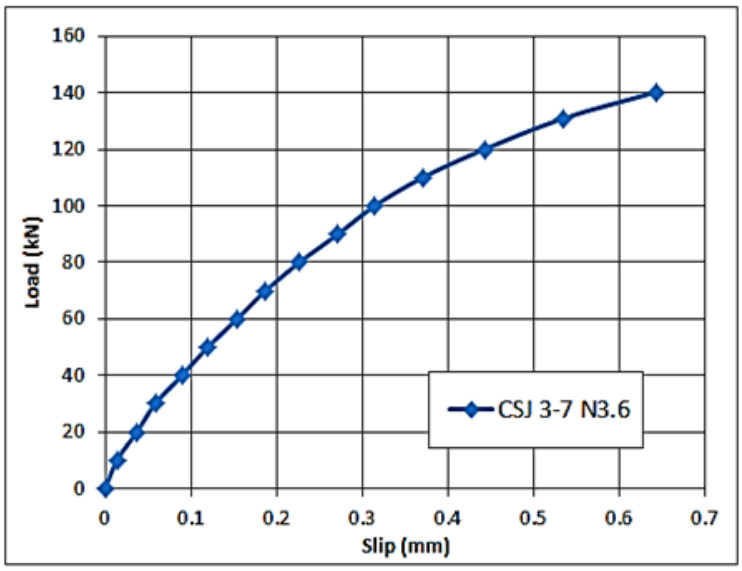

Figure 4.52 Continued.

Table 4.14 Experimental slip at ultimate load for COWSJ specimens.

Specimen No.	Ultimate Load Capacity, P_u (kN)	Experimental Slip (mm)
CSJ 1-1 SF 5.1	160.153	0.837
CSJ 2-2 SF 5.1	155.495	0.699
CSJ 3-3 SF 5.1	137.892	0.803
CSJ 3-4 SF 5.1	139.684	0.728
CSJ 3-5 N 5.1	135.157	0.753
CSJ 3-6 SF 3.6	145.978	0.611
CSJ 3-7 N 3.6	140.286	0.643

4.5.4 Load- Strain Curves of all COWSJ Specimens

Each COWS joist had six uniaxial strain sensors, the location of these sensors was at the same location which used in the HOWSJS test program, thus the location of the strain gauges' sensors were at six critical points of the COWSJ specimens, two at the horizontal leg of angles of the top and bottom chords, two at the vertical leg of angles of top and bottom chords at a section distances which was near closely for mid-span section of (50mm),and two at the center of the length of the diagonal interior web members near the support, as showed previously in Figure (3-12). The experimental results of the strain gauges reading of each specimen will be discussed in section 4.6.3 and the load strain curves for each specimen where plotted in the following sub sections.

The strain gauge readings of bottom chord, top chord, and interior web members near the supports were illustrated the behavior for all COWSJ specimens during the test, as shown in Figures (4-53) to (4-73).

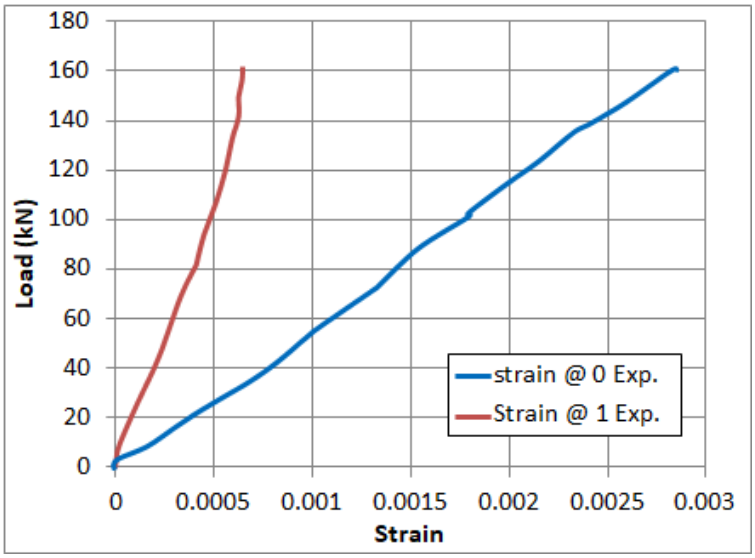

Figure 4.53 Load – strain curve of bottom chord of CSJ1-1 SF5.1 specimen.

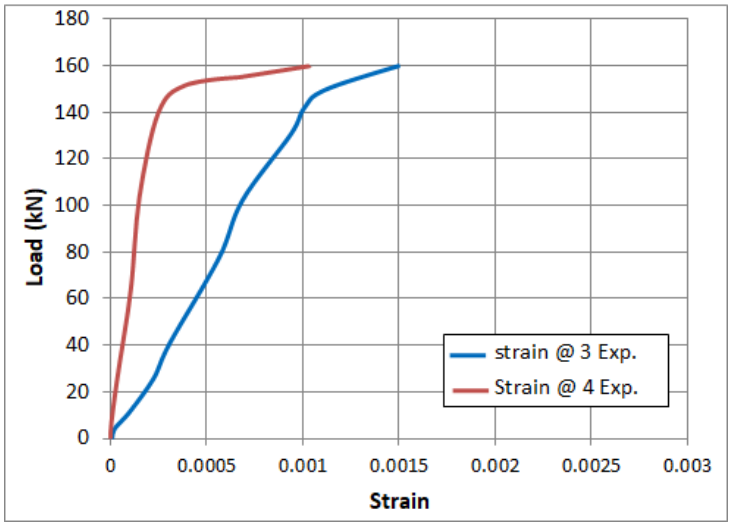

Figure 4.54 Load – strain curve of top chord of CSJ1-1 SF5.1 specimen.

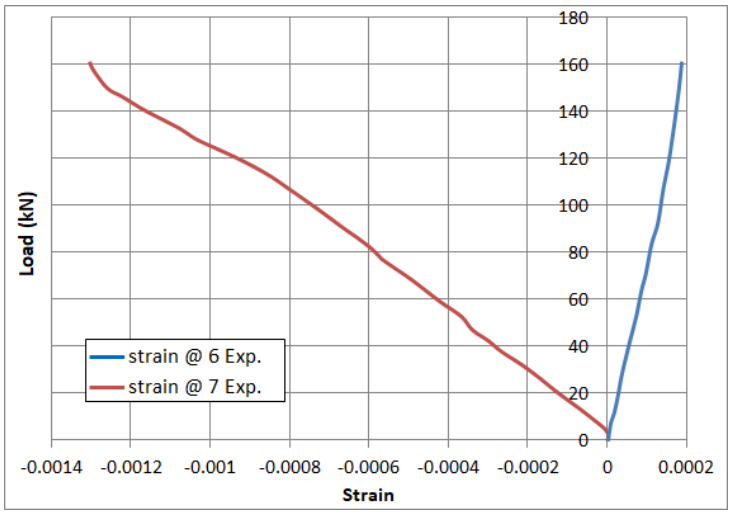

Figure 4.55 Load – strain curve of the diagonal interior webs near the support of CSJ1-1 SF5.1 specimen.

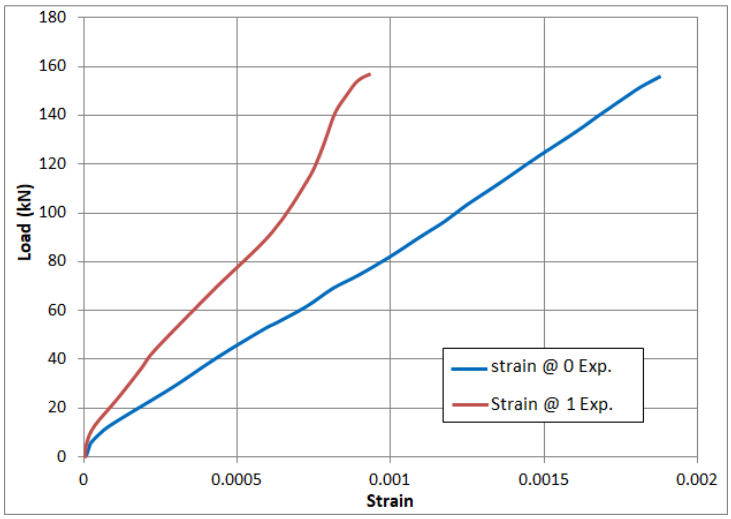

Figure 4.56 Load – strain curve of bottom chord of CSJ2-2 SF5.1 specimen.

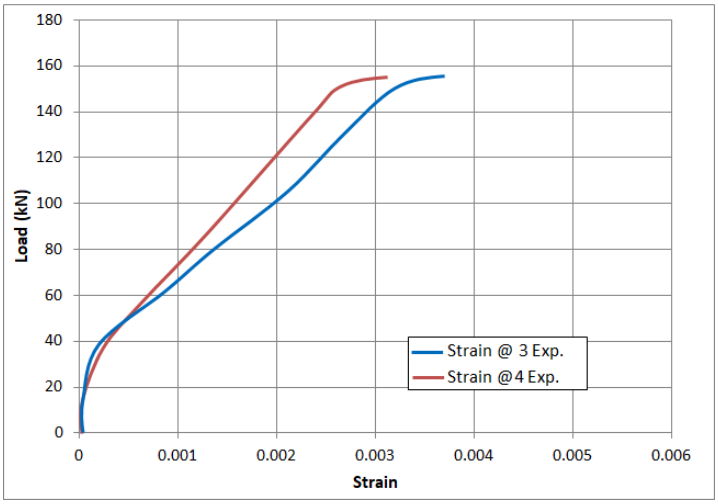

Figure 4.57 Load – strain curve of top chord of CSJ2-2 SF5.1 specimen.

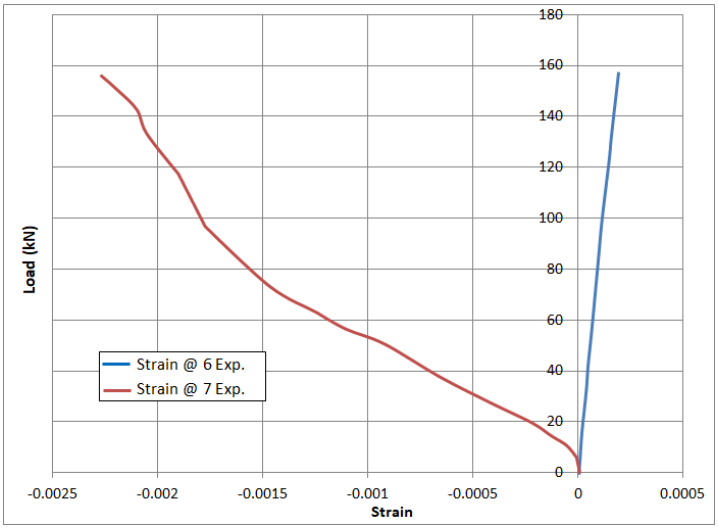

Figure 4.58 Load – strain curve of diagonal the interior webs near the support of CSJ2-2 SF5.1 specimen.

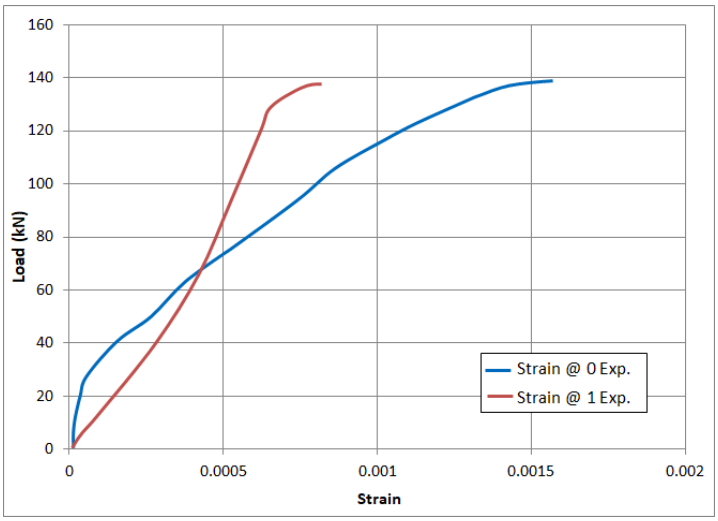

Figure 4.59 Load – strain curve of bottom chord of CSJ3-3 SF5.1 specimen.

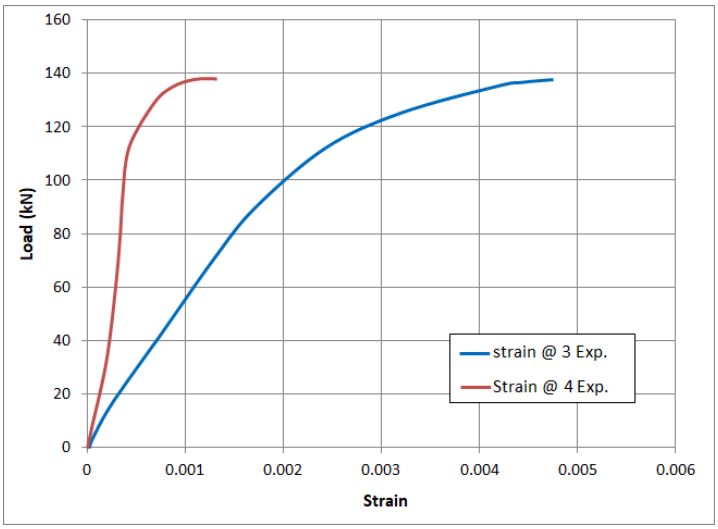

Figure 4.60 Load – strain curve of top chord of CSJ3-3 SF5.1 specimen.

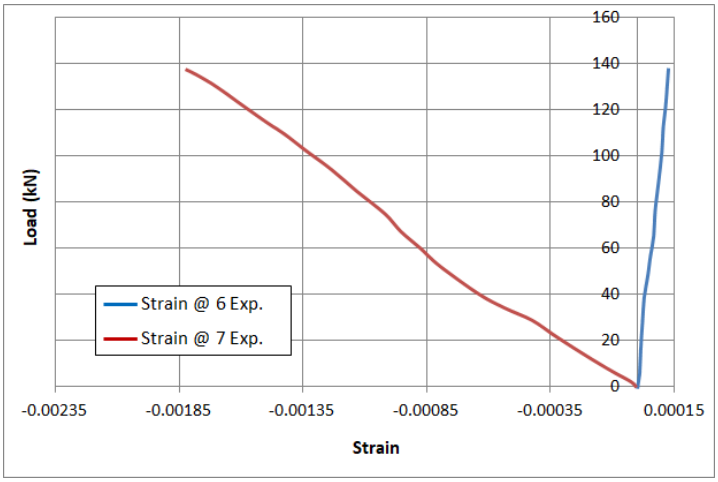

Figure 4.61 Load – strain curve of the diagonal interior webs near the support of CSJ3-3 SF5.1 specimen.

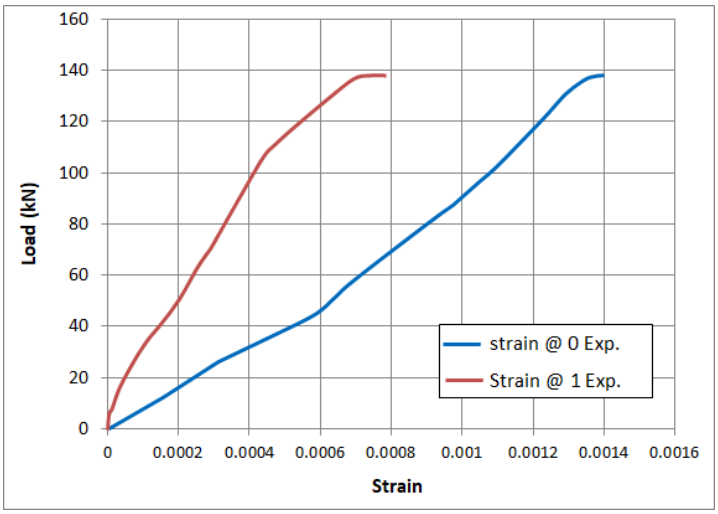

Figure 4.62 Load – strain curve of bottom chord of CSJ3-4 SF5.1 specimen.

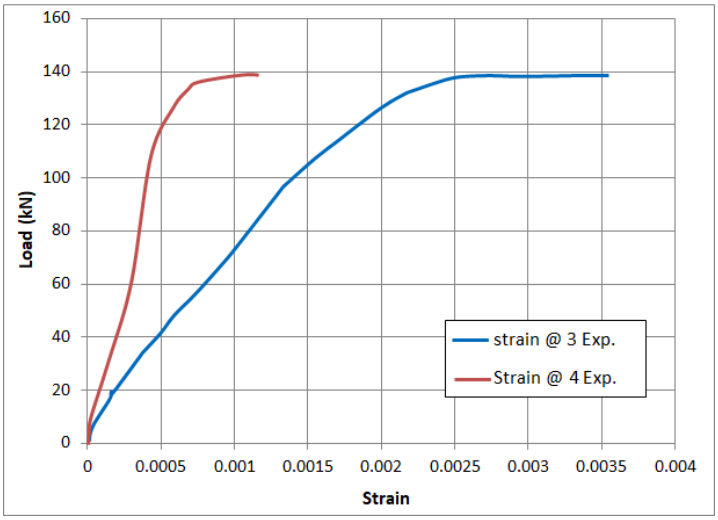

Figure 4.63 Load – strain curve of top chord of CSJ3-4 SF5.1 specimen.

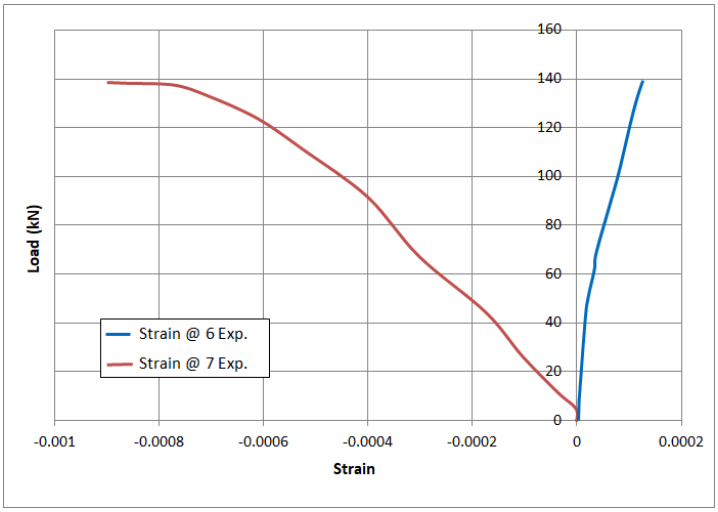

Figure 4.64 Load – strain curve of the diagonal interior webs near the support of CSJ3-4 SF5.1 specimen.

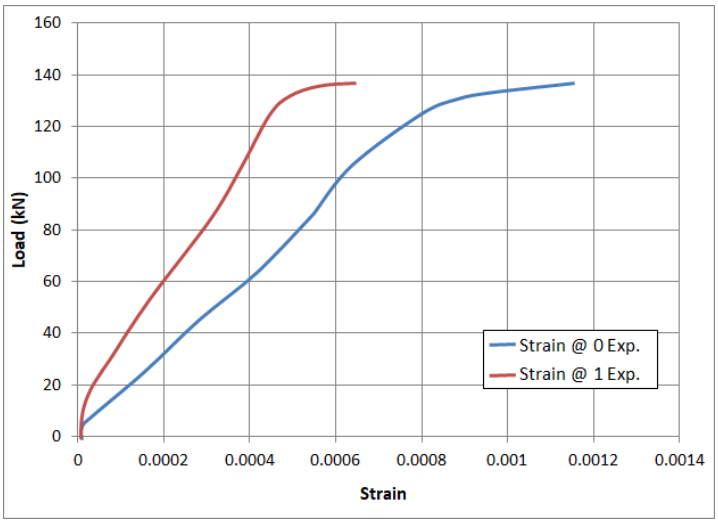

Figure 4.65 Load – strain curve of bottom chord of CSJ3-5 N5.1 specimen.

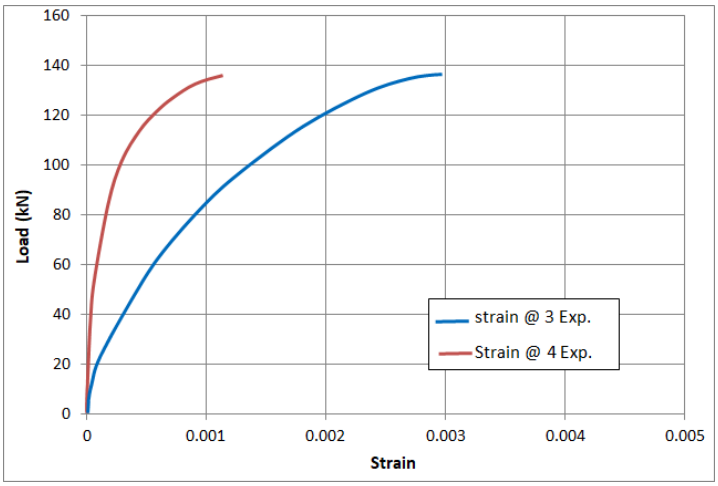

Figure 4.66 Load – strain curve of top chord of CSJ3-5 N5.1 specimen.

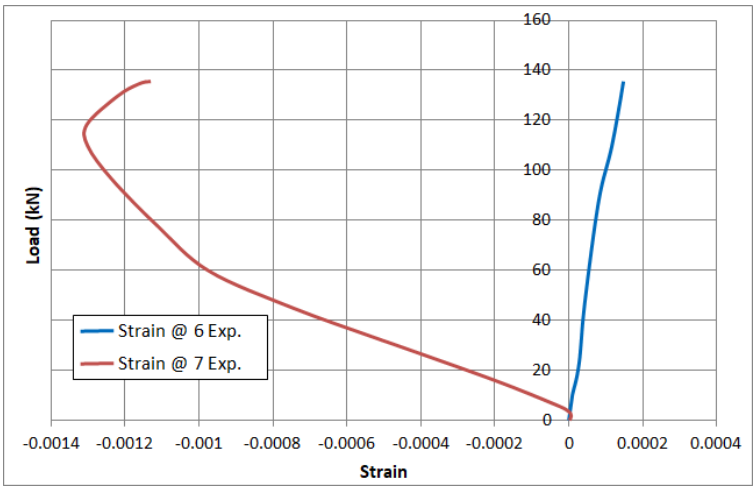

Figure 4.67 Load – strain curve of interior the diagonal webs near the support of CSJ3-5 N5.1 specimen.

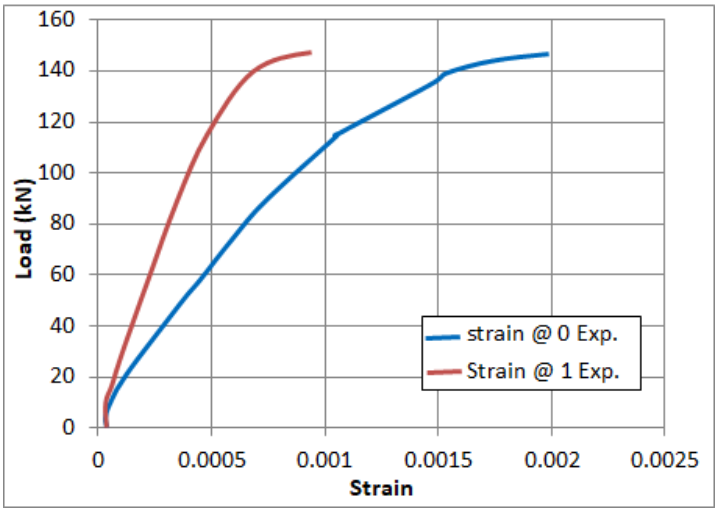

Figure 4.68 Load – strain curve of bottom chord of CSJ3-6 SF3.6 specimen.

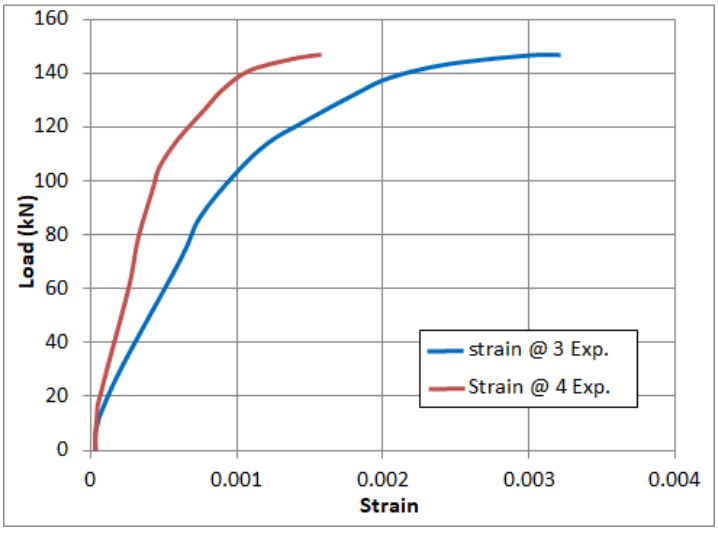

Figure 4.69 Load – strain curve of top chord of CSJ3-6 SF3.6 specimen.

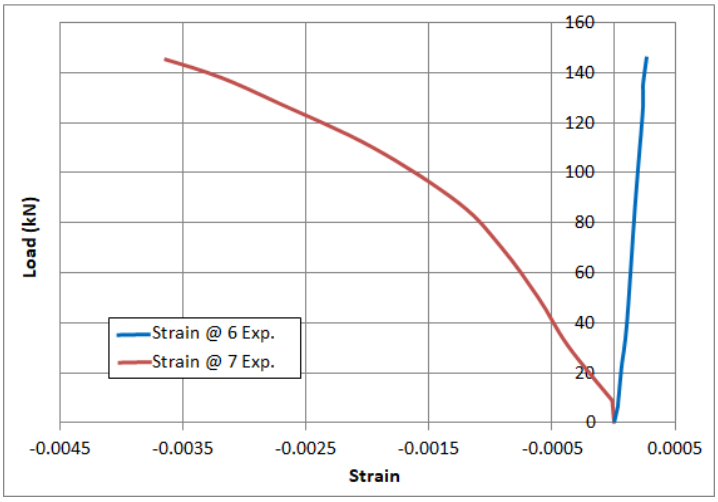

Figure 4.70 Load – strain curve of the diagonal interior webs near the support of CSJ3-6 SF3.6 specimen.

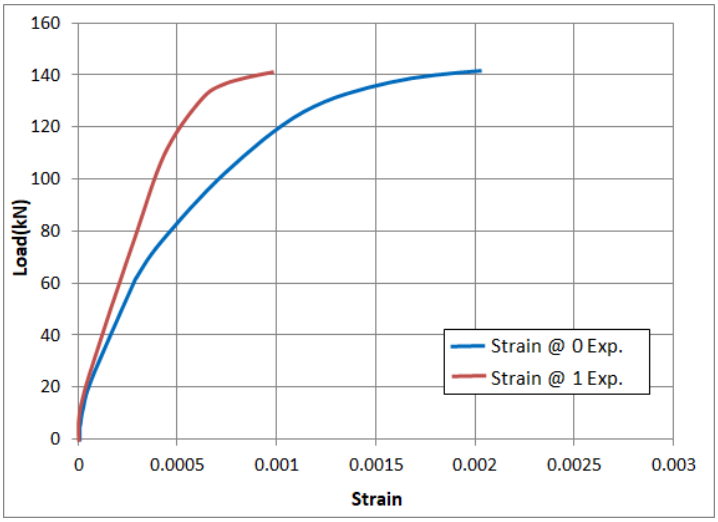

Figure 4.71 Load – strain curve of bottom chord of CSJ3-7 N5.1 specimen.

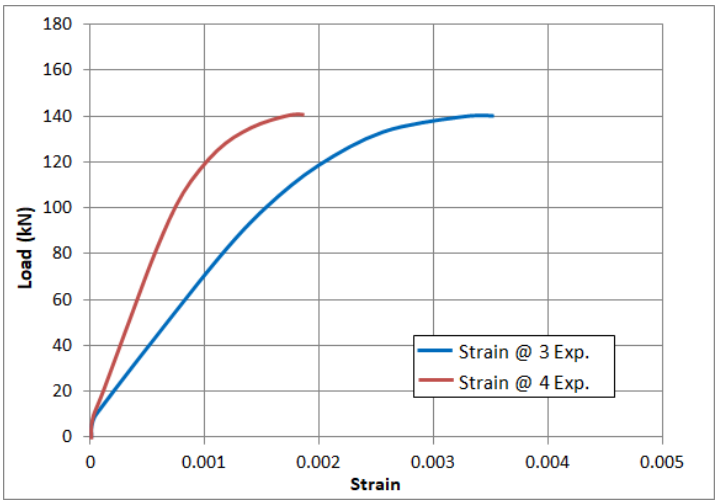

Figure 4.72 Load – strain curve of top chord of CSJ3-7 N5.1 specimen.

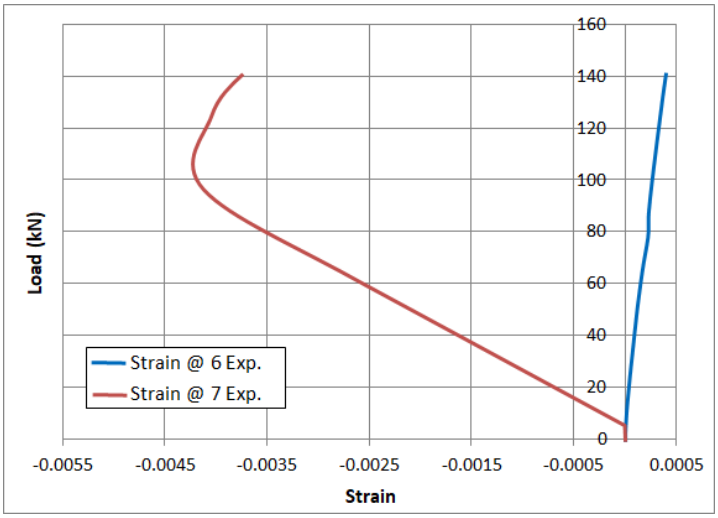

Figure 4.73 Load – strain curve of the diagonal interior webs near the support of CSJ3-7 N5.1 specimen.

4.6 Results Summary of COWSJ Specimens

4.6.1 Modes of Failure

For the seven COWSJ Specimens were tested under monotonic loading in this study, the failure modes in the concrete of composite specimens were observed after bottom chord yielding and it was started with small cracks in the bottom surface beneath the region of subjecting load. It may be caused by the existing of shear connectors in that region. These cracks followed by little longitudinal or transverse cracks in the middle upper surface of the concrete slab. Among all the

seven COWSJ Specimens, one distinct mode of concrete crushing were observed after bottom chord yielding. This mode was governed by the span/depth ratio and the type of concrete deck slab, where for the composite joist which having span/depth ratio of 3.6 and casted with non fibrous concrete, excessive concrete crushing under the mid span load was occurred. Also, lower initial visible crack load was observed when span/depth ratio decreases from 5.1 to 3.6.

Generally, the modes of failure of all specimens observed in this study were yielding of the bottom chord, buckling of diagonal interior web members, failure at welded joints between the vertical legs of top and bottom chords and interior webs, and cracks of concrete within mid span. Where Firstly, the bottom chords yielded at the mid span as designed. Then, as the load progressed, interior web members yielding followed by concrete slab cracking were observed.

Finally, the relative slip which occurred in the COWSJ specimens casted with SFRC was less than from that occurred in the specimens which their concrete slab were casted with NC.

4.6.2 Load- Mid Span Deflection Behavior

The ultimate load capacity of the COWS joists specimens was affected by using a different shapes of the cross section of the HOWSJ, where when used the steel joist with back to back angles of top and bottom chords enhanced the ultimate load capacity by about ((2.91%) and (13.89%) compared with cross section of face to face angles, and face to face angles with gap, respectively. But at the same time the specimen with back to back angles had a deflection at the ultimate load less than for specimens with cross section of face to face angles, and face to face angles with gap by about (4.01%) and (18.33%), respectively. So it can be concluded that the stiffness of the specimen with back to back angles and face to face angles were closed, while the stiffness for the specimen of face to face angles with gap was less

than the other two specimens but at the same time it was more ductile from both of them.

The results of test emphasized that when the location of the neutral axis moved up, the behavior of the of COWS joists was affected and the stiffness of the COWS joists was increased slightly.

For the COWSJ Specimens, the type of the concrete used to cast the concrete slab was affect the initial visible crack load, where The initial visible crack loads for specimens casted with SFRC were higher than that of the specimens casted with NC . Also, the experimental results showed that the using of SFRC had a slightly effect on increasing the ultimate load capacity, the ductility, and the stiffness of the COWSJ specimens.

Finally, the length to the depth ratio (L/D) was affected on the behavior of the COWSJ specimens for both type of the concrete slab, where the ultimate strength capacity was decreased when the L/D ratio increased. While the mid span deflection at ultimate capacity was increased when the L/D ratio increased.

4.6.3 Strain Results

4.6.3.1 Strains at the Top Chord

For all seven COWSJ specimens the strain gauges readings of the top chord (ϵ_3 and ϵ_4) at mid-span were in tension from beginning of the test, which means that the neutral axis was within the concrete slab. Regarding the strain gauges reading on the vertical leg of the angle of the top chord (strain at 3, ϵ_3) showed that when comparing the three different cross section of HOWSJ, the strain of CSJ3-3 SF5.1specimen was more than that for CSJ1-1 SF5.1 and CSJ2-2 SF5.1 by about (68.14%) and (22.31%), respectively. While the strain gauges reading on the horizontal leg of the angle of the top chord (strain at 4, ϵ_4) of CSJ2-2 SF5.1specimen was more than that for CSJ1-1 SF5.1 and CSJ3-3 SF5.1 by about (68.06%) and (60.28%), respectively.

Regarding the strain at (ϵ_3 and ϵ_4) of CSJ3-4 SF5.1 specimen which had an effective width of concrete slab of (500mm) were less than the strain of CSJ3-3 SF5.1 which had an effective width of concrete slab of (400mm), but they had same concrete type of slab and the same cross section of HOWSJ by (24.43%) and (8.06%), respectively. From these results it can be concluded that the increasing of the effective width of concrete slab by (20%) yield to decreasing the strains at the top chord.

The strain readings at (ϵ_3 and ϵ_4) of CSJ3-4SF5.1 specimen were more than the strain of CSJ3-5N5.1 which had a different concrete type of slab by (17.41%) and (7.60%), respectively. From the other hand the strain at (ϵ_3 and ϵ_4) of CSJ3-6SF3.6 specimen were lower than the strain of CSJ3-7N3.6 which also they had a different concrete type of slab by (8.65%)and (13.53%), respectively. From these comparisons it can be noticed that the type of concrete slab was affected by the span /depth ratio, where when the span/depth ratio was (3.6), the strains of the top chord were decreased in case of using SFRC slab compared with NC slab specimens, whereas the strains of the top chord were increased in case of using SFRC slab when the span/depth ratio was (5.1).

Finally, the strain at (ϵ_3) of CSJ3-4SF5.1 specimen was more than the (ϵ_3) strain of specimen CSJ3-6SF3.6 which had lower span/depth ratio by about (9.94%), while the strain at (ϵ_4) of CSJ3-4SF5.1 specimen was lower than the (ϵ_4) strain of specimen CSJ3-6SF3.6 which had lower span/depth ratio by about (28.36%), that is when comparing the specimens which they had SFRC slab. While regarding the specimens which they had NC slab, the strain at (ϵ_3 and ϵ_4) of CSJ3-5N5.1 specimen were lower than the strain of specimen CSJ3-7N3.6 which had lower span/depth ratio by about (16.22%) and (42.69%), respectively.

4.6.3.2 Strains at the Diagonal Interior Web Members

From the figures of the load – strain for the interior end diagonal interior web tension members for all COWSJ specimens, it can be observed that the behavior of these tension members was linear up to the failure load. And the first compression diagonal web members for the five COWSJ specimens which their concrete slabs were casted with SFRC also showed a good linear behavior until the specimens were reached to the ultimate load capacity. While the behavior of the first compression diagonal interior web members for the two COWSJ specimens which their concrete slabs were casted with NC was linear from the beginning of the test. But as the load progressed, the strains were increased to record their maximum, then the strains readings were decreased until the specimens reached to their ultimate capacity. This indicates that these interior web members buckled and lost their strength until failure of these two specimens.

The experimental results showed that the strain readings of the diagonal interior web tension members (ϵ_6) for all COWSJ specimens was less than the strain readings of the diagonal interior web compression members (ϵ_7) by about (84.20%-93.96%). However, the test results showed that when comparing the three different cross section of HOWSJ, the strain at the compression diagonal interior web members (ϵ_7) of CSJ2-2 SF5.1specimen was more than that for CSJ1-1 SF5.1 and CSJ3-3 SF5.1 by about (48.21%) and (21.40%), respectively.

Regarding the strain at (ϵ_7) of CSJ3-4 SF5.1 specimen which had an effective width of concrete slab of (500mm) were less than the strain of CSJ3-3 SF5.1 which had an effective width of concrete slab of (400mm), but they had same concrete type of slab and the same cross section of HOWSJ by (47.50%). From these results it can be concluded that the increasing of the effective width of concrete slab by (20%) yield to decreasing the strains at the web compression members.

The strain readings at (ϵ_7) of CSJ3-4SF5.1 specimen were less than the strain of CSJ3-5N5.1which had a different concrete type of slab by (26.99%) and from the other hand the strain at (ϵ_7) of CSJ3-6SF3.6 specimen was lower than the strain of CSJ3-7N3.6which also they had a different concrete type of slab by (14.81%).

Finally, the strain at (ϵ_7) of CSJ3-4SF5.1 specimen was less than the (ϵ_7) strain of specimen CSJ3-6SF3.6 which had lower span/depth ratio by about (73.66%), that is when comparing the specimens which they had SFRC slab. While regarding the specimens which they had NC slab, the strain at (ϵ_7) of CSJ3-5N5.1 specimen was less than the strain of specimen CSJ3-7N3.6 which had lower span/depth ratio (3.6) by about (69.27%). From this comparison it can be concluded that the increasing of the slenderness ratio of the diagonal interior web members by (24.48%) yield to increase the strain in the interior compression web members by about (74%) for COWSJ specimens with SFRC slab and by about (69%) for COWSJ specimens with NC slab.

4.6.3.3 Strains at the Bottom Chord

In all seven COWSJ specimens the bottom chord yielded at the mid-span as designed. Regarding the strain gauges reading on the horizontal leg of the angle of the bottom chord (strain at 0, ϵ_0) showed that when comparing the three different cross section of HOWSJ, the strain of CSJ1-1 SF5.1specimen was more than that for CSJ2-2 SF5.1 and CSJ3-3 SF5.1 by about (33.56%) and (45.33%), respectively. While the strain gauges reading on the vertical leg of the angle of the bottom chord (strain at 1, ϵ_1) of CSJ1-1 SF5.1specimen was lower than that for CSJ2-2 SF5.1 and CSJ3-3 SF5.1 by about (29.34%) and (23.65%), respectively.

Regarding the strain at (ϵ_0 and ϵ_1) of CSJ3-4 SF5.1 specimen which had an effective width of concrete slab of (500mm) were less than the strain of CSJ3-3 SF5.1 which had an effective width of concrete slab of (400mm), but they had same concrete type of slab and the same cross section of HOWSJ by (9.09%) and

(8.64%), respectively. From these results it can be concluded that the increasing of the effective width of concrete slab by (20%) yield to decreasing the strains at the bottom chord by about (8%-9%). Also the strain at (ϵ_0 and ϵ_1) of CSJ3-4SF5.1 specimen were more than the strain of CSJ3-5N5.1which had a different concrete type of slab by (14.28%) and (15.11%), respectively. From the other hand the strain at (ϵ_0 and ϵ_1) of CSJ3-6SF3.6 specimen was lower than the strain of CSJ3-7N3.6which also they had a different concrete type of slab by (6.83%)and (6.21%), respectively. From these comparisons it can be noticed that the type of concrete slab was affected by the span /depth ratio, where when the span/depth ratio was (3.6), the strains of the bottom chord were decreased in case of using SFRC slab compared with NC slab specimens, whereas the strains of the bottom chord were increased in case of using SFRC slab when the span/depth ratio was (5.1).

Finally, the strain at (ϵ_0 and ϵ_1) of CSJ3-4SF5.1 specimen was lower than the strain of specimen CSJ3-6SF3.6 which had lower span/depth ratio by about (27.76%) and (12.43%), respectively, that is when comparing the specimens which they had SFRC slab. While regarding the specimens which they had NC slab, the strain at (ϵ_0 and ϵ_1) of CSJ3-5N5.1 specimen was lower than the strain of specimen CSJ3-7N3.6 which had lower span/depth ratio by about (42.30%) and (29.84%), respectively. From these comparisons it can be concluded that the strains at the bottom chord increasing when the span/depth ratio decreased and this increasing became larger when using COWSJ with NC slab.

4.7 Comparison between HOWSJ and COWSJ Specimens

The comparison between the results of the HOWSJ and COWSJ specimens for the three different shapes of HOWSJ cross section were plotted in Figures from (4-74) to (4-76). All of the three COWSJ specimens which fabricated either by using HOWSJ Model A or Model B or Model C, the deck slab of SFRC was enhanced the failure state, especially when used HOWSJ Model A. In general, the use of

the deck slab of SFRC will not enhanced only the ultimate load capacity, but also enhanced the stiffness and toughness of the specimens and it was improved the stability of interior web members and chords, within a reasonable ductility. Table (4.15) illustrate a comparison of ultimate capacity between the results of COWSJ and HOWSJ specimens, where the mean values of ultimate load capacity of each two specimen for the same model of HOWSJ were adopted in this table.

Regarding the strain gauges readings showed that the top chord strains, bottom chord strains, and the diagonal interior web members strains of COWSJ specimens were reached to their yielding stress at a higher ultimate load capacity compared with the ultimate load capacity of HOWSJ specimens. And the strains of the diagonal interior web tension members where their strain readings in the CSJ1-1 SF5.1, CSJ2-2 SF5.1, and CSJ3-3 SF5.1 were less than from that for HOWSJ Model A, Model B, and Model C by about (92.69%), (88.89%), and (88.17%), respectively.

Table 4.15 Comparison of the ultimate load capacity experimental results between COWSJ and HOWSJ specimens.

COWSJ specimen	Ultimate Load Capacity, P_u (kN)	HOWSJ Specimen	Ultimate Load Capacity, P_u (kN)	Increment in Ultimate Load Capacity (%)
CSJ 1-1 SF 5.1	160.153	SJ 1-1	100.99	36.94
CSJ 2-2 SF 5.1	155.495	SJ 2-2	93.53	39.85
CSJ 3-3 SF 5.1	137.892	SJ 3-3	86.31	37.41

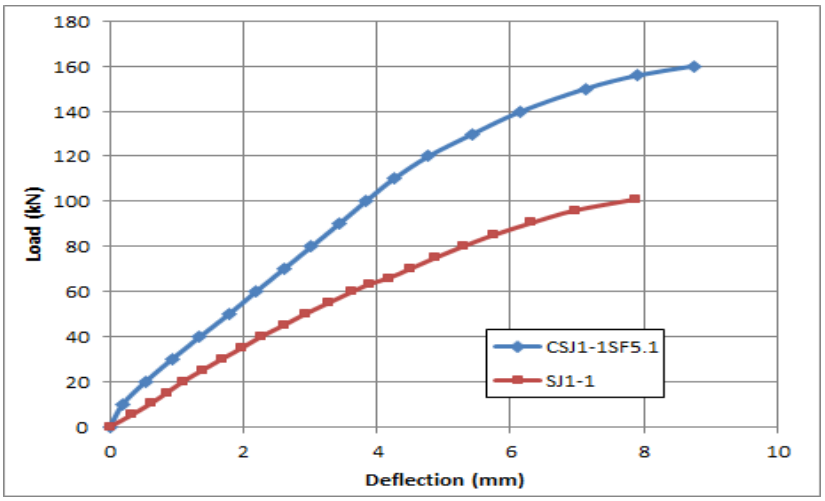

Figure 4.74 Comparison of experimental results of load- mid span deflection curve between CSJ 1-1 SF5.1 and SJ1-1 specimens.

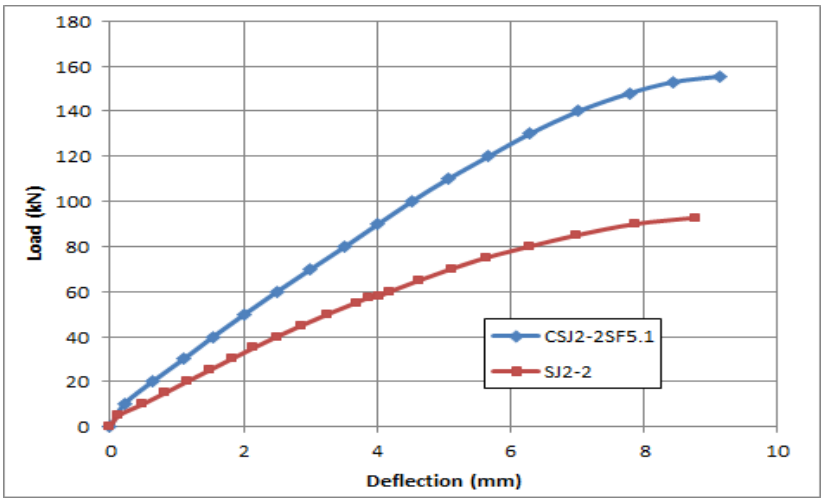

Figure 4.75 Comparison of experimental results of load- mid span deflection curve between CSJ 2-2 SF5.1 and SJ2-2 specimens.

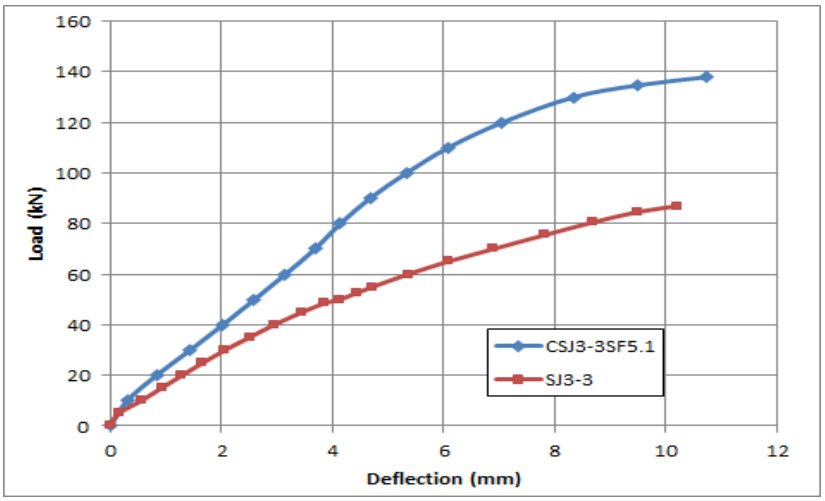

Figure 4.76 Comparison of experimental results of load- mid span deflection curve between CSJ 3-3 SF5.1 and SJ3-3 specimens.

CHAPTER 5

LATERAL TORSIONAL BUCKLING BEHAVIOR OF HOWSJ

5.1 General

This Chapter includes the results of lateral torsional buckling from experimental testing. Experimental testing measured the lateral displacement of top and bottom flanges of the HOWSJ specimens at the joist mid span, thus only the lateral deformations and the mechanism of failure was discussed in HOWSJ mid span.

The maximum lateral displacements of the top and bottom chord flanges were measured at the mid-span of the HOWS joists, the top chord flanges of HOWSJ underwent greater maximum lateral displacements compared to the maximum lateral displacements of the bottom chord flanges. Therefore, the HOWS joists experienced some rotation separate from the lateral displacement. Rotation (or angle of twist) of the HOWS joist was calculated by the following formula.

$$\phi = \tan^{-1}\frac{u}{h_s} \tag{5.1}$$

where

$u = \frac{u_{uf}+u_{lf}}{2}$

u_{uf} : the measured lateral displacement of the top chord flange of HOWSJ.

u_{lf} : the measured lateral displacement of the bottom chord flange of HOWSJ.

h_s : the distance between u_{uf} and u_{lf}.

By using the above formula, the load- deformation curves $(P-u)$ and $(P-\phi)$ can be plotted for all models. The lateral bending stiffness of the five different models used in this work was predicted from the load – deformation curves obtained from the experimental work by using the derived equation for the theoretical model suggested in this study. Then these lateral bending stiffness was used to make a fair comparison between all models.

5.2 Experimental Results

5.2.1 Load – Lateral Deflection Curves

Load versus lateral deflection curves at the mid-span of all the ten specimens were plotted and introduced in Figures (5-1) to (5-5) where each one introduces the results of two specimens for the same model.

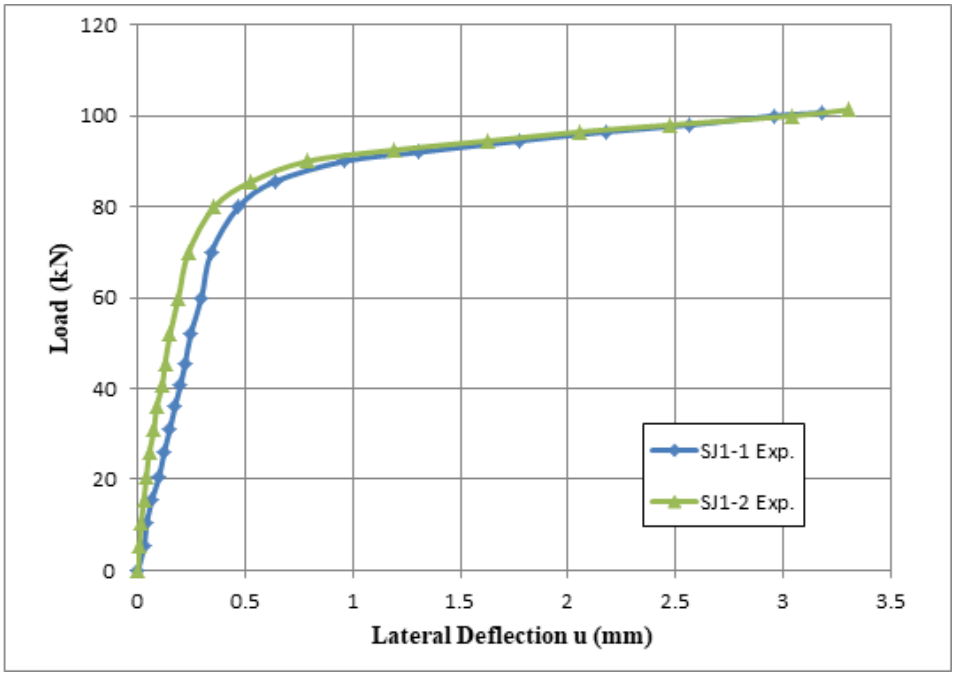

Figure 5.1 Load- lateral deflection curve for SJ1-1 and SJ1-2 Specimens.

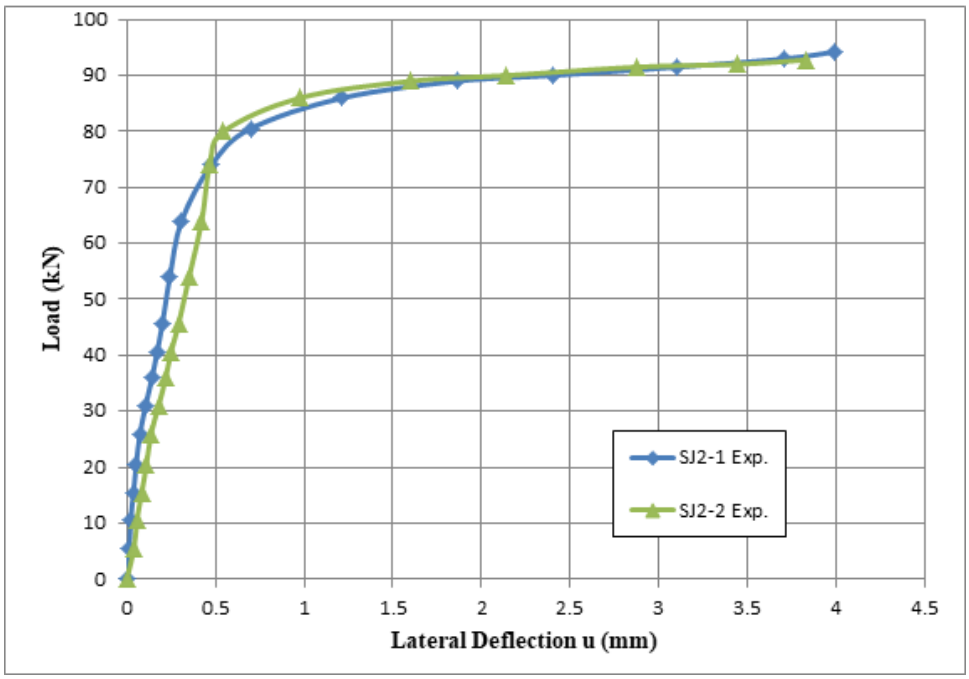

Figure 5.2 Load- lateral deflection curve for SJ2-1 and SJ2-2 Specimens.

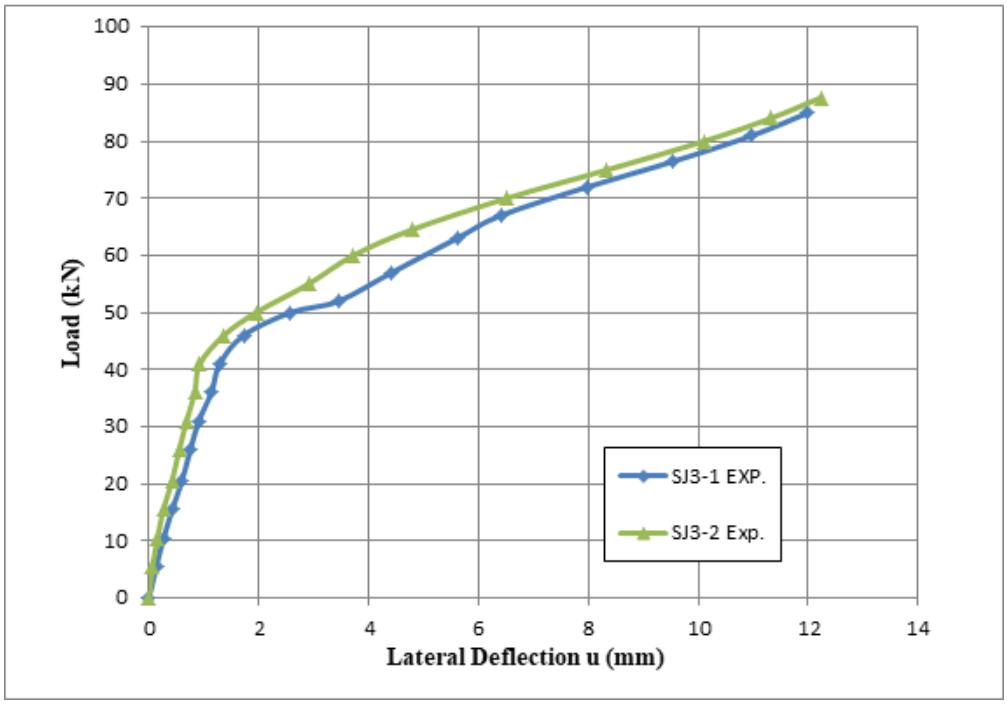

Figure 5.3 Load- lateral deflection curve for SJ3-1 and SJ3-2 Specimens.

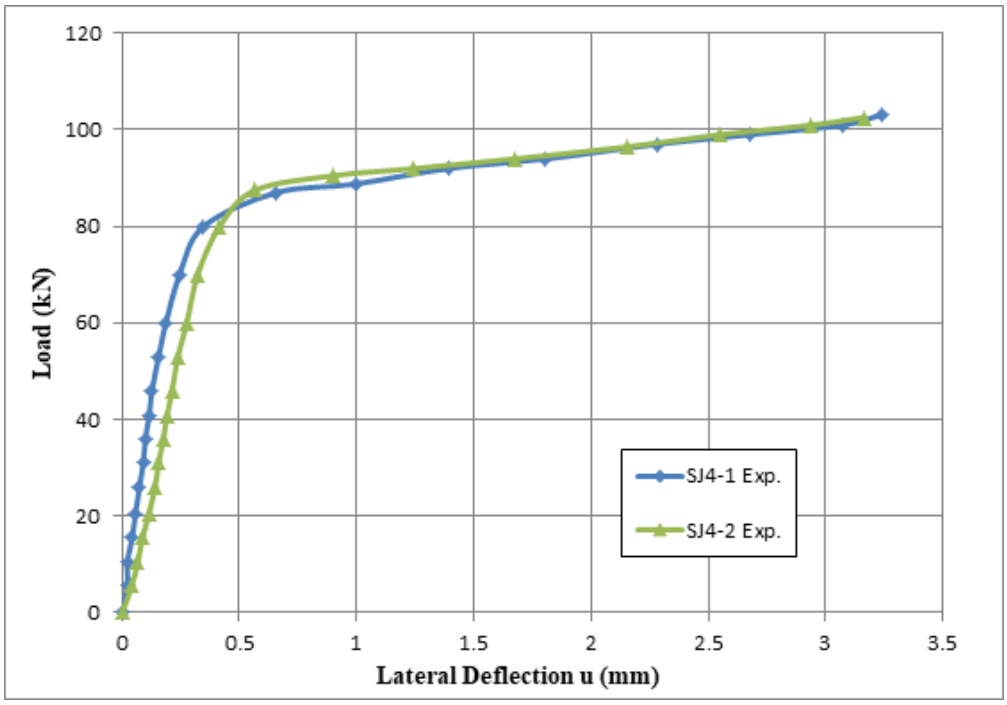

Figure 5.4 Load- lateral deflection curve for SJ4-1 and SJ4-2 Specimens.

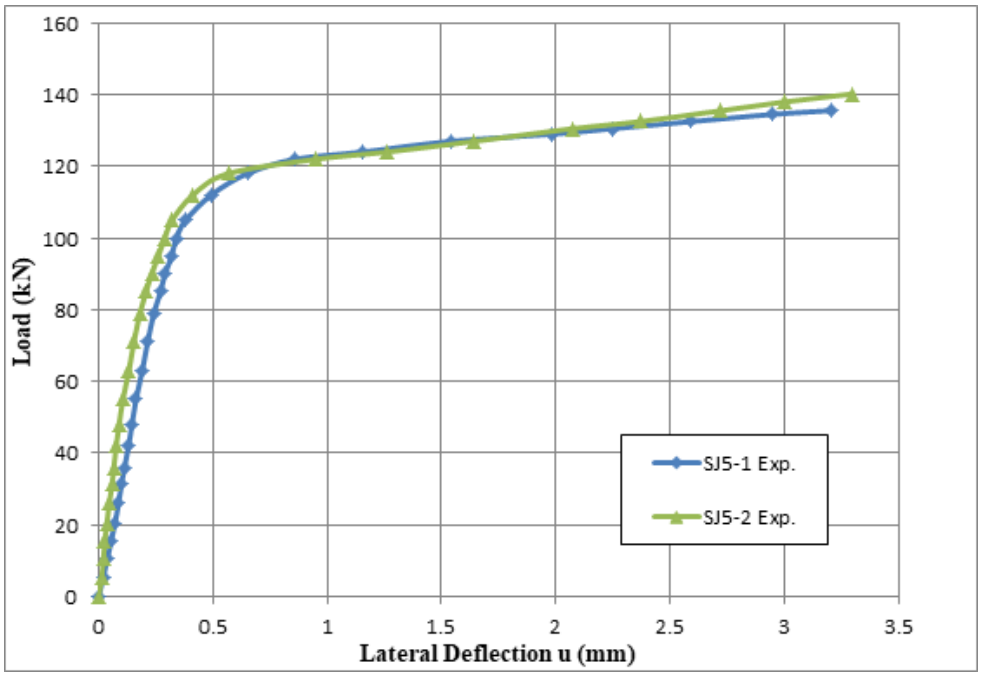

Figure 5.5 Load- lateral deflection curve for SJ4-1 and SJ4-2 Specimens.

5.2.2 Load – Rotation Curves

Load versus lateral deflection curves at the mid-span of all the ten specimens were plotted and introduced in Figures (5-1) to (5-5), where each one introduces the results of two specimens for the same model.

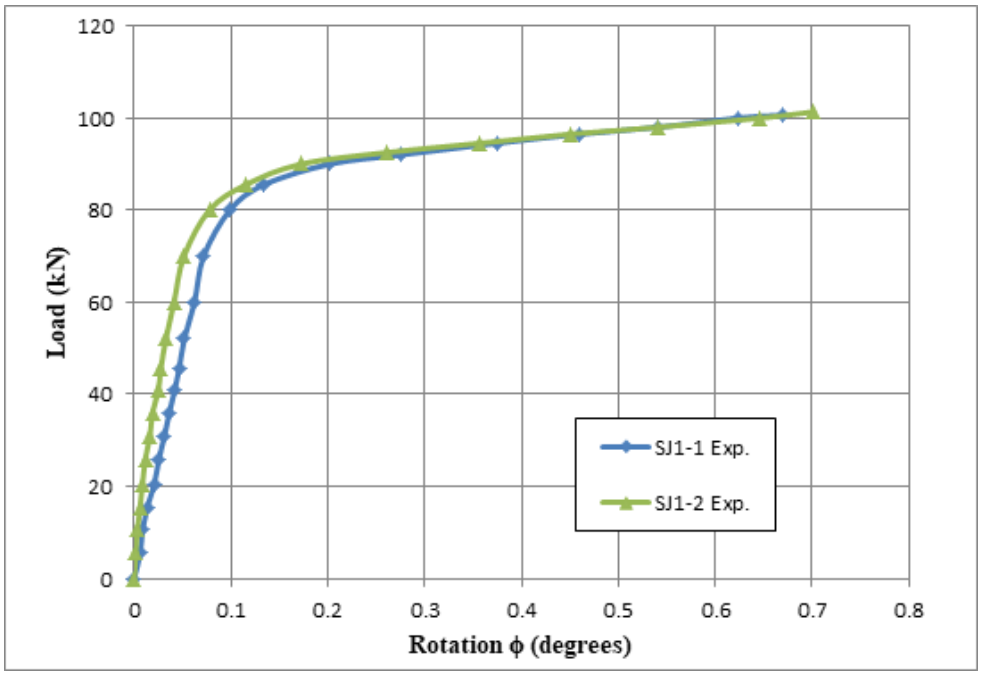

Figure 5.6 Load- rotation curve for SJ1-1 and SJ1-2 specimens.

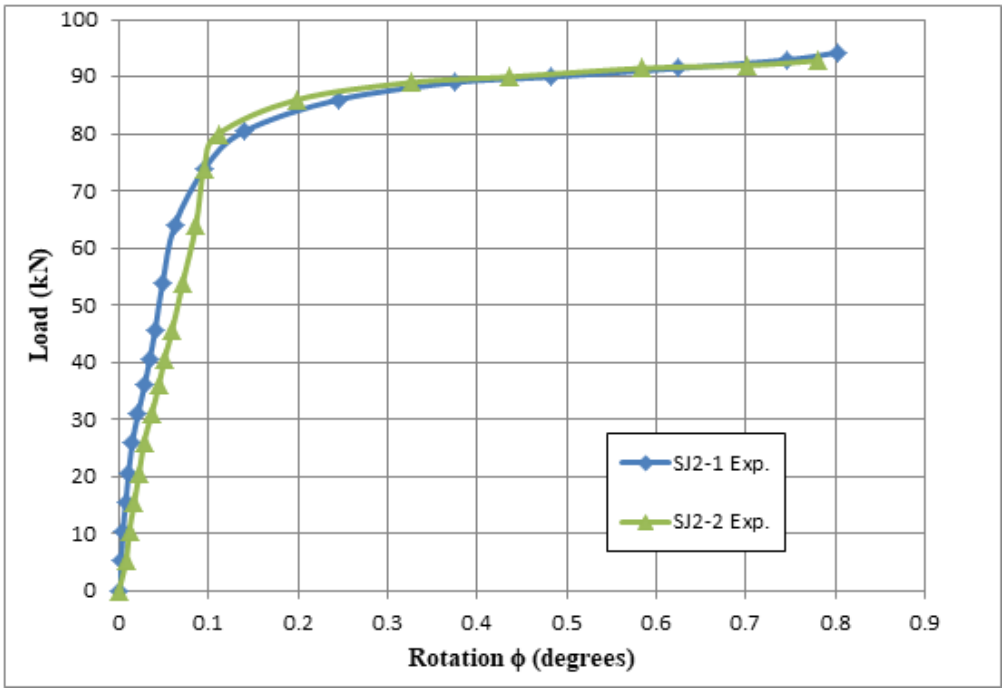

Figure 5.7 Load- rotation curve for SJ2-1 and SJ2-2 specimens.

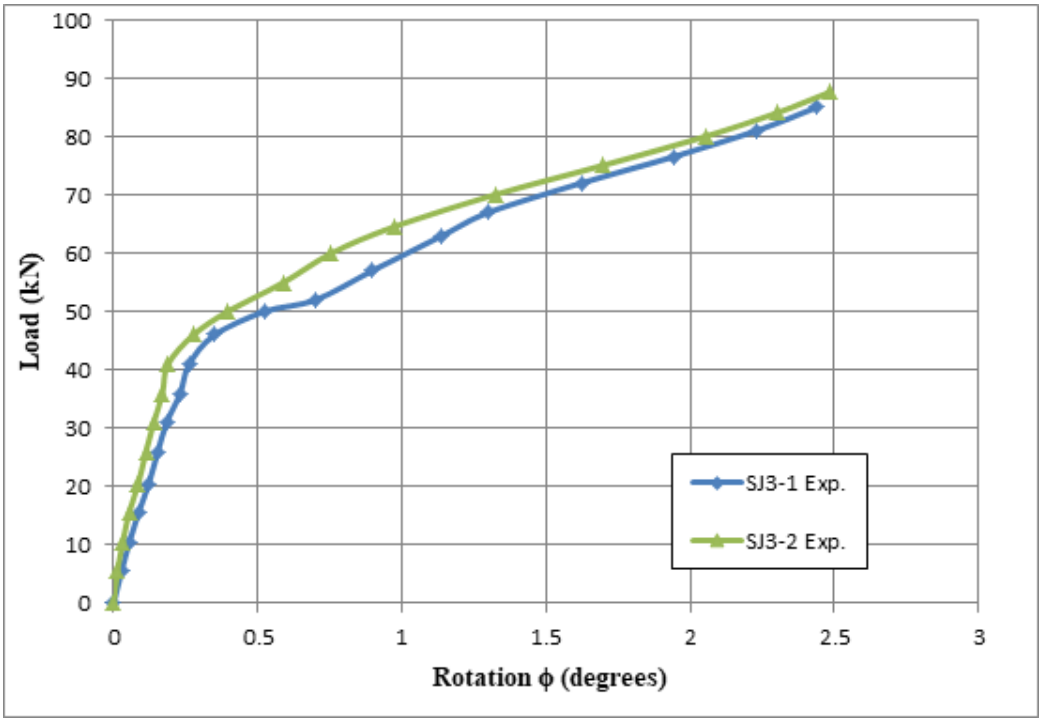

Figure 5.8 Load- rotation curve for SJ3-1 and SJ3-2 specimens.

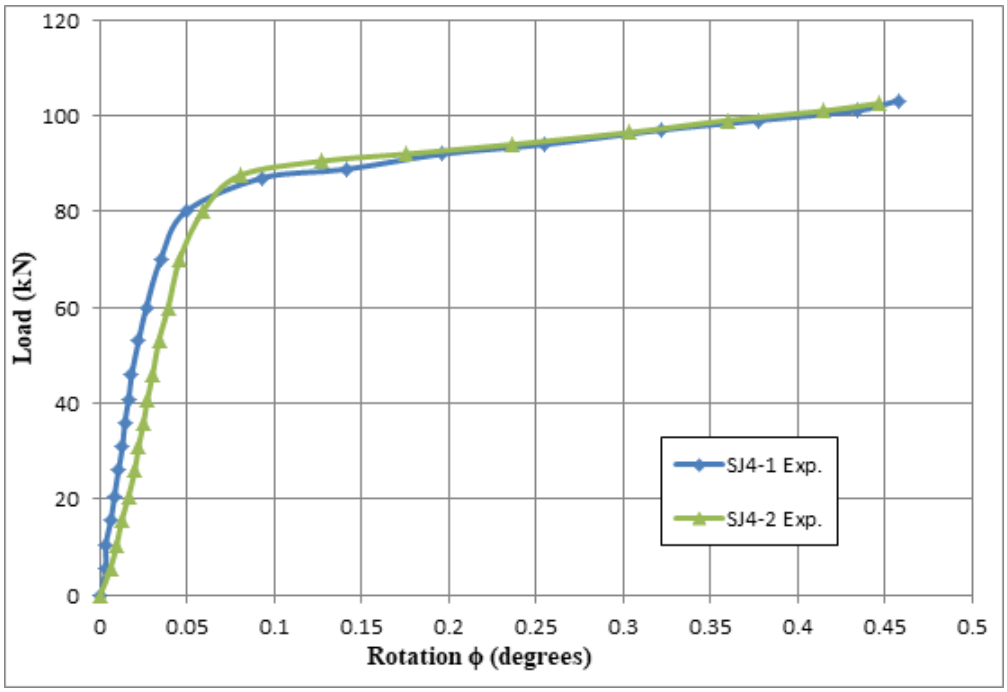

Figure 5.9 Load- rotation curve for SJ4-1 and SJ4-2 specimens.

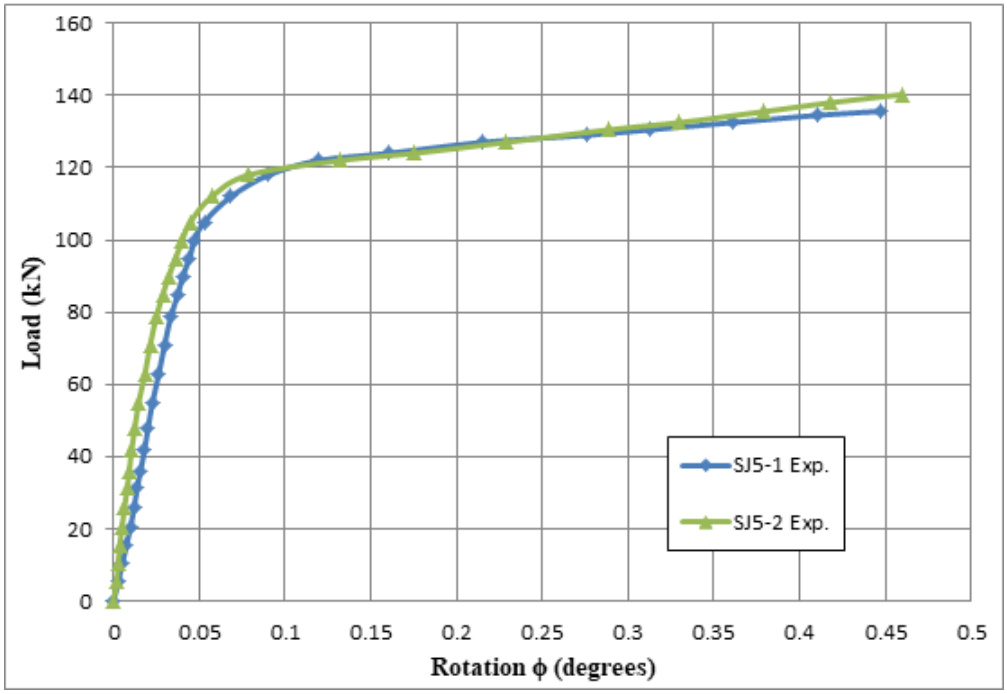

Figure 5.10 Load- rotation curve for SJ5-1 and SJ5-2 specimens.

For each specimen, a summary of the lateral buckling test results for the maximum load, maximum lateral deflection, and maximum rotation mentioned in the above curves were listed in Table (5-1).

Table 5.1 Lateral buckling test results for HOWSJ specimens.

Models	Specimen No.	Ultimate Load, P_u (kN)	Max. Lateral Deflection, u_{max} (mm)	Max. Rotation, ϕ_{max} (degrees)
Model A	SJ 1-1	101.34	3.178	0.669
	SJ 1-2	100.65	3.302	0.701
Model B	SJ 2-1	94.24	3.991	0.803
	SJ 2-2	92.81	3.834	0.779
Model C	SJ 3-1	84.97	11.995	2.438
	SJ 3-2	87.65	12.234	2.487
Model D	SJ 4-1	103.16	3.241	0.457
	SJ 4-2	102.54	3.161	0.445
Model E	SJ 5-1	136.59	3.210	0.447
	SJ 5-2	140.23	3.301	0.459

5.2.3 Results Discussion of the Load- Lateral Deformations of HOWSJs

5.2.3.1 Failure Mechanism

Regarding the previous curves it can observed that every two specimens of each model had the same behavior, thus to compare the results for different models, the average measured out of deformations of each two HOWSJ specimens for the same model was displayed in Table (5-2) where (P_u) represented the recorded experimental lateral torsional buckling capacity of HOWS joist used in this work. Also Figures (5-11) and (5-12) show a comparison between the behavior for all models, where the mean value for each two specimens for the same model were plotted.

According to these curves it can be noticed that Models A, D, and E specimens were had a small lateral deflections and rotations while the joist was still elastic, but these increased as the load increased towards the elastic lateral buckling load and they accelerated after yielding originated, and reached relatively high values as the failure load was approached. The experimental test displayed that for Models A, D, and E specimens test specimens the same ultimate failure mechanism was observed, which was a local buckling of the horizontal legs of

angles of the compression top chord. A little local buckling in the mid span diagonal interior web member were occurred, and all HOWSJ specimens for these three models had a slightly lateral buckling during the loading phase until they reached their ultimate capacity. While there was no local buckling observed on the vertical leg of the top chord angles at mid span of the joist. This mode of failure called flexural lateral torsional buckling, Plate (5-1) displayed the failure mode of these models.

For Model C specimens, it can be seen from Figures (5-11) and (5-12) that the HOWSJ specimens had larger lateral deformations compared wit models A, D, and E specimens while the joist still elastic. The compressive stresses were increased near the horizontal and vertical legs of the angles of compression top chord of the joists. From the experimental work it can be observed that the lateral deflections increased the compressive stresses near the horizontal legs of the compression top chord , vertical legs of the top chord, and the diagonal interior web members at the mid span of the HOWSJ, and this failure occurred before reached to a maximum load. Final failure was accompanied by high local buckling at the compression flange-web connection, Plate (5-2). And this mode of failure called flange distortional buckling.

From Figures (5-11) and (5-12) it can be observed that the behavior of Model B specimens was between the behavior of Models A, D, and E specimens and the behavior of Model C specimens. The experimental test showed that the lateral deflections increased the compressive stresses near the vertical legs of the top chord, the diagonal interior web members at the mid span of the HOWSJ specimens. Plate (5-3) shown the modes of failures for Model B specimens. And this mode of failure called lateral distortional buckling, which is possible occurs for beams with slender flexible webs and rigid flanges.

5.2.3.2 Effect of the HOWSJ Cross Section Shapes on the Failure Modes

Figures (5-11) and (5-12) illustrate that the lateral bending stiffness of Model A, D, and E specimens are close to each other and are also close to the lateral bending stiffness of the Model B specimens, but together they have a much greater lateral bending rigidity than the Model C specimens. The reason of this large differences it was caused by the large lateral deformations occurred during the test. The reason of generated of these large deformations was may be due to the fact that the method used in the manufactured of Model A, D, and E specimens ensured that the distribution of the section materials was close to the shear center location of the section, especially the interior web members which were responsible of transfer the shear force between the top and bottom chords of the HOWSJ specimens, thus the interior web in these models were more stiffer against local buckling at the joist mid span.

For Model C specimens which were prefabricated as previously mentioned in Section (3.2.1.3), with chord width of (200 mm), it can be noticed that the locations of the interior web members were far from the location of the shear center of the HOWSJ, so a torsional moment was produced because the shear forces transferred by these inner webs were become far from the shear center location. At mid span of the joist a high local buckling occurred at the vertical and horizontal legs of the top chord because top chord of these HOWSJ specimens were connected together by welding a steel plates at a specified distance which made most of the horizontal legs of angles of the top chord were unrestrained against the local buckling deformations.

Regarding Model B specimens cross section which were prefabricated as their interior webs was closer to the shear center location than Model C specimens, so the local buckling of their interior webs and the vertical legs of the top chord at the joist mid span were less than the local buckling which occurred in Model

C specimens. There was no local buckling occurred in the horizontal legs of top compression chord of Model B because they undergoes to behave as a restrained members, since the top chord was manufactured by welding the horizontal legs of angles face to face at a specified distance .

Table 5.2 Average values of measured deformations for HOWSJ specimens.

Models	Average Ultimate Load, P_u (kN)	Average of Max. Lateral Deflection, u_{max} (mm)	Average of Max. Rotation, ϕ_{max} (degrees)
Model A	100.99	3.240	0.685
Model B	93.53	3.913	0.791
Model C	86.31	12.115	2.463
Model D	102.85	3.201	0.451
Model E	138.41	3.256	0.453

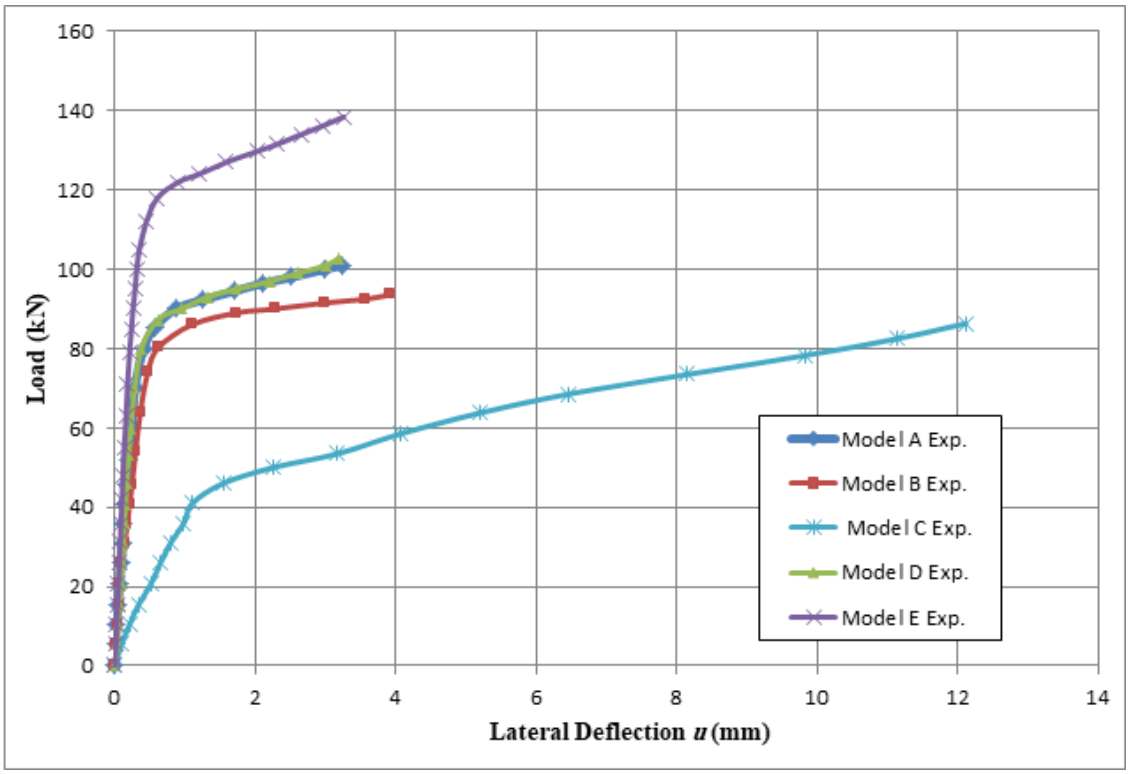

Figure 5.11 Comparison of load- lateral deflection curves for all models.

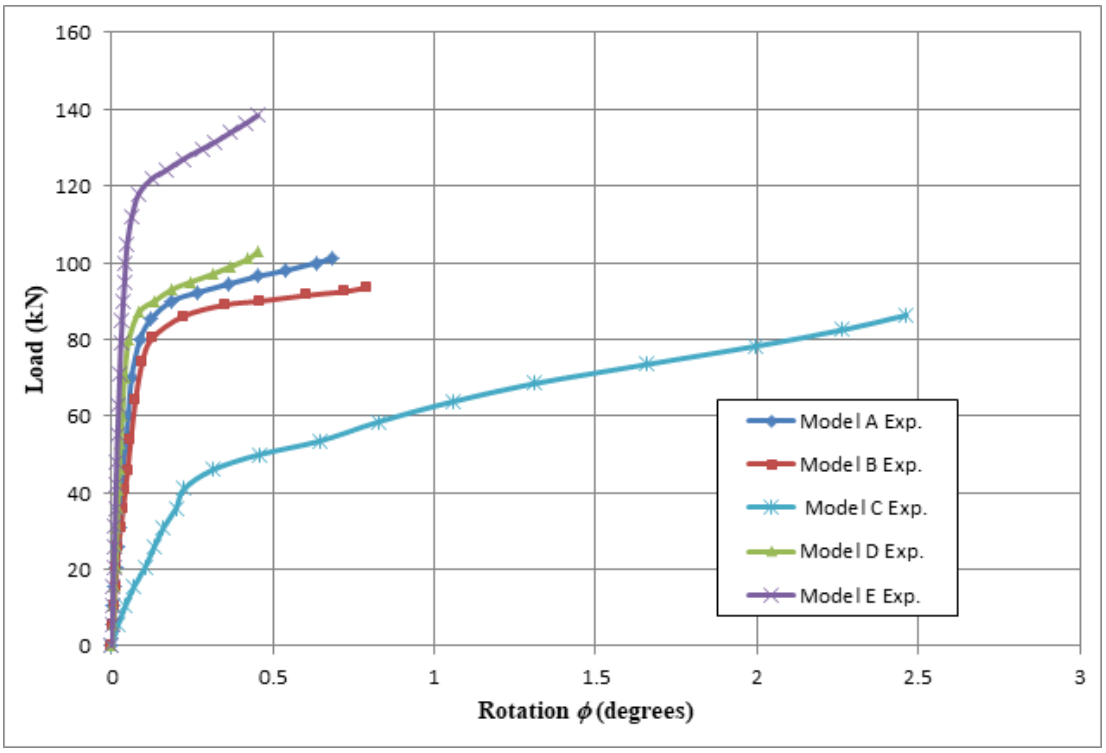

Figure 5.12 Comparison of load- rotation curves between HOWSJ models.

Plate 5-1 Failure modes of models A, D, and E.

Plate 5-2 Failure modes of model C.

Plate 5-3 Failure modes of model B.

5.2.3.3 Effect of the Lateral Rigidity on the Behavior of HOWSJ Models

The experimental results shown in Figures (5-11) and (5-12) suggest that the strengths of models A, D, and E are methodically higher than the strengths of models B and C, which made that the comparison between the different HOWSJ models an fair, because each model had a different cross section details.

As it is scientifically known that the sections with higher heights in comparison to their width have a large lateral deformations compared to the sections with lower heights, and this contradicted what was observed in the Figures (5-11) and (5-12), where the values of the lateral deformations for Model A specimens of height (350 mm) were greater than the lateral deformations for both Model D and Model E which they had a height of (500 mm). As for the models B and C which their lateral deformations were supposed to be less than the other models, because they had a greater theoretical lateral stiffness than the models A, D, and E, which were calculated for each cross section of the models as a built up sections as explained earlier in the section (3.2.1), Table(3-1). And this also absolutely contradicted with the experimental results shown in Figures (5-11) and (5-12).

Therefore, a theoretical method was proposed in this study to find an equation that enables estimating the lateral rigidity value for each model based on the details of the cross-sections of these models and also on the slope of the lateral deformation curves obtained from the experimental test program to know the real behavior of each model according to the strength of its cross-section and the maximum load reached by each model. And this theoretical derived method will be explained in the next sections.

5.3 Elastic Lateral Torsional Buckling

In lateral-torsional buckling, the beam is loaded in the plane of its major axis until it buckles by a sudden simultaneous lateral deflection and twisting of the

cross-section [106]. As an example of this behaviour, consider a simply supported I-section beam. When loaded by a uniformly distributed load, the top flange is compressed whereas the bottom flange is tensioned. The compressed flange is prone to buckle as a strut but is partly restrained by the web in the vertical direction so it will instead buckle laterally. The tension flange however does not need to buckle and is, together with the web, partly restricting the lateral deformation of the compression flange. The imbalance in lateral deflection between the two flanges also lead to torsion of the cross-section.

Elastic stability must satisfy two basic criteria, the ability of the structure to support the imposed loading (strength) and the capacity of the structure to resist distortions (stiffness). In contrast, inelastic instability is the condition where the structure does not return to its initial position when slightly disturbed, even when the yield stress is assumed to be infinitely large. Elastic buckling instability is frequently associated with large changes of geometry which often occur quickly as the structural member moves from one geometrical position of equilibrium to another [107].

Two different theoretical methods have been used to calculate the critical lateral-torsional buckling load for I-beams; the differential equations of equilibrium method and the strain energy method. The differential equations of equilibrium method for lateral-torsional buckling instability in I-beams is based on the elastic bending theory of beams. The problem to mathematically define the critical lateral torsional buckling load using the differential equations of equilibrium method is non-linear for large deflections, but linearization for small deflections is possible [108].

The linearization process develops a linear fourth-order ordinary differential equation for deflections. The critical lateral-torsional buckling load is found by solving the linear fourth-order ordinary differential equation using the supported

end conditions as boundary conditions. The strain energy method uses the equilibrium of the overall energy of the system. When an I-beam experiences lateral-torsional buckling instability, the strain energy increases as the applied load is transformed into axial deflection, lateral deflection and rotation of the I-beam. The point of load application moves downwards and laterally producing work in the system. The critical lateral-torsional buckling load is found by equating the increase of the strain energy in the system to the work done by the system. The strain energy method uses an approximate function for the angle of twist of the I-beam that must satisfy the boundary conditions defined by the supported end conditions [34].

Thus, the two methods, the differential equation of equilibrium method and the strain energy method use the boundary conditions to mathematically define the critical lateral-torsional buckling load. Besides of the boundary conditions, stiffness properties including the lateral bending stiffness of the I-beam and the torsional rigidity of the I-beam are needed to calculate the critical lateral-torsional buckling load. The present research was focused on the study of the lateral-torsional buckling instability of HOWS joists. The derivation of the equations to calculate lateral bending rigidity of HOWS joists was based on the analysis of elastic torsional buckling.

5.4 Definitions and Description of Concepts

5.4.1 Coordinate System

The beams in this research are orientated according to the coordinate system presented in Figure (5-13), where the x-axis lies along the beam, the positive y-direction is vertical pointing upwards and the z-direction is horizontal, perpendicular to the x-axis.

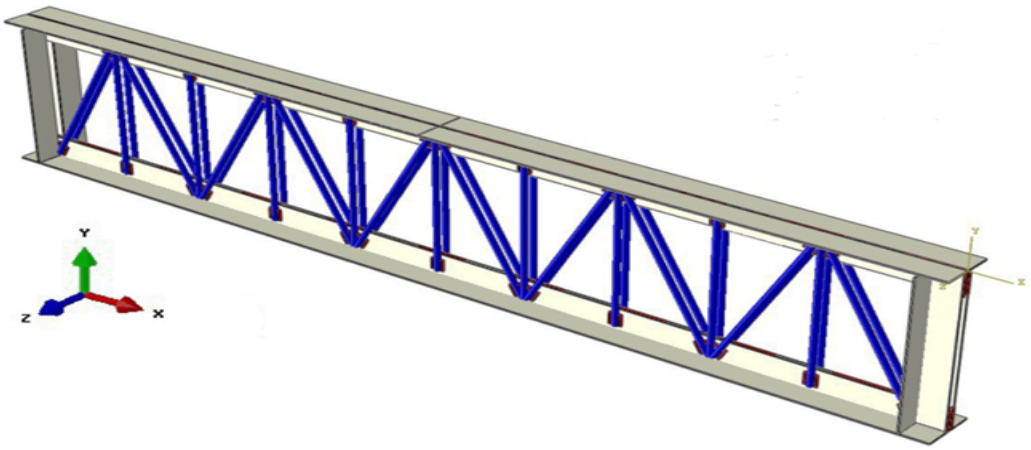

Figure 5.13 Orientation of (HOWSJ) coordinates.

When a beam is subjected to a vertical load the z-axis is considered its major axis, and it will deflect in the y-direction. While the y-axis is considered its minor axis, deflecting in the z-direction. Bending about the z-axis will consequently be called major axis bending and bending about the y-axis called minor axis bending. The bending about the y-axis (i.e the minor axis) sometimes called lateral bending or bending about the weak axis, Figure (5-14).

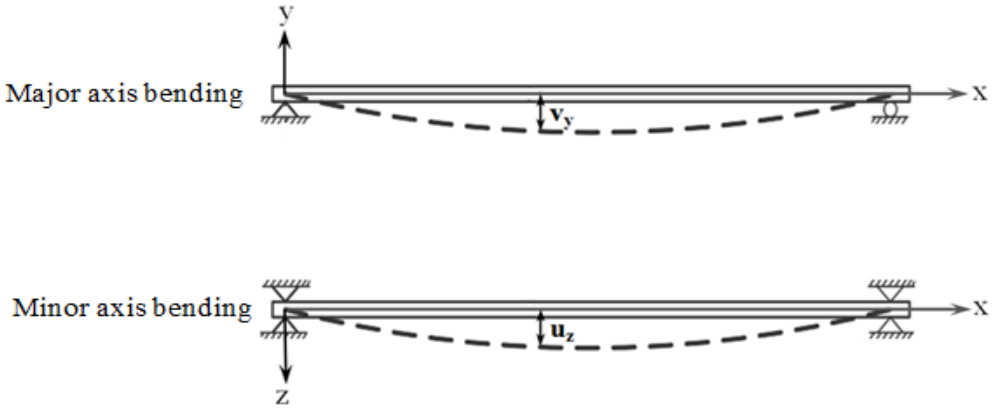

Figure 5.14 Beams subjected to major and minor axis bending.

5.4.2 Degrees of Freedom

A beam element can be considered to have seven degrees of freedom in each node, translations in the x-, y- and z-direction and rotations about the x-, y- and z-axis and warping.

5.4.3 Supported End Conditions

To obtain the equations to calculate the critical lateral-torsional buckling load for either the differential equations of equilibrium method or the strain energy method, it is necessary to take into account the mathematical relations of the boundary conditions.

In this study a fork support was used to analyse lateral-torsional buckling for a single span beam that was simply supported on each end. In a fork support, the translation in y and z- axes was restrained at both ends and at one end the translation in x was locked. The rotation about the x-axis was prevented due to the geometry of a fork support but rotations about the y- and z-axis and warping were allowed at both ends. The fork support for each end was shown in Figure (5-15).

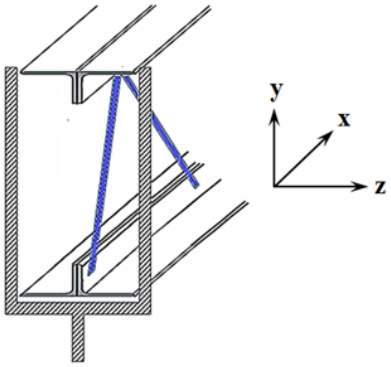

Figure 5.15 Fork support.

5.4.4 Warping Torsional Constant of HOWSJ

When a double-symmetric HOWSJ rotates, shear forces will arise due to lateral deflection of the flanges. These warping effects can found by calculating the resulting moment from the shear forces in the flanges. In the warping torsional constant formulation, the horizontal legs of angles of top and bottom chords of an open-web steel joist were considered to be the only components of the HOWSJ that contribute to the lateral stability of the joist. The lateral deflection of one of the chords flange due to warping, u_w , can approximately be expressed in terms of the rotation, ϕ; as shown in Figure (5-16).

$$u_w = \frac{h_s}{2}\phi \tag{5.2}$$

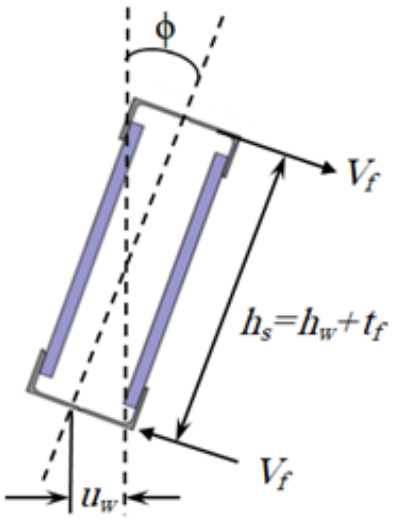

Figure 5.16 Shear forces induced by lateral bending of the chord flanges (warping).

This lateral deflection creates a bending moment M_w and a shear force V_f in the flange of chord. Differentiating Equation(5-2) three times with respect to x gives[109]:

$$\frac{d^3u_w}{dx^3} = \frac{h_s}{2}\frac{d^3\phi}{dx^3} \tag{5.3}$$

For one chord flange of HOWSJ the curvature is:

$$\frac{d^2u_w}{dx^2} = \frac{-M_{flange}}{EI_{y,flange}} \tag{5.4}$$

since, $V_{flange} = dM/dx$,thus:

$$\frac{d^3u_w}{dx^3} = \frac{-V_{flange}}{EI_{y,flange}} \tag{5.5}$$

Using Equations (5-3) and (5-5) gives

$$V_{flange} = -EI_{y,flange}.(\frac{h_s}{2})\frac{d^3\phi}{dx^3} \tag{5.6}$$

The torsional moment component M_w, causing lateral bending of the flanges $=V_f \ . \ h_s$. This assume no shear resistance to warp is contributed by the web [109].

$$M_w = V_{flange}.h_s = -EI_{y,flange}.(\frac{h_s^2}{2})\frac{d^3\phi}{dx^3} \tag{5.7}$$

$$M_w = -E.C_w.\frac{d^3\phi}{dx^3} \tag{5.8}$$

where:

C_w=warping torsional constant.

$$C_w = I_{y,flange}.(\frac{h_s^2}{2}) \tag{5.9}$$

The Second moment of inertia about y-axis and the warping torsional constant of one chord flange of each model of HOWSJ which studied in this work will be derived as follows, Figure (5-17) shown the details of each model. In this study the top and bottom chord flanges of HOWSJ are manufactured by using equal legs angles (L50×50×4)mm, so $b_1 = b_2 = b'$, and $t_1 = t_2 = t'$.

where:

b': the length of the angle's leg (mm).

t': the thickness of the angle's leg (mm).

Thus:

1- For models A, B, D, and E specimens:

$$I_{y,flange} = (\frac{b_1^3.t_f}{3} + \frac{b_2^3.t_f}{3}) = \frac{2}{3}.b'^3.t' \tag{5.10}$$

$$C_w = \frac{1}{3} b'^3 . t' . h_s^2 \tag{5.11}$$

2- For model C specimens:

$$I_{y,flange} = 2(\frac{b'^3 . t'}{12} + b' . t' . d_1^2) \tag{5.12}$$

$$C_w = (\frac{b'^3 . t'}{12} + b' . t' . d_1^2) . h_s^2 \tag{5.13}$$

In the above formulation, the horizontal legs of angles of the top and bottom chords of an open-web steel joist were considered to be the only components of the joist that contribute to the lateral stability of the joist.

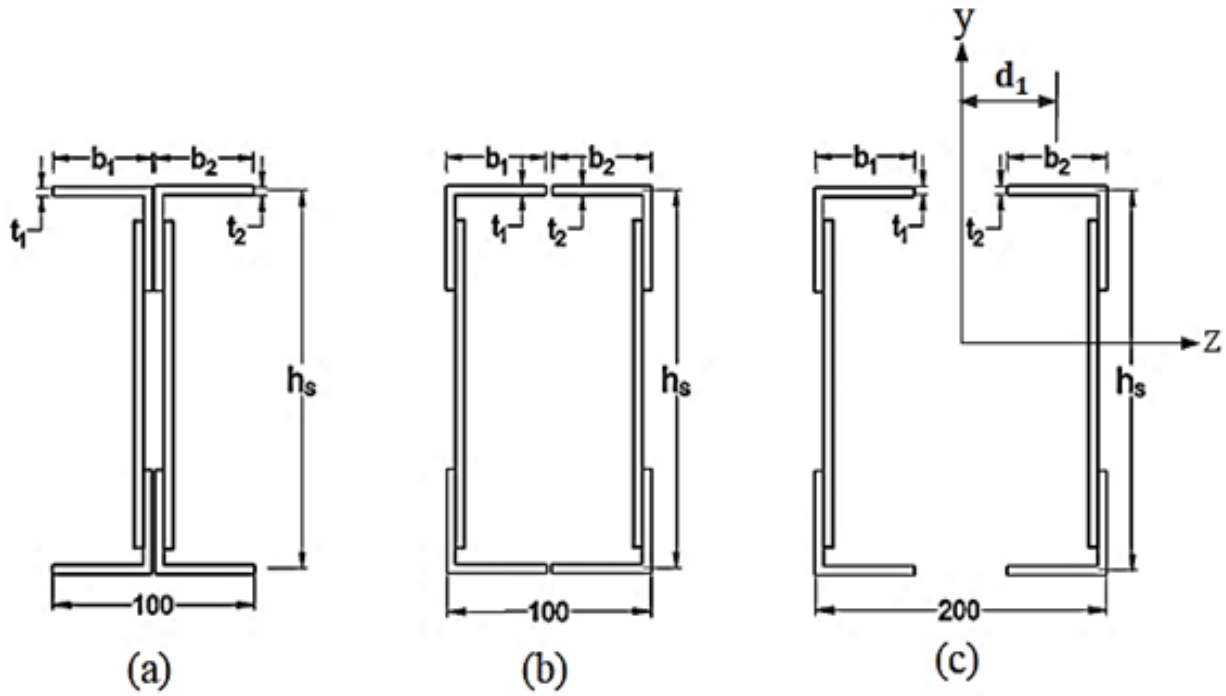

Figure 5.17 Cross sections of HOWSJ models.(a) Models A, D, and E. (b) Model B. (c) Model C.

5.4.5 Torsional Constant of HOWSJ

According to the Saint-Venant torsion theory the typical torsion stresses occur only when free warping can take place. The basic equation for torsion is according to Saint-Venant is as follows:

$$M_s = GJ\frac{d\phi}{dx} \tag{5.14}$$

where:

M_s = Torsion

ϕ = Angle of twist, see Figure (5.16)

G = Shear modulus of elasticity = E/(2(1+ν))

J = Saint-Venant torsional constant

E = Young's modulus of elasticity.=207986 N/mm^2, as had been established from the tensile test done in this study, Table (3.2).

ν = Poisson's ratio which was used =0.3 in this study. For a cross section built up by rectangular parts, the torsional constant, often related to Saint-Venant's theory, is most commonly expressed as [110]:

$$J = \sum_{i=1}^{n}(h_i t_i^3)/3 \tag{5.15}$$

where; h_i : Length of cross section part, t_i : Thickness of cross section part; and n : Number of cross section parts. Thus for all models of HOWSJ this expression was became as:

$$J = 4[1/3(b't'^3 + (b' - t')t'^3)] \tag{5.16}$$

The values of warping torsional constant and torsional constant of each model of HOWSJ was be calculated and listed in Table (5.3).

Table 5.3 Warping torsional constant and torsional constant of HOWSJ.

Model No.	$I_{yflange}(mm^4)$	$C_w(mm^6)$	$J(mm^4)$
Model A	333333.33	1.9953×10^{10}	8192
Model B	333333.33	1.9953×10^{10}	8192
Model C	2333333.33	1.3967×10^{11}	8192
Model D	333333.33	4.1003×10^{10}	8192
Model E	333333.33	4.1003×10^{10}	8192

Timoshenko and Gere [34] included effects of warping, which made it possible to describe the torsion of I-section beams correctly. it was developed a theory included a non-uniform torsion along a beam to take restraint warping into account, the theory was called non-uniform torsion of an I- beam and it can be applied to the analysis of a thin-walled bar of any open cross section. The non-uniform torsion of the cross section along a beam can be described by the following equation:

$$M_x = M_s + M_w \tag{5.17}$$

5.5 Elastic Lateral Bending Rigidty (EI_y)

The lateral bending stiffness of the HOWSJ (EI_y) is the capacity of the joist to resist normal to the plane of the web deformations when a normal to the plane of the web loading is applied to the joist. In the general case and for anisotropic materials the lateral bending stiffness is determined by elastic material properties of the beam such as elastic moduli and shear moduli, by geometric properties of the beam such as the moment of inertia of the cross-section and the length of the beam and by the loading and end supported conditions of the beam. The derivation of lateral bending rigidity equation for HOWS joists in this research was obtained as explained in the following sections.

Because the case of loading used in this study was by applying a concentrated load on the top chord flange at mid span, so the case of a simply supported I-beam loaded by concentrated load at mid span at the neutral axis by (Timoshenko and

Gere) [34] was utilized to estimate the elastic lateral bending stiffness (EI_y) of HOWSJs.

5.5.1 Differential Equations of Equilibrium Method

Lateral-torsional buckling instability is accompanied by a vertical displacement v, a lateral displacement u and a twist ϕ about the neutral axis parallel to the x-axis. The general coordinate system of the un-deformed HOWS joist is defined as $x - y - z$, and its fixed at the centroid of any cross-section. The coordinate system which rotates with the HOWS joist when it undergoes lateral-torsional buckling instability is defined as $x' - y' - z'$. Equations (5.18) ,(5.19), and (5.20) are the governing bending equations in the planes $x'z'$ and $y'z'$, describing the displacement of the centroid in the y –direction (v), and the lateral displacement (u) in the z –direction. Both coordinate systems are shown in Figure (5-18).

$$EI_z(d^2v/dx^2) = M_{z'} \tag{5.18}$$

$$EI_y(d^2u/dx^2) = M_{y'} \tag{5.19}$$

The differential equation for twisting of the buckled beam is:

$$M_{x'} = GJ(d\phi/dx) + EC_w(d^3\phi/dx^3) \tag{5.20}$$

The moments of the reaction force (P/2) with respect to axes through the centroid of the section (m-n), parallel to the x, y, and z axes, are:

$$M_x = -P/2(-u_1 + u)$$

$$M_y = 0 \tag{5.21}$$

$$M_z = P/2(L/2 - x)$$

where:

P : the applied load about the neutral axis parallel to the plane of the web, see Figure (5.18 b).

u_1 : the lateral deflection of the centroid of the middle cross section.

u : the deflection at any cross section (m-n).

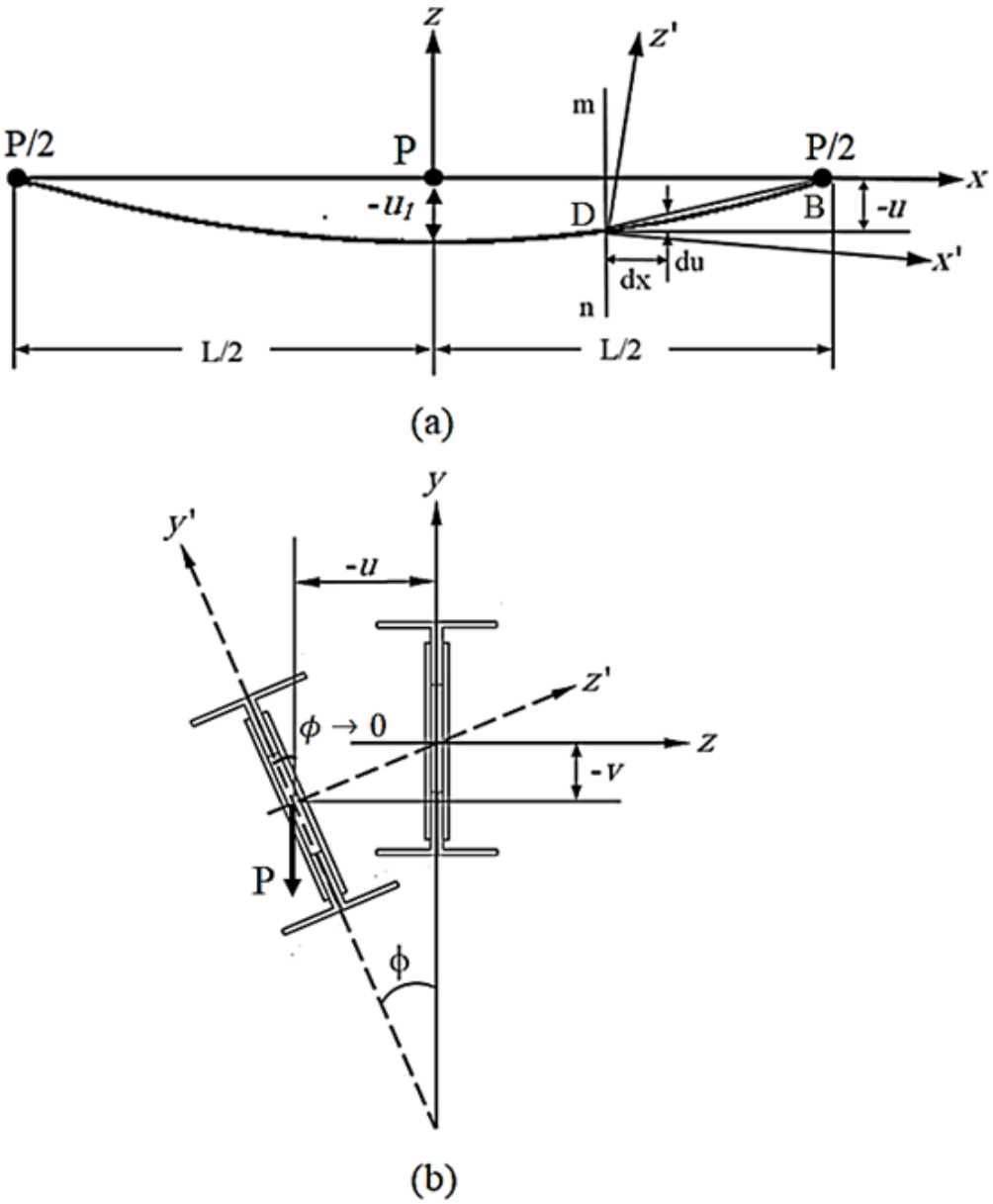

Figure 5.18 Lateral-torsional buckling of a simply supported HOWSJ. (a) Top view of the longitudinal axis; (b) section (m-n).

The quantities (Mx'), (My') and (Mz') are related to the projection of the applied moments (Equations (5.21)) onto the x', y' and z' axes, as shown in Figure (5-18). Linearization of the system assumes that the deformation quantities v, u and ϕ are very small . Also neglecting quantities of higher order, the following relations are obtained [34].

$$M_{z'} = (P/2)(L/2 - x)$$

$$M_{y'} = (P/2)(L/2 - x)\phi \tag{5.22}$$

$$M_{x'} = -(P/2)(L/2 - x)(d_u/d_x) + (P/2)(u_1 - u)$$

Because of the assumption of small deformation. It is assumed that the properties $I_{x'}$ and $I_{y'}$ equal to I_x and I_y, respectively and also I_x is large compared to I_y, so that Equation (5.23) not linked to Equation (5.24) and (5.25). Thus vertical displacement v in the plane of bending does not affect the torsional function ϕ [109]. Substituting Equations (5.22) into Equations (5.18) to (5.20), the following differential equations of equilibrium for the buckled beam Figure (5-18) were obtained.

$$EI_z(d^2v/dx^2) = (P/2)(L/2 - x) \tag{5.23}$$

$$EI_y(d^2u/dx^2) = (P/2)(L/2 - x)\phi \tag{5.24}$$

$$GJ(d\phi/dx) - EC_w(d^3\phi/dx^3) - (P/2)(u_1 - u) = -(P/2)(L/2 - x)(du/dx) \tag{5.25}$$

Eliminating u from Equations (5.24) and (5.25), Equation (5-26) can be obtained:

$$EC_w(d^4\phi/dx^4) - GJ(d^2\phi/dx^2) - (P^2/(4EI_y))(L/2 - x)^2\phi = 0 \tag{5.26}$$

The function $\phi(x)$ for the angle of twist for a simply supported beam was described by Timoshenko [34], satisfying the conditions at the ends of the beam.

$$\phi(x) = \sum_{n=1}^{\infty} a_{(2n-1)}.cos(\frac{(2n-1)\pi x}{L}) \tag{5.27}$$

By using a single term in Function (5.27), the accuracy of the solution is suitable for practical applications and by integrating the Equation (5.24), then an equation to estimate the lateral rigidity of HOWSJ (EI_y) can be derived as follow:

$$EI_y(\frac{d^2u}{dx^2}) = \int_0^{L/2}\int_0^{L/2}(\frac{P}{2})(\frac{L}{2}-x)(acos(\frac{\pi x}{L}))dxdx \tag{5.28}$$

After integration the following was obtained :

$$u = \frac{PL^3a}{4\pi^2EI_y} \tag{5.29}$$

The angle of twist of HOWSJ which investigated in this research was calculated by the formula (5.1) as shown previously. Equations (5.1) and (5.29) can be rewritten as in the Equation (5.30) below in terms of the slope of the load-lateral deflection curve (P/u) or in terms of the slope of the load-angle of twist curve $(P/\sqrt{\phi})$ which was obtained from the results of the experimental work in this research.

$$EI_y = (\frac{P}{u})\frac{a.L^3}{4\pi^2} = k_1(\frac{P}{u}) \tag{5.30}$$

Where: $k_1 = (a.L^3)/(4\pi^2)$

The constant (a) must be calculated to estimate the lateral rigidity of HOWSJ, thus the strain energy method will be used to obtained this constant as explained in Section (5.5.2) below.

5.5.2 Strain Energy Method

By using the energy method the assumption of some small lateral deflection of the system was assumed. This deflection means an increase ΔU in the strain energy of the system. At the same time the load P will move through a small distance and do work equal to ΔT [34], and the work done by the force P is:

$$\Delta T = P.\delta \tag{5.31}$$

The system is stable in its un deflected form if ($\Delta U > \Delta T$) and unstable if ($\Delta U < \Delta T$), thus the critical value of the load P was found from Equation (5.32) shown below, which represent the condition when the equilibrium configuration changes from stable to unstable.

$$\Delta U = \Delta T \tag{5.32}$$

For determining the lowering of the load P during lateral buckling, considered an element (dx) of the longitudinal axis of the beam at the point D , Figure (5-18). Owing to bending of this element in the ($x'z'$) plane and with the cross section (m-n) considered as fixed, the end B of the beam describes an infinitely small arc ($(d^2u/dx^2)(L/2 - x)dx$) in the ($x'z'$) plane, the vertical component of which was:

$$\phi(\frac{d^2u}{dx^2})(\frac{L}{2} - x)dx \tag{5.33}$$

The lowering of the point of application of the load P due to lateral buckling of the beam was obtained by summation of the vertical components Equation(5.33) for all elements of the beam between $x = 0$ and $x = L/2$. Thus the following

expression for the work done by the load was obtained.

$$\Delta T = P \int_0^{L/2} \phi(\frac{d^2u}{dx^2})(\frac{L}{2} - x)dx \tag{5.34}$$

Taking into consideration the symmetry of the buckled form of the joist as shown in Figure (5-18), it can be found the increase in strain energy due to lateral buckling show below in Equation (5.35), in which the three terms represent, respectively, the strain energy due to lateral bending, twisting, and warping of the beam.

$$\Delta U = EI_y \int_0^{L/2} (\frac{d^2u}{dx^2})^2 dx + GJ \int_0^{L/2} (\frac{d\phi}{dx})^2 dx + EC_w \int_0^{L/2} (\frac{d^2\phi}{dx^2})^2 dx \tag{5.35}$$

Using Equations (5.24), (5.32), and (5.35), The equation for determining the critical value of the load will be expressed as:

$$\frac{P^2}{4EI_y} \int_0^{L/2} \phi^2(\frac{L}{2} - x)^2 dx = GJ \int_0^{L/2} (\frac{d\phi}{dx})^2 dx + EC_w \int_0^{L/2} (\frac{d^2\phi}{dx^2})^2 dx \tag{5.36}$$

Now to estimate the parameter a, Equations (5.24), (5.31), and (5.34) of action fulfilled can be used, thus:

$$P_{cr}.\delta_{cr} = \frac{(P_{cr})^2}{2EI_y} \int_0^{L/2} (\frac{L}{2} - x)^2 \phi^2 dx \tag{5.37}$$

Therefore,

$$\delta_{cr} = \frac{(\pi^2 + 6)}{96\pi^2 EI_y} P_{cr} a^2 L^3 \tag{5.38}$$

and

$$a^2 = \frac{96\pi^2 EI_y \delta_{cr}}{(\pi^2 + 6)P_{cr} L^3} \tag{5.39}$$

The lateral displacement δ_{cr} at the critical state can be expressed as a function of the torsional twist at the critical state as [111]:

$$\delta_{cr} = \frac{M_{cr}\phi_{cr}}{P_{cr}} \tag{5.40}$$

Also at $x = 0$ it can be recognized that for simply supported HOWSJ under concentrated load at mid- span , $M = PL/4$, therefore Equation (5.39) can be re expressed as show in the Equation (5.41) below:

$$a = \sqrt{\frac{24\pi^2\phi_{cr}EI_y}{(\pi^2+6)P_{cr}L^2}} = \sqrt{\phi_{cr}}\sqrt{\frac{(24\pi^2EI_y)}{(\pi^2+6)P_{cr}L^2}} \tag{5.41}$$

Substituted Equation (5.41) into Equation (5-.30), taking in the consideration that $tan\phi = \phi$ for small angles, thus the lateral displacement can be expressed as $u = \phi.h_s$, then the following equation can be obtained to estimate the value of the lateral rigidity of the HOWSJ in terms of the slope $(\frac{P}{\sqrt{\phi}})$ of the rotation curve.

$$EI_y = (\frac{P}{\phi.h_s})\frac{\sqrt{\phi}\cdot\sqrt{\frac{24\pi^2EI_y}{(\pi^2+6)P_{cr}L^2}}L^3}{4\pi^2} = (\frac{P}{\sqrt{\phi}})(\frac{a_1.L^3}{4\pi^2h_s}) = k_2(\frac{P}{\sqrt{\phi}}) \tag{5.42}$$

Where: $k_2 = (a_1.L^3)/(4\pi^2h_s)$, and $a_1 = \sqrt{\frac{24\pi^2EI_y}{(\pi^2+6)P_{cr}L^2}}$

5.6 Critical Lateral-Torsional Buckling Load

As mentioned before the estimating of the stiffness of lateral rigidity dependent on the value of critical lateral torsional buckling load, Equation (5.42).

The differential equations of equilibrium describing the lateral-torsional buckling instability, Equation (5.26) have a closed-form solution only for few cases found in practice. Another approach, the strain energy method, Equation (5.36) can be used to investigate the lateral-torsional buckling instability of HOWS joists

by replacing complicated solutions of the differential equations of equilibrium with the calculation of integrals with available solutions [34]. The strain energy method is widely used in lateral-torsional buckling instability in research rather than in practice where higher degree of accuracy is necessary [112].

Also by using the energy method, the extent of the effect of point of load application can be obtained, because it is assumed in the previous derivations that the load P is applied at the centroid of the middle cross section of the beam. It is apparent that the critical value of the load is decreased when the point of application is raised and increased when it is lowered, it is only necessary to take into consideration the additional lowering or raising of the load P during lateral buckling due to rotation of the middle cross section.

Since it was assumed that the load applied to the HOWSJ to derive the equation for the increase in the strain energy in the HOWS joist were applied through the neutral axis, and that the curvature of the HOWS joist used to develop the expressions for the work done by the applied load to the steel joist was the curvature of the neutral axis, so Equation (5.36) can be correctly used only for loads applied at the neutral axis of the joists. Equation (5.36) is widely used in the literature along with adjusting factors to research different loading and supported end conditions on I-beams composed of different structural materials [34]. However, in this research, loading it was applied at the top surface of the top chord of the HOWSJ and therefore the effects of applying the load in a higher position relative to the neutral axis must be investigated . These effects are important for HOWSJs with large depth to width ratio than for shorter joists.

If (c) represent the vertical distance from the neutral axis of the HOWSJ to the point of the applied load, and it was positive when above the centroid, an approximate expression for the work done by the additional displacement that the load undergoes can be obtained by considering the rotation of the cross-

section during lateral-torsional buckling instability of the HOWSJ. By geometry considerations from Figure (5.18 b), Equation (5.43) was derived to account the additional lowering of the load [34].

$$P.c(1-cos\phi) \approx P.c(\phi)^2/2 \tag{5.43}$$

Inserting Equation (5.43) into Equation (5.36), Equation (5.44) was obtained to calculate the critical lateral-torsional buckling load when the load is applied at the top chord flange of the HOWS joist and at any point along the joist span.

$$\frac{Pc(\phi)^2}{2} + \frac{P^2}{4EI_y}\int_0^{L/2}\phi^2(\frac{L}{2}-x)^2dx = GJ\int_0^{L/2}(\frac{d\phi}{dx})^2dx + EC_w\int_0^{L/2}(\frac{d^2\phi}{dx^2})^2dx \tag{5.44}$$

This equation can be solved for the static critical value of P by taking (ϕ) in the form of the series Equation (5.27) for a simply supported beam by using a single term in this equation, the accuracy of the solution is suitable for practical applications [34]. Solving Equation (5.44) [113], the following equation for the static critical lateral-torsional buckling load was obtained for a simply supported HOWSJ.

$$P_{cr} = \sqrt{(\frac{24\pi^2cEI_y}{(\pi^2+6)L^3})^2 + \frac{EI_yGJ + (\frac{\pi hEI_y}{2L})^2}{\frac{(\pi^2+6)L^4}{48\pi^4}}} - \frac{24\pi^2cEI_y}{(\pi^2+6)L^3} \tag{5.45}$$

In this research the load was applied at the top chord of the HOWSJ so that $(c = h/2)$, then Equation (5.45) can be rewritten for a simply supported HOWS joist with the effects of the warping shear stresses as follows:

$$P_{cr} = \frac{\pi^2EI_yh}{L^3}[\sqrt{\frac{144}{(\pi^2+6)^2} + \frac{12}{(\pi^2+6)}(\frac{GJ.L^2}{EC_w}+\pi^2)} - \frac{12}{(\pi^2+6)}] \tag{5.46}$$

5.7 Calculation Results of Lateral Rigidity

The lateral bending stiffness of the HOWS joists was calculated using Equation (5.42). The slope of the load- square root of the rotation curve was taken within the displacement range from (0.1 - 0.25) degrees, this range was chosen in order to avoid initial loading effects due to the attachment of the test specimen with the testing machine. The mean of two specimens for each model was taken to find the value of the lateral rigidity for each model, the results are shown in Table (5-4).

Table 5.4 Theoretical estimation of the lateral rigidity for all models specimens.

Model No.	Slope (P/$\sqrt{\phi}$)	P_{cr}	$EI_y (N.mm^2)$
Model A	335477	$1.271\times10^{-}6EI_y$	2.696×10^{11}
Model B	258689	$1.271\times10^{-}6EI_y$	2.078×10^{11}
Model C	131336	$1.236\times10^{-}6EI_y$	1.071×10^{11}
Model D	554196	$1.786\times10^{-}6EI_y$	2.629×10^{11}
Model E	694635	$1.786\times10^{-}6EI_y$	3.296×10^{11}

When comparing the results shown in Table (5-4) above, it can be noticed that the lateral rigidity of Model A increased by (60.3%) when compared with Model C and by (23 %) when compared it with Model B, the reason for the increased in lateral stiffness for this model may be due to the shape of the cross section used in its manufacture and in which the interior webs were close to the location of the shear centre, which reduced the occurrence of the torsional moment, unlike what happened with the Model B and C, where the interior webs were placed at a distance from the shear centre location of the section. This caused the torsional moment to occur, causing buckling in the horizontal and vertical legs of the top chord, as well as the interior web members. But on the other hand, it was found that the Model B had a greater lateral rigidity by (48.5%) more than Model C, Which made it more stable against the flange distortional buckling than the Model C; the first reason for this increase was the chord width of the model was (100mm) which it was less than the width of Model C specimens, so the interior webs in

this model were closer to the location of the shear center than the Model C, which had a chord width of (200 mm), and the second it was because the top chord was welded together face to face without leaving a distance between them, which made them more restrained members against the local buckling on the top chord legs than Model C top chord which welded together face to face with a gap.

Also, the strength capacity of the joist of Model C specimens was less than Model A and Model B specimens because these HOWSJs had weak slenderness about the y-axis; therefore, the elastic buckling occurred at the top chord when the web just had been buckled, and the compressive stress was increased on the top part of the section (compressive zone). Because the interior webs of the joist failed to support the top chord when the compressive stress has been eliminated, then the tensile stress prevents the movement in a diagonal direction. The Plates (5-2) and (5-3) previously emphasized that the failure of the Model C was due to top chord buckling, while the failure of Model B was due to the interior web buckling and tension field action.

The results in Table (5-4) also explained that the enhancement in lateral rigidity has reached to (20.2%) for the Model E compared with Model D which were they had the same cross section shape but this enhancement was because using the diameter of rebar of the interior web with (15.85 mm) in Model E manufacturing, which may have added a sufficient stability to the section against lateral buckling , while the rebar diameter was (11.97 mm) used to fabricate the interior webs of Model D, which led to the section's behaviour being closer to the behaviour of the slenderness sections.

5.8 Discussion of Rotation and Lateral Deflection Deformations Results

After obtaining the lateral rigidity for each model, it was possible to make a normalized comparison of the different models used in this research, depending on the lateral stiffness that the section has and the ultimate load it has reached, as

shown in the Figures (5-19) and (5-20). These curves of the normalized lateral deflection $(u_{Nor.})$, and normalized rotation deformations $(\phi_{Nor.})$ show the real behavior of all models during the test. where Equations (5.46) and (5.47) was written as shown below depending on Equations (5.30) and (5.42),respectively.

$$u_{Nor.} = (u.\frac{EI_y}{P_u.k_1}) \tag{5.47}$$

$$\phi_{Nor.} = (\sqrt{\phi}.\frac{EI_y}{P_u.k_2})^2 \tag{5.48}$$

where; P_u: the ultimate load capacity for each model.

From Table (5.5), Figure (5.19), and Figure (5.20) it can be recognized that the Model D specimens had a maximum rotation at ultimate load about (13.2%) more than the specimens of Model E, because the interior webs of Model D were manufactured from rebar of diameter (11.97 mm), which made the slenderness ratio of the diagonal interior web members of Model D more than from that for Model E by about (24.48%).

And the rotation of Model D were more than the rotation of Model A specimens by (42.5%), Also the rotation of Model E specimens were (33.8%) more than of Model A, that's because the models D and E were had a span to the depth ratio L/D of 3.6, which made them behaved as a deep beams. While Model A specimens were had a span to the depth ratio L/D of 5.1.

Regarding the specimens of models A, B, and C, which they had the same L/D ratio of 5.1, it can be observed that the lateral deformations of Model A specimens was more than Model B specimens about (19.2%) for rotation and about (21.9%) for lateral deflection. And also Model A specimens were more than specimens of Model C by (25.1%) for rotation and about (30.7%) for lateral deflection.

Consequently, the specimens of Model B were more than Model C specimens deformations by about (7.3%) for rotation and (11.2%) for lateral deflection deformation. Although the top chord legs of Model C specimens model were subjected to a local buckling before reaching to the ultimate capacity of these joist specimens, this buckling was occurred because their top chord flanges were welded face to face with a gap between them, which made the horizontal leg of the angles of the top chord behaved as an unrestrained members against the distortional buckling.

Through the previous comparisons, it can be concluded that the cross section for the Model C, in which the shape of the top and bottom chords of the HOWSJ was face to face with gab and welded together at equal spacing was more stable against the lateral deformations than Model A and Model B specimens.

Also, it can be concluded that in the case of manufacturing this type of HOWSJ for all three cross section shape, rebar with a larger diameter must be used in the event that the height of the joist increases in order to avoid the local buckling that occurs in the diagonal interior web which had a higher slenderness ratio.

Table 5.5 Normalized lateral deflection and rotation deformations for all models specimens.

Model No.	$u_{Nor.}$	$\phi_{Nor.}$
Model A	7.497	7.609
Model B	5.849	6.147
Model C	5.197	5.702
Model D	11.225	13.235
Model E	10.114	11.488

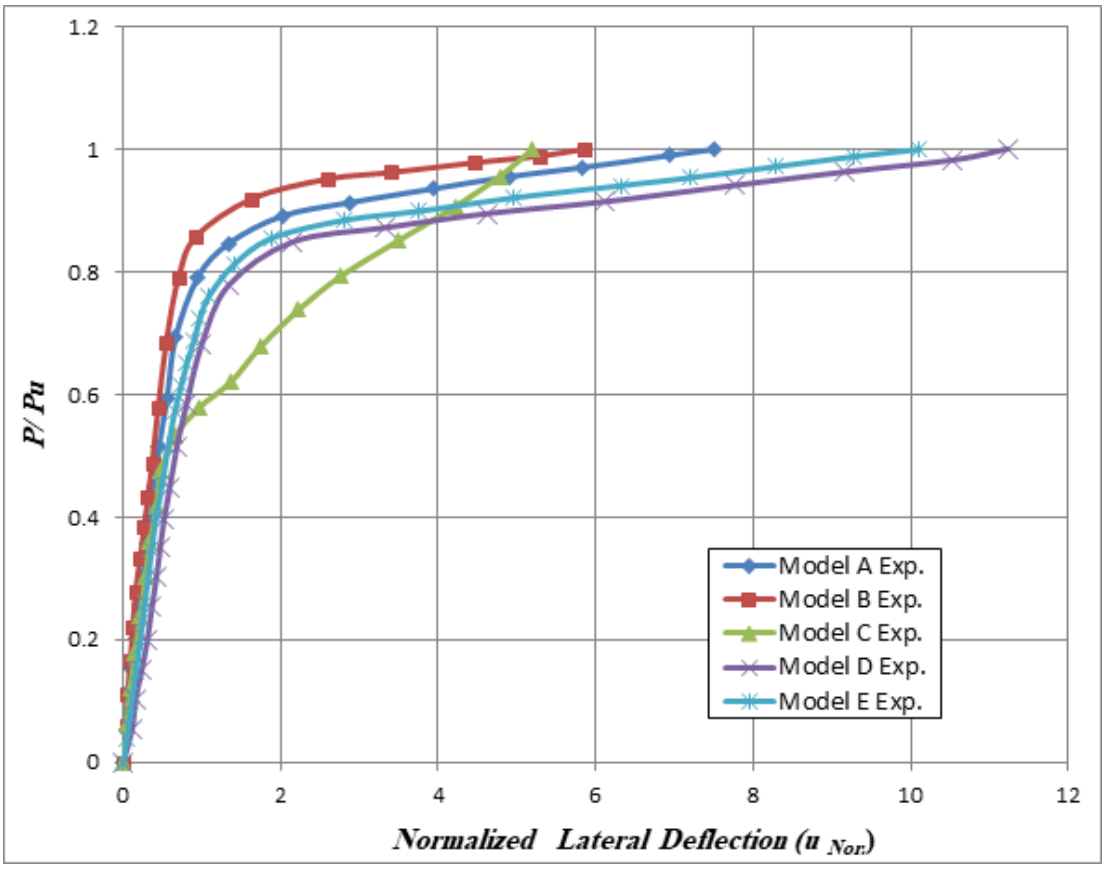

Figure 5.19 Normalize load- lateral deflection curves for all models.

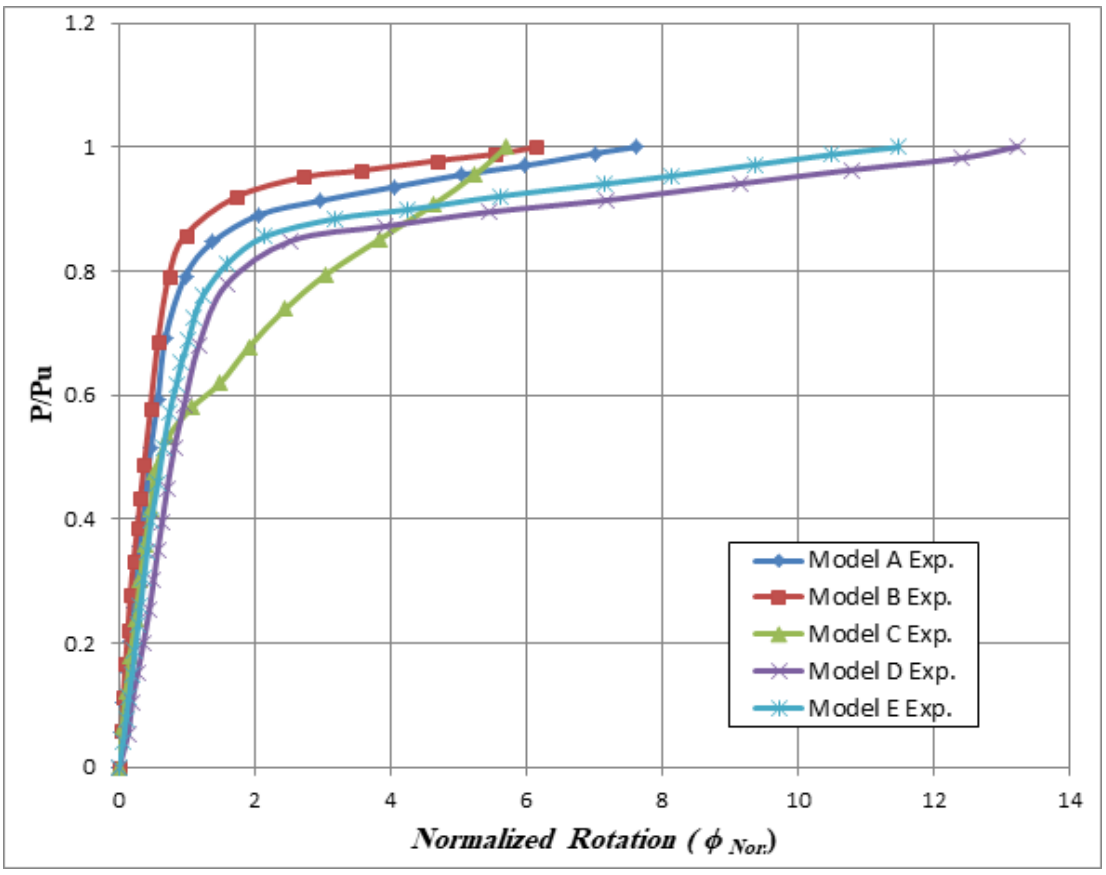

Figure 5.20 Normalize load-rotation curves for all models.

CHAPTER 6

FINITE ELEMENT ANALYSIS

6.1 Introduction

The present study implemented a finite element analysis for the HOWS joist Models and composite open web steel joists. The numerical results are compared with the experimental results.

(ABAQUS) finite element program was used to perform this analysis, the ABAQUS /CAE is the Complete ABAQUS Environment that provides a simple, consistent interface for creating ABAQUS models, interactively submitting and monitoring ABAQUS jobs, and evaluating results obtained from ABAQUS simulations. The comparison between the finite element program analysis and the experimental test was made in terms of the load capacity, deflection, strains, and stress distribution.

6.2 Finite Element Modeling

The commercial software ABAQUS/CAE 2019 various tasks were should be performed to develop the three-dimensional Finite Element models of the HOWS joists and composite open web steel joists as follows:

• Sketching 3D geometry and creating seven different parts including two chords (top and bottom), vertical column-like members, welds (three types) as shell, interior webs as a beam element, and eight-node three-dimensional solid element for concrete slab.

• Defining the material properties (for angels, rebar, welds, WWF, and concrete) and section properties of the each created parts.

• Assembling the model according to the final fabricated details.

• Configuring the analysis procedure and output requests.

• Applying loads and boundary conditions to the model.

• Mesh the parts separately.
• Creating a job and submit it for analysis.
• Viewing the results of the analysis.

The kind of analysis steps available in ABAQUS/Explicit were general analysis steps, which can be used to analyze linear or nonlinear problems. Also, elements were used to model the interactions and contact behavior, which were mainly general contact, contact pair, and interface elements.

6.2.1 Element Type

In this study were different components of the HOWSJ and composite open web steel joist should be modeled such as steel joist, welded joints, concrete slab, welded wire mesh, and shear connectors. Thus, these components were meshed using different types of elements, Figure (6-1) show the elements types were used in this study, also Figure (6-2) illustrate the element types with final model shape of the composite open web steel joist . These types of elements are explained in the following sub sections.

6.2.1.1 Top and Bottom Chords and Vertical Angles at the Ends of the Joist

(S4R) is a 4-node shell element with reduced integration was a suitable element used to model the steel top and bottom chords, and the vertical angles at the ends of the HOWSJ. This element has six degrees of freedom (three translations and three rotations).

S4R is a 4-node, quadrilateral, stress/displacement shell element with reduced integration and a large-strain formulation. These elements allow transverse shear deformation. They use thick shell theory as the shell thickness increases and become discrete thin shell elements as the thickness decreases; the transverse shear deformation becomes very small as the shell thickness decreases. They also account for finite membrane strains and arbitrarily large rotations. This element

types can be degenerated to triangles. Reduced integration with hourglass control was used in this modeling to reduce running time.

6.2.1.2 Interior Web Members

A beam element type (B31) with size (0.001m) was used to model the vertical and diagonal interior web members for the HOWSJ models. Timoshenko beams (B31 and its "hybrid" equivalent) allow for transverse shear deformation. They can be used for thick "stout" as well as slender beams. For beams made from uniform material, shear flexible beam theory can provide useful results for cross-sectional dimensions up to 1/8 of typical axial distances or the wavelength of the highest natural mode that contributes significantly to the response. ABAQUS assumes that the transverse shear behavior of Timoshenko beams is linear elastic with a fixed modulus and, thus, independent of the response of the beam section to axial stretch and bending. For most beam sections ABAQUS will calculate the transverse shear stiffness values required in the element formulation. The Timoshenko beams can be subjected to large axial strains. The axial strains due to torsion are assumed to be small. In combined axial-torsion loading, torsional shear strains are calculated accurately only when the axial strain is not large.

The effective transverse shear stiffness of the section of a shear flexible beam is defined in ABAQUS as [114]:

$$\bar{K}_{\alpha 3} = f_P^{\alpha} K_{\alpha 3} \tag{6.1}$$

Where $\bar{K}_{\alpha 3}$:is the section shear stiffness in the -direction; f_P^{α}: is a dimensionless factor used to prevent the shear stiffness from becoming too large in slender beam elements: $K_{\alpha 3}$:is the actual shear stiffness of the section, which have units of force; and $\alpha = 1.2$, which represent the local directions of the cross-section.

The dimensionless factors f_P^α are always included in the calculation of transverse shear stiffness and are defined as:

$$f_P^\alpha = l/(1 + \xi * SCF(l^2 A)/(12 I_{\alpha\alpha})) \tag{6.2}$$

where l: is the length of the element, A: is the cross-sectional area, $I_{\alpha\alpha}$: is the inertia in the α-direction, SCF: is the slenderness compensation factor (with a default value of 0.25), and ξ: is a constant of value (1.0) for first-order elements and (10^{-4}) for second-order elements.

6.2.1.3 Welding

A four-node shell element (S4R) with size (0.001-0.0025m) was used to model all welded points were used in experimental work in this study.

6.2.1.4 Welded Wire Mesh (WWF) and Shear Connectors

The welded wire mesh and shear connectors were modeled with two-node three-dimensional linear truss elements (T3D2). They were modeled as embedded rebar element in the region surrounding the concrete.

6.2.1.5 Concrete Slab

The eight-node continuum three-dimensional brick element named (C3D8R) with reduced command integration which is available in ABAQUS. This element has three degrees of freedom at each node, translations in x, y, and z direction. And is capable of modeling material and geometrical nonlinearities in addition to large deformations[114]. Reduced integration technique which is adopted by ABAQUS for solid and shell elements was selected to reduce higher order solid requirements without impacting the accuracy of recorded responses. Hourglass problems which is normally happened with continuum linear solid elements are taken into account for this element type.

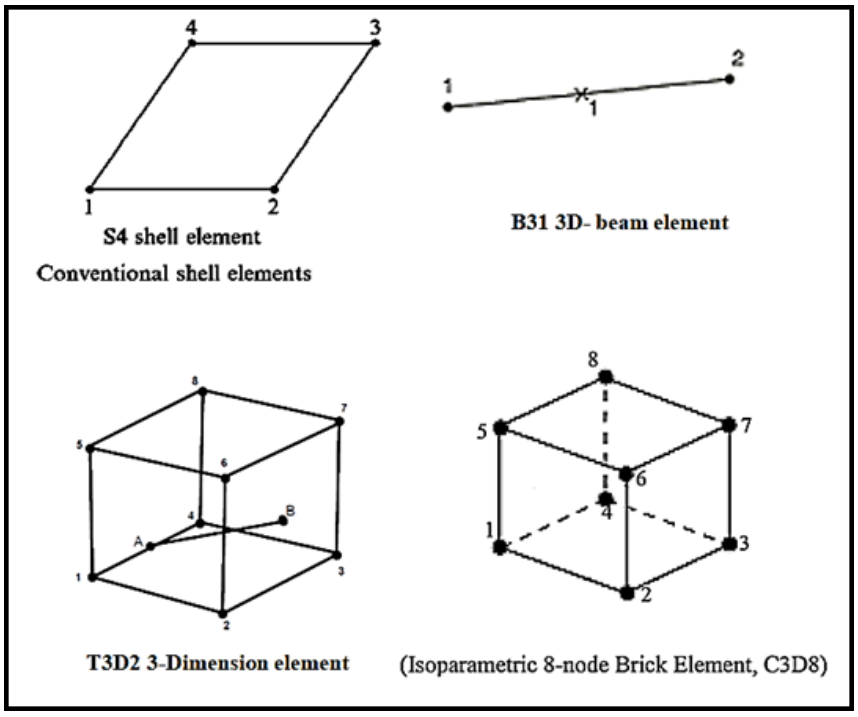

Figure 6.1 Geometry of ABAQUS elements used in this study.

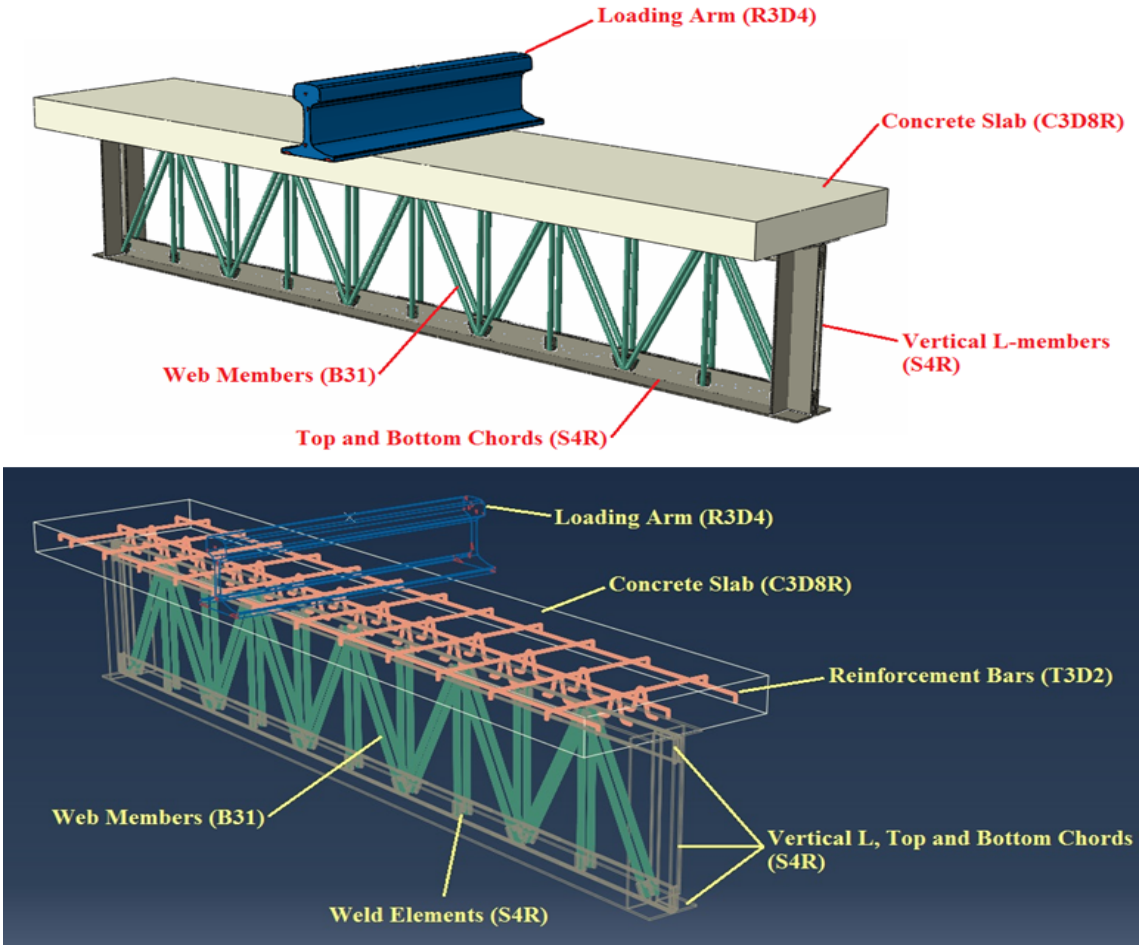

Figure 6.2 Details of the finite element mesh type used for modeling the composite OWS joists in this study.

6.2.2 Creating Material Modeling in ABAQUS

The present work included modeling of all types of materials which were used in the experimental work of this study such as steel angles, reinforcing bar, welding, shear connectors, WWF reinforcement, NC and SFRC concrete. The properties and characteristics for every type of these materials obtained from the experimental tests were assigned to their corresponding listed in the material module in (CAE) file of ABAQUS program for each specimen.

6.2.2.1 Steel Modeling

The composite open web steel joists which studied in this work had different elements and sizes of steel materials, namely, angles, interior webs of reinforcement steel, welding, shear connectors, and WWF reinforcement. In order to define steel materials in ABAQUS, elastic and plastic behavior parameters must represented. When ductile metals are loaded beyond elastic range, the initial linear stress response will give way to a complicated nonlinear response, characterized by a much-reduced modulus and different stress behavior along load and unloading path. The turning point of an idealized stress-strain curve in uniaxial tension is called elastic limit, the corresponding stress F_y is called the yield stress. Finite element elastic-plastic analysis is much more delicate than simple elastic analysis. In this study all the members of the composite open web steel joist are made of different steel and assumed to be elastoplastic with Poisson's ratio of 0.3, density of ($7850 kg/m^3$). Young's modulus was measured experimentally for angles, steel plates, and reinforcing bars, and it was taken of ($200 GPa$) as typical values for other components. For each material, three behaviors including "density, elastic and plastic", were used. To define the plastic behavior, the engineering stress –strain relation extracted from tensile test of steel material should be converted to a true relation through using the equations (6.3) and (6.4). True stress and the logarithmic strain should be described according to Hibbit et al [115].

$$\sigma_{true} = \sigma_{nominal}(1 + \epsilon_{nominal}) \tag{6.3}$$

$$\epsilon_s^{pl} = \epsilon_s^t - \epsilon_s^{el} = \epsilon_s^t - (\sigma_s^t / E_s) \tag{6.4}$$

where

ϵ_s^{pl}: is true plastic strain in steel. ϵ_s^t: is true total strain in steel.

ϵ_s^{el}: is true elastic strain in steel. σ_s^t: is true stress in steel.

E_s: is elastic modulus of elasticity of steel.

6.2.2.2 Concrete Modeling (NC and SFRC)

The concrete analysis in the ABAQUS/CAE software program was represented on three models; standard when vulnerable concrete cracks, standard and explicit when concrete prone to damage plasticity, and finally explicit when concrete behaves as a brittle crack [114].

The model concrete damage plasticity was being dominant in the present analysis to represent the concrete in ABAQUS. Where this model was used in ABAQUS/ Standard and also in ABAQUS/Explicit. The inputs of ABAQUS software require compression and tension stress-strain relationships to define the behavior of the concrete material [116].

However, the damaged plasticity model (CDP), or discrete-crack approach was conducted for modeling concrete, which was provided quasi-brittle materials. In this model, capable of representing the inelastic behavior of concrete depends on the combination of isotropic tensile and compressive plasticity. Material properties of concrete which were defined in chapter three were used here. Also, this model takes in account the degradation in the material stiffness and the effect of stiffness recovery under cyclic loading. Therefore, there are two variables related to the damage mechanism in compression and tension should be defined, dc and dt , respectively. These variables change in limits (from 0 to 1) where zero mean un

damaged material and 1 refers to completely lost for material strength. In this study the Density of concrete was used equal to ($2.4 ton/m^3$) and the Poisson's ratio was (0.2).

6.2.2.3 Behavior in Compression

The compressive behavior for concrete under uniaxial compressive load is firstly linear until initial yield point (σ_{co}), in the second stage stress hardening occurs until reaching the ultimate compressive stress value (σ_{cu}), finally the last stage which is strain hardening. The flowing equations were used to calculate the damage parameters d_t (at tension) and d_c (at compression) [117]:

$$d_t = 1 - (\sigma_t/\sigma_{tu}) \tag{6.5}$$

$$d_c = 1 - (\sigma_c/\sigma_{cu}) \tag{6.6}$$

A standard stress-strain relation of uniaxial concrete compressive in the finite element model show in Figure (6.3). In current study, the results of the experimental stress-strain curves at compression which plotted in chapter four, Figure (4-26) was used to represent the concrete types (NC and SFRC) behavior in ABAQUS by using a relation that suggested by Saenz [118],[119]. In order to provide the required data for CDP model in compression the experimental stress-strain curves must be converted to stress-inelastic strain relations. The inelastic strain can be calculated by equation (6.7):

$$\epsilon_c^{in} = \epsilon_c - \epsilon_c^{el} \tag{6.7}$$

where

$\epsilon_c^{el} = (\sigma_c/E_c)$.

ϵ_c^{in}: inelastic strain in concrete. ϵ_c: total strain in concrete.

ϵ_c^{el}: elastic strain in concrete. σ_c: stress in concrete.

E_c: elastic modulus of elasticity of concrete.

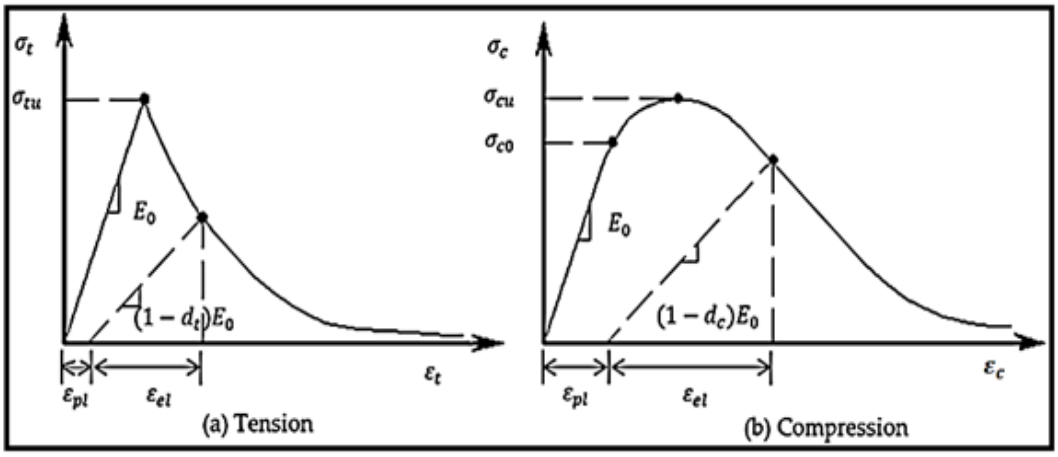

Figure 6.3 Concrete response to uniaxial loading based on manual of the ABAQUS theory [112].

6.2.2.4 Behavior in Tension

Three different methods to represent tension softening behavior of concrete in ABAQUS, which are: stress - strain relation, stress -displacement relation or using fracture energy (G_f) [115]. In the present study, stress–strain relationship of concrete in tension was modeled by using a relation that suggested by Massicotte et al. [120], as explained in Figure (6.4). As in compression behavior, stress-strain curves in tension were converted to stress-inelastic strain relations.

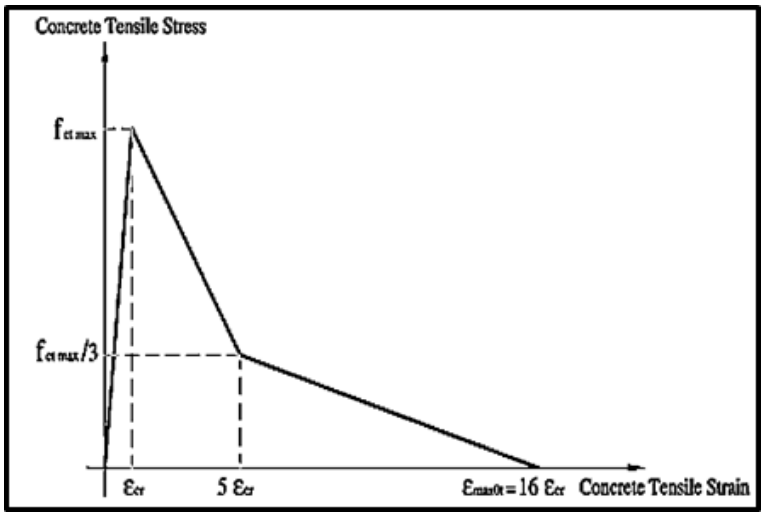

Figure 6.4 Tension softening curve proposed by Massicotte et al.[118]

6.2.2.5 Plasticity Parameters

The required plasticity parameters for the CDP model in ABAQUS are:

* The dilation angle ψ, which is the ratio of volume strain to shear strain, which ranges from 0° to 56.3° [121]. Increasing value of ψ means that the specimen has higher ductility and strength. For normal concrete, the dilation angle in the range of 30° to 40° was suggested to obtain the best agreement with the experimental responses. Upper values are more ductile behavior, whereas lower values are more brittle. According to Malm [122], better agreement was reached with the experimental findings for dilation angles between 30^0 to 40^0 and for normal concrete ψ equal 30^0 considers suitable.

* Eccentricity (ϵ), which defines the change rate of plastic flow potential function, the default value of the flow potential eccentricity is 0.1 in the ABAQUS software. Rising this value increases the curvature of the flow potential.

* The ratio $(\frac{\sigma_{bo}}{\sigma_{co}})$, which is the ratio between the bi-directional compressive yield stress to the stress-strain compressive yield stress. The default value of this ratio in ABAQUS is 1.16.

* The parameter (K_c), which is the ratio of the second stress invariant in the tensile meridian to compressive meridian and the value of K_C is in range (0.5-1) and its default value that used in ABAQUS is 2/3.

* The viscosity parameter (μ), which represents the viscosity parameter which is used in ABAQUS to improve the convergence. Its default value was zero.

6.2.3 Interaction and Constraints Modeling between Surfaces.

To assign the characteristics of the interaction between any two contacted components of the studied models in ABAQUS, great care must be taken. Because the composite open web steel joist models contain more than two components, the assignment of interactions and constraints between various surfaces allowed models proximity to accurately simulate the observed behavior of the tested

HOWSJs and COWSJs specimens from the experimental work, Figure (6.5). The modeled was done in various ways, as specified below, :

6.2.3.1 Contact Interaction

A surface to surface contact interaction between the lower surface of concrete slab and the upper surface of top chord was applied. A hard contact property was specified in the direction normal to the interface plane, while a friction mode was chosen in the tangential direction so as to avoid occurring penetration into each other. For tangential behavior, the penalty method was used with a coefficient of friction 0.6 [123], while for normal interaction where hard contact was chosen also the separation after contact was allowed in the model of interaction as recommended by Prakash et al. [75]. The top surface of steel flange was modeled as (master), and the lower surface of the concrete slab was modeled as (slave). It is worth mentioning that the interaction type was a (surface to surface contact- standard) when modeling specimens.

Additionally, a contact interaction was used to specify the rigid body surfaces as master surfaces for the contact applications of the loading cylinder and steel I-beam, which were utilized in this study for the analysis of the HOWSJs and composite OWSJs, respectively. The direction of the master surfaces' outward normal is critical for proper detection of contact, the stress will be transmitted from the steel cylinder and I-beam to the top surface of concrete. These contact surfaces could play an important function in communication with their nearest neighbors, therefore; specifying this step accurately is considered imperative state, the external surface of steel loading was considered as (master) surface, while upper surface of concrete slab is considered as (slave) surface.

6.2.3.2 Embedded Region

The welded wire mesh was modeled by using an embedding bond technique provided in ABAQUS, which was considered as an embedded element and the host object was the concrete slab, as shown in Plate (6-1), where the cross-sectional area of WWF and spacing between bars were defined previously. This technique was used to achieve deformation coordination between the contact surfaces.

6.2.3.3 Tie Constraint

To simulate the contact between the top chord and shear connectors as well as the contact between the chords, welding, and interior web members, a tie constraint technique was used. The master surface and slave surface to be defined properly so the adjacent nodes would be contacted completely on both surfaces, as shown in Plate (6-2).

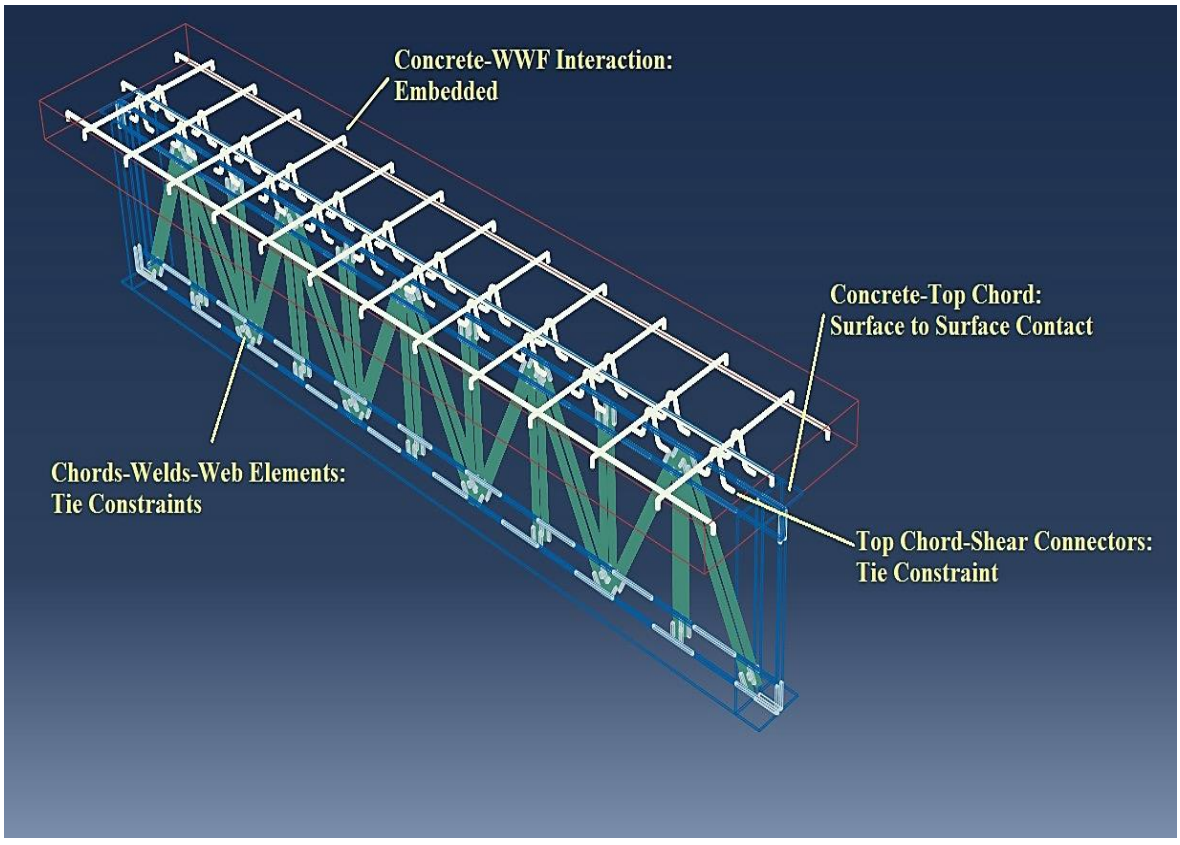

Figure 6.5 Contact interaction of the joist's components.

Plate 6-1 Defining of embedded region and host region.

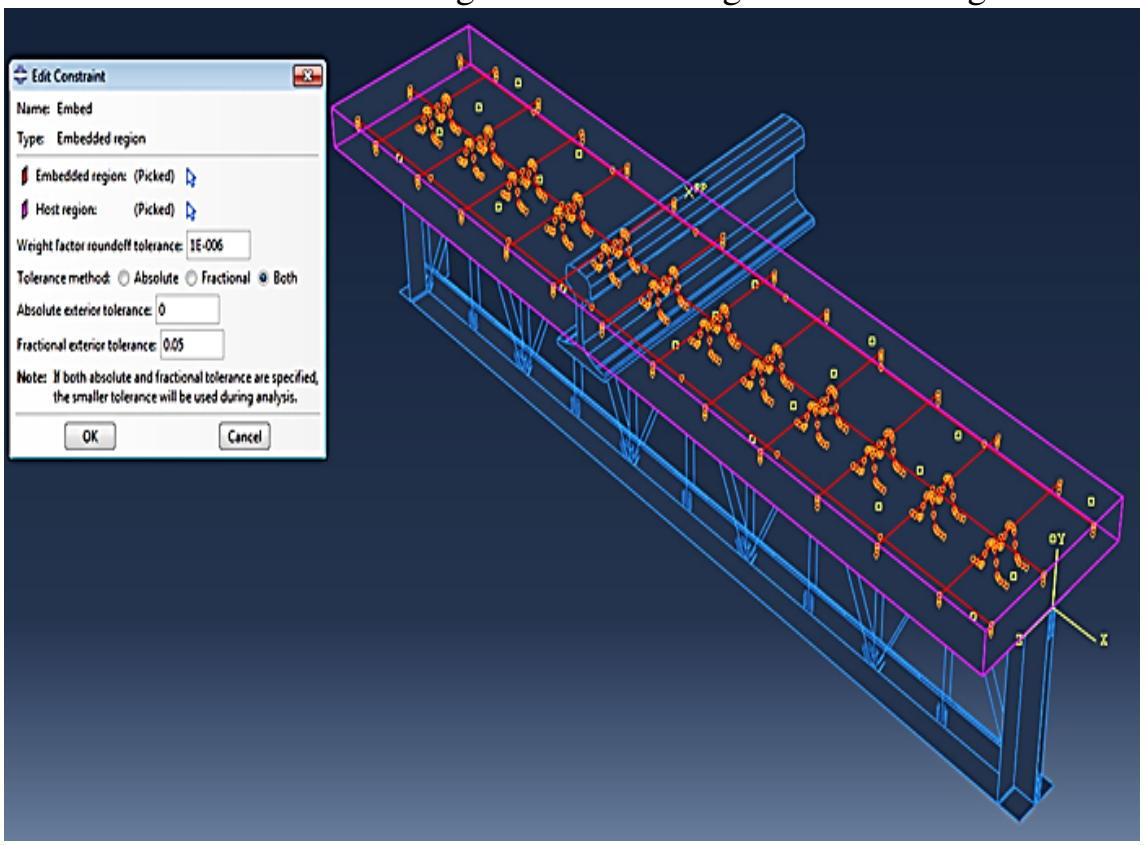

Plate 6-2 Defining of tie constraints of shear connectors.

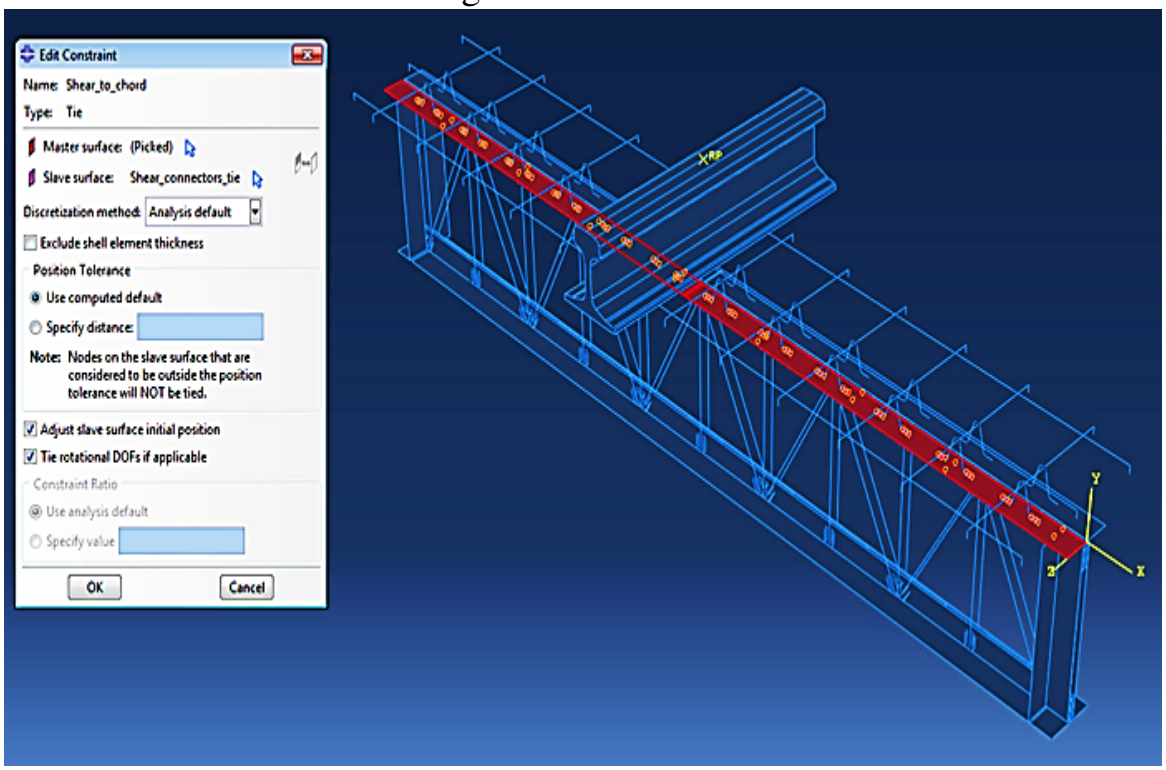

6.2.4 Loading and Boundary Conditions Applications

A “Rigid elements” R3D4 which are 4-node, bi linear quadrilateral rigid elements that can be used in three-dimensional analysis to represent the loading application in this study. The positive normal for R3D4 elements is given by the right-hand rule going around the nodes of the element in the order that they are given in the element’s connectivity. In this simulation a loading cylinder and the loading steel I-beam which used in this study for HOWSJs and composite OWSJs, respectively were applied in the negative 2-direction to the top center of the joist as a contact interaction. The boundary conditions were performed to simulate the experimental test conditions. The ends of the HOWS joists and composite OWS joists were supported vertically and laterally. Plates (6-3) and (6-4) show the Loading and boundary condition was conducted in the present analysis for HOWSJs and composite OWSJs, respectively.

Plate 6-3 Loading and boundary conditions of HOWSJ.

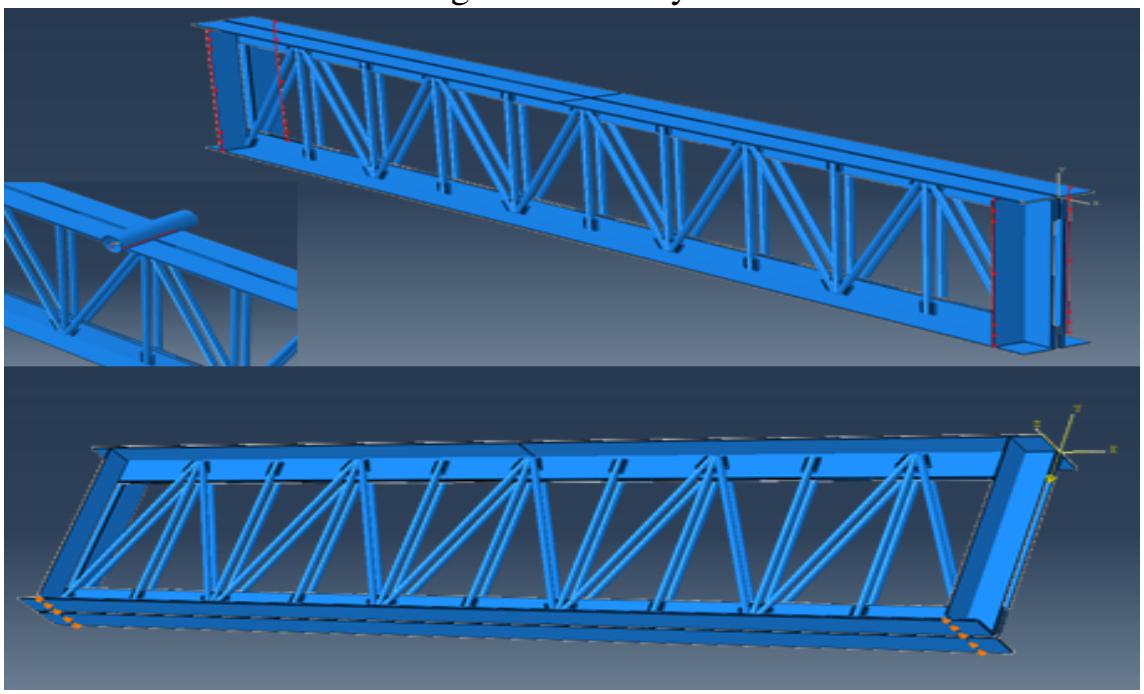

Plate 6-4 Loading and boundary conditions of composite OWSJ.

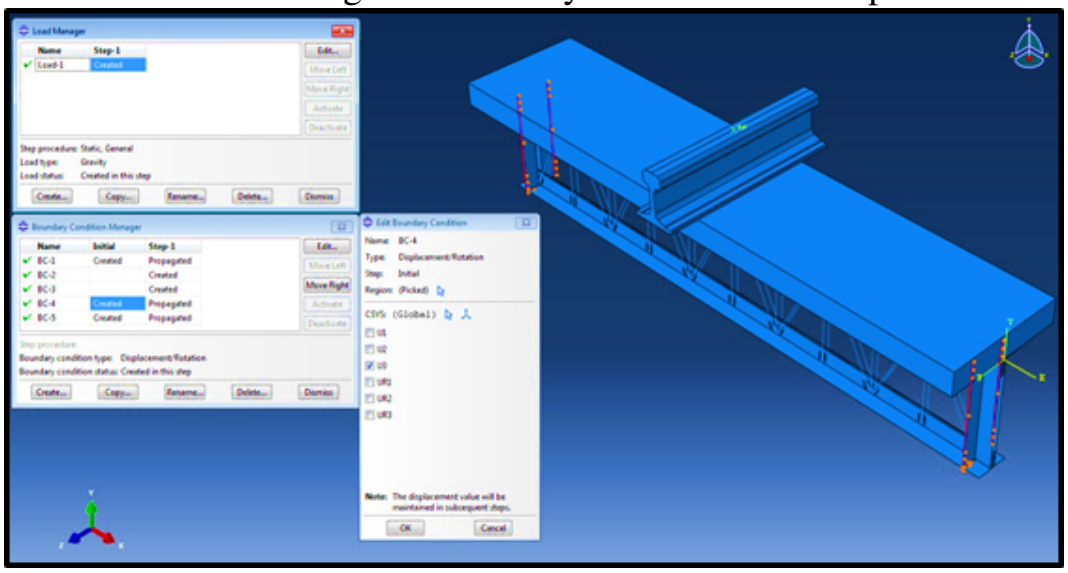

6.2.5 Creating the Mesh

A prior study was conducted to choose an appropriate mesh size for HOWS joist models based on the computational effectiveness and accuracy in comparison to the experimental results. As a result, the elements in the sizes of 5mm S4R for angels, 1mm B31 for interior web members, 0.5mm R3D4 for loading cylinder and I-beam, 1-2.5mm S4R for welds, and 25mm C3D8R for concrete were used. Final each meshed HOWSJ model have about (23377 nodes) and (22413 elements). The finite element mesh appearance for COWSJ shown in Plate(6-5).

Plate 6-5 Meshing of the composite OWS joist's components.

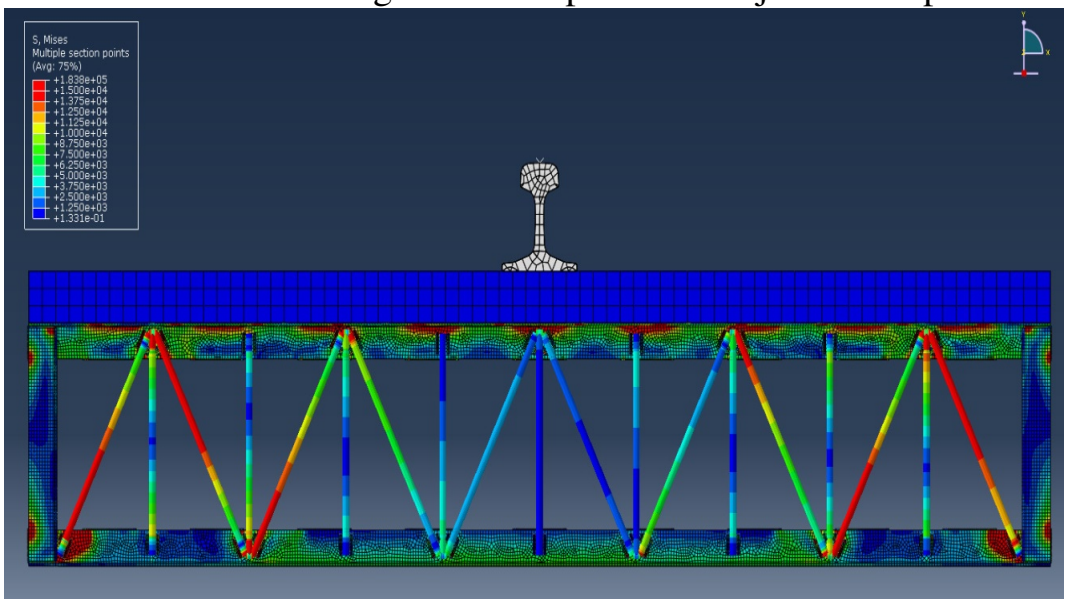

6.3 Finite Element Analysis Results and Comparison

All experimental works were modeled to analyze by performing the finite element method and using the ABAQUS software program. The purpose of employing finite element method generally for simulating the experimental program carried out in the present study. Furthermore, for verifying if that analysis can be performed on HOWSJS and composite OWSJS, where it is characterized by reliability, the quick, and cost effectively; in addition of obtaining more information about stresses.

6.3.1 Hybrid Open Web Steel Joists Results

The finite element results of the HOWS joists subjected to monotonic loading are presented in terms of load-mid span deflection curves, load- strain curves, ultimate loads, deflections at the ultimate load, failure mode, distribution of stresses, and lateral torsional buckling results.

6.3.1.1 The Load-Mid Span Deflection Curves of HOWSJs

The results of the numerical analysis, which were performed by the ABAQUS program, were compared with the experimental results of deflection versus load relationship. The comparative curves show a good agreement between the finite element analyzes curves and the experimental curves for all Models specimens, as explained in Figures from (6.6) to (6.10). The mode of failure and the out of plane deformation was coincided between the experimental results and numerical analysis for all Models, as explained in Figures from (6.11) to (6.15).

The ultimate loads and deflections at ultimate loads predicted by the finite element analysis simulation and the experimental results were listed in Table (6-1) and (6-2), respectively. From the comparisons illustrate in these tables it can be observed that the relative difference between the experimental ultimate load and that achieved by ABAQUS is less than (8%). While the biggest difference in the mid span deflection values not exceed (10.72%) between the numerical and

experimental results. This suggested that the finite element models were able to assess the capacity of HOWSJ joists with reasonable accuracy.

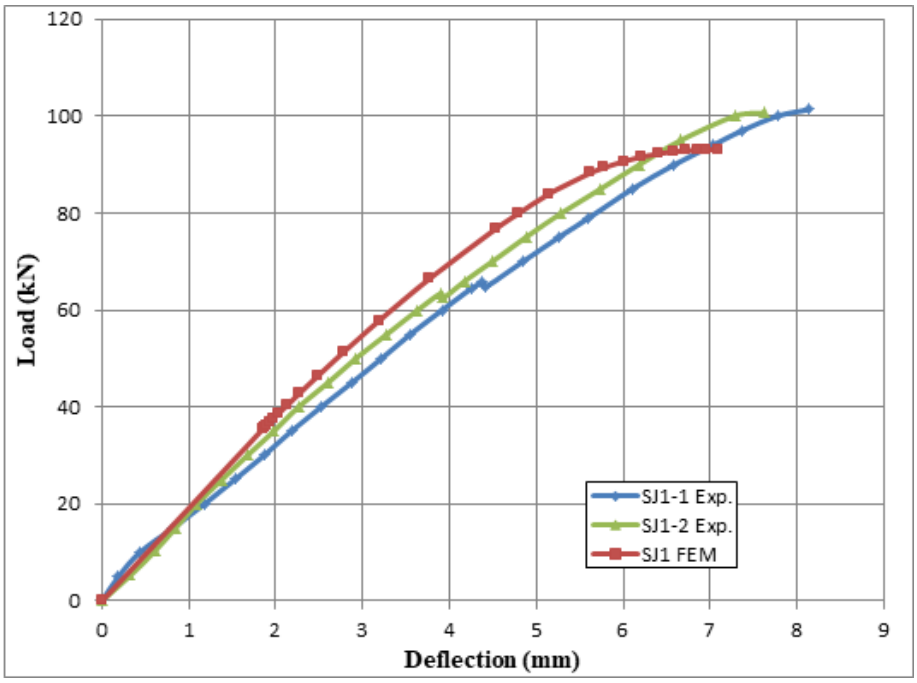

Figure 6.6 Comparison of experimental and finite element load-deflection curve for model A specimens.

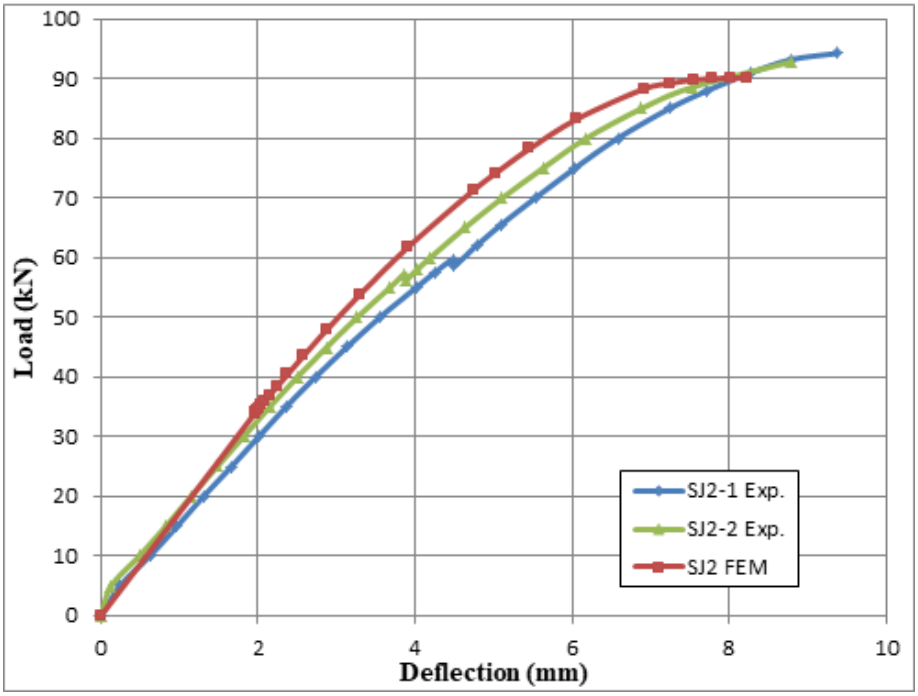

Figure 6.7 Comparison of experimental and finite element load-deflection curve for model B specimens.

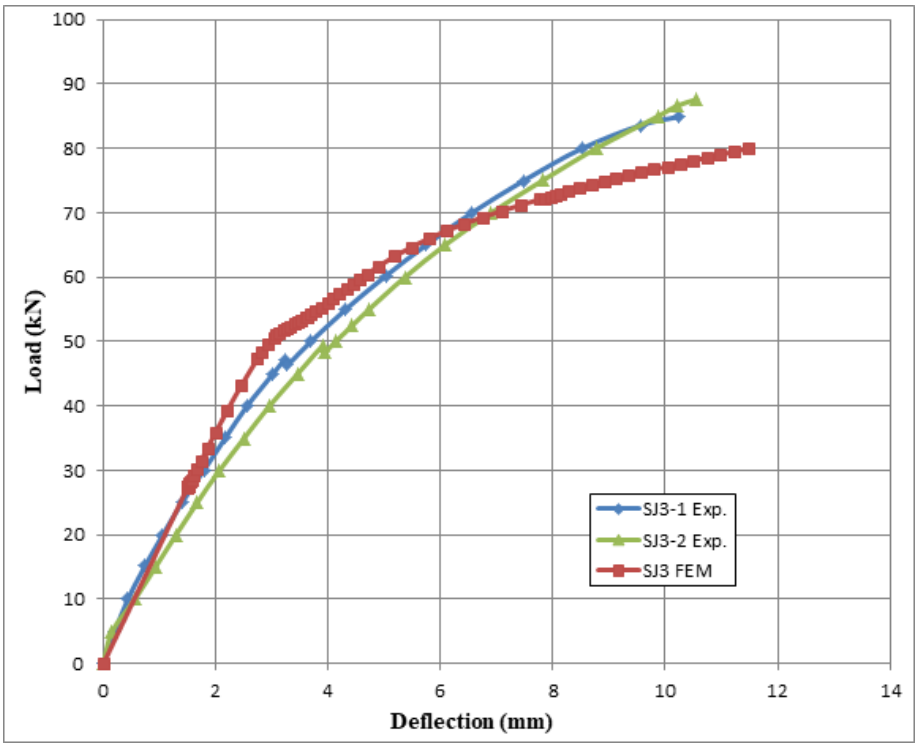

Figure 6.8 Comparison of experimental and finite element load-deflection curve for model C specimens.

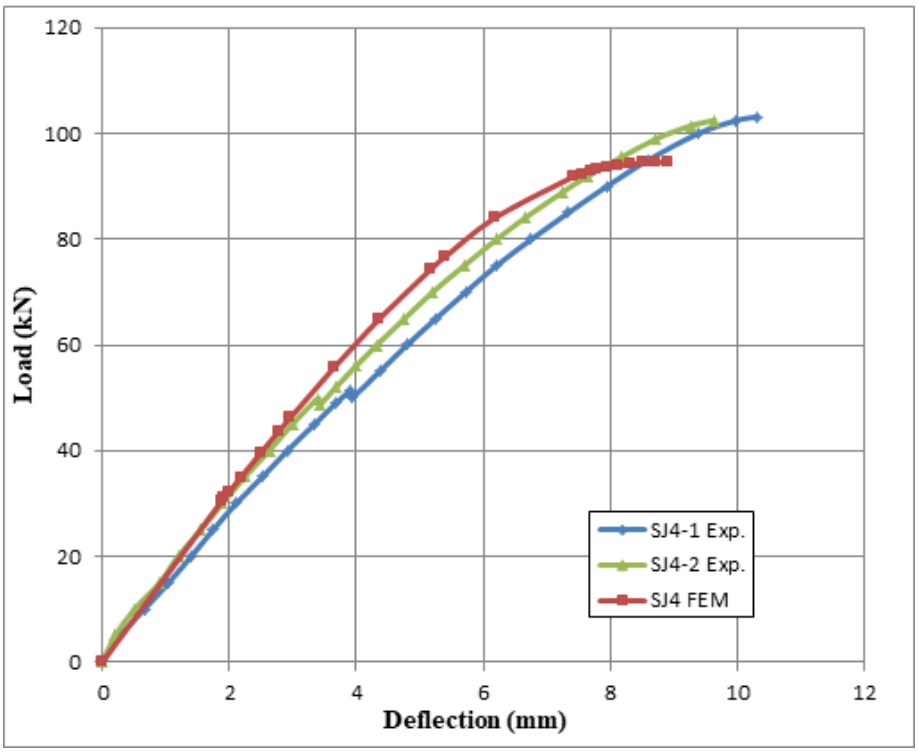

Figure 6.9 Comparison of experimental and finite element load-deflection curve for model D specimens.

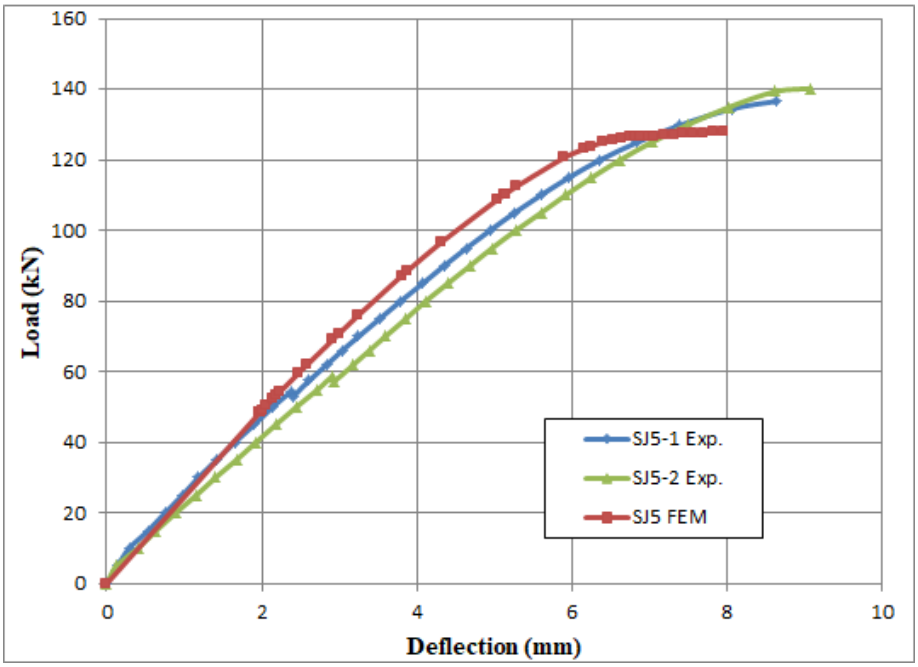

Figure 6.10 Comparison of experimental and finite element load-deflection curve for model E specimens.

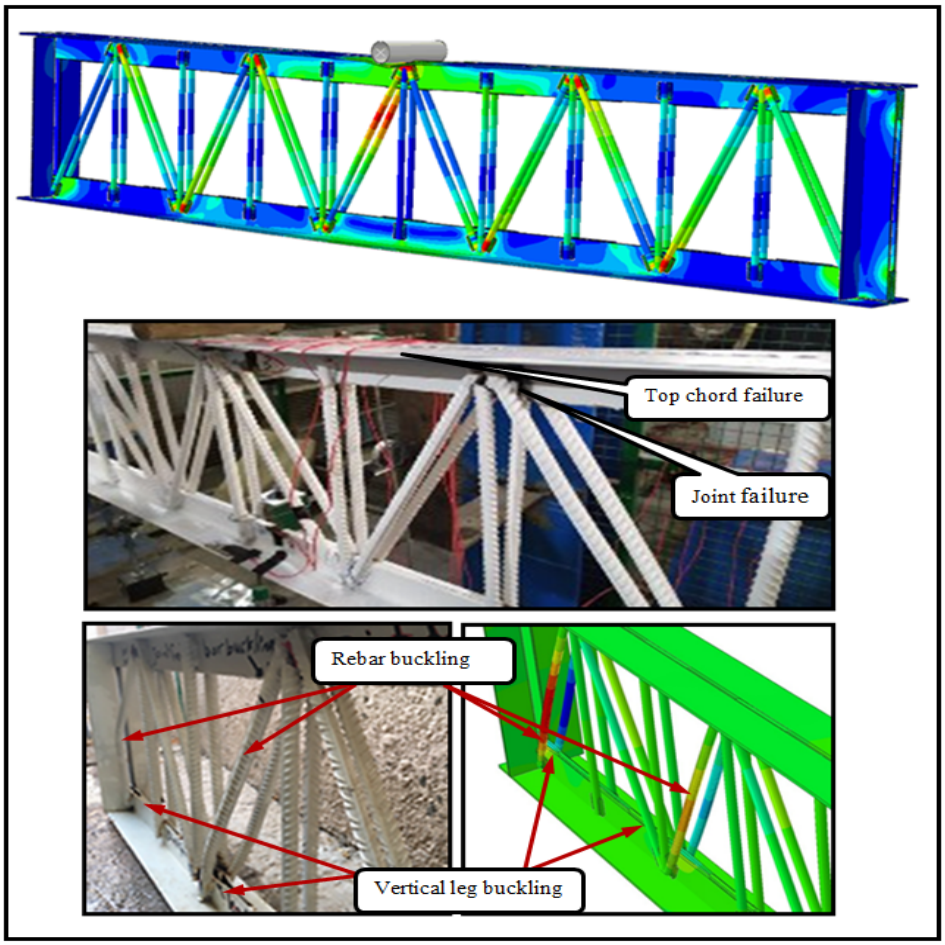

Figure 6.11 Failure shape of the numerical and experimental tests for Model A.

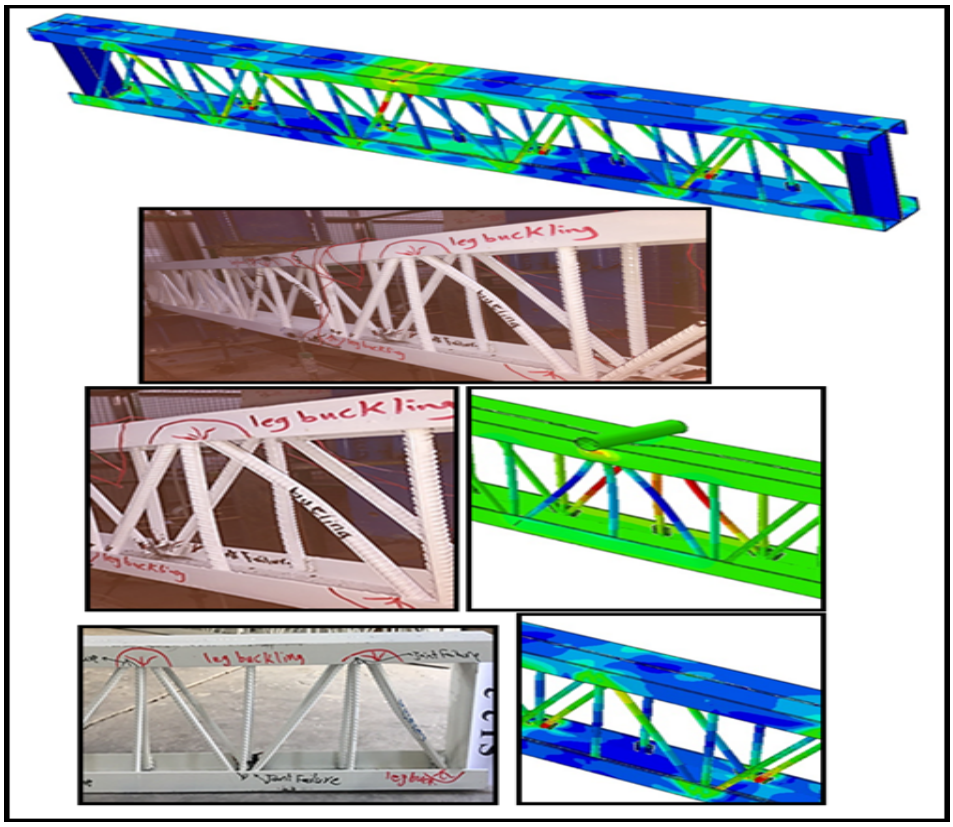

Figure 6.12 Failure shape of the numerical and experimental tests for Model B.

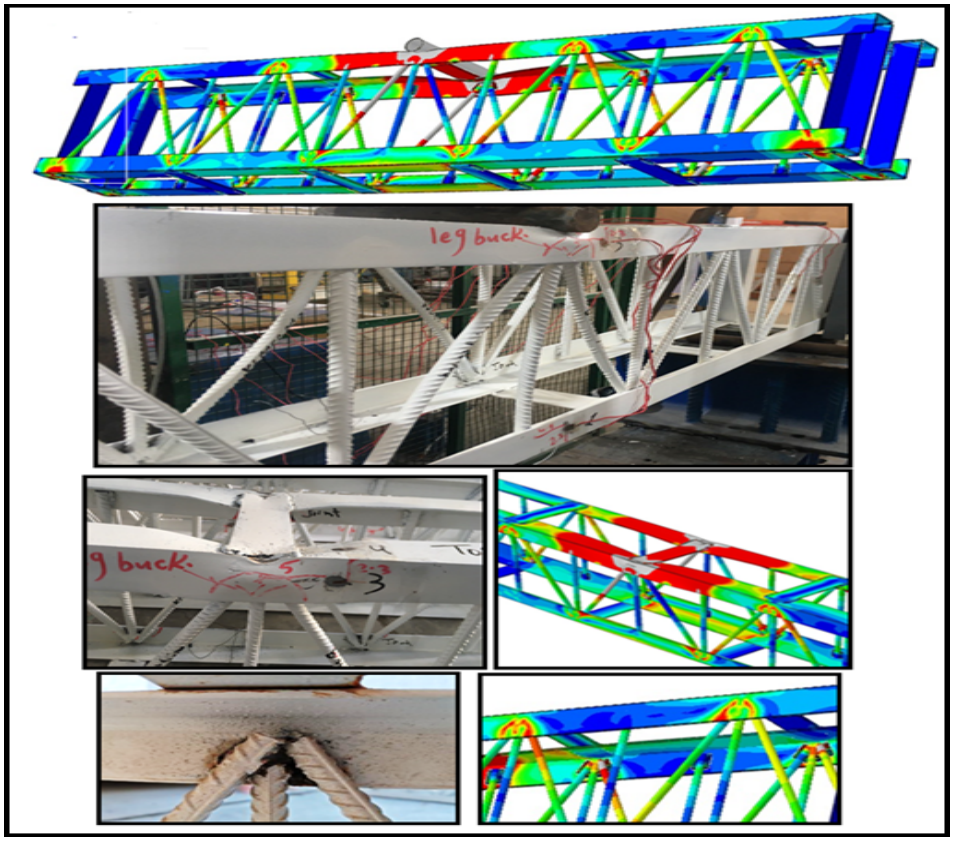

Figure 6.13 Failure shape of the numerical and experimental tests for Model C.

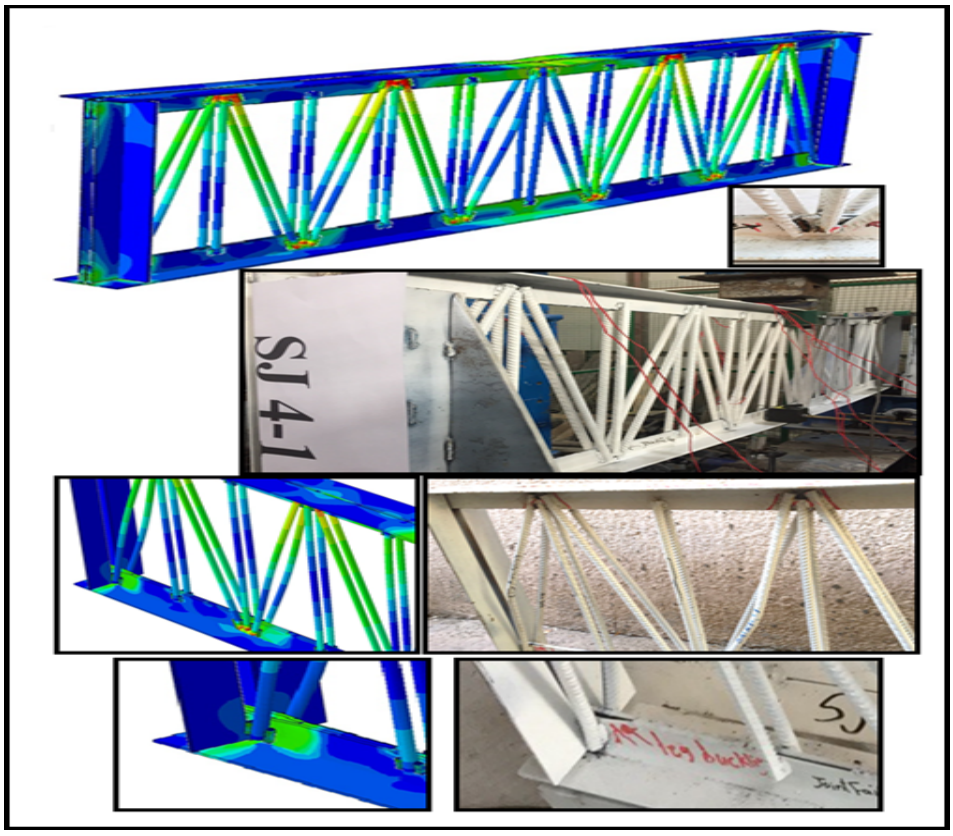

Figure 6.14 Failure shape of the numerical and experimental tests for Model D.

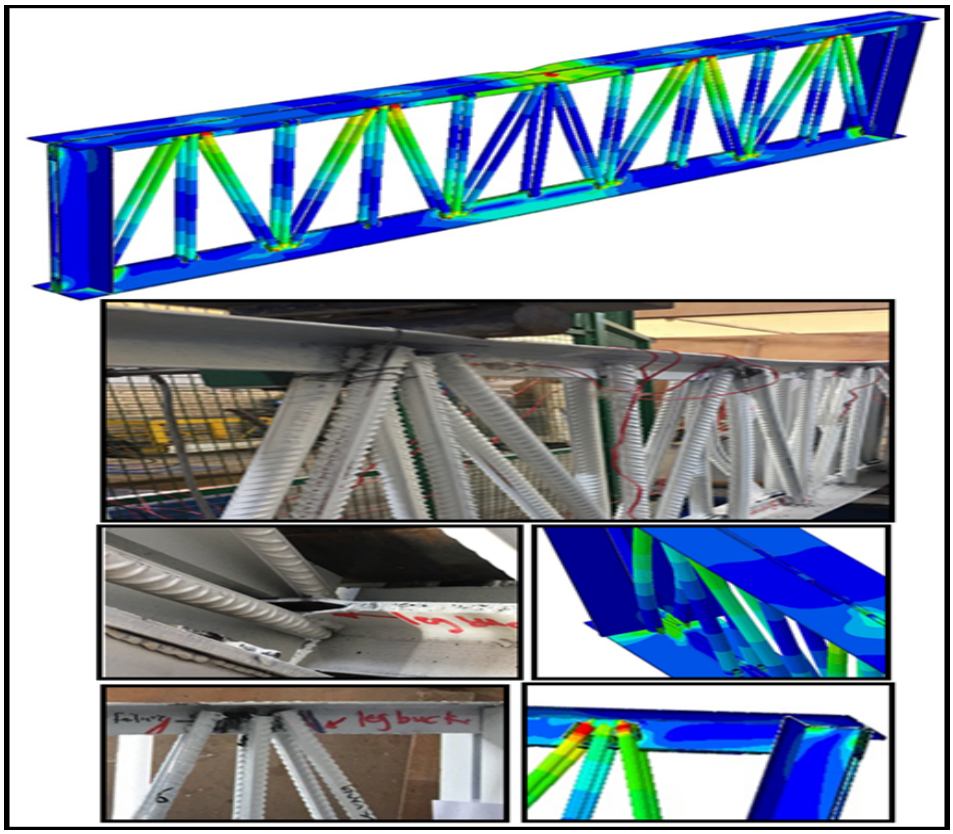

Figure 6.15 Failure shape of the numerical and experimental tests for Model E.

Table 6.1 Comparison between experiments and FEM of ultimate loads for HOWSJs.

Models	Specimens No.	Experimental Ultimate Load (kN)	Mean Exp. Ultimate Load (kN)	FEM Ultimate Load (kN)	Relative Difference (%)
Model A	SJ 1-1	101.34	100.99	93.12	7.79
	SJ 1-2	100.65			
Model B	SJ 2-1	94.24	93.53	90.16	3.60
	SJ 2-2	92.81			
Model C	SJ 3-1	84.97	86.31	79.96	7.35
	SJ 3-2	87.65			
Model D	SJ 4-1	103.16	102.85	94.65	7.97
	SJ 4-2	102.54			
Model E	SJ 5-1	136.59	138.91	127.97	7.88
	SJ 5-2	140.23			

Table 6.2 Comparison between experiments and FEM of mid span deflections for HOWSJs.

Models	Specimens No.	Experimental Deflection (mm)	Mean Exp. Deflection (mm)	FEM Deflection (mm)	Relative Difference (%)
Model A	SJ 1-1	8.056	7.80	7.07	9.36
	SJ 1-2	7.544			
Model B	SJ 2-1	9.367	9.07	8.24	9.15
	SJ 2-2	8.782			
Model C	SJ 3-1	10.251	10.41	11.47	-10.18
	SJ 3-2	10.562			
Model D	SJ 4-1	10.311	9.98	8.91	10.72
	SJ 4-2	9.6428			
Model E	SJ 5-1	8.626	8.85	7.96	10.06
	SJ 5-2	9.075			

6.3.1.2 Load-Strain Relations of HOWSJs

Figures From (6.16) to (6.30), show a comparison between the experimental results and numerical analysis for the strain curves for all models. It can be noticed that the overall behavior was converged, so the model of the finite element analysis can simulate the behavior of HOWS in a good manner.

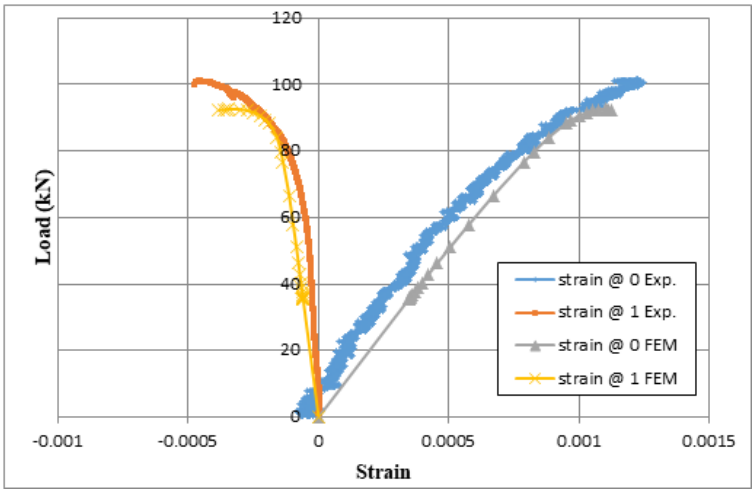

Figure 6.16 Comparison of experimental and finite element load-strain curve of bottom chord for Model A HOWSJ specimens

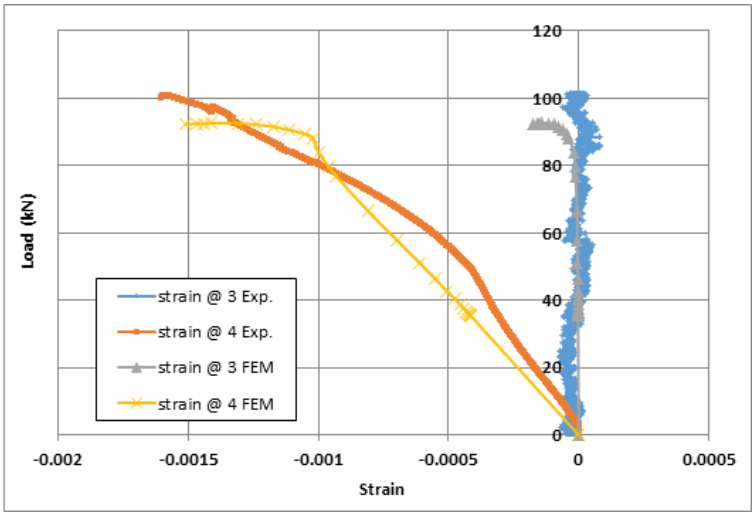

Figure 6.17 Comparison of experimental and finite element load-strain curve of top chord for Model A HOWSJ specimens.

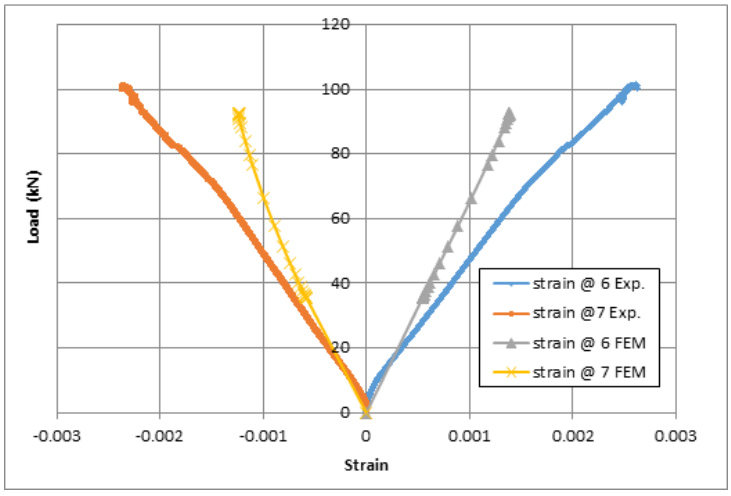

Figure 6.18 Comparison of experimental and finite element load-strain curve of the diagonal interior webs for Model A HOWSJ specimens.

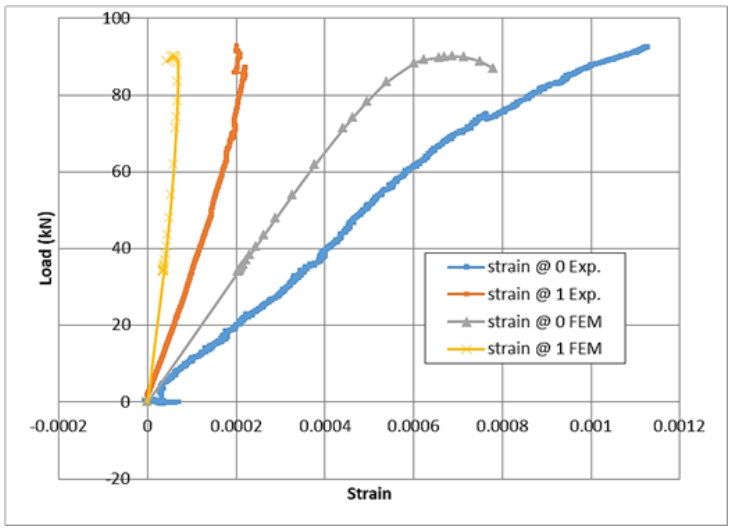

Figure 6.19 Comparison of experimental and finite element load-strain curve of bottom chord for Model B HOWSJ specimens.

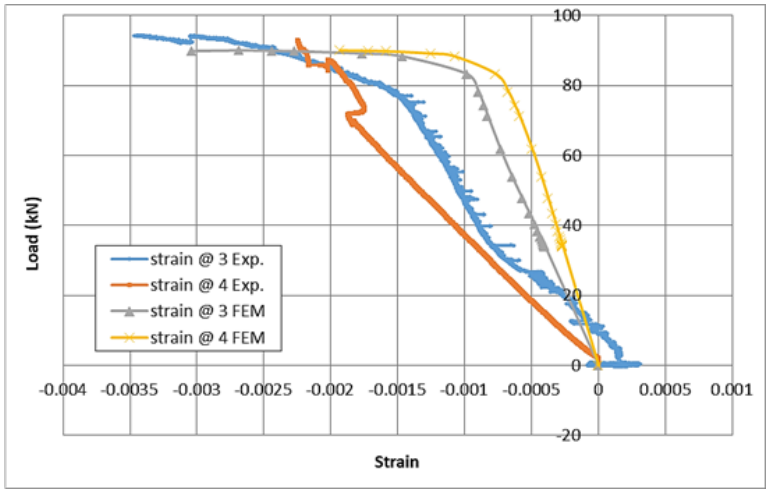

Figure 6.20 Comparison of experimental and finite element load-strain curve of top chord for Model B HOWSJ specimens.

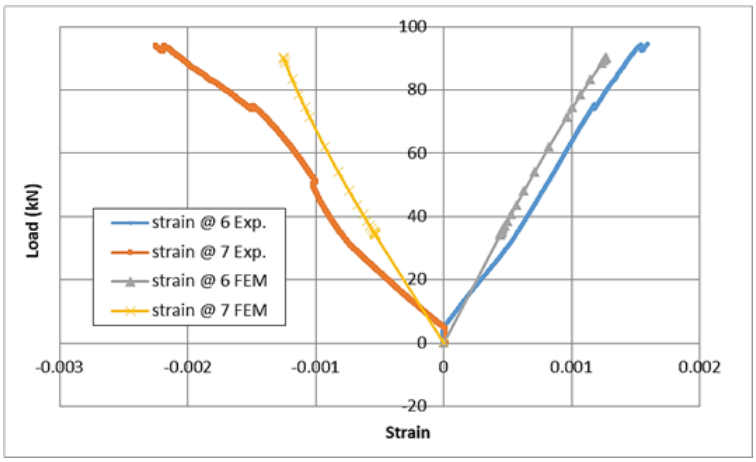

Figure 6.21 Comparison of experimental and finite element load-strain curve of the diagonal interior webs for Model B HOWSJ specimens.

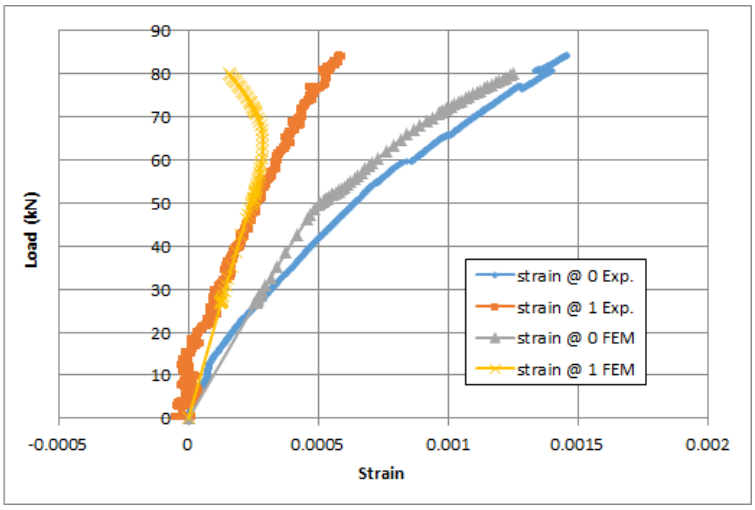

Figure 6.22 Comparison of experimental and finite element load-strain curve of bottom chord for Model C HOWSJ specimens.

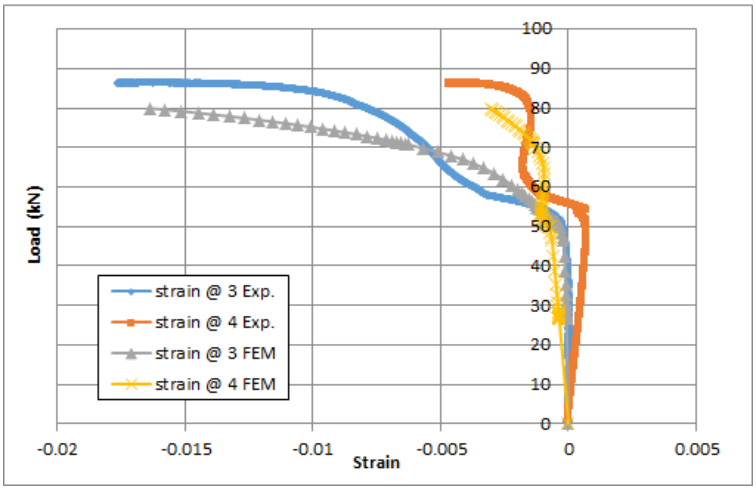

Figure 6.23 Comparison of experimental and finite element load-strain curve of top chord for Model C HOWSJ specimens.

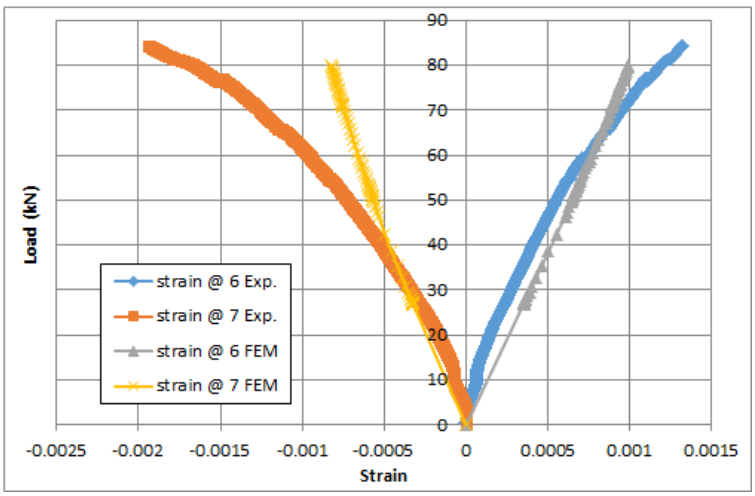

Figure 6.24 Comparison of experimental and finite element load-strain curve of the diagonal interior webs for Model C HOWSJ specimens.

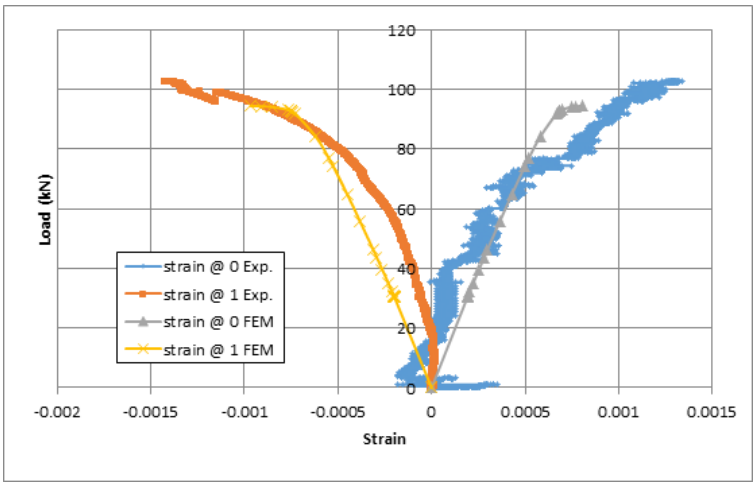

Figure 6.25 Comparison of experimental and finite element load-strain curve of bottom chord for Model D HOWSJ specimens.

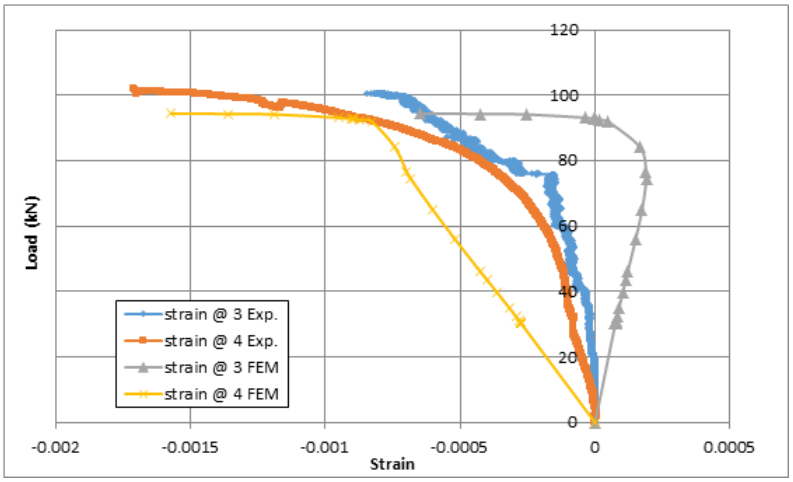

Figure 6.26 Comparison of experimental and finite element load-strain curve of top chord for Model D HOWSJ specimens.

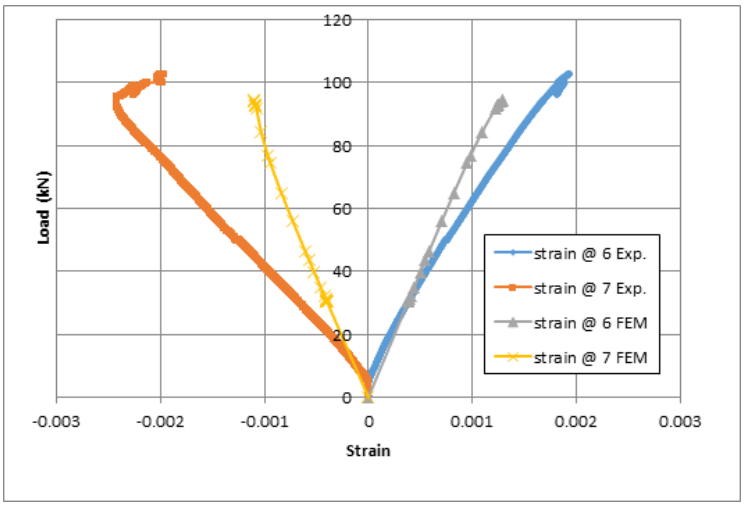

Figure 6.27 Comparison of experimental and finite element load-strain curve of interior diagonal webs for Model D HOWSJ specimens.

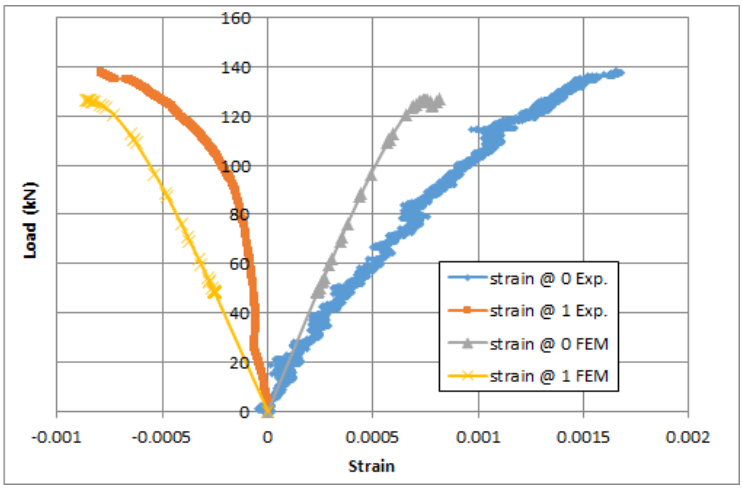

Figure 6.28 Comparison of experimental and finite element load-strain curve of bottom chord for Model E HOWSJ specimens.

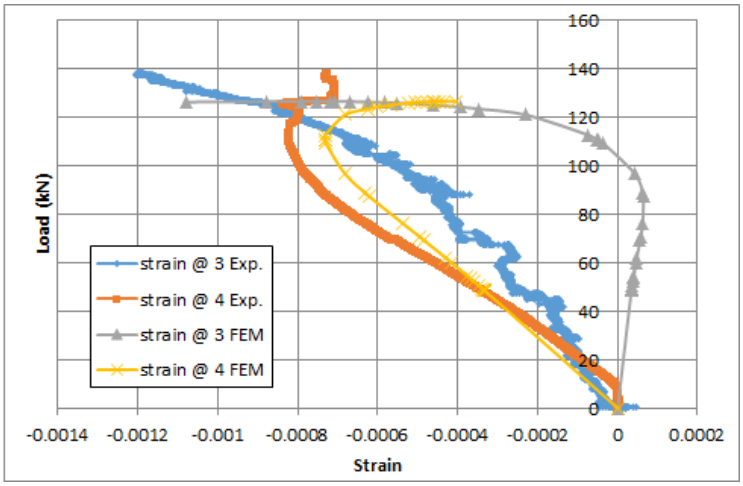

Figure 6.29 Comparison of experimental and finite element load-strain curve of top chord for Model E HOWSJ specimens.

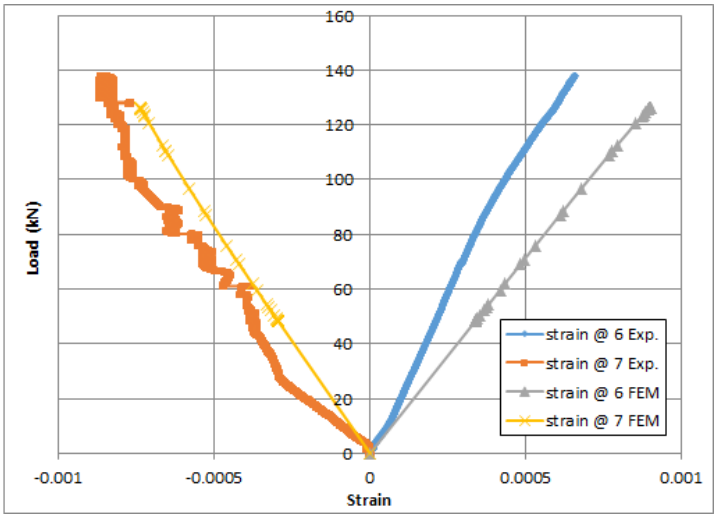

Figure 6.30 Comparison of experimental and finite element load-strain curve of the diagonal interior webs for Model E HOWSJ specimens.

6.3.1.3 Von Mises Stress Distribution of HOWSJs

The stress distribution through the components of the tested HOWS joists is not an easy task in the laboratory, therefore the numerical analysis is employed herein to obtain a precise mapping of it. Von Mises stress distribution was used to show high stresses zones for each specimen as presented in Figure (6.31).

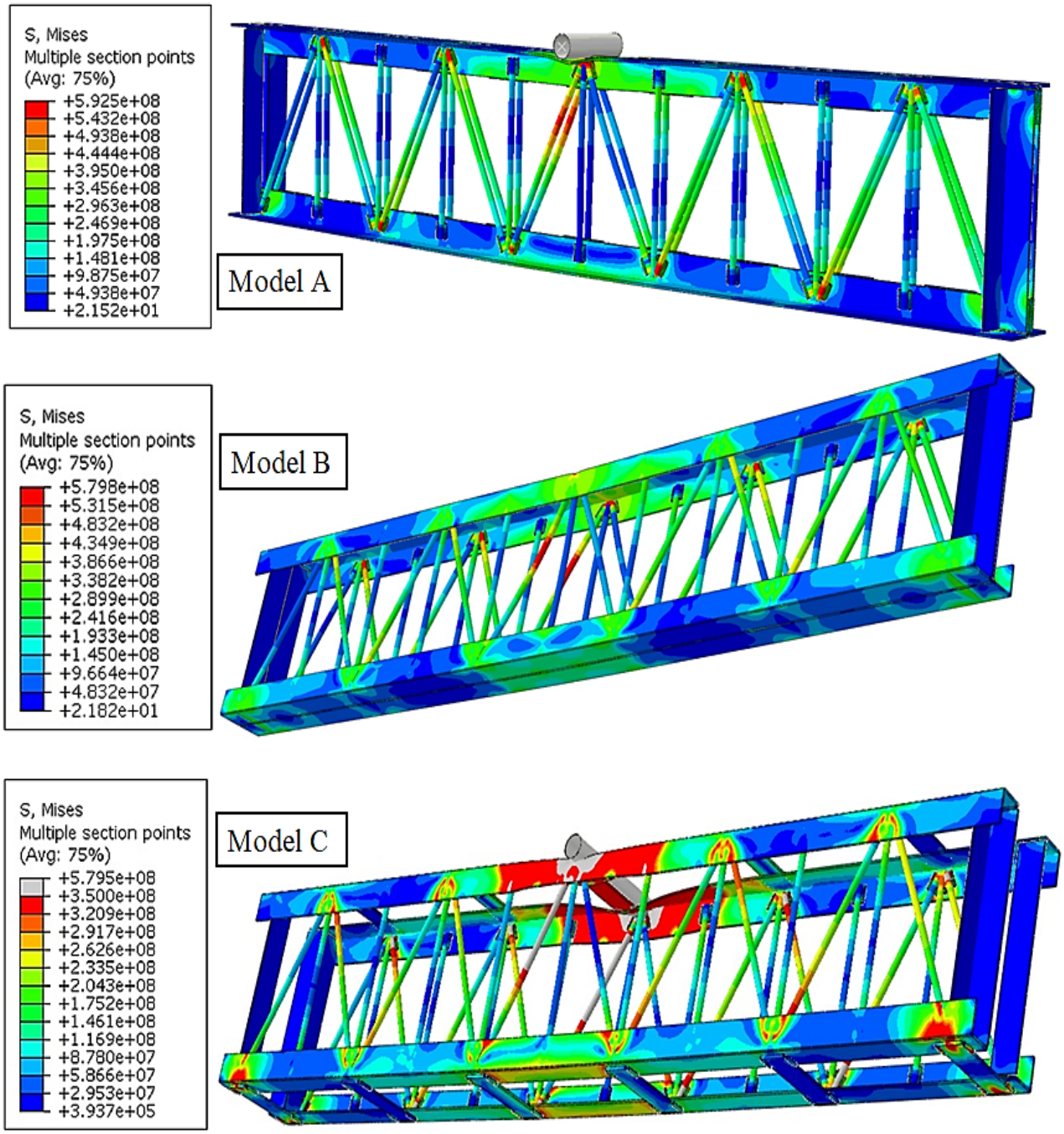

Figure 6.31 Von Mises analysis for All the HOWS Joist Models.

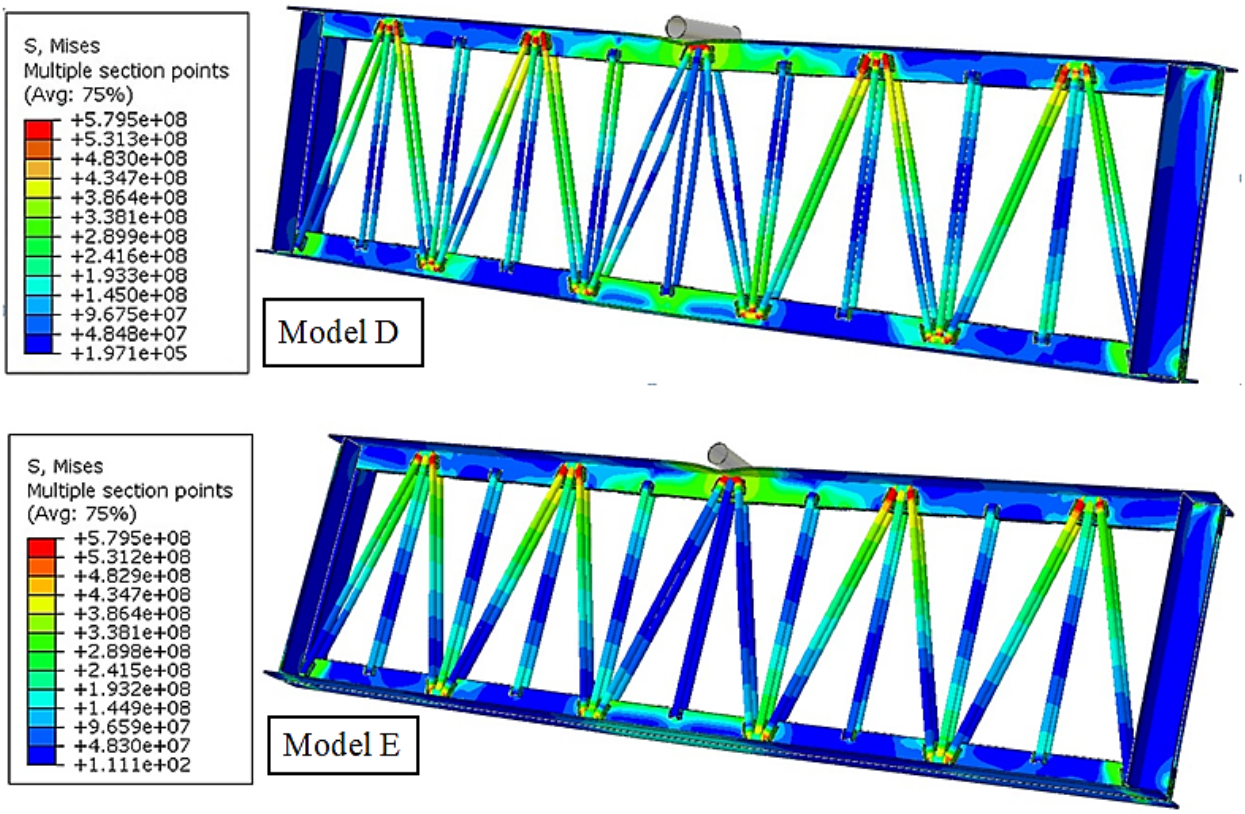

Figure 6.31 Continued.

6.3.1.4 Lateral Torsional Buckling Results of HOWSJs

Lateral torsional buckling of HOWS joists was analyzed by finite element method, the comparison between the results of experimental works and numerical analysis showed a good convergence in the results of the lateral deflection and angle of rotation of the HOWSJ for all models used in this study, as shown in Figures (6.32) to (6.41).

From the comparisons illustrate in Tables (6-3) and (6-4) it can be observed that the relative difference between the experimental lateral deflection and that achieved by ABAQUS is less than (6%). While the biggest difference in the angle of rotation values not exceed (8.87%) between the numerical and experimental results. This suggested that the finite element models were able to assess the L.T.B behavior of HOWSJ joists with reasonable accuracy.

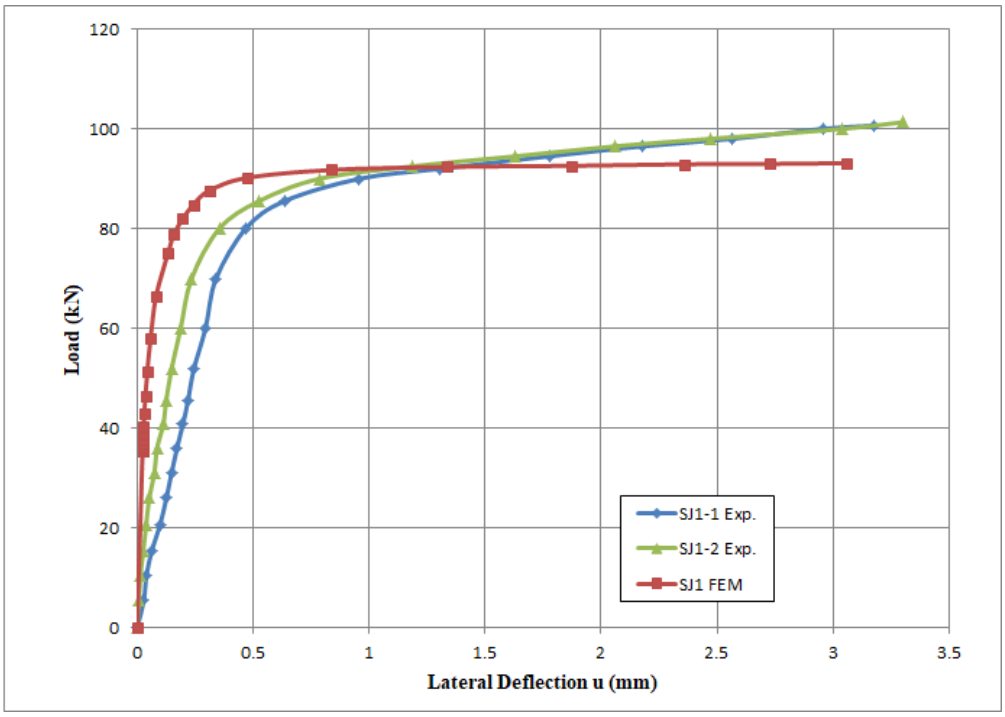

Figure 6.32 Comparison of experimental and finite element load-lateral deflection curve for Model A HOWSJ specimens.

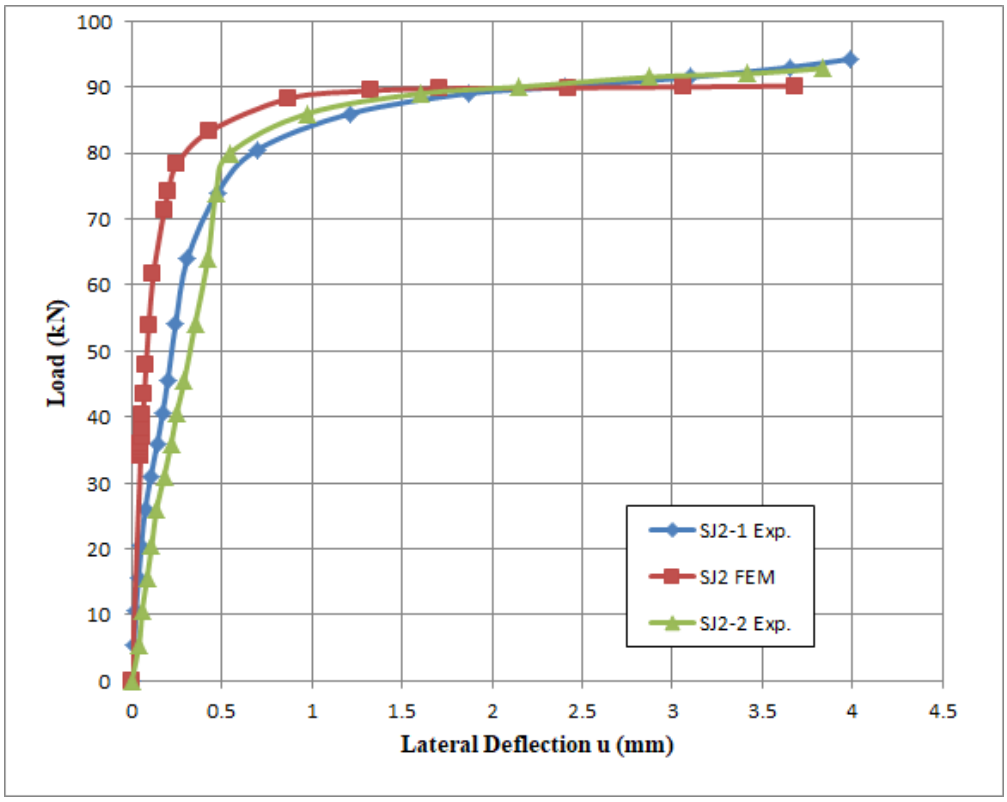

Figure 6.33 Comparison of experimental and finite element load-lateral deflection curve for Model B HOWSJ specimens.

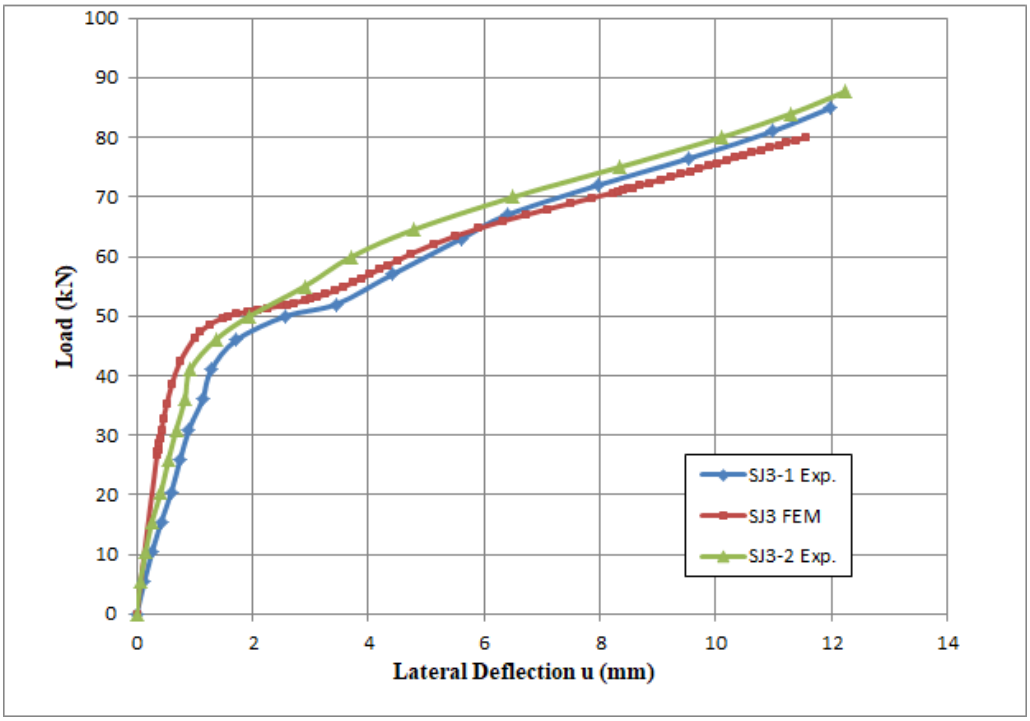

Figure 6.34 Comparison of experimental and finite element load-lateral deflection curve for Model C HOWSJ specimens.

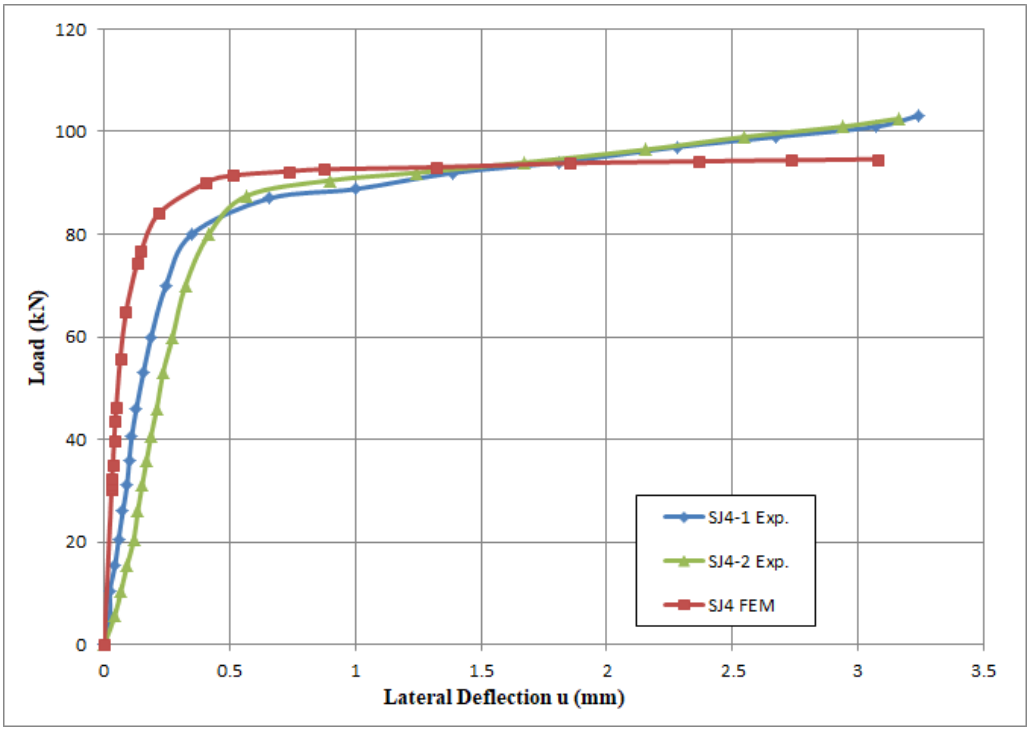

Figure 6.35 Comparison of experimental and finite element load-lateral deflection curve for Model D HOWSJ specimens.

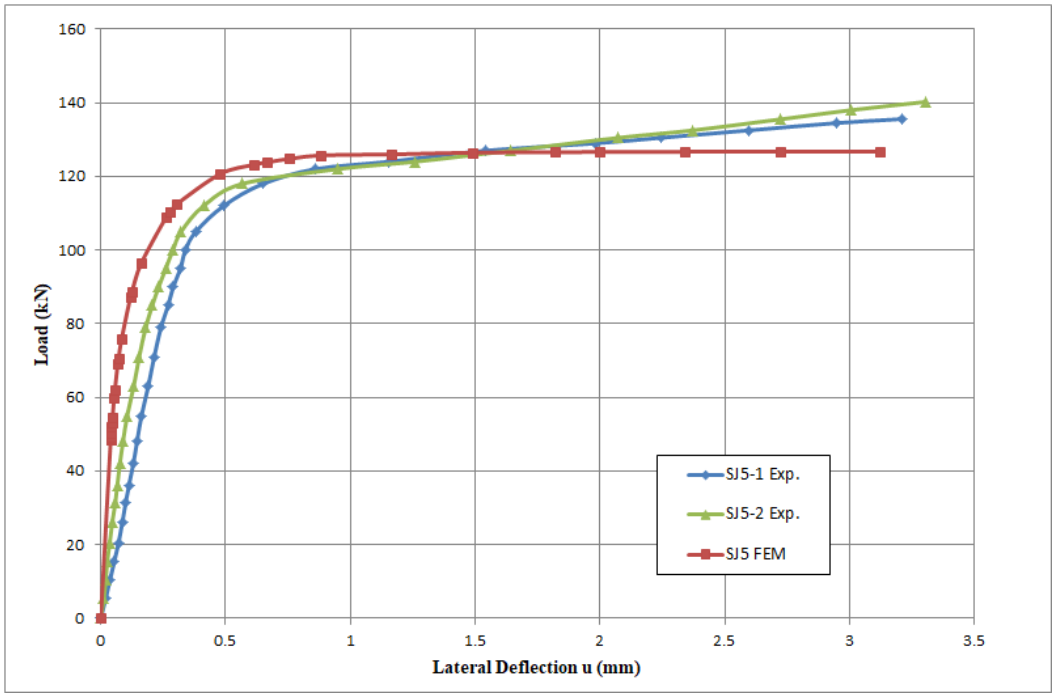

Figure 6.36 Comparison of experimental and finite element load-lateral deflection curve for Model E HOWSJ specimens.

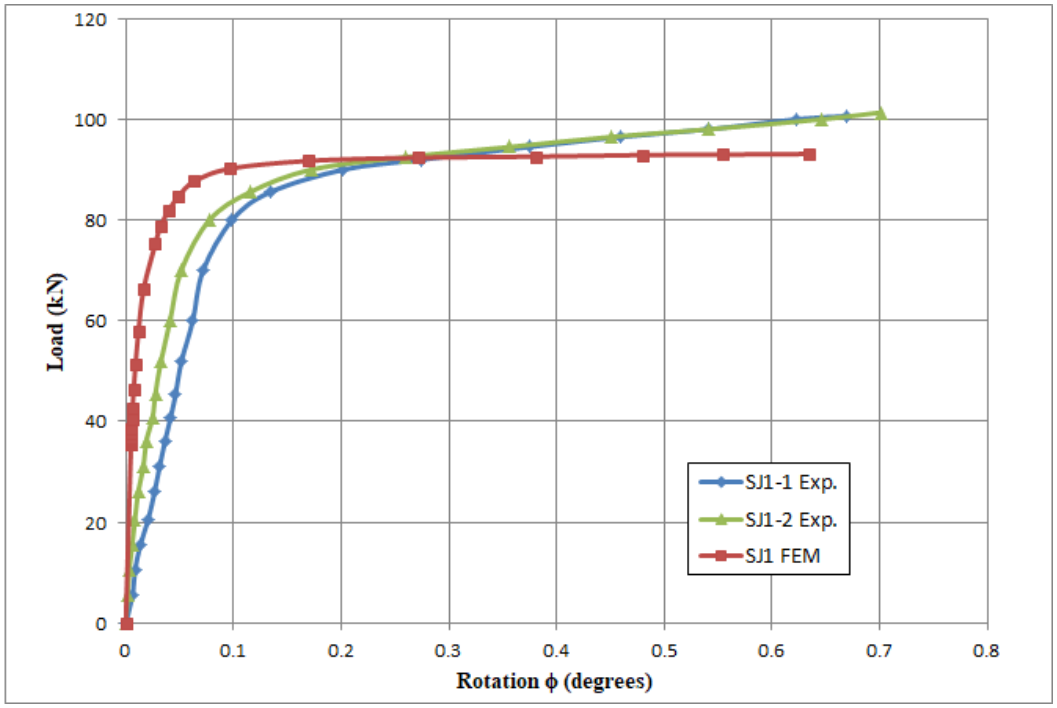

Figure 6.37 Comparison of experimental and finite element load-rotation curve for Model A HOWSJ specimens

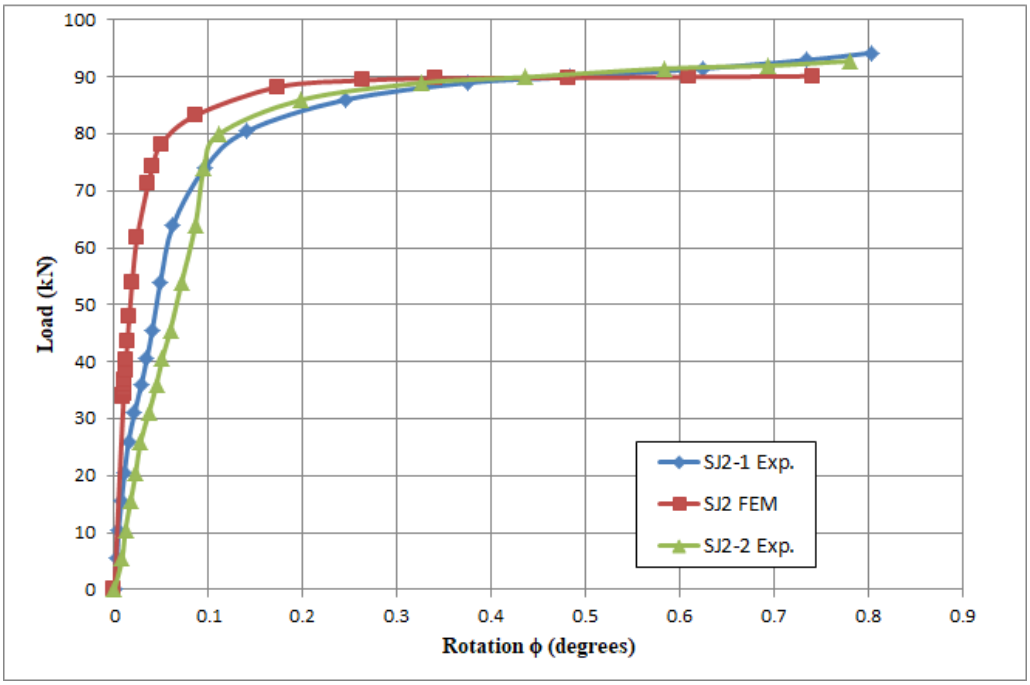

Figure 6.38 Comparison of experimental and finite element load-rotation curve for Model B HOWSJ specimens

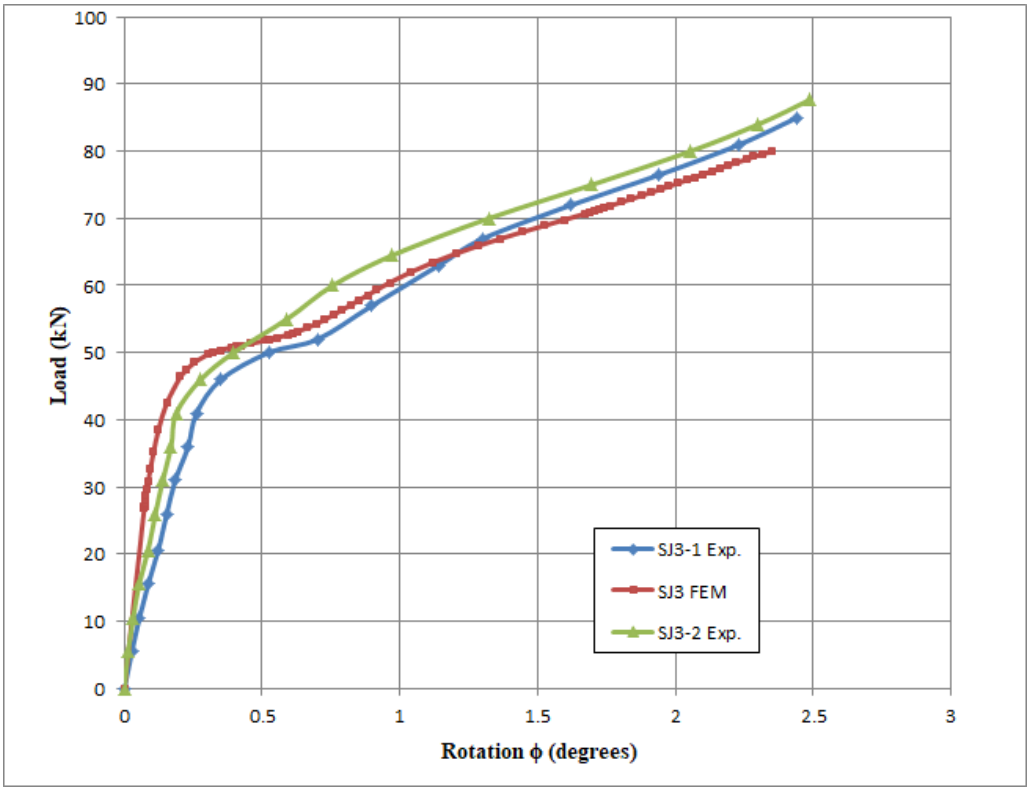

Figure 6.39 Comparison of experimental and finite element load-rotation curve for Model C HOWSJ specimens

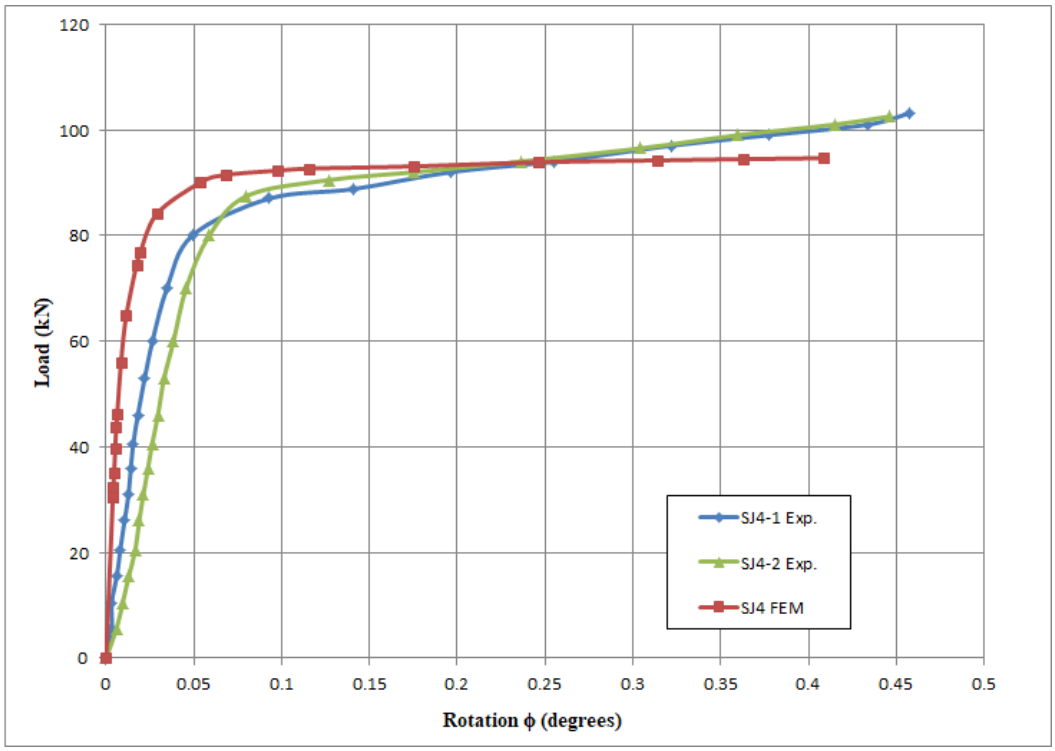

Figure 6.40 Comparison of experimental and finite element load-rotation curve for Model D HOWSJ specimens

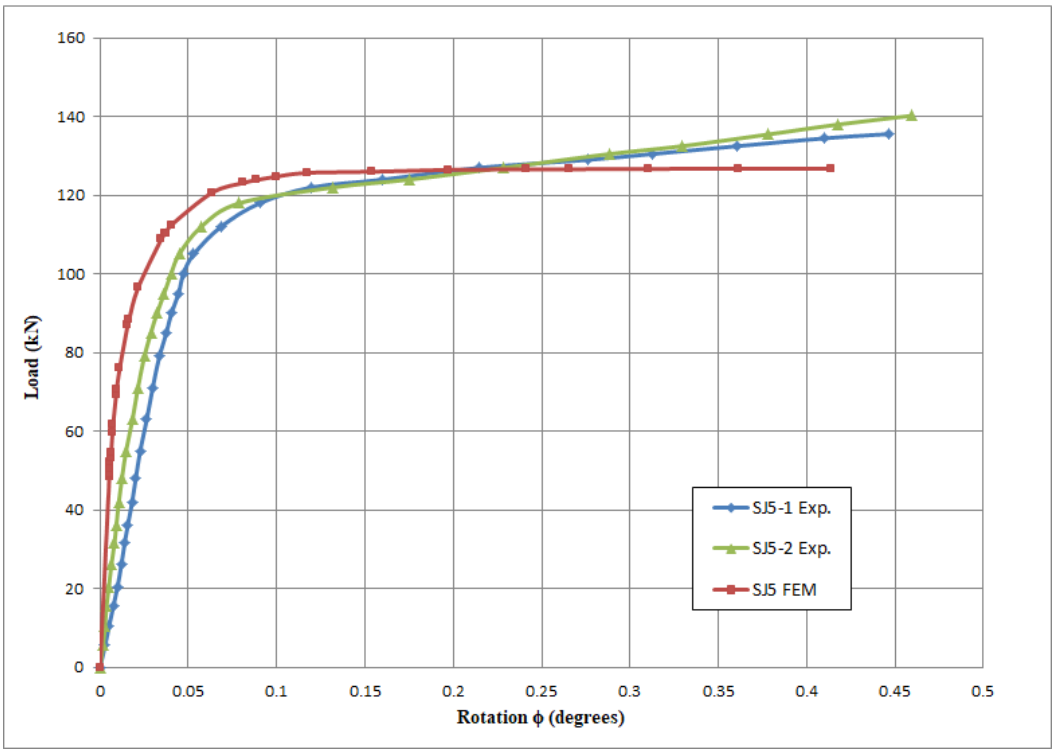

Figure 6.41 Comparison of experimental and finite element load-rotation curve for Model E HOWSJ specimens

Table 6.3 Comparison between experiments and FEM of lateral deflections for HOWSJs.

Models	Specimens No.	Experimental Lateral Deflection (mm)	Mean Exp. Lateral Deflection (mm)	FEM Lateral Deflection (mm)	Relative Difference (%)
Model A	SJ 1-1	3.178	3.240	3.057	5.65
	SJ 1-2	3.302			
Model B	SJ 2-1	3.991	3.913	3.681	5.93
	SJ 2-2	3.834			
Model C	SJ 3-1	11.995	12.115	11.562	4.56
	SJ 3-2	12.234			
Model D	SJ 4-1	3.241	3.201	3.076	3.91
	SJ 4-2	3.161			
Model E	SJ 5-1	3.210	3.256	3.117	4.27
	SJ 5-2	3.301			

Table 6.4 Comparison between experiments and FEM of rotation angles for HOWSJs.

Models	Specimens No.	Experimental Rotation (degrees)	Mean Exp. Rotation (degrees)	FEM Lateral Rotation (degrees))	Relative Difference (%)
Model A	SJ 1-1	0.669	0.685	0.635	7.29
	SJ 1-2	0.701			
Model B	SJ 2-1	0.803	0.791	0.738	6.70
	SJ 2-2	0.779			
Model C	SJ 3-1	2.438	2.463	2.350	4.59
	SJ 3-2	2.487			
Model D	SJ 4-1	0.457	0.451	0.411	8.87
	SJ 4-2	0.445			
Model E	SJ 5-1	0.447	0.453	0.414	8.61
	SJ 5-2	0.459			

6.3.2 Composite Open Web Steel Joists Results

The finite element results of the composite open web steel joists subjected to monotonic loading are presented in terms of load-deflection, load- slip curves, ultimate loads, deflections at ultimate load, and distribution of stresses.

6.3.2.1 The Load-Deflection Relations of COWS Joists

The ultimate loads capacity and deflections obtained by the finite element method and the experimental test results are illustrate in Tables (6-5) and (6-6), respectively. Comparisons between load- deflection curves predicted by simulation and experimental results are presented in Figures (6.42) to (6.48). The results show that the finite element analysis correlated well with experimental results, and they are almost the same in the initial stage of monotonic loading. The peak loads of theoretical analysis were more than those of the experimental results within only (9.5%) for all specimens. And the relative difference of deflections at ultimate loads between the FEM and experimental results was less than (10 %). This suggested that the finite element models were able to assess the capacity of composite open web joists with reasonable accuracy.

Table 6.5 Comparison between FEM and experimental ultimate loads for COWSJs.

Specimens No.	Experimental Ultimate Load (kN)	FEM Ultimate Load (kN)	Relative Difference (%)
CSJ 1-1 SF 5.1	160.153	165.595	3.28
CSJ 2-2 SF 5.1	155.495	158.921	2.16
CSJ 3-3 SF 5.1	137.892	146.878	6.11
CSJ 3-4 SF 5.1	139.684	149.591	6.62
CSJ 3-5 N 5.1	135.157	147.494	8.36
CSJ 3-6 SF 3.6	145.978	158.186	7.72
CSJ 3-7 N 3.6	140.286	155.012	9.49

Table 6.6 Comparison between FEM and experimental deflection at ultimate loads for COWSJS.

Specimens No.	Experimental Deflection (mm)	FEM Deflection (mm)	Relative Difference (%)
CSJ 1-1 SF 5.1	8.754	9.448	7.35
CSJ 2-2 SF 5.1	9.120	9.409	3.07
CSJ 3-3 SF 5.1	10.719	9.755	−9.88
CSJ 3-4 SF 5.1	10.775	9.812	−9.81
CSJ 3-5 N 5.1	10.387	9.517	−9.14
CSJ 3-6 SF 3.6	10.631	9.674	−9.89
CSJ 3-7 N 3.6	10.265	9.483	−8.25

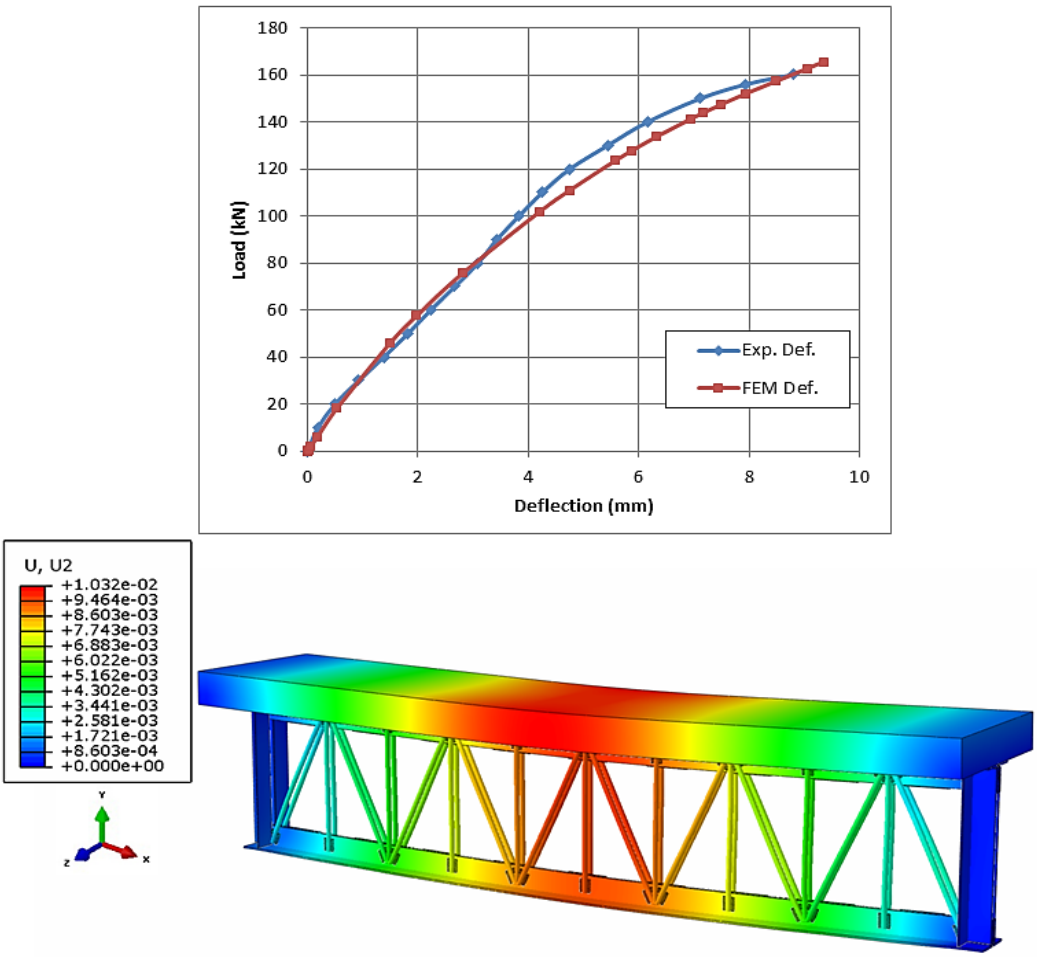

Figure 6.42 Comparison of experimental and finite element load-deflection curve for CSJ 1-1 SF 5.1 specimen.

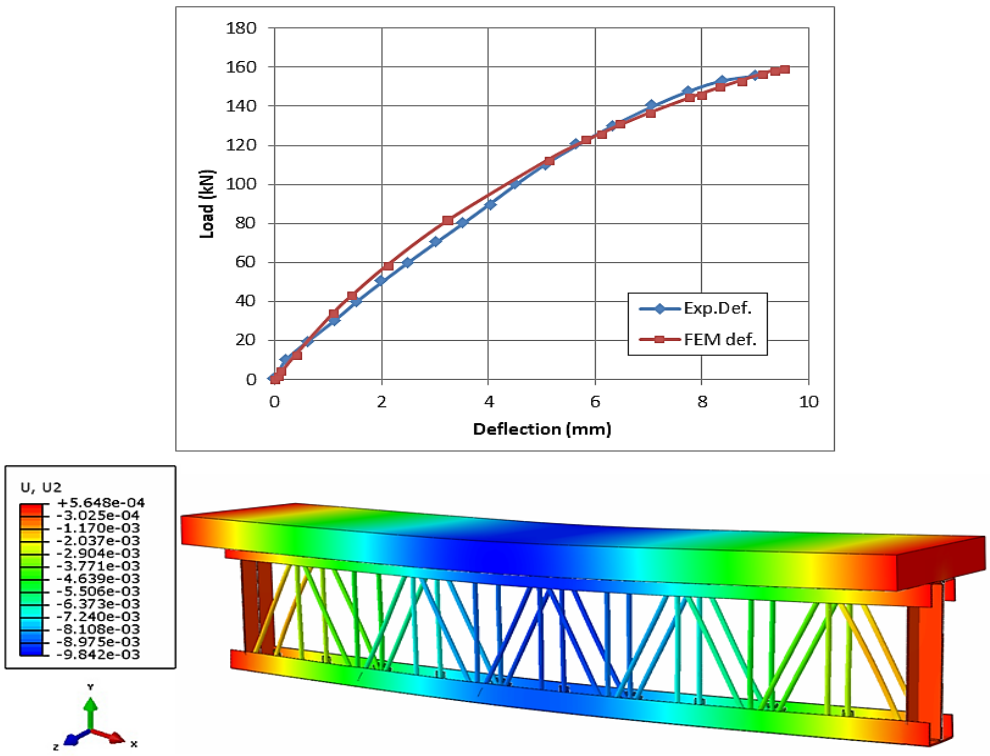

Figure 6.43 Comparison of experimental and finite element load-deflection curve for CSJ 2-2 SF 5.1 specimen.

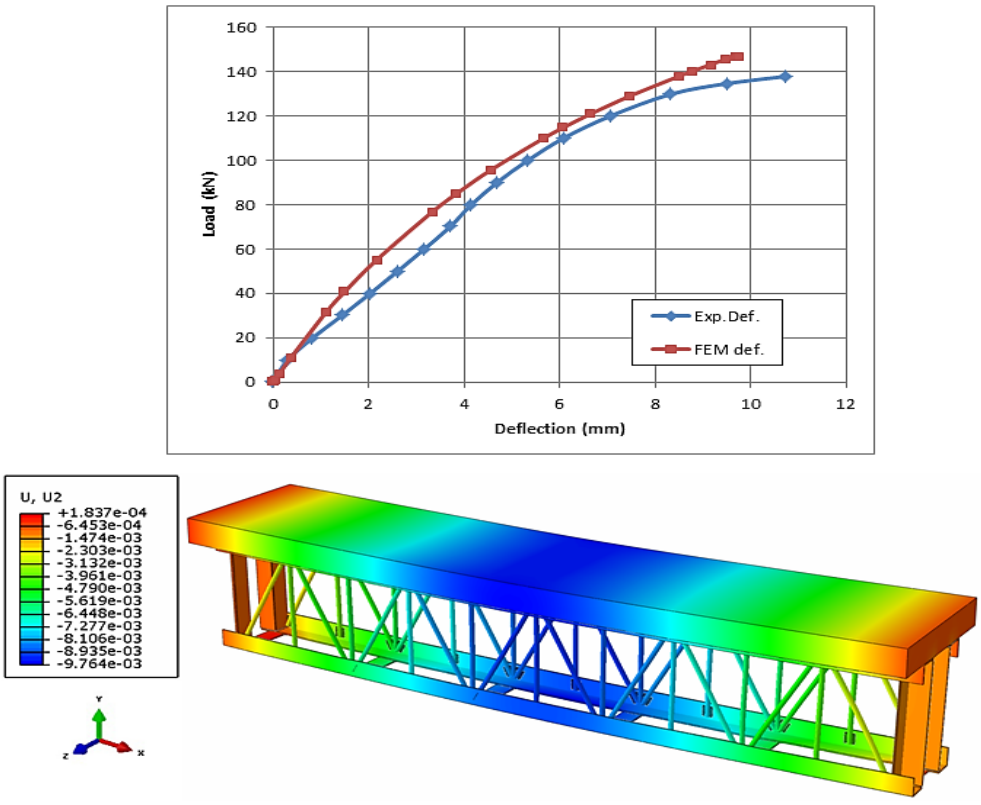

Figure 6.44 Comparison of experimental and finite element load-deflection curve for CSJ 3-3 SF 5.1 specimen.

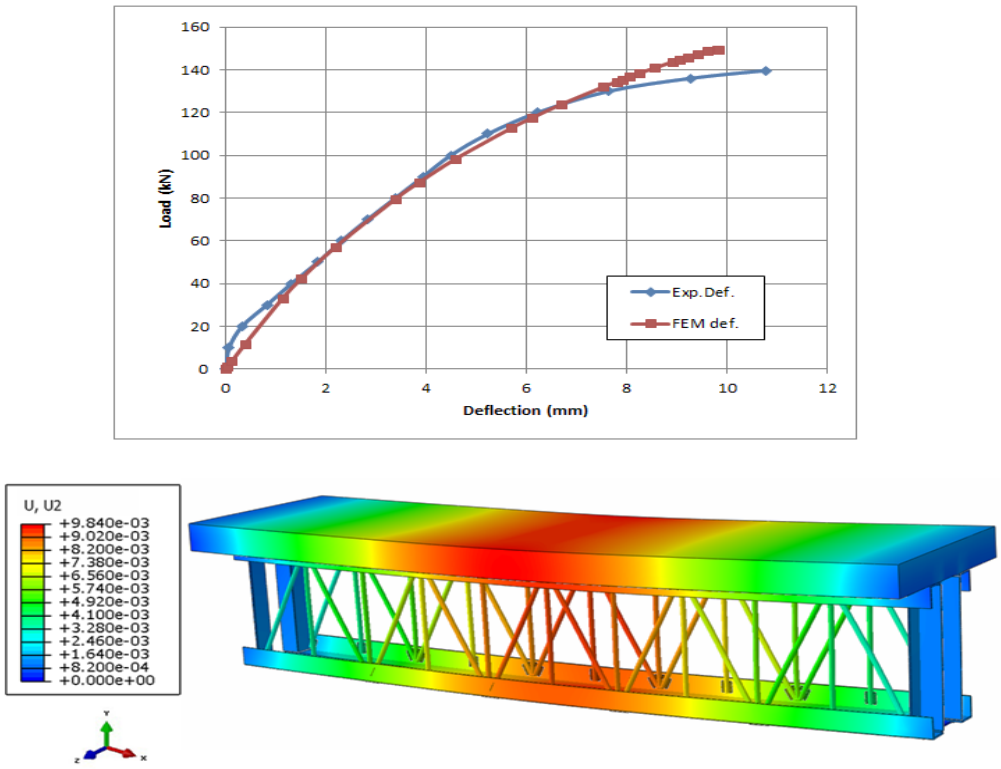

Figure 6.45 Comparison of experimental and finite element load-deflection curve for CSJ 3-4 SF 5.1 specimen.

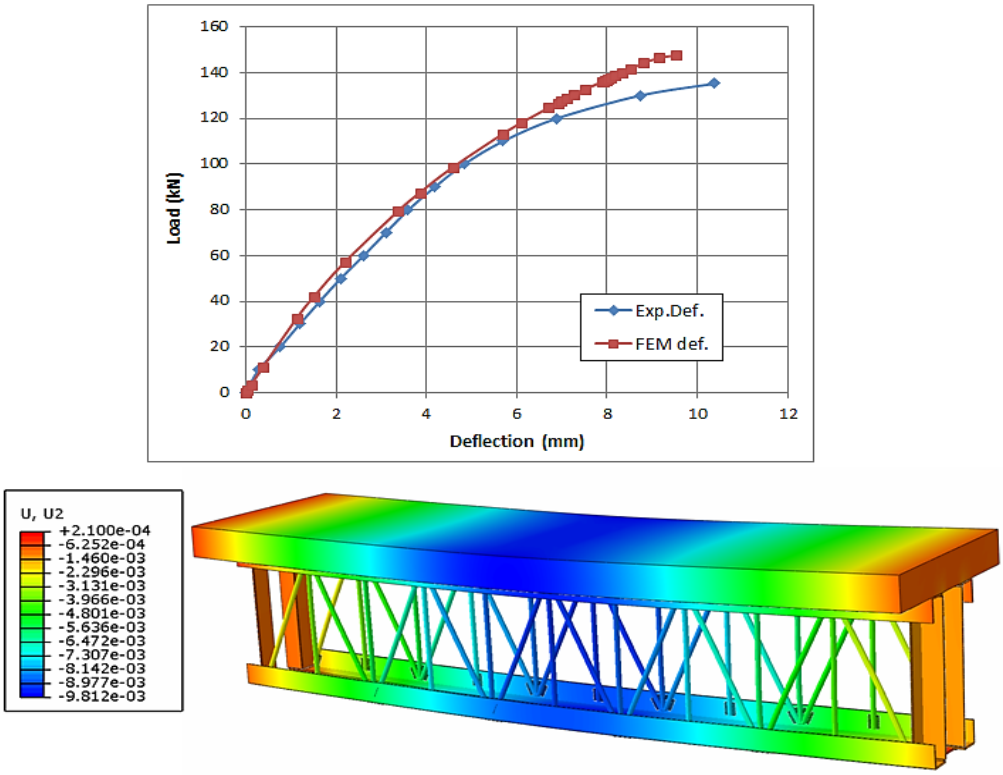

Figure 6.46 Comparison of experimental and finite element load-deflection curve for CSJ 3-5 N 5.1specimen.

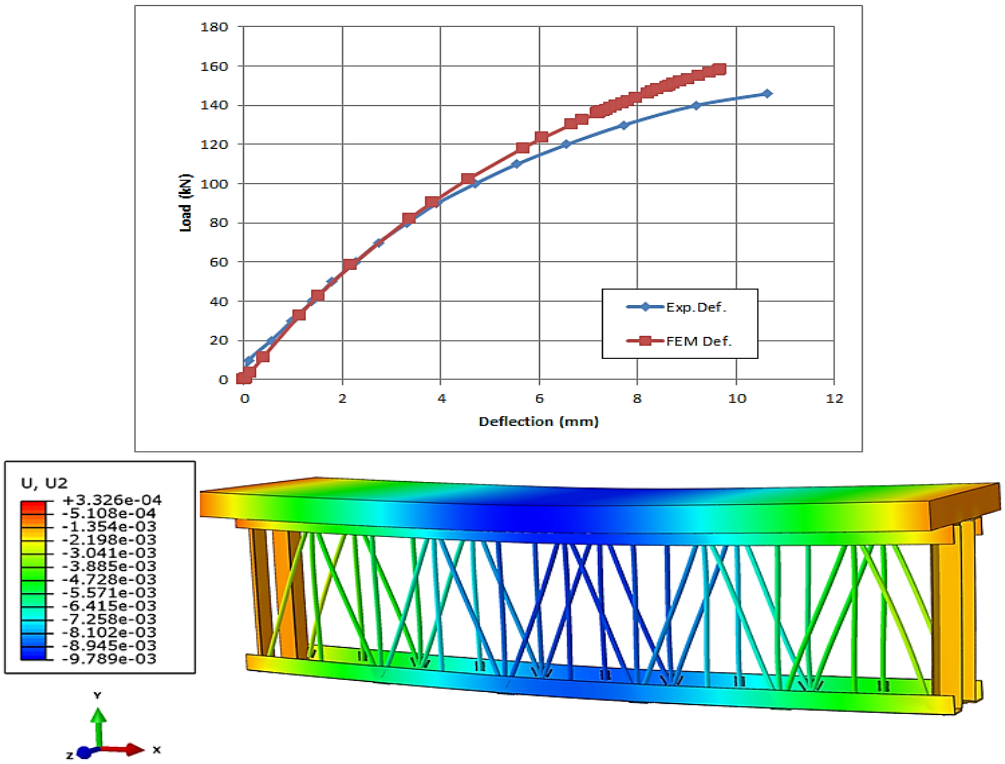

Figure 6.47 Comparison of experimental and finite element load-deflection curve for CSJ 3-6 SF 3.6 specimen.

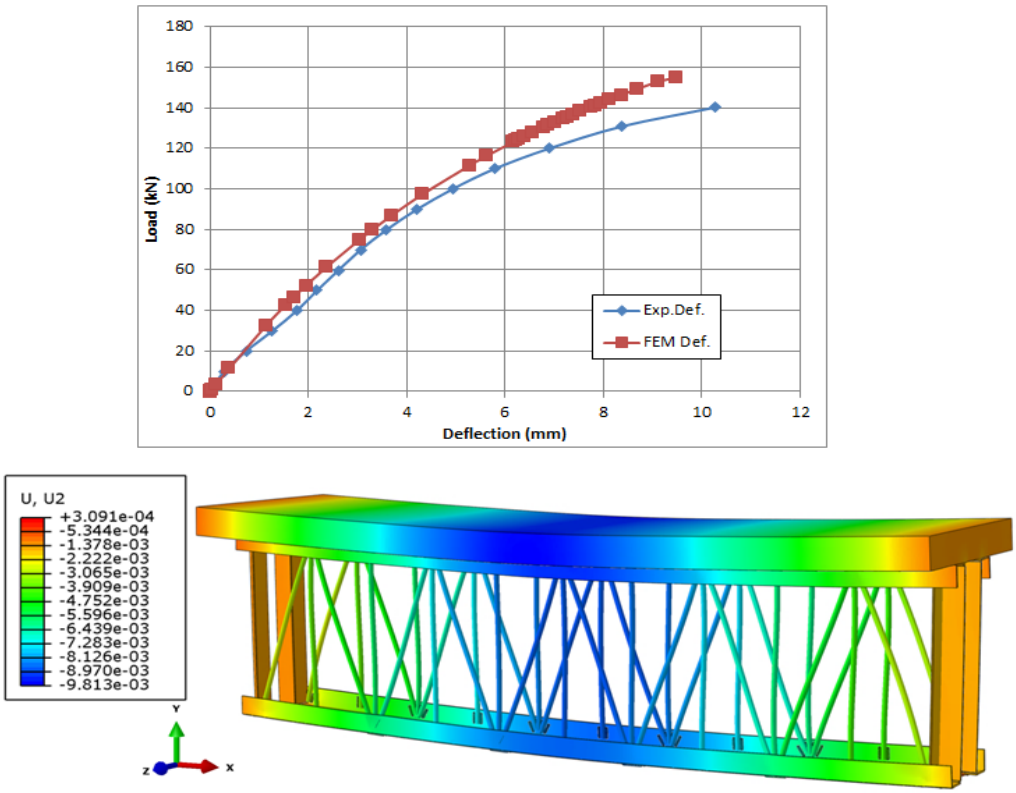

Figure 6.48 Comparison of experimental and finite element load-deflection curve for CSJ 3-7 N 3.6 specimen.

6.3.2.2 Load-Slip Relations of COWS Joists

The slip between the HOWSJ and concrete slab at the ends was analyzed numerically by the software ABAQUS, comparison of the relative slip at the ultimate load obtained from the experimental work and the FEM simulation illustrate in Table (6-8). The Figures (6.49) to (6.55) show the slip recorded experimentally and the corresponding slip obtained by finite element analysis for every specimen separately. The models of finite element analysis seemed able to simulate the slip behavior of the composite open web joist with a good agreement. It can be concluded that the type of contact between different materials modeled in finite element adopted can predict the behavior of the specimens well, where the maximum relative difference between the FEM and the experimental value was less than (3%).

Table 6.7 Comparison between FEM and experimental slip at ultimate loads for COWSJS.

Specimens No.	Experimental Slip(mm)	FEM Slip(mm)	Relative Difference (%)
CSJ 1-1 SF 5.1	0.837	0.862	2.9
CSJ 2-2 SF 5.1	0.699	0.720	2.92
CSJ 3-3 SF 5.1	0.803	0.825	2.67
CSJ 3-4 SF 5.1	0.727	0.749	2.93
CSJ 3-5 N 5.1	0.753	0.775	2.84
CSJ 3-6 SF 3.6	0.611	0.629	2.86
CSJ 3-7 N 3.6	0.643	0.661	2.72

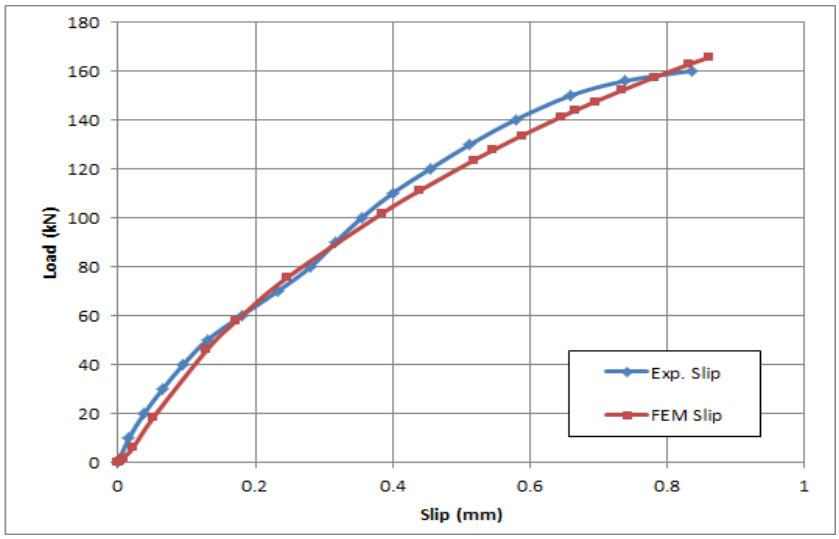

Figure 6.49 Comparison of experimental and finite element load-slip curve for CSJ 1-1 SF 5.1.

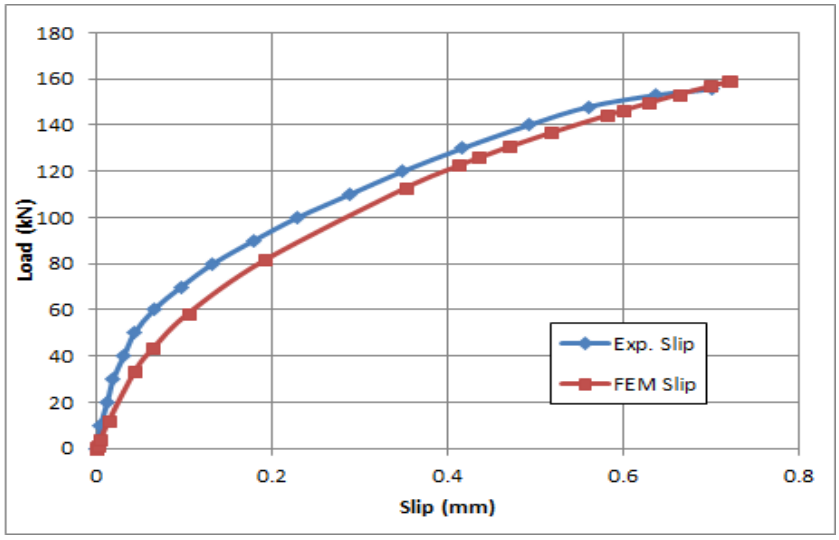

Figure 6.50 Comparison of experimental and finite element load-slip curve for CSJ 2-2 SF 5.1.

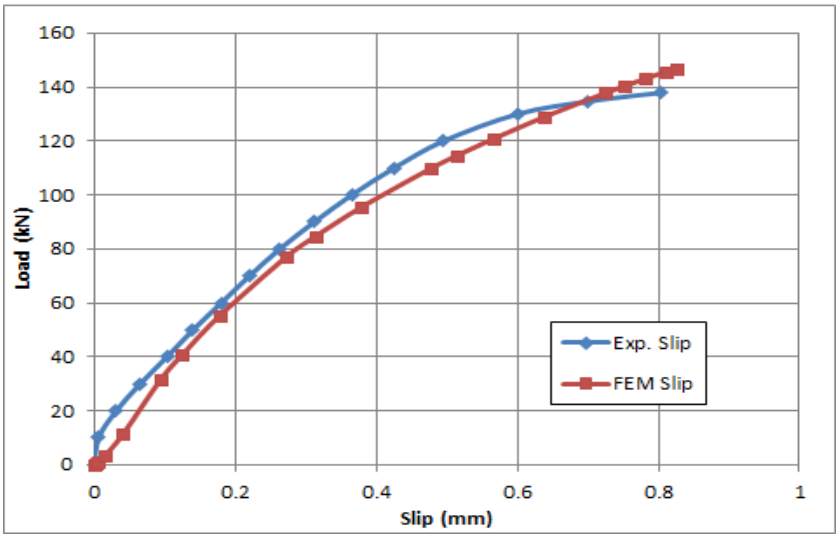

Figure 6.51 Comparison of experimental and finite element load-slip curve for CSJ 3-3 SF 5.1.

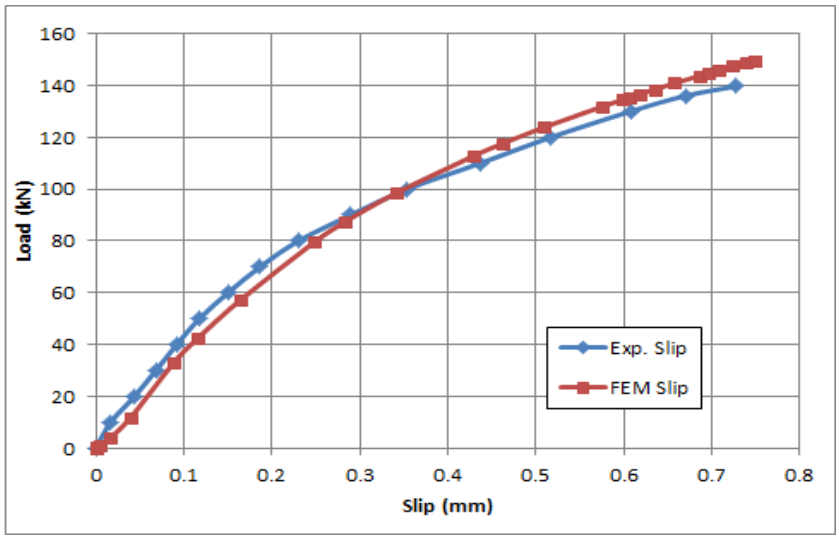

Figure 6.52 Comparison of experimental and finite element load-slip curve for CSJ 3-4 SF 5.1.

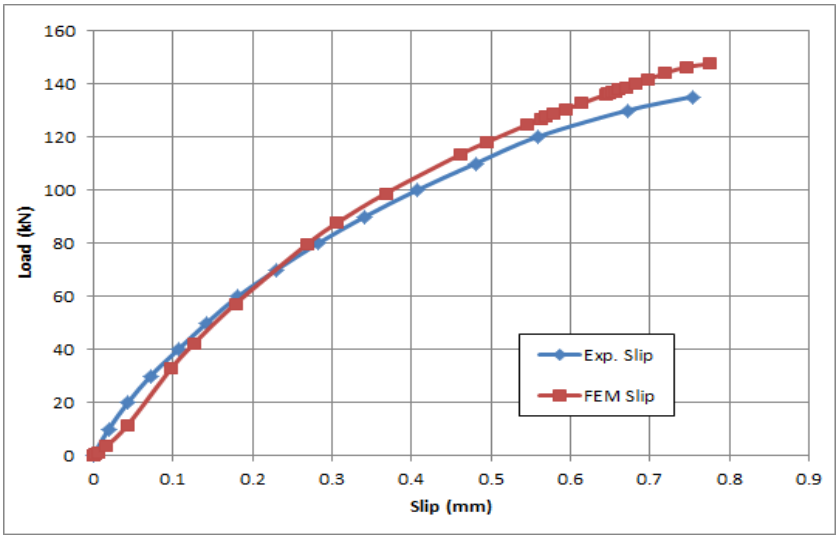

Figure 6.53 Comparison of experimental and finite element load-slip curve for CSJ 3-5 N 5.1.

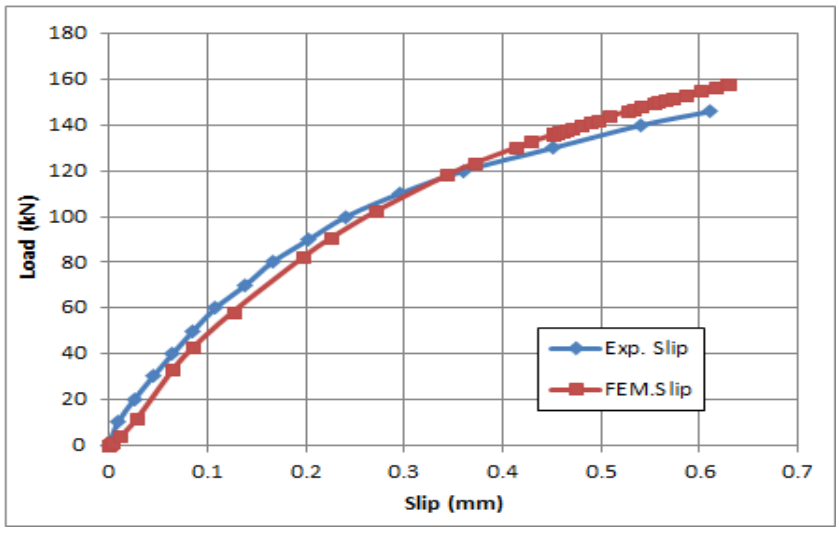

Figure 6.54 Comparison of experimental and finite element load-slip curve for CSJ 3-6 SF 3.6.

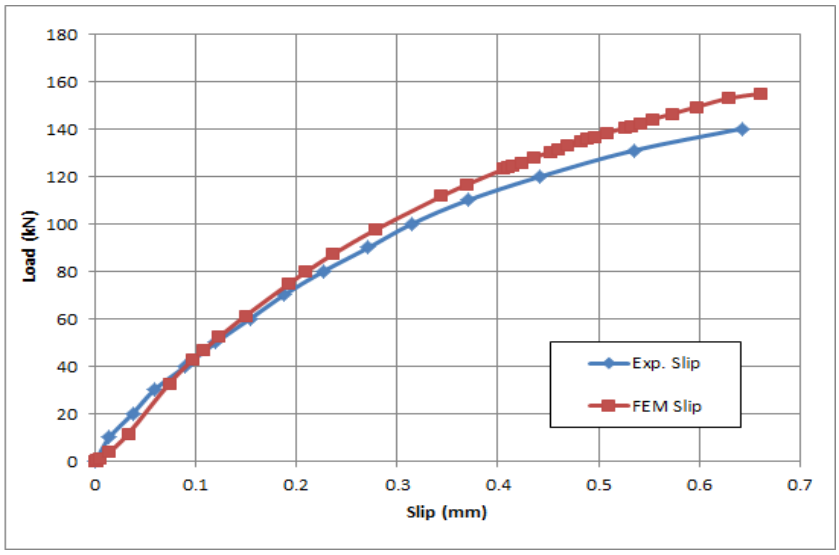

Figure 6.55 Comparison of experimental and finite element load-slip curve for CSJ 3-7 N 3.6.

6.3.2.3 Von Mises Stress Distribution of COWS Joists

The stresses distribution through the components of the tested composite open web steel joists were analyzed numerically by ABAQUS, Von Mises stress distribution was used to show high stresses zones for each specimen as presented in Figures (6-56) to (6-62). It can be recognized that the greater stresses are obtained in the composite open web steel joists were occurred in the interior web members and in the joints of welding and these failures were happened exactly in the experimental work.

Also it was good to remove some parts to notice the stresses which obtained in the shear connectors and the WWF reinforcement for all specimens, as shown in plates from (6-6) to (6-12), from these plates it can be recognized that the higher stresses of the WWF reinforcement occurred in mid span of the composite and the stresses in the headed studs are increased gradually towards supports.

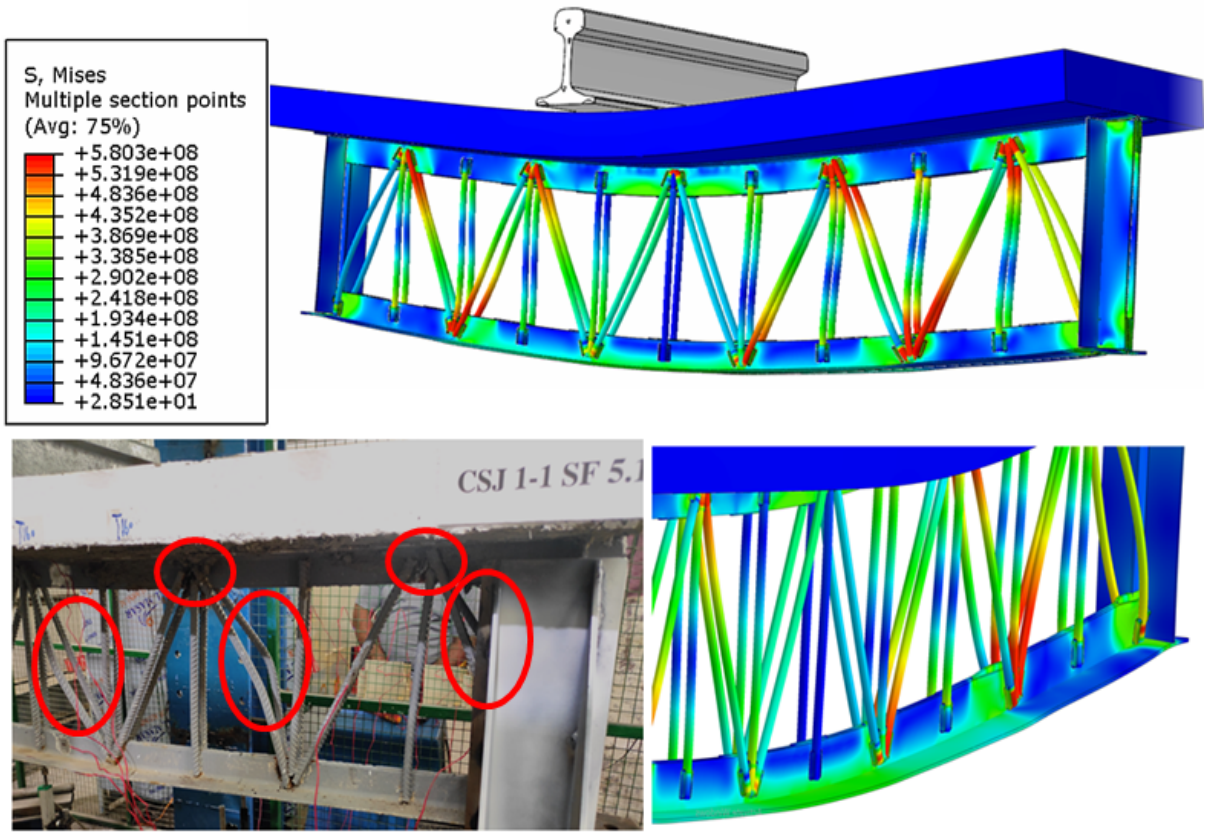

Figure 6.56 Von Mises stress distribution of CSJ 1-1 SF 5.1 specimen.

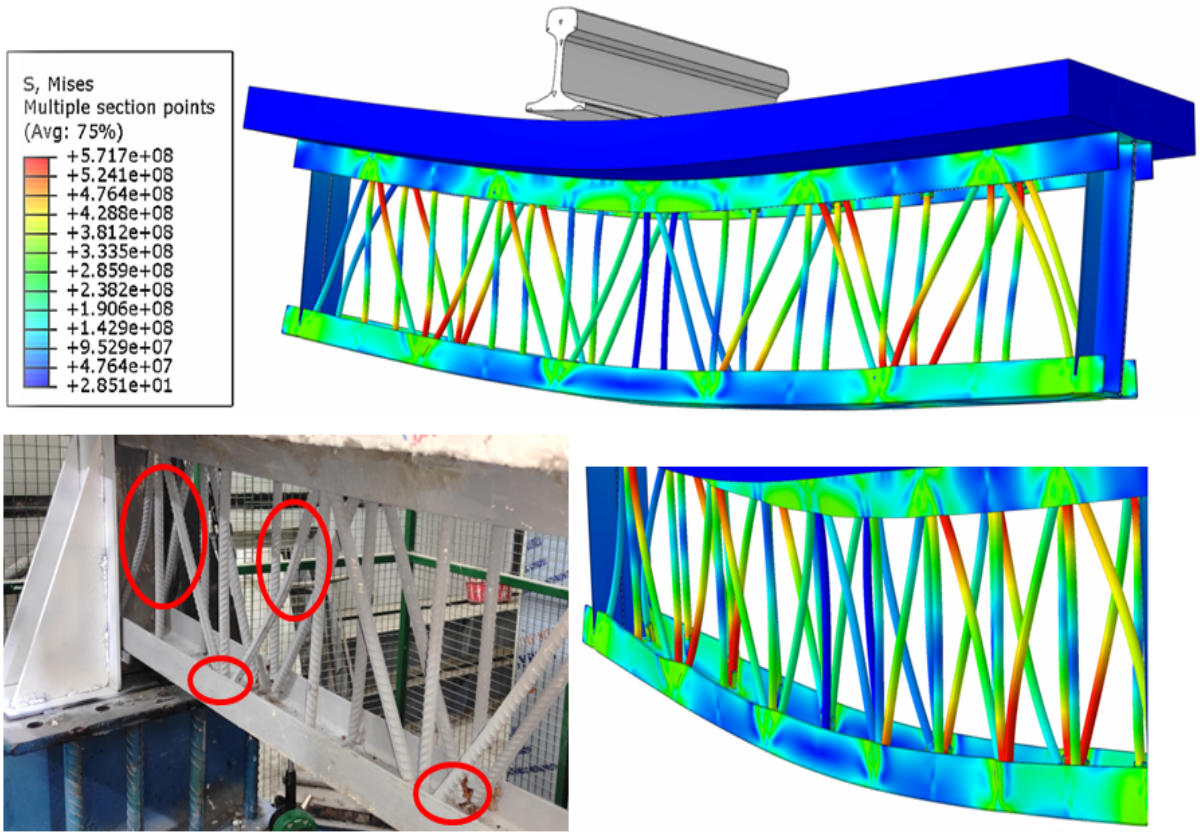

Figure 6.57 Von Mises stress distribution of CSJ 2-2 SF 5.1 specimen.

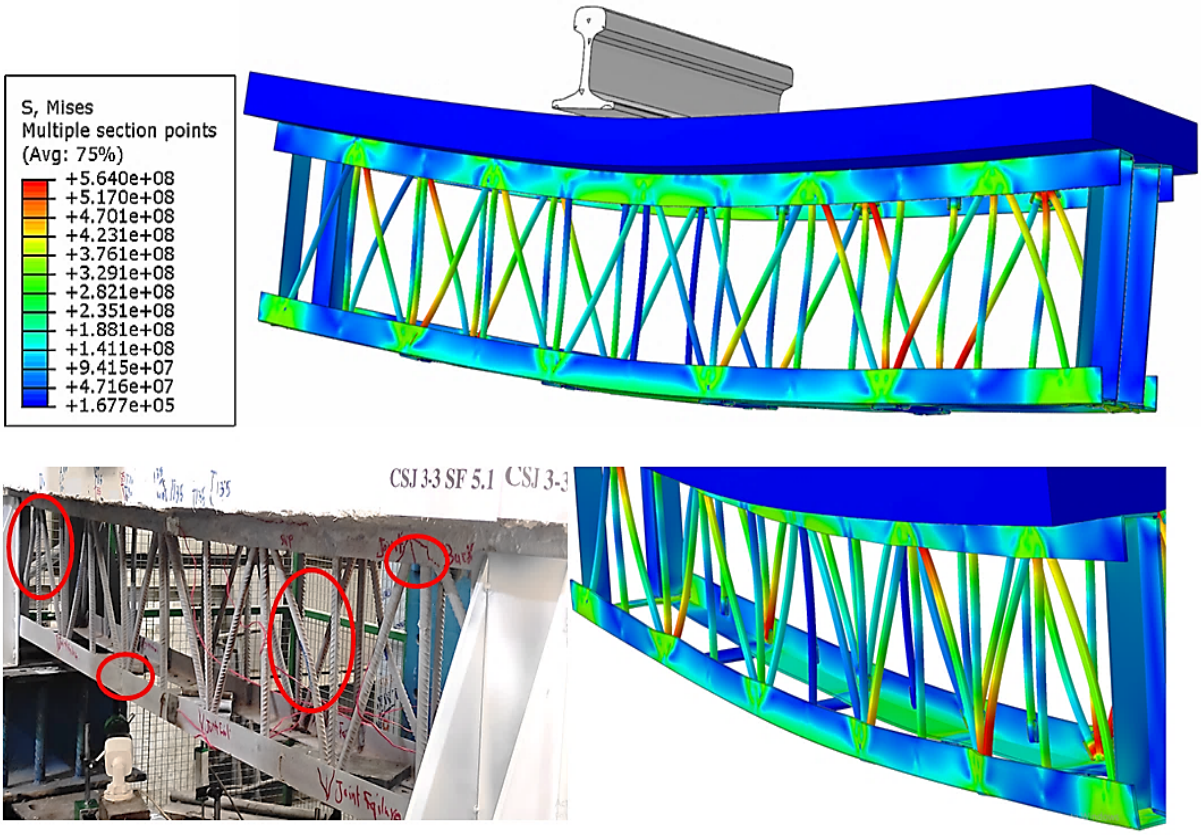

Figure 6.58 Von Mises stress distribution of CSJ 3-3 SF 5.1 specimen.

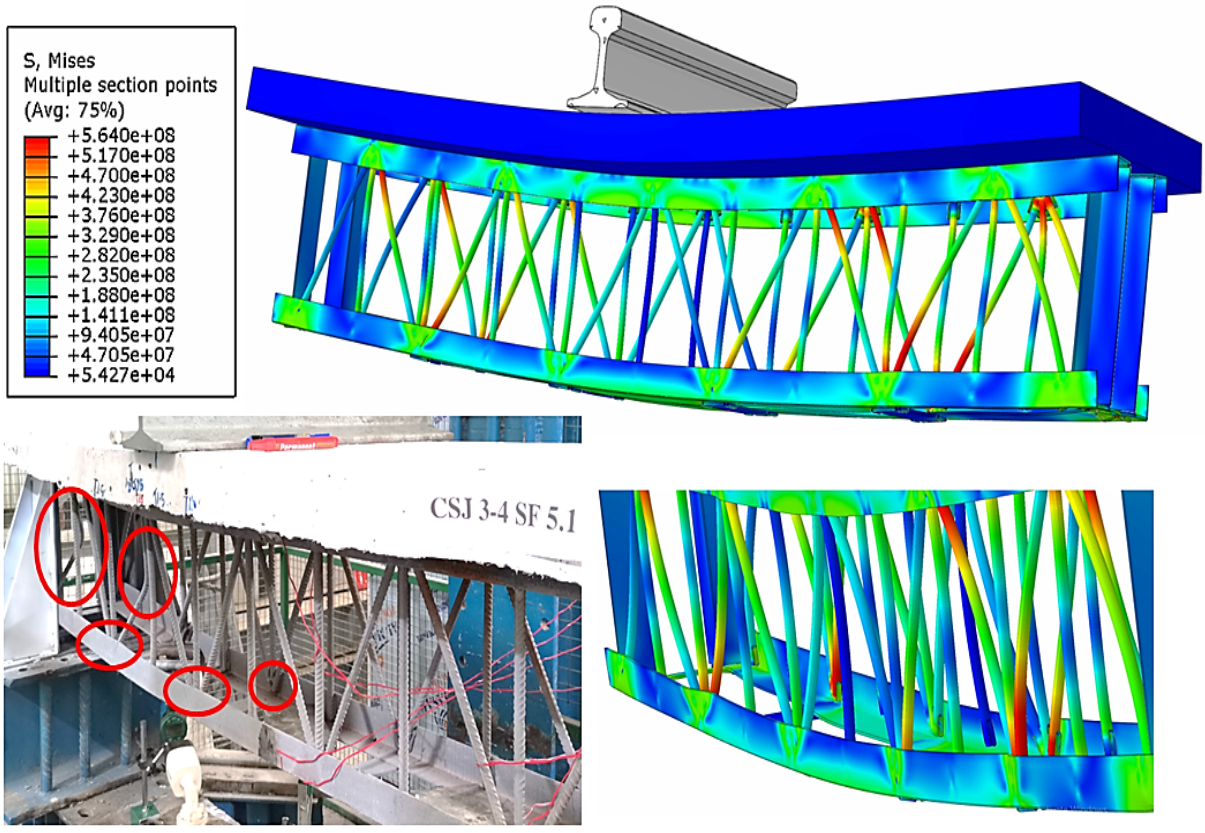

Figure 6.59 Von Mises stress distribution of CSJ 3-4 SF 5.1 specimen.

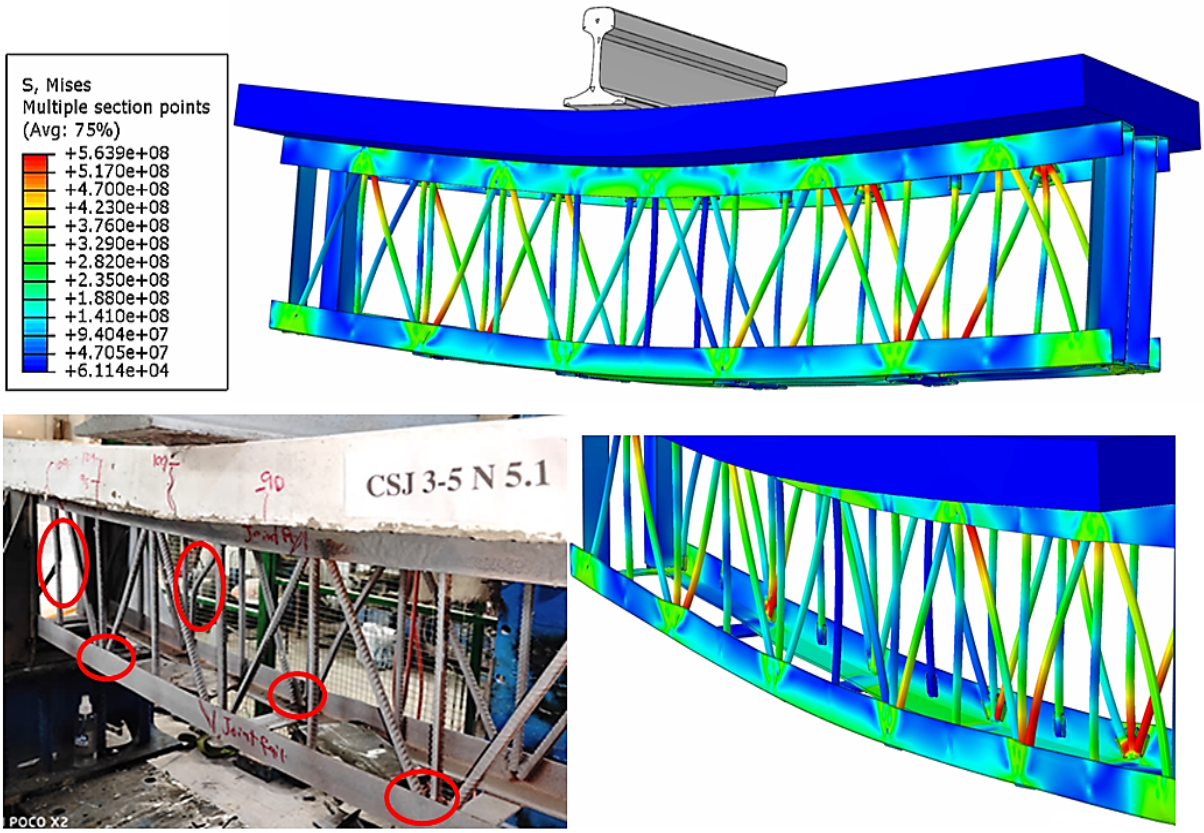

Figure 6.60 Von Mises stress distribution of CSJ 3-5 N 5.1 specimen.

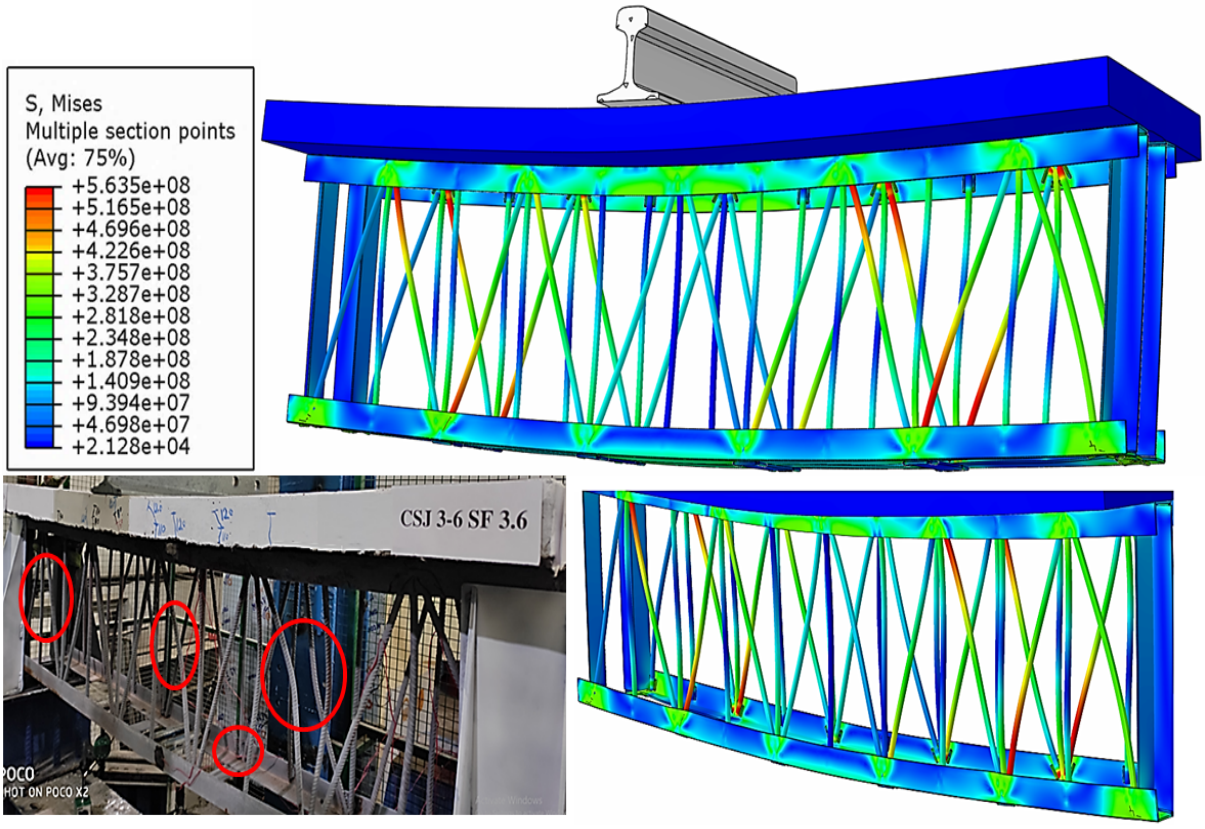

Figure 6.61 Von Mises stress distribution of CSJ 3-6 SF 3.6 specimen.

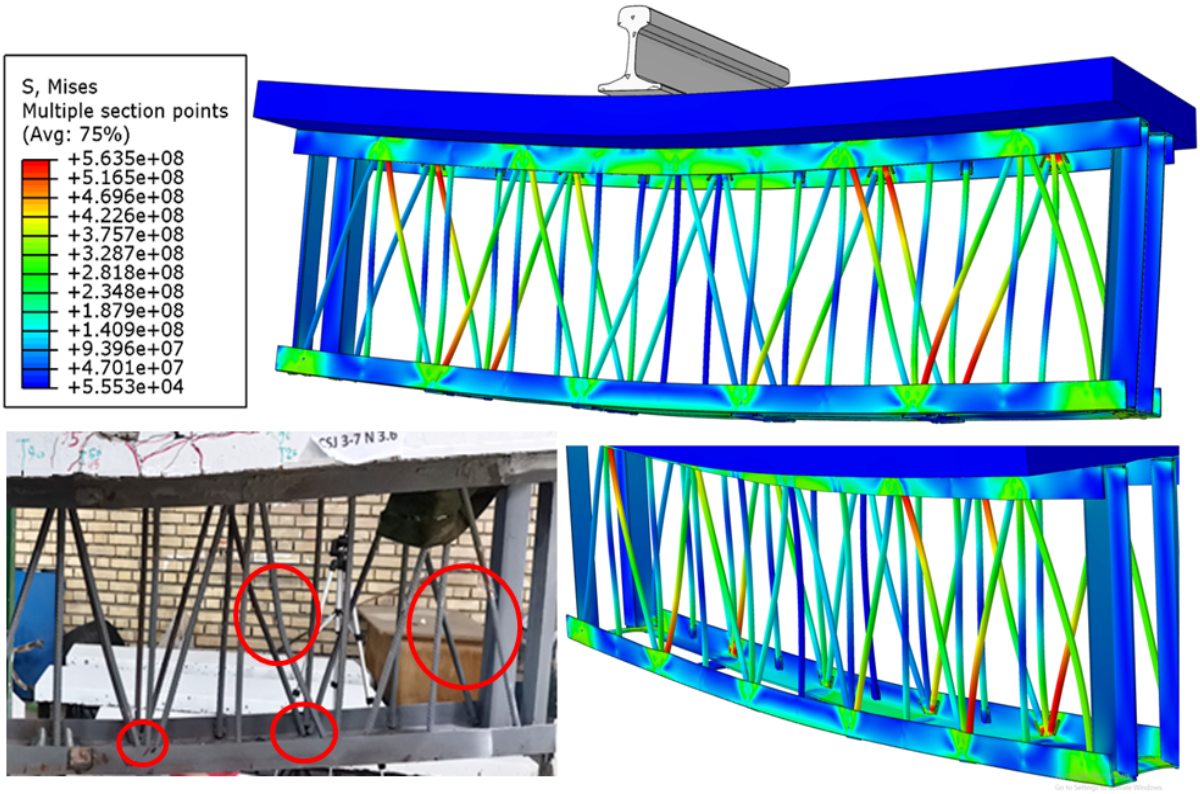

Figure 6.62 Von Mises stress distribution of CSJ 3-7 N 3.6 specimen.

Plate 6.6 Von Mises stress distribution of shear studs and WWF reinf. for CSJ 1-1 SF 5.1.

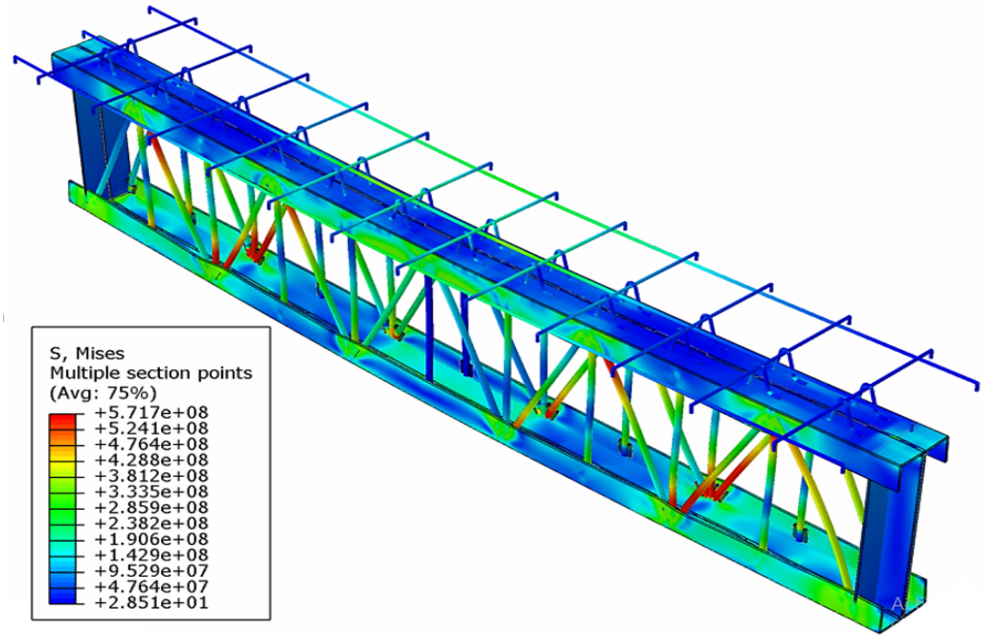

Plate 6.7 Von Mises stress distribution of shear studs and WWF reinf. for CSJ 2-2 SF 5.1.

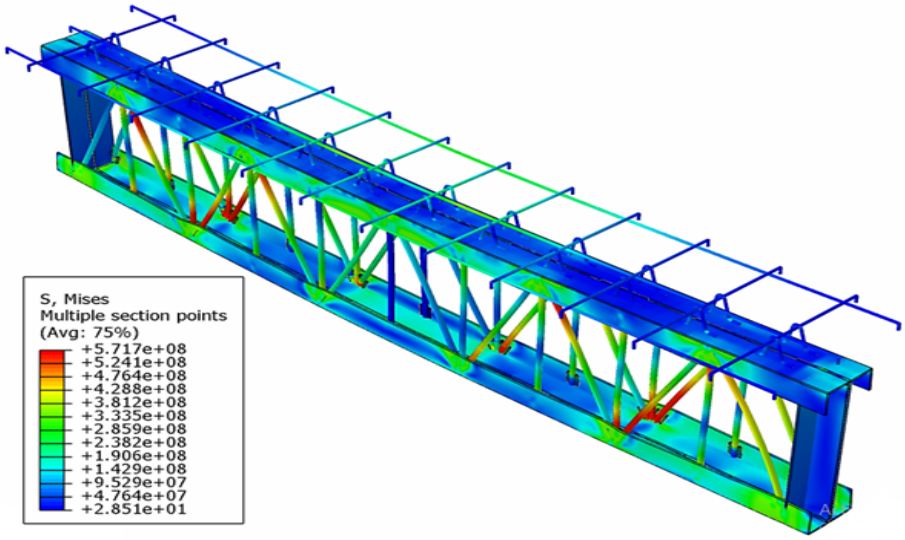

Plate 6.8 Von Mises stress distribution of shear studs and WWF reinf. for CSJ 3-3 SF 5.1.

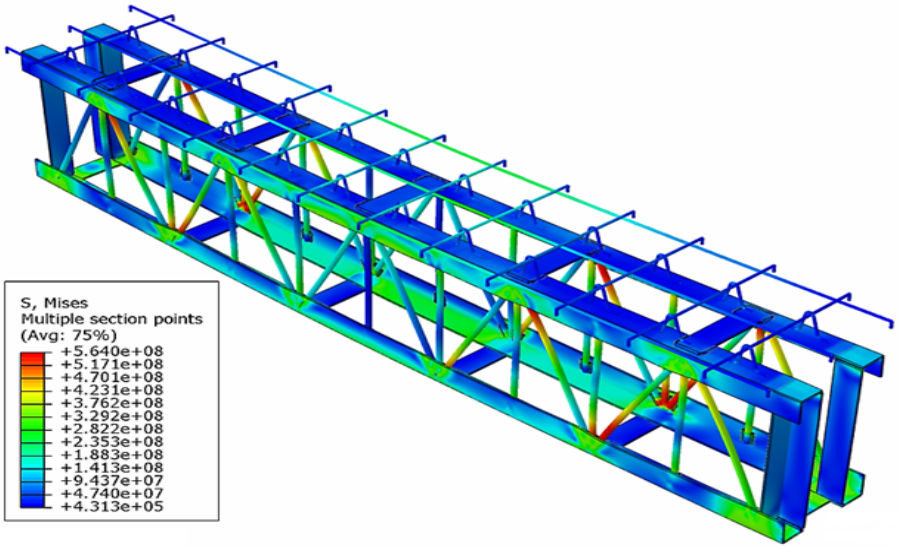

Plate 6.9 Von Mises stress distribution of shear studs and WWF reinf. for CSJ 3-4 SF 5.1.

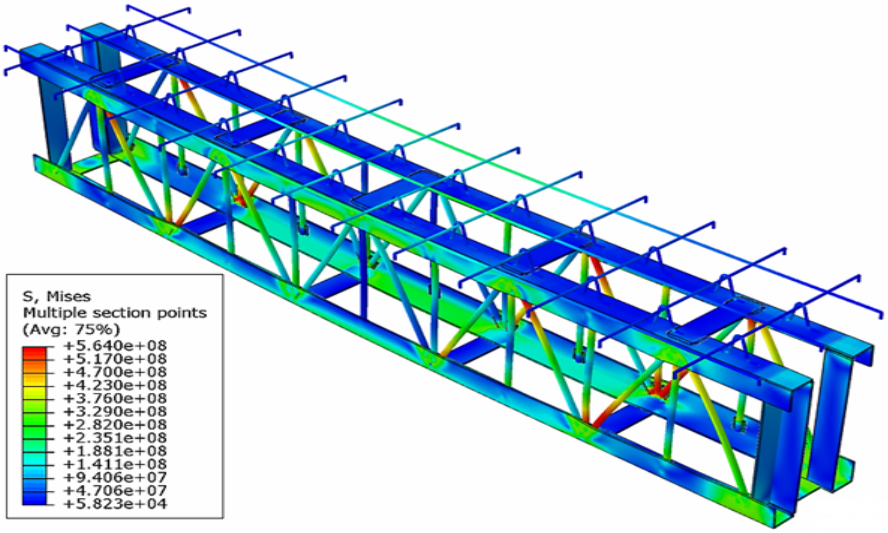

Plate 6.10 : Von Mises stress distribution of shear shear connectors CSJ 3-5 N 5.1.

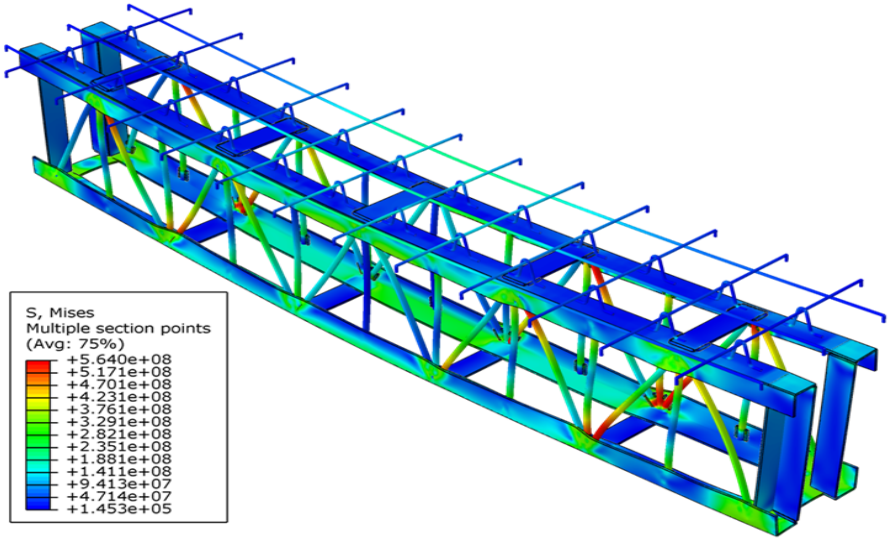

Plate 6.11 : Von Mises stress distribution of shearshear connectors CSJ 3-6 SF 3.6.

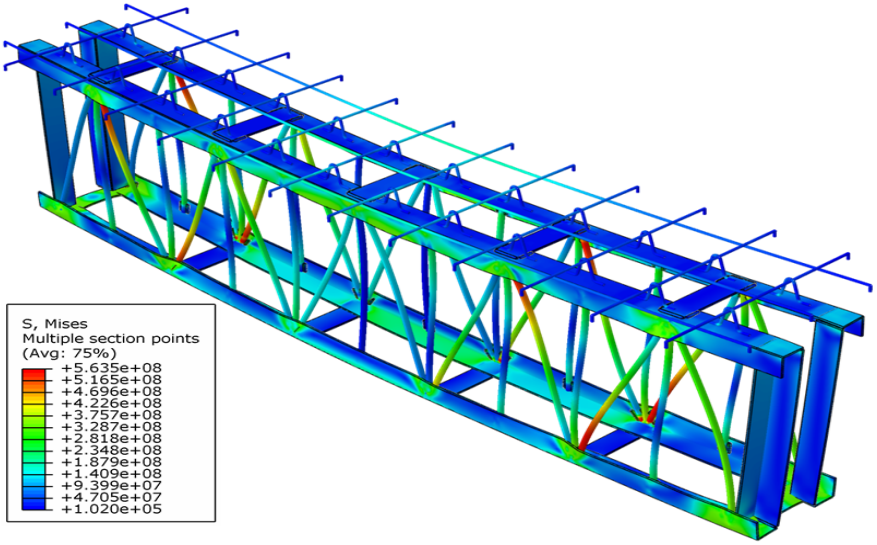

Plate 6.12 : Von Mises stress distribution of shear shear connectors CSJ 3-7 N 3.6.

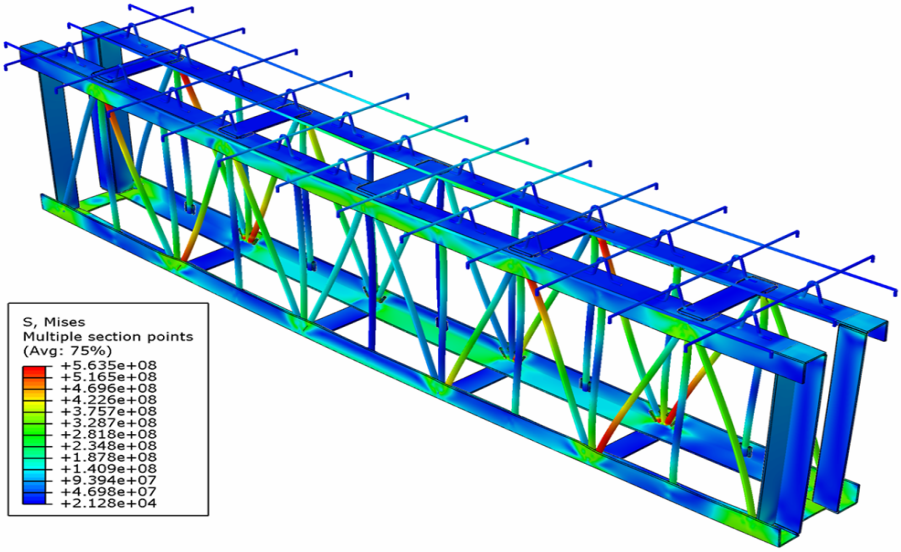

6.3.2.4 Tensile Stresses in Concrete

By using ABAQUS program the stress contours in the concrete slab at the ultimate loading capacity can be investigated, thus the concrete cracks indicated by the tensile damage variable " DAMAGET" for each specimen were compared with experimental results as illustrate in Figures from (6.63) to (6-69), from these figures it can be seen that the shape of the tensile cracks in the concrete slab that occurred in the experimental tests for all COWSJ specimens was largely identical with that obtained from the theoretical results using the ABAQUS program. It can be perceived that the high tensile stress regions of the concrete slab were greatest in specimen CSJ 2-2 SF 5.1 among the specimens which had the same (span/depth) ratio of 5.1 and had a different shapes of steel joist cross section as shown by stress contours.

Regarding the specimens which had the same shape of the steel joist cross section it can be noticed that the tensile stress regions of the concrete slab were became great when (span/depth) ratio increased from 3.6 to 5.1 for both types concrete slab due to the reduce of stiffness in specimens CSJ3-4 SF5.1 and CSJ3-5 N5.1. Also, the specimens CSJ3-5 N5.1 and CSJ3-7 N3.6 which had a NC slab showed that the maximum stresses extended adjacently to the middle span of the concrete slab more than the specimens CSJ3-4 SF5.1 and CSJ3-6 SF3.6 which had a SFC slab as shown by stress contours, which indicates that the slip between the concrete slab and steel joist was occurred in NC more than the SFC slab and that's what was happened also in the experimental test.

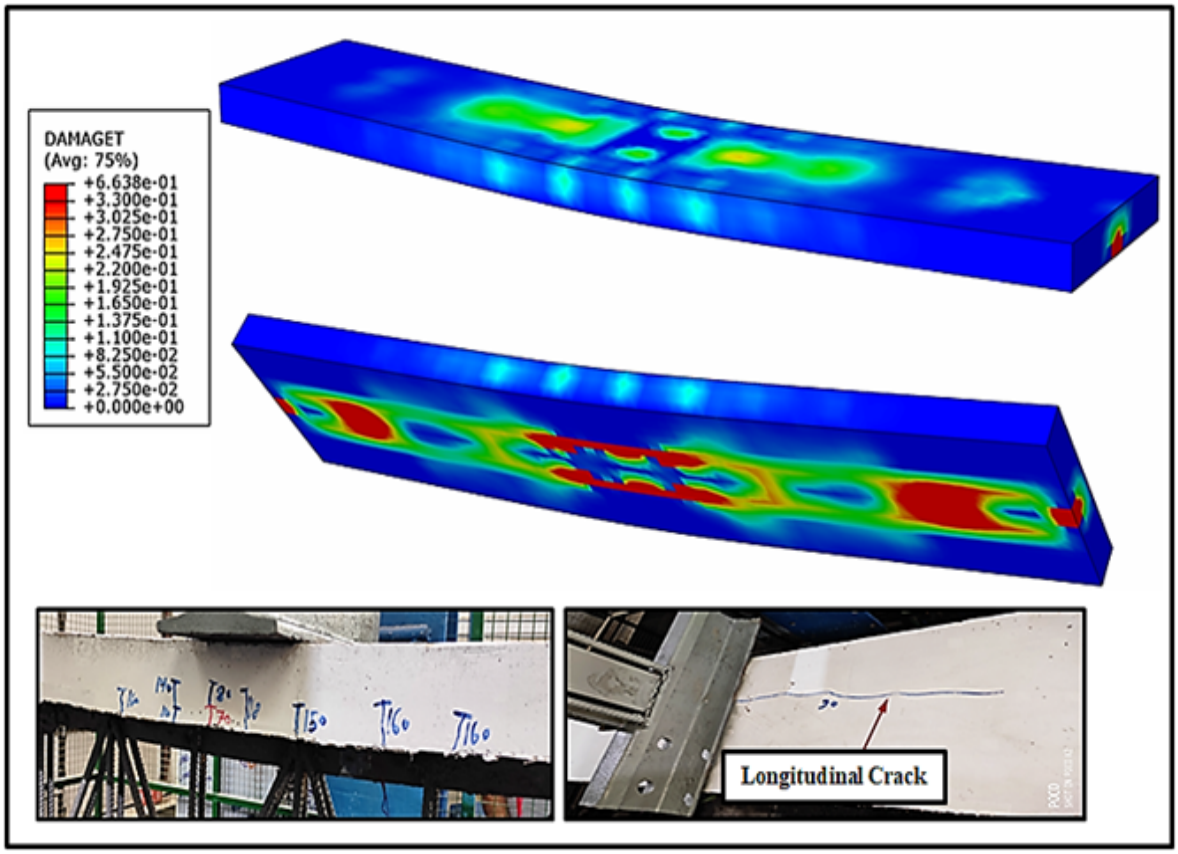

Figure 6.63 Tensile cracks in the concrete slab of CSJ 1-1 SF 5.1 specimen.

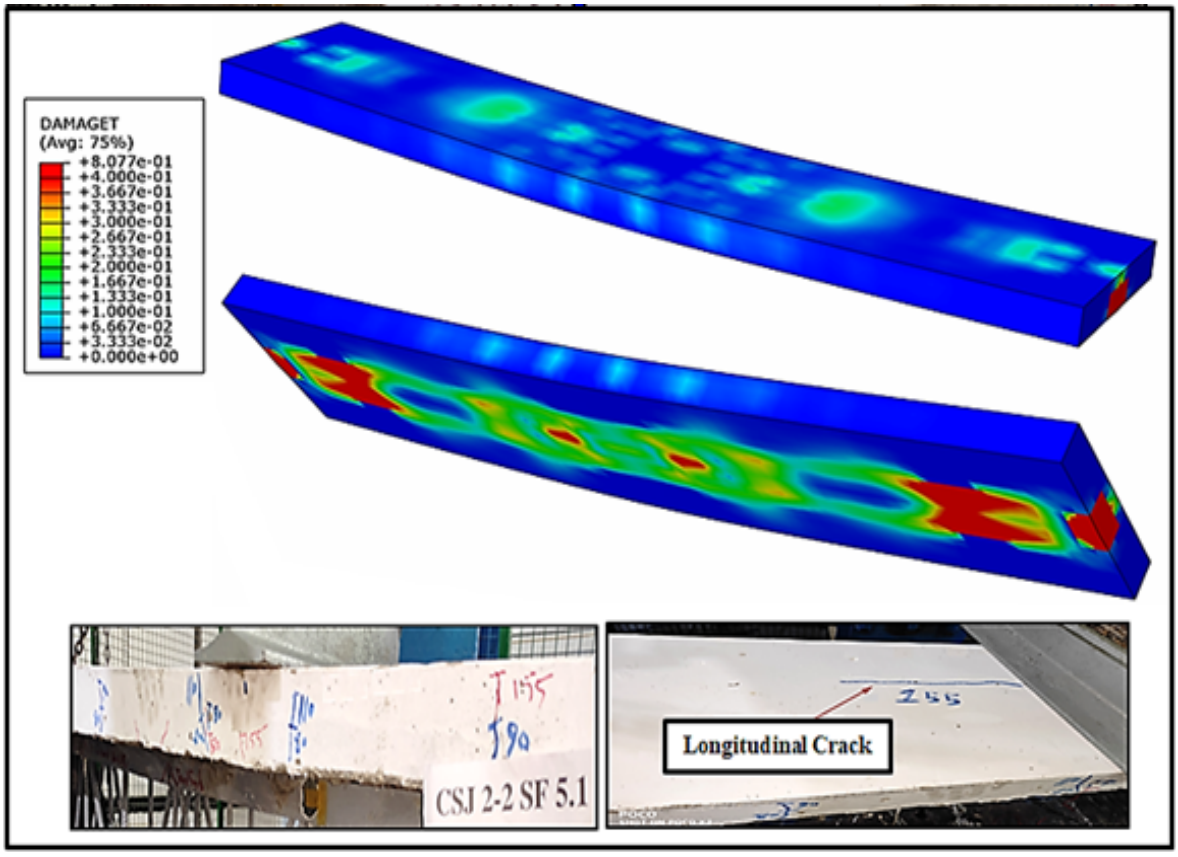

Figure 6.64 Tensile cracks in the concrete slab of CSJ 2-2 SF 5.1 specimen.

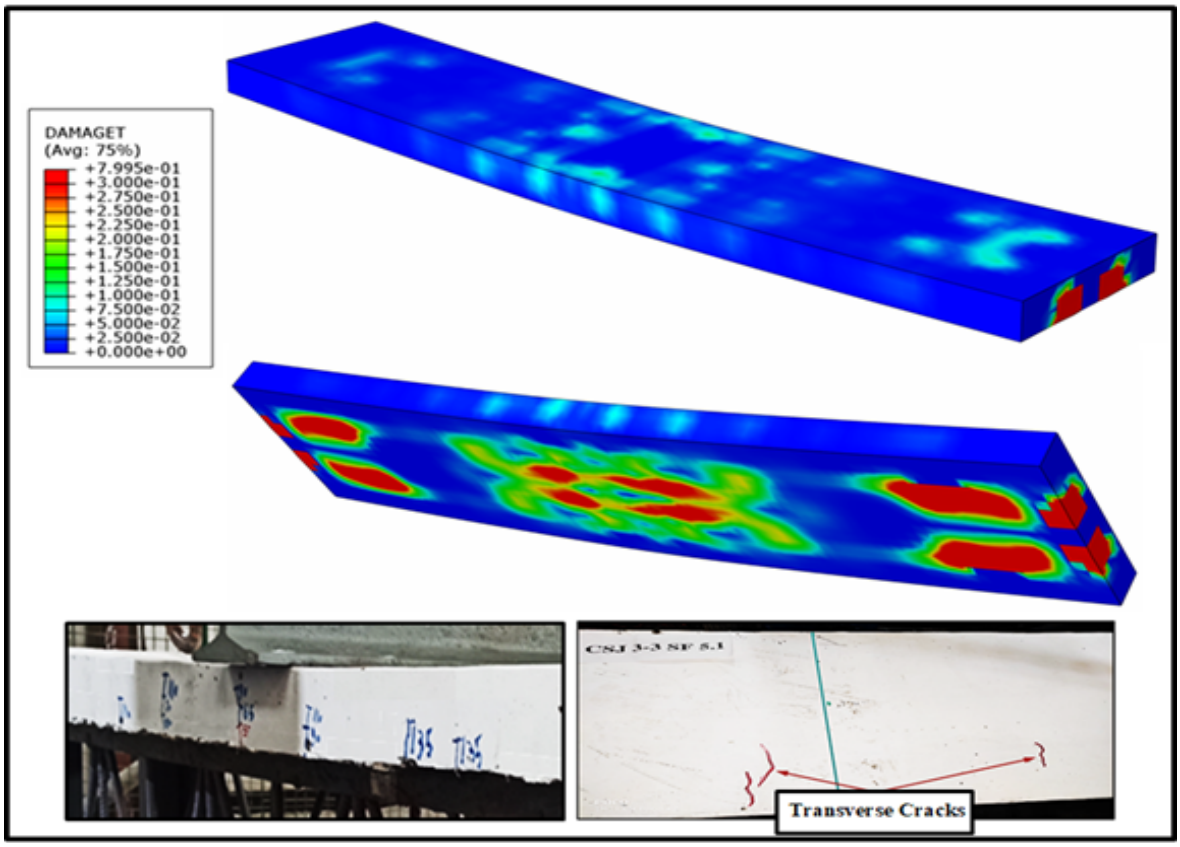

Figure 6.65 Tensile cracks in the concrete slab of CSJ 3-3 SF 5.1 specimen.

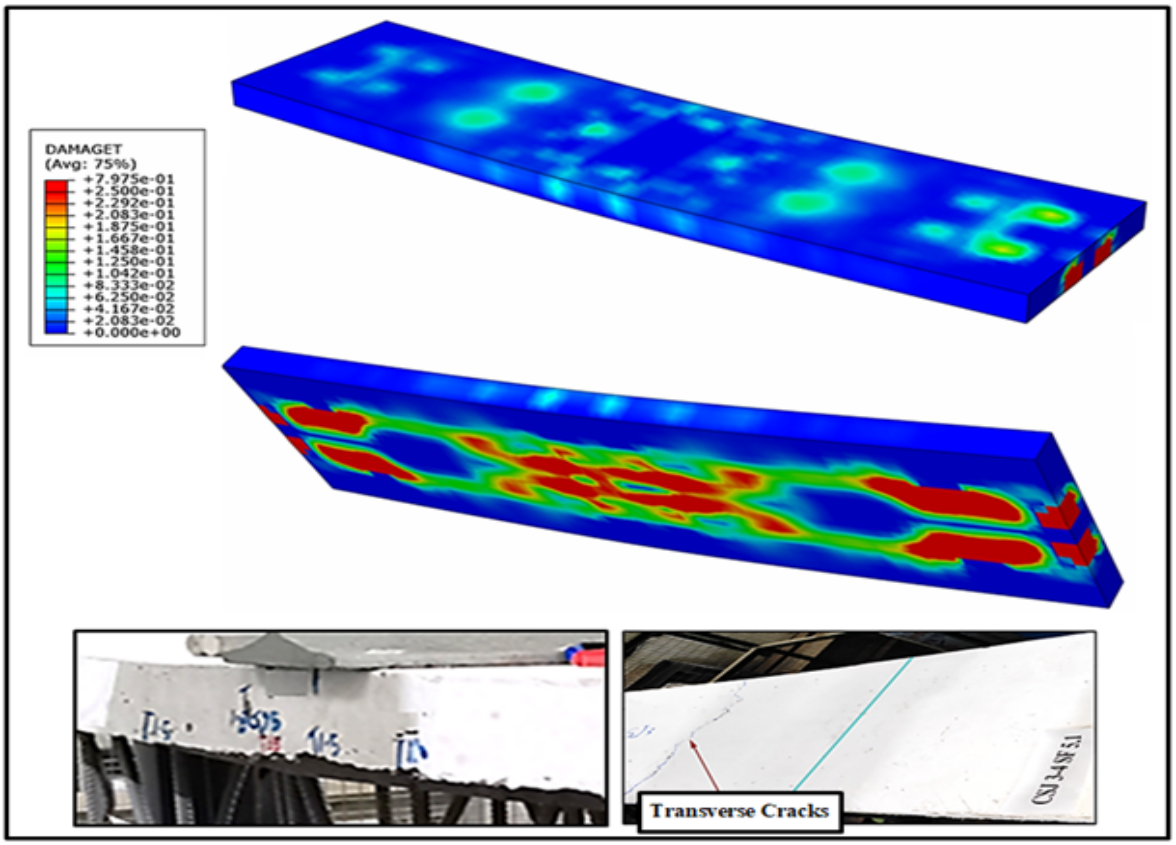

Figure 6.66 Tensile cracks in the concrete slab of CSJ 3-4 SF 5.1 specimen.

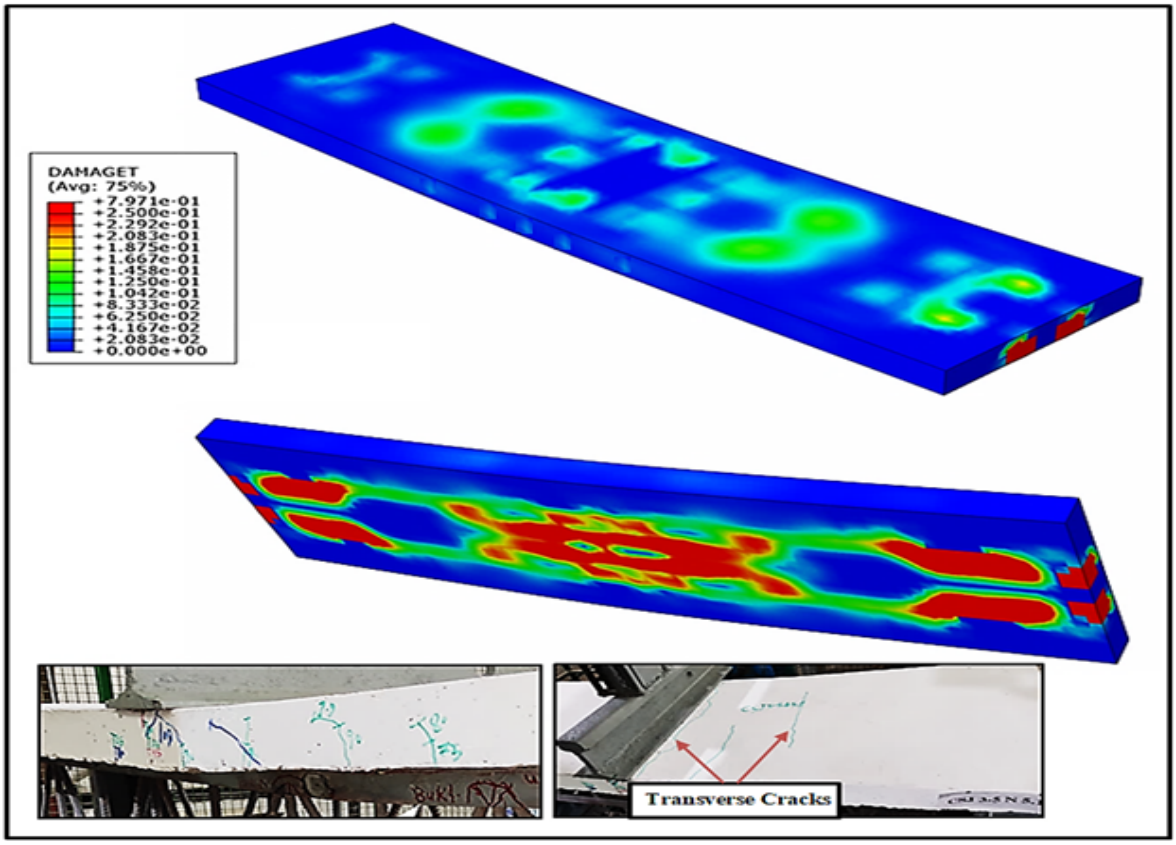

Figure 6.67 Tensile cracks in the concrete slab of CSJ 3-5 N 5.1 specimen.

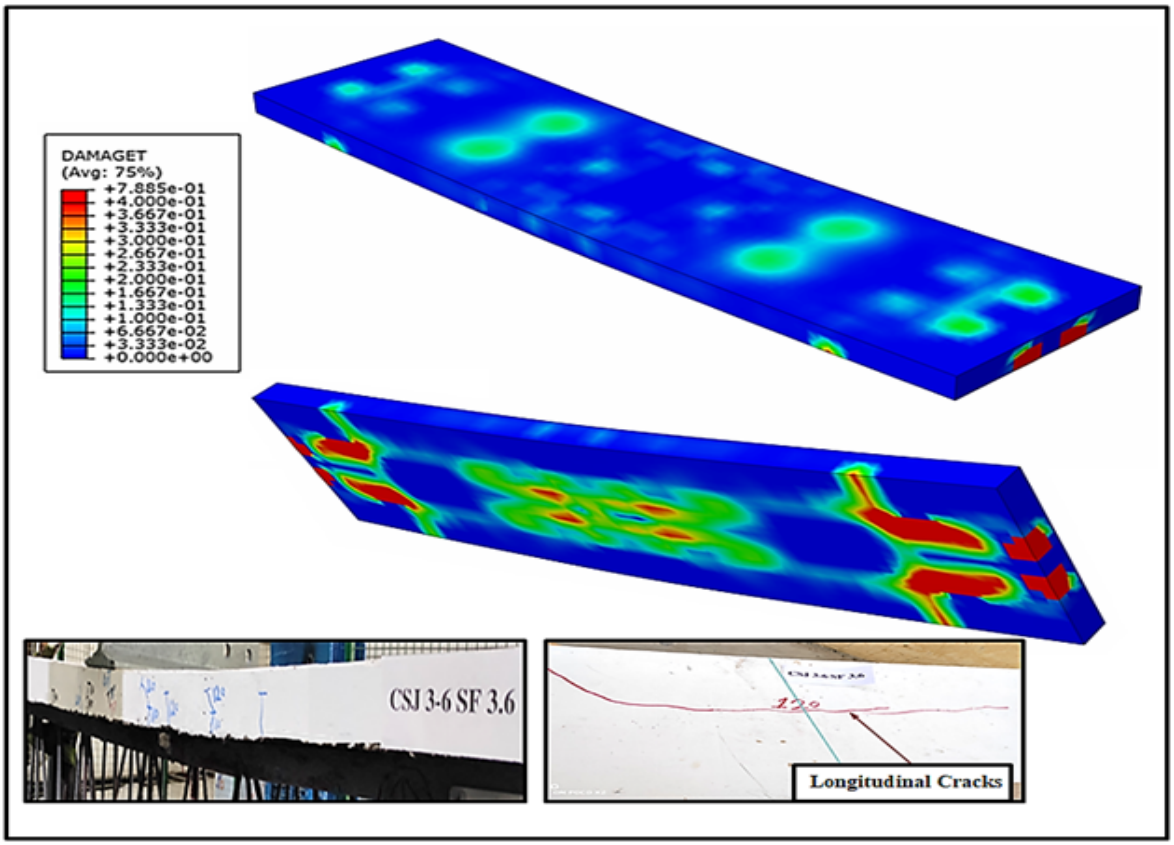

Figure 6.68 Tensile cracks in the concrete slab of CSJ 3-6 SF 3.6 specimen.

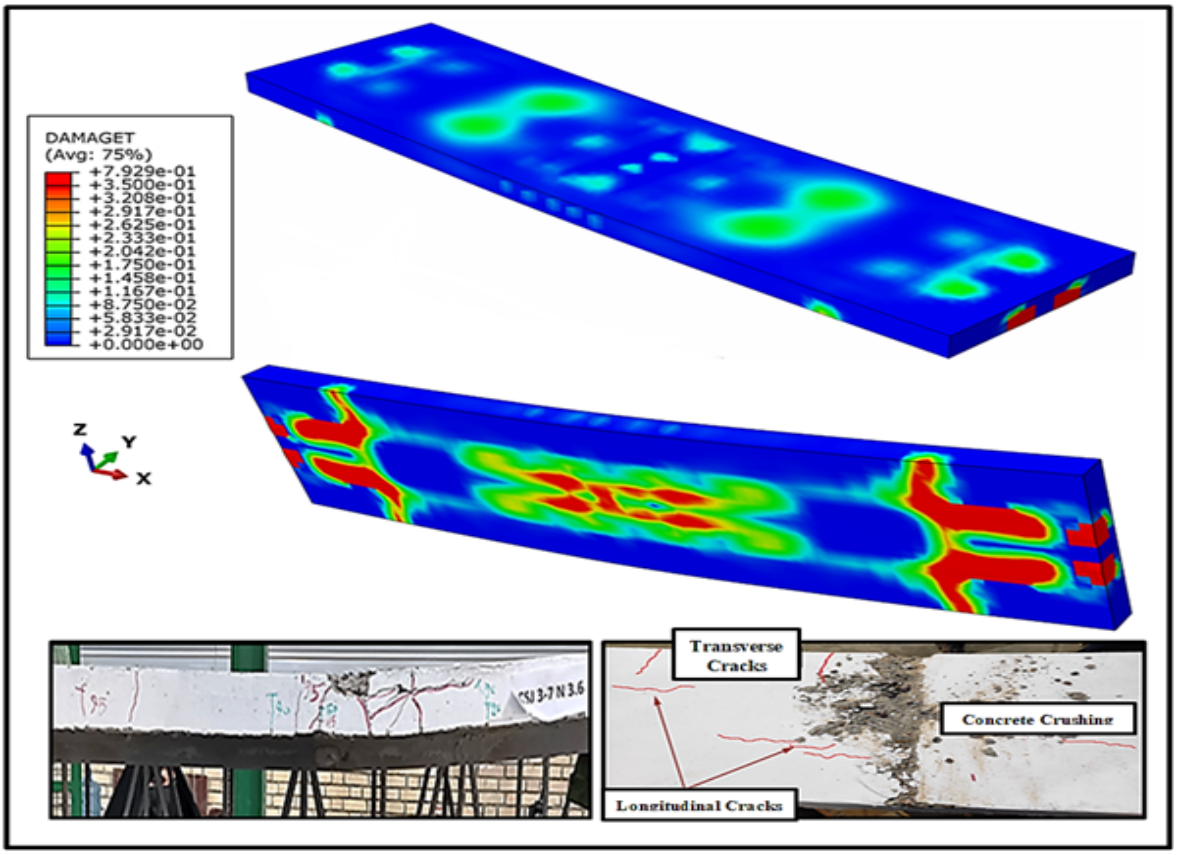

Figure 6.69 Tensile cracks in the concrete slab of CSJ 3-7 N 3.6 specimen.

CHAPTER 7

CONCLUSIONS AND RECOMMENDATIONS

7.1 CONCLUSIONS

The present study adopted a new type of Hybrid open web steel joist girders used to manufacture a composite open web steel joist, thus an experimental test was carried out to study the behavior of these two structural elements. The following conclusions were drawn from the present experimental investigation.

7.2 EXPERIMENTAL TEST RESULTS

7.2.1 Shear and Flexural Results of Hybrid Open Web Steel Joists

1- For all models of HOWS joists, a crimped-end web members failure occurred due to the local buckling of the diagonal interior web members near the supports before mid-span, but when increasing the diameter bar of interior webs by about (24.48%), the strain at the compression end web member was decreased about (63%).

2- when the L/D decreased, the improvement of the ultimate capacity was very slight, about 1.81 %; this slight increase was in the case of using the same bar diameter for the interior web used in prefabricated joists with L/D of 5.1 and joists with L/D of 3.6; but, when the interior web's bar diameter was increased by about (24.48 %), which led to a decrease in the slenderness ratio of the diagonal interior web members for HOWSJ, the increasing in the ultimate capacity of became about 25.7% and the deflection decreased by about 11.3%.

3- The shape of the cross-section of HOWSJ had a significant effect on their behavior, where for the HOWSJ, which was fabricated by welding angles of the top and bottom chord back to back, the ultimate capacity was increased by almost (7.4%) and (14.5%) when compared with specimens which were fabricated by welding angles of the chords either face-to-face without a gap or face-to-face with a gap.

4- The results indicated that the stiffness of specimens with back-to-back welded angles cross-section was significantly higher than those with face-to-face without a gap and those with face-to-face with a gap cross-section by about (11.7%) and about (14.7%), respectively.

5- Regarding the index of hardness, the results of tests showed that the HOWSJ specimens which had back-to-back welded angles cross-section shapes had the highest hardness value among other specimens, which was about (20.4%) higher than the specimens which had face-to-face without a gap cross-section shape, despite a significant increase in the hardness compared with specimens which had face-to-face with a gap cross-section shape by about (35.98%).

6- On the other hand, it found that the ductility of the HOWSJ increased when the width of the chords of HOWSJ increased, which led to an increase in the distance between the interior web members in the cross-section direction of the joist. As mentioned that for model C the value of the capacity has decreased by almost(14.5%), while the ductility index has increased by (34.3%) compared with Model A, and this was a significant increase for the ductility index, which is considered one of the essential factors in structures design. Therefore, sections similar to Model C can be used, but at the same time, must be found a way to strengthen the top cord against local buckling to increase the stiffness of this model.

7- Finally, comparing by shape of cross- section it can be concluded that Model A was the best among the models in terms of the ultimate load capacity, the flexural stiffness, and the flexural failure mode. As for Model C was the best in terms of ductility, while Model B had a moderate behavior between Models A and B.

7.2.2 Lateral Torsional Buckling Results of HOWSJs

1- From the experimental test, it can be noticed that the HOWSJ models, which had back-to-back welded angles cross-section, had a small lateral deflections and rotations while the joist was still elastic, but these increased as the load

increased towards the elastic lateral buckling load and they accelerated after yielding originated and reached relatively high values as the failure load was approached. The ultimate failure mechanism was a buckling of the horizontal angles legs of the compression top chord, and a minimal local buckling in the mid-span interior web member occurred. All HOWSJ specimens for models A, D, and E had a slightly lateral buckling during the loading phase until they reached their ultimate capacity. At the same time, there was no buckling observed on the vertical leg of the top chord angles. This mode of failure is called flexural lateral-torsional buckling.

2- For the HOWS joists model, which had face-to-face with gap cross-section, the compressive stresses were increased near the horizontal legs of the angles of the top compression chord of the joists. The experimental work shows that these lateral deflections increased the compressive stresses near the horizontal and vertical legs of the top chord and interior inner web at the mid-span of the HOWSJ, and this failure occurred before reached to a maximum load. final failure was accompanied by high local buckling at the compression chord-web connection. This mode of failure is called flange distortional buckling.

3- Regarding HOWS joists which had face-to-face without gap cross-section, it was observed that they behavior lay between the behavior of two previous models. Also, it was observed that the lateral deflections increased the compressive stresses near the vertical legs of the top chord and the interior webs at the mid-span of the HOWSJ specimens. This mode of failure is called lateral distortional buckling, which is possible to occur for beams with slender flexible webs and rigid flanges.

4- A theoretical method was proposed in this study to find an equation that enables estimating the lateral stiffness rigidity value for each model based on the details of the cross-sections of these models and also on the slope of the lateral deformation curves obtained from the experimental test program, by using this equation it can be observed that lateral rigidity of Model with back to back cross-section increased by (60.3%) when compared with Model which had face to face with gap cross-

section and by (23%) when compared it with the model which had face-to-face welded angles cross-section.

5- The results also explained that the enhancement in lateral rigidity has reached (20.2%) for the model, which had back-to-back welded angles cross-section and the diameter of rebar of the interior web (15.8 mm), which may have added sufficient stability to the section against lateral buckling compared with another model which had the same cross-section shape but with a diameter of rebar of the interior web members of (11.97 mm), which led to the section's behavior being closer to the behavior of the slenderness sections.

6- When the slenderness ratio of the diagonal interior web members increased by (24.48%), the maximum normalized rotation and lateral deflection of the HOWS joist also increased at the ultimate load by about (13.2%) and (9.9%), respectively.

7- The rotation of HOWSJ specimens increased by about (42.5%) when the span to the depth ratio (L/D) decreased from (5.1) to (3.6) in the case of using the same diameter size of the interior web members. This increase in the rotation decreased to (33.8 %) when the diameter size of interior web members increased by about (24.48 %).

8- Regarding the specimens in which the shape of the top and bottom chords of the HOWSJ was face to face with gab was more stable against the lateral deformations than the other two cross-sections, where they have had a normalized rotation and lateral deflection less than specimens with a cross-section of back-to-back welded angles by about (25.1%) and (30.7%), respectively. Also, they had a rotation and lateral deflection less than of specimens with a cross-section of face to face without gap welded angles by about (7.3%) and (11.2%), respectively.

7.2.3 Push-Out Test Results

1- The specimens cast with steel fiber reinforced concrete with (1 %) fraction volume of steel fiber had a shear capacity of the connector that was approximately (7.87%) greater than the non fibrous concrete specimens.

2- The load-slip curves for both types of concrete had nonlinear behavior because the failure was caused by both the steel shear connector and the concrete at the same time.

3- Using fiber reinforced concrete with a (1%) fraction volume of steel fiber improved the stiffness and the toughness of the shear connector in the composite system.

4- There were no cracks or crushing in the vicinity of shear studs embedded in SFC slabs of push-out specimens in contrast to the specimens in which slabs were cast with NC, which was another advantage of adding steel fibers to the concrete.

5- At peak load, the relative slip is approximately (3.02 mm) for NC specimens and (2.53 mm) for SFC specimens. This means that using steel fiber with a fraction volume of (1%) reduced slip at the ultimate shear capacity by about (16.23 %).

6- The shear resistance of the new type of shear studs proposed in this paper for normal and steel fiber reinforced concrete can be calculated using conservatively specified equations in some standard design codes.

7.2.4 Results of COWS Joists

1- Among the seven COWSJ Specimens, one distinct mode of concrete crushing was observed after bottom chord yielding. This mode was governed by the span/depth ratio and the type of concrete deck slab, where for the composite joist, which has a span/depth of 3.6 and casted with non fibrous concrete, excessive concrete crushing under the mid-span load has occurred. Also, a lower initial visible crack load was observed when the span/depth ratio decreased from 5.1 to 3.6.

2- The experimental results showed that the shape of the cross-section of the HOWSJ used to manufacture the COWSJ specimens had a significant effect on the behavior of the COWSJ specimens, where the OWSJ specimen, which had manufactured by using a HOWSJ with a cross-section of back to back welded angles was had ultimate load capacity greater than the specimens which were

manufactured by using face to face and face to face with gap cross-section by about (2.91%) and (13.89%), respectively. But at the same time, this specimen had a deflection at the ultimate load less than the other two specimens by about (4.01%) and (18.33%), respectively. From these results, it can be concluded that the specimens made of HOWSJ had a face-to-face with gap cross-section that was more ductile than the other two COWSJ specimens; in other words, they had more extended load versus deflection curves.

3- The results revealed that when increasing the width of the deck slab by about (20%) (i.e., the location of the neutral axis of COWSJ moved up), the failure load of the specimens was closed, but the normalized load- mid-span deflection showed that there was a slightly increased in the stiffness of the COWS joists, and the normalized deflection was decreased by (19.58%).

4- From the experimental results, it can be concluded that the maximum load capacity of the COWS joists casted of SFRC was more than that for the specimens casted of NC. the percentage of increase in the ultimate capacity was not exceed (3.89 %). From these comparisons, it can be concluded that when using the SFRC on COWSJS, the ultimate strength enhancement was slightly affected because on all COWSJS specimens, the failure mode was due to the steel joist failure before reaching the concrete slab to its ultimate strength. And when comparing the results of the mid-span deflection, it can be noticed that the increment in the deflection of specimens casted with SFRC was not exceeding (3.60%) compared with specimens casted with NC .

5- It can be concluded that the type of concrete used to cast the concrete slab of COWSJ was enhanced each of the ultimate strength, the ductility, and the stiffness of the specimens slightly, and these little enhancements may be because of the difference between the compressive strength of NC and SFRC which used in this study was not exceed (9.46%).

6- COWS joists with a higher span/depth (L/D) ratio for the two types of concrete slab have normalized deflections that are approximately (31%) greater

than COWSJs with a lower L/D ratio. While decreasing the span/depth ratio improves the ultimate load capacity by about (3.66%) and (4.31%) for the NC deck slab and SFRC deck slab, respectively.

7- The relative slip between the concrete slab and the steel joist which occurred in specimens casted with SFRC was less than the slip of specimens casted using NC by about (3.45 %) for specimens with (L/D) ratio of (5.1), and about (4.98%) for specimens with (L/D) ratio of (3.6).

8- From the test results comparisons, it can be noticed that the type of concrete slab was affected by the span /depth ratio, where when the span/depth ratio was equal to (3.6), the strains of the top and bottom chords of the HOWSJ were decreased in case of using SFRC slab compared with NC slab specimens. In contrast, the strains of the top and bottom chords were increased when using the SFRC slab compared with the NC slab when the span/depth ratio was equal to (5.1).

9- From comparisons of the experimental results, it can be concluded that the increase of the slenderness ratio of the diagonal interior web members by (27.88%) yields to increase in the strain in the interior compression web members near the end supports by about (74%) for COWSJ specimens with SFRC slab and by about (69%) for COWSJ specimens with NC slab.

10- Using the deck slab of SFRC in the three COWSJ specimens either with back-to-back welded angles cross-section HOWSJ or with face to face without gap or by using face to face with a gap, was enhanced the ultimate load capacity, enhanced the stiffness of the specimens, and improved the stability of interior web members and chords, within a reasonable ductility comparing with the results of HOWSJ specimens.

11- The strain gauge readings showed that the top chord strains, bottom chord strains, and the interior web members strains of COWSJ specimens reached their yielding stress at a higher ultimate load capacity than the ultimate load capacity of HOWSJ specimens. And the strain gauge readings of the diagonal interior web tension members of the CSJ1-1 SF5.1, CSJ2-2 SF5.1, and CSJ3-3 SF5.1 were

less than that for HOWSJ Model A, Model B, and Model C by about (92.69%), (88.89%), and (88.17%), respectively.

7.3 FINITE ELEMENT RESULTS

1- The finite element program ABAQUS has been found adequate in simulating the behavior of the HOWS joists, where the maximum differences from the experimental test do not exceed (7.97%), and (10.72%) for the ultimate strength capacity and the mid-span deflection at ultimate load, respectively.

2- From the comparison between the experimental results and numerical analysis for the strain curves for all models. It can be noticed that the overall behavior was converged, so the model of the finite element analysis can simulate the behavior of HOWS in a good manner.

3- The comparison results of the numerical analysis of the lateral torsional buckling of the HOWSJ showed an accepted convergence with test results, where the differences for the rotation deformation and lateral deflection were less than (9%) and (6%), respectively.

4- Also, the finite element results for the COWS joist had a good agreement with the experimental results, where the maximum difference in the ultimate strength capacity, relative slip, and the mid-span deflection at ultimate load was not exceeded (9.5%), (9.89%), and (2.93%), respectively.

5- The shape of the tensile cracks in the concrete slab that occurred in the experimental tests for all COWSJ specimens was largely identical to that obtained from the theoretical results using the ABAQUS program.

6- The shapes and locations of the experimental deformations at failure load for all HOWS joist specimens and COWS joist specimens were coincided with analysis by numerical methods.

7- The models of finite element analysis showed a good simulation for the slip behavior of the composite beams, whether for specimens casted with SFRC or NC. It can be concluded that the types of contact between different materials modeled

in the finite element method adopted in this study can predict the specimens' behavior well.

7.4 RECOMMENDATIONS

From the present study and based on the experimental and numerical investigations it is recommended to study some topics related to the same structure:

1- Studying the behavior of the HOWS joists and COWS joists which adopted in this study under the impact load.

2- Studying the effect of using steel angles for top chord with size smaller than the angles which used for the bottom chord for the same joist.

3- Studying the behavior of HOWS joists used in this study without using the vertical interior web members.

4- Studying the effect of using UHPC in casting the composite open web steel joists. This may be used for enhancing strength and stiffness of the composite joists.

5- Studying the effect of using another shear connector type on the ultimate strength and stiffness of COWS joists.

6- Studying the behavior of the continuous COWS joists has a HOWS joists and SFRC deck slab.

7- Studying the effect of using a steel deck sheet for casting the concrete deck slab of COWS joists which proposed in this study.

REFERENCES

1. Rackham, J., Couchman, G. H. and Hicks, S. Composite slabs and beams using steel decking: best practice for design and construction. 2009.

2. Pashan, A. *Behaviour of channel shear connectors: push-out tests*. Ph.D. Thesis. University of Saskatchewan. 2006.

3. Ibrahim Muhammad, A. Behaviour of Open Web Steel Joist in Composite Deck Floor System. MSc. Thesis, University of Windsor, Ontario, Canad, 2015.

4. Moore, W. P. An overview of composite construction in the United States. *Composite Construction in Steel and Concrete*. ASCE. 1987. 1–17.

5. Uy, B. and Liew, J. Composite steel-concrete structures. *Civil Engineering Handbook,*, 2003.

6. Standard specification for CJ-series composite steel joists. American National Standard SJI 200 – 2015, Steel Joist Institute. 2016.

7. Canam Buildings.Joists and Joist Girders. https://www.canam-construction.com/wp-content/uploads/2014/12/15-3296-canam-joist-girder-catalogue-canada-mise-a-jour-07-2015web4.pdf. 2015.

8. Samuelson, D. and Fares, S. Composite Joists: New 2 ND Edition, Specifications and New Technical Digest No. 13, SJI Webinars. 2017.

9. Kwon, G. *Strengthening Existing Steel Girder Bridges by the use of Post-Installed Shear Connectors*. Ph.D. Thesis. Department of Civil, Architectural and Environmental, University of Texas at Austin. 2008.

10. Brothersen, B. F. and Holtermann, T. Bridging – How it Works and What to Work Around. 2017.

11. ACI Committee 544. Guide for Specifying, Mixing, Placing, and Finishing Steel Fiber Reinforced Concrete (ACI-544.1R-96), American Concrete Institute, Detroit. 1996. (Reapproved 2002).

12. ACI Committee 544 . Design considerations for steel fiber reinforced concrete, ACI 544.4R-89, American Concrete Institute, Detroit. 2006.

13. Edgington, J., Hannant, D. and Williams, R. Steel fiber reinforced concrete. *Current paper CP*, 1974. 69: 74.

14. Balaguru, P. N. and Shah, S. P. *Fiber-reinforced cement composites*. McGraw-Hill International edition, New York.1992.

15. ACI Committee 211 . Standard practice for selecting proportions for normal, heavy weight and mass concrete, ACI 211.1-91, ACI Manual of concrete practice. 1999.

16. Lembeck, H. G. *Composite design of open web steel joists*. Ph.D. Thesis. Washington University. 1965.

17. Wang, P. and Kaley, D. COMPOSITE ACTION OF CONCRETE SLAB AND OPEN WEB JOIST (WITHOUT USE OF SHEAR CONNECTORS). *ENGINEERING JOURNAL-AMERICAN INSTITUTE OF STEEL CONSTRUCTION INC*, 1967. 4(1): 10.

18. Tide, R. and Galambos, T. Composite open-web steel joists. *ENGINEERING JOURNAL-AMERICAN INSTITUTE OF STEEL CONSTRUCTION INC*, 1970. 7(1): 27.

19. Cran, J. *Design and testing composite open web steel joists*. 1972.

20. Atkinson, A. and Cran, J. The design and economics of composite open-web steel joists. *Canadian Structural Engineering Conference*. 1972, vol. 55.

21. Azmi, H. M. *Composite open-web trusses with metal cellular floor*. Ph.D. Thesis. 1972.

22. Fahamy, E. H. *Inelastic analysis of composite open-web steel joists*. Ph.D. Thesis. Thesis (M. Eng.)–McMaster University. 1975.

23. Robinson, H. and Fahmy, E. The design of partially connected composite open-web joists. *Canadian Journal of Civil Engineering*, 1978. 5(4): 611–614.

24. Leon, R. T. and Curry, J. H. Behavior of Long-Span Composite Joists. *Building Structures*. ASCE. 1987. 390–403.

25. Alsamsam, I. *An experimental investigation into the behavior of composite open web steel joists*. Ph.D. Thesis. University of Minnesota. 1988.

26. Patras, W. and Azizinimini, A. Open Web Composite Joist Systems Utilizing Ultra-High Strength Concrete. *MASc Thesis, College of Engineering and Technology, University of Nebraska–Lincoln, NE*, 1991.

27. Brattland, A. and Kennedy, D. L. Flexural tests of two full-scale composite trusses. *Canadian Journal of Civil Engineering*, 1992. 19(2): 279–295.

28. Easterling, W. S., Gibbings, D. R. and Murray, T. M. Strength of shear studs in steel deck on composite beams and joists. *Engineering Journal, American institute of steel construction*, 1993. 30(2): 44–54.

29. Mujagic, J., Easterling, W. and Murray, T. Design and behavior of light composite steel–concrete trusses with drilled standoff screw shear connections. *Journal of Constructional Steel Research*, 2010. 66(12): 1483–1491.

30. Hedaoo, N. A., Gupta, L. M. and Ronghe, G. N. Design of composite slabs with profiled steel decking: a comparison between experimental and analytical studies. *International Journal of Advanced Structural Engineering*, 2012. 4(1): 1–15.

31. Lakshmikandhan, K., Sivakumar, P., Ravichandran, R. and Jayachandran, S. A. Investigations on efficiently interfaced steel concrete composite deck slabs. *Journal of structures*, 2013. 2013.

32. Hadeed, A. F., Al-Hadithy, L. K. and Aziz, R. J. Experimental investigation on behavior of composite open web steel joists. *Al-Nahrain Journal for Engineering Sciences*, 2018. 21(3): 393–404.

33. de Seixas Leal, L. A. A. and de Miranda Batista, E. Experimental investigation of composite floor system with thin-walled steel trussed beams and partially prefabricated concrete slab. *Journal of Constructional Steel Research*, 2020. 172: 106172.

34. Timoshenko, S. and Gere, J. *Theory of Elastic Stability.* 2nd ed., McGraw-Hill, New York. 1961.

35. Xykis, C. and Galambos, T. V. Lateral torsional stability analysis of large order space frame systems. *Engineering Structures*, 1990. 12(4): 235–242.

36. Galambos, T. and Xykis, C. The effect of lateral bracing on the stability of steel trusses. *Journal of Constructional Steel Research*, 1991. 20(4): 251–258.

37. Put, B. M., Pi, Y.-L. and Trahair, N. S. Lateral buckling tests on cold-formed channel beams. *Journal of Structural Engineering*, 1999. 125(5): 532–539.

38. Zirakian, T. and Showkati, H. Experiments on distortional buckling of I-beams. *Journal of Structural Engineering*, 2007. 133(7): 1009–1017.

39. Sharifi, Y. and Tohidi, S. Lateral-torsional buckling capacity assessment of web opening steel girders by artificial neural networks - elastic investigation. *Journal of Frontiers of structural and Civil Engineering*, 2014. 8(2): 167–177.

40. Swamy, R. and Mangat, P. FLEXURAL STRENGTH OF STEEL FIBRE REINFORCED CONCRETE. *Proceedings of the Institution of Civil Engineers*, 1974. 57(4): 701–707.

41. Soroushian, P. and Lee, C.-D. Distribution and orientation of fibers in steel fiber reinforced concrete. *Materials journal*, 1990. 87(5): 433–439.

42. Nataraja, M., Dhang, N. and Gupta, A. Steel fibre reinforced concrete under compression. *Indian concrete journal*, 1998. 72(7): 353–356.

43. Poon, C. S., Shui, Z. and Lam, L. Compressive behavior of fiber reinforced high-performance concrete subjected to elevated temperatures. *Cement and concrete Research*, 2004. 34(12): 2215–2222.

44. Löfgren, I. Fibre-reinforced concrete for industrial construction. PhD Thesis, Department of Civil and Environmental Engineering, Chalmers University of Technology, Gothenburg, Sweden. 2005.

45. Nataraja, M., Nagaraj, T. and Basavaraja, S. Reproportioning of steel fibre reinforced concrete mixes and their impact resistance. *Cement and concrete research*, 2005. 35(12): 2350–2359.

46. Nagaraj, T. and Zahida Banu, A. Relative efficacies of different concrete mix proportioning methods. *J Struct Engg, India*, 1999. 26: 107–112.

47. Lau, A. and Anson, M. Effect of high temperatures on high performance steel fibre reinforced concrete. *Cement and concrete research*, 2006. 36(9): 1698–1707.

48. Yazıcı, Ş., İnan, G. and Tabak, V. Effect of aspect ratio and volume fraction of steel fiber on the mechanical properties of SFRC. *Construction and Building Materials*, 2007. 21(6): 1250–1253.

49. Thomas, J. and Ramaswamy, A. Mechanical properties of steel fiber-reinforced concrete. *Journal of materials in civil engineering*, 2007. 19(5): 385–392.

50. Olivito, R. and Zuccarello, F. An experimental study on the tensile strength of steel fiber reinforced concrete. *Composites Part B: Engineering*, 2010. 41(3): 246–255.

51. Syed Mazharul Islam, R. R. H. and Morshed, M. A. Z. Fiber-reinforced concrete incorporating locally available natural fibers in normal- and high-strength concrete and a performance analysis with steel fiber-reinforced composite concrete. *Journal Of Composite Materials*, 2012. 46(1): 111–122.

52. Mohod, M. V. Performance of steel fiber reinforced concrete. *International Journal of Engineering and Science*, 2012. 1(12): 1–4.

53. Rana, A. Some studies on steel fiber reinforced concrete. *International journal of emerging technology and advanced engineering*, 2013. 3(1): 120–127.

54. Sabariman, B., Soehardjono, A., Wisnumurti, W., Wibowo, A. and Tavio, T. Stress-strain behavior of steel fiber-reinforced concrete cylinders spirally confined with steel bars. *Advances in Civil Engineering*, 2018. 2018.

55. Gilani, A. M. *Various durability aspects of slurry infiltrated fiber concrete.* Ph.D. Thesis. Ph. D Dissertation in Middle East Technical University. 2007.

56. Zheng, Y., Wu, X., He, G., Shang, Q., Xu, J. and Sun, Y. Mechanical properties of steel fiber-reinforced concrete by vibratory mixing technology. *Advances in Civil Engineering*, 2018. 2018.

57. Suksawang, N., Wtaife, S. and Alsabbagh, A. Evaluation of elastic modulus of fiber-reinforced concrete. 2018.

58. Babaie, R., Abolfazli, M. and Fahimifar, A. Mechanical properties of steel and polymer fiber reinforced concrete. *Journal of the Mechanical Behavior of Materials*, 2019. 28(1): 119–134.

59. Assi, A. D. Estimation of some mechanical properties for similar & dissimilar Welded joints. *Wasit Journal of Engineering Sciences*, 2014. 2(1): 59–76.

60. Ogbunnaoffor, C., Odo, J. and Nnuka, E. The Effect of Welding Current and Electrode Types on Tensile Properties of Mild Steel. *International Journal of Scientific & Engineering Research*, 2016. 7(5): 1120–1123.

61. Nassar, A., Lefta, R. and Abdulsada, M. Experimental study of the effect of welding electrode types on tensile properties of low carbon steel AISI1010. *Kufa Journal of Engineering*, 2018. 9(4): 163–173.

62. ASTM. E8/E8M-09, Standard Test Methods for Tension Testing of Metallic Materials 1. ASTM International, Designation: E8/E8M– 09, 2010.

63. Rezaeian, A., Keshavarz, M. and Hajjari, E. Mechanical properties of steel welds at elevated temperatures. *Journal of Constructional Steel Research*, 2020. 167: 105853.

64. AL-Obaidi, A., Yasir, A. and Thahab, S. Influence of addition Tio_2 nanopartielcs on the mechanical properties of welding joints for low carbon steel base plate by electric arc welding. *Journal of Engineering Science and Technology*, 2020. 15(3): 2077–2089.

65. Topkaya, C., Yura, J. A. and Williamson, E. B. Composite shear stud strength at early concrete ages. *Journal of structural engineering*, 2004. 130(6): 952–960.

66. CP 117-1. Composite construction in structural steel and concrete. Simply-supported beams in building, 1965.

67. Hicks, S., Cao, J., McKenzie, C., Chowdhury, M. and Kaufusi, R. *Evaluation of shear connectors in composite bridges*. 602. 2016.

68. Siess, C. P., Viest, I. M. and Newmark, N. M. *Studies of slab and beam highway bridges: part III: small-scale tests of shear connectors and composite t-beams*. Technical report. University of Illinois at Urbana Champaign, College of Engineering, Engineering Experiment Station bulletin series 49, no.45. 1952.

69. Viest, I. *Investigation of stud shear connectors for composite concrete and steel T beams*. Technical report. Department of Theoretical and Applied Mechanics. College of Engineering. University of Illinois at Urbana-Champaign. 1955.

70. Viest, I. Test of Stud Shear Connectors, Parts I, II, III and IV. *Test Data, Nelson Stud Welding, Lorain, Ohio*, 1956.

71. Thurlimann, B. Fatigue and static strength of stud shear connectors. *Journal Proceedings*. 1959, vol. 55. 1287–1302.

72. Viest, I. M., Colaco, J. P., Furlong, R. W., Griffis, L. G., Leon, R. T. and Wyllie, L. A. Composite construction design for buildings. McGraw–Hill, New Yor, 1997.

73. Hosain, M. and Pashan, A. Channel shear connectors in composite beams: Push-out tests. In: *Composite Construction in Steel and Concrete V*. 501–510. 2006.

74. Wang, Q., Liu, Y., Luo, J. and Lebet, J.-P. Experimental study on stud shear connectors with large diameter and high strength. *2011 International Conference on Electric Technology and Civil Engineering (ICETCE)*. IEEE. 2011. 340–343.

75. Prakash, A., Anandavalli, N., Madheswaran, C. and Lakshmanan, N. Modified push-out tests for determining shear strength and stiffness of HSS stud connector-experimental study. *International Journal of Composite Materials*, 2012. 2(3): 22–31.

76. Titoum, M., Mazoz, A., Benanane, A. and Ouinas, D. Experimental study and finite element modelling of push-out tests on a new shear connector of I-shape. *Advanced Steel Construction*, 2016. 12(4): 487–506.

77. Yanez, S. J., Dinehart, D. W. and Santhanam, S. Composite steel joist analysis using experimental stiffness factor from push-out tests. *Journal of Constructional Steel Research*, 2017. 137: 1–7.

78. ASTM A370-15. Standard test methods and definitions for mechanical testing of steel products. West Conshohocken, PA 19428-2959, United States: ASTM International, 2015.

79. ASTM A 36/A 36M-19. Standard Specification for Carbon Structural Steel. ASTM International West Conshohocken (PA, USA), 2019.

80. ASTM A 615/A 615M. Standard Specification for Deformed and Plain Carbon-Steel Bars for Concrete Reinforcement. West Conshohocken: American Society for Testing and Materials, 2008.

81. AWS A5.1/A5.1M. Specification for Carbon Steel Electrodes for Shielded Metal Arc Welding. *American Welding Society*, 2012.

82. Maha, G. *Structural Behavior of Hybrid Reinforced Concrete Beam-Column Joints*. Ph.D. Thesis. University of Babylon, Babylon, Iraq. 2019.

83. Dhafer, M. *Experimental and Numerical Modeling of The Impact Behavior of Composite Ductal Decks Corrugated Web Steel Girders*. Ph.D. Thesis. University of Babylon, Babylon, Iraq. 2020.

84. Marwah, S. A. *Behavior of Composite Open Web Steel Joist Under Static and Repeated Loading*. Ph.D. Thesis. University of Technology, Baghdad, Iraq. 2020.

85. Iraqi Standard Specification No.5,Portland Cement. *Central Organization for Standardization & Quality Control (COSQC), Baghdad, Iraq*, 1984.

86. Iraqi Standard Specification No.45. Natural Aggregate Resources used in Concrete and Construction. *Central Agency for Standardization and Quality Control, Baghdad, Iraq*, 1984.

87. ASTM C 33/C 33M-08. Standard Specification for Concrete Aggregates. ASTM INTERNATIONAL, West Conhoshocken, PA. 2008.

88. IQS. 1703/1992. *Water used in concrete, Iraq*, 1992.

89. ASTM C494-19. Standard specification for chemical Admixtures for concrete. American Society for Testing and Material International. 2019.

90. AASHTO. Standard Specifications For Highway Bridges .Adopted by The American Association of State Highway Officials , Eleventh Edition,PP469. 1973.

91. Roger, L. B. and Frederick, S. M. *Structural steel designer's handbook, Fourth Edition, AISC, AASHTO, AISA, ASTM, AREAMA, and ASCE-07 Design Standards, The McGraw-Hill Companies,*. 2004.

92. ACI Committee 318. Commentary on Building Code Requirements for Structural Concrete (ACI 318-19) and Commentary (ACI 318R-19). 2019.

93. ASTM A 1064/A 1064M – 09. Standard Specification for Steel Wire and Welded Wire Reinforcement, Plain and Deformed, for Concrete. ASTM International, West Conshohocken, PA 19428-2959, United States. 2009.

94. ASTM C 143/C 143M – 12. Standard Test Method for Slump of Hydraulic-Cement Concrete. ASTM INTERNATIONAL, West Conshohocken, PA: www. astm. org. 2012.

95. BS 5400-5:2005. Steel, concrete and composite bridges—Part 5: Code of practice for the design of composite bridges. *British Standards Institution, BS*, 2005: 5400–5.

96. AWS, D. 1/D1. 1M: 2010 An American National Standard Structural Welding Code Steel, 2010.

97. ASTM C 39/C 39M – 18. Standard Test Method for Compressive Strength of Cylindrical Concrete Specimens. ASTM International. 2018.

98. ASTM C 78 – 02. Standard Test Method for Flexural Strength of Concrete (Using Simple Beam with Third-Point Loading). West Conshohocken, PA 19428-2959, United States.: ASTM International. 2002.

99. ASTM C 496/C 496M – 04. Standard Test Method for splitting tensile strength of cylindrical concrete specimen. West Conshohocken, PA 19428-2959, United States.: ASTM International. 2004.

100. ASTM C469 – 02. Standard test method for static modulus of elasticity and Poissons ratio of concrete in compression. Annu. B. ASTM Standard, vol. 4. 2002.

101. Flayyih, A. S. *Flexural Behavior of Reinforced Concrete Composite Continuous T-Beam with Hybrid Reinforcement under Repeated Load* . Ph.D. Thesis. University of Babylon, Babylon, Iraq. 2020.

102. Buckley, E. T., Dinehart, D., Green, P., Gross, S. and Yost, J. *Experimental study of open web steel joists with crimped critical web members*. Ph.D. Thesis. Villanova University. 2007.

103. AASHTO. LRFD. Bridge design specifications. 2nd ed. *American association of state highway and transportation officials, Washington, DC*, 1998.

104. ENV. 1994-2. Eurocode 4: Design of composite steel and concrete structures. Part 2:. *General rules and rules for bridges* . *CEN*, 1997.

105. GB. 50017–2017. Code for Design of Steel Structures. *Ministry of Housing and Urban-rural Development of Peoples' Republic of China, Beijing, China,*, 2017.

106. Galambos, T. V. and Surovek, A. E. *Structural stability of steel: concepts and applications for structural engineers*. John Wiley & Sons. 2008.

107. Kirby, P. and Nethercot, D. A. *Design for structural stability*. John Wiley & Sons. 1979.

108. Bažant, Z. 2.02-Stability of Elastic, Anelastic, and Disintegrating Structures, and Finite Strain Effects: An Overview. *Fundamental Theories and Mechanisms of Failure*, 2007: 47–80.

109. Salmon, C. G., Johnson, J. E. and Malhas, F. A. *STEEL STRUCTURES-Design and Behaviour*. Pearson Prentice Hall. 2009.

110. Lundh, H. Hållfasthetslära-Grundläggande hållfasthetslära. *Instant Book AB, Stockholm*, 2007.

111. Beyer, A. *On the Design of Steel Members with Open Cross-Sections Subject to Combined Axial Force, Bending and Torsion*. Ph.D. Thesis. Université de Lorraine. 2017.

112. Roberts, T. M. Influence of shear deformation on buckling of pultruded fiber reinforced plastic profiles. *Journal of Composites for Construction*, 2002. 6(4): 241–248.

113. Aguilar, J. M. V. *Lateral-Torsional Buckling Instability Caused by Individuals Walking on Wood Composite I-Joists*. Ph.D. Thesis. Virginia Polytechnic Institute and State University. 2012.

114. Systemes, Dassault. Abaqus 6.14 documentation–theory guide. *Providence, RI*, 2015.

115. Hibbitt, K., Karlsson, B. and Sorenson, E. ABAQUS/Standard theory manual. *Sorenson Inc*, 2016. 421: 422.

116. Tejchman, J. and Bobiński, J. *Continuous and discontinuous modelling of fracture in concrete using FEM*. Springer Science & Business Media. 2012.

117. Yu, T., Teng, J., Wong, Y. and Dong, S. Finite element modeling of confined concrete-II: Plastic-damage model. *Engineering structures*, 2010. 32(3): 680–691.

118. Saenz, L. P. Discussion of" Equation for the Stress-Strain Durve of Concrete" by Desayi and Krishana. *Proceedings of ACI*, 1964. 61(9): 1229–1235.

119. Tao, Y. and Chen, J.-F. Concrete damage plasticity model for modeling FRP-to-concrete bond behavior. *Journal of composites for construction*, 2015. 19(1): 04014026.

120. Massicotte, B., Elwi, A. E. and MacGregor, J. G. Tension-stiffening model for planar reinforced concrete members. *Journal of Structural Engineering*, 1990. 116(11): 3039–3058.

121. Pham, D.-D. and Nguyen, P.-C. Finite element modelling for axially loaded concrete-filled steel circular tubes. In: *CIGOS 2019, Innovation for Sustainable Infrastructure*. Springer. 75–80. 2020.

122. Malm, R. *Shear cracks in concrete structures subjected to in-plane stresses. Lic*. Ph.D. Thesis. Thesis, Royal Institute of Technology (KTH), Stockholm. 2006.

123. Rabbat, B. and Russell, H. Friction coefficient of steel on concrete or grout. *Journal of Structural Engineering*, 1985. 111(3): 505–515.

Appendix A Deflection Curves along the Span of the HOWSJ and COWSJ Specimens at Ultimate Load Capacity

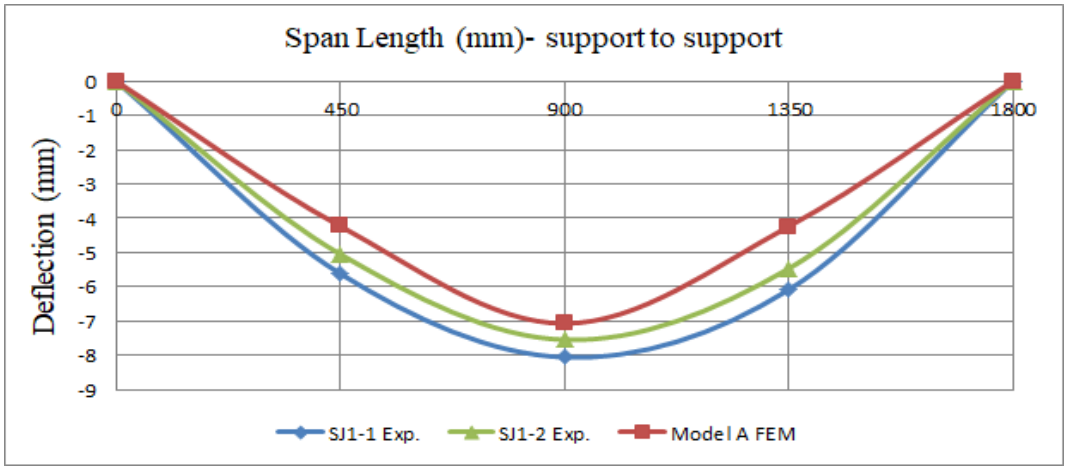

Figure A.1 Longitudinal deflection curves at ultimate load capacity for Model A specimens.

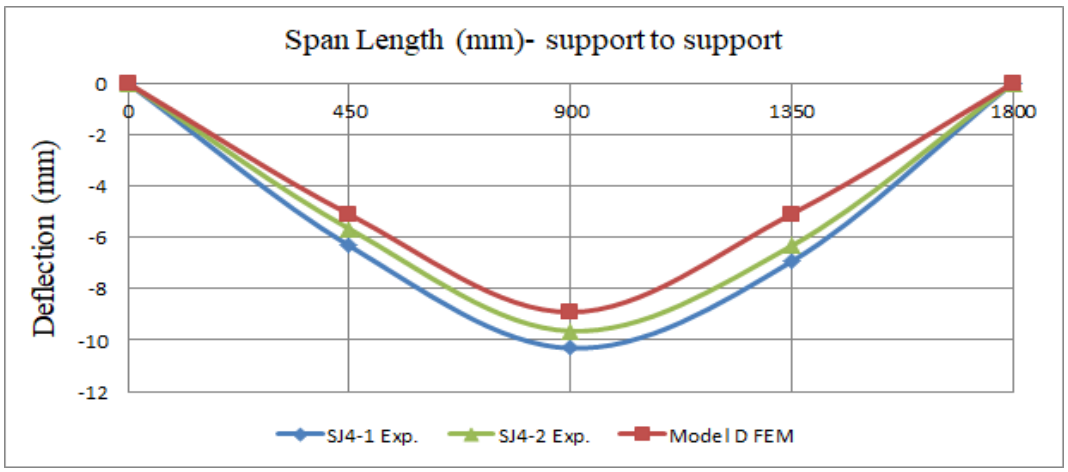

Figure A.2 Longitudinal deflection curves at ultimate load capacity for Model D specimens.

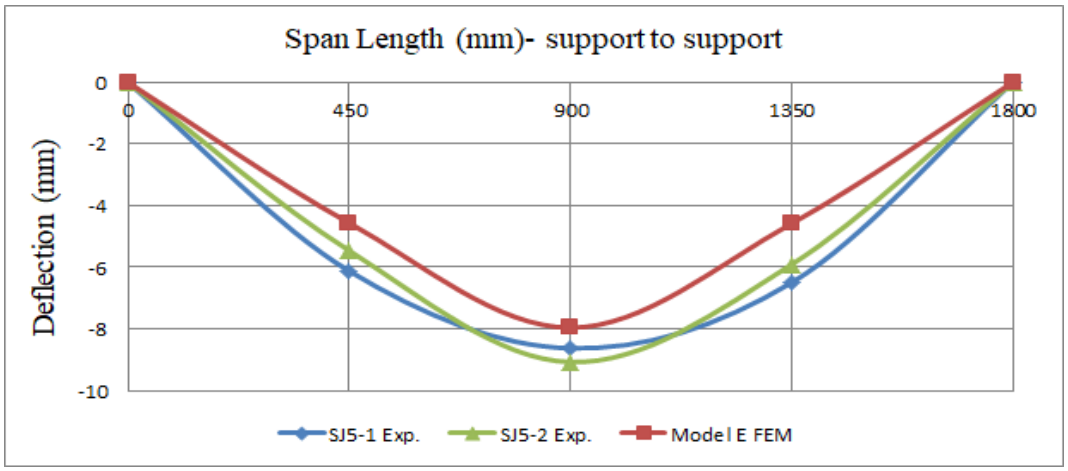

Figure A.3 Longitudinal deflection curves at ultimate load capacity for Model E specimens.

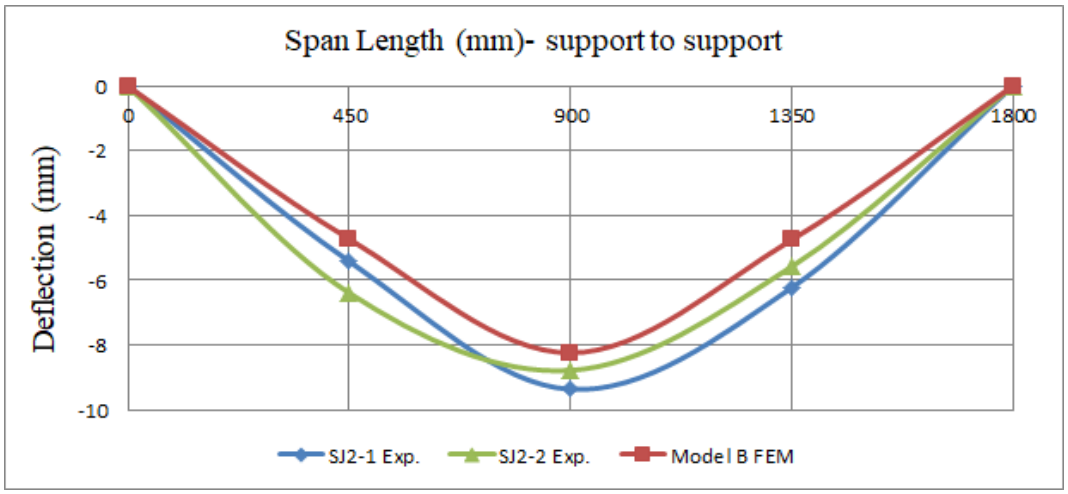

Figure A.4 Longitudinal deflection curves at ultimate load capacity for Model B specimens.

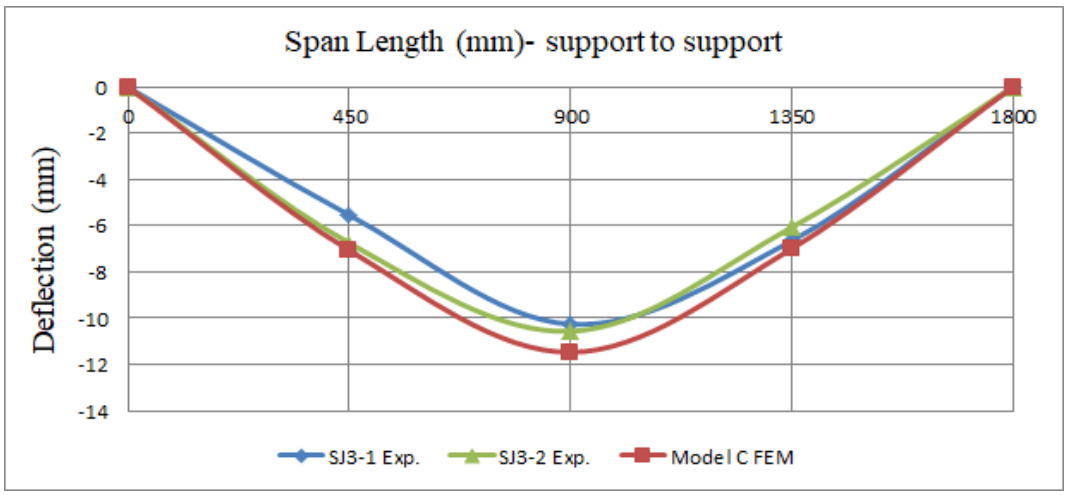

Figure A.5 Longitudinal deflection curves at ultimate load capacity for Model C specimens.

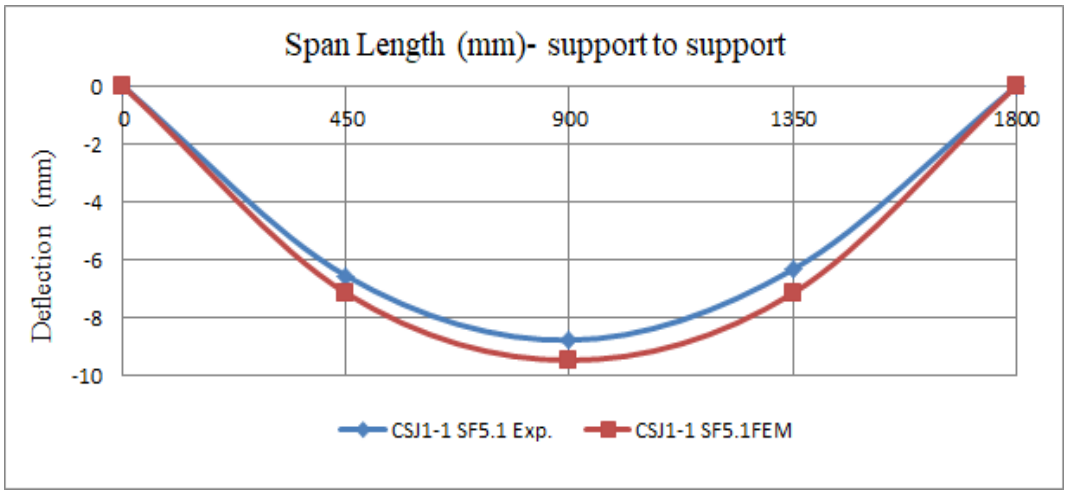

Figure A.6 Longitudinal deflection curves at ultimate load capacity for CSJ1-1 SF5.1 specimen.

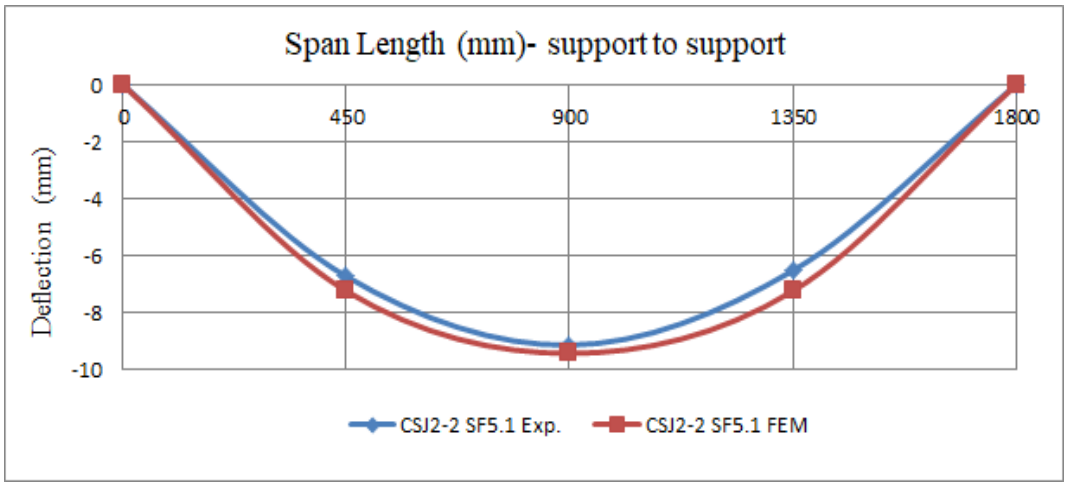

Figure A.7 Longitudinal deflection curves at ultimate load capacity for CSJ2-2 SF5.1 specimen.

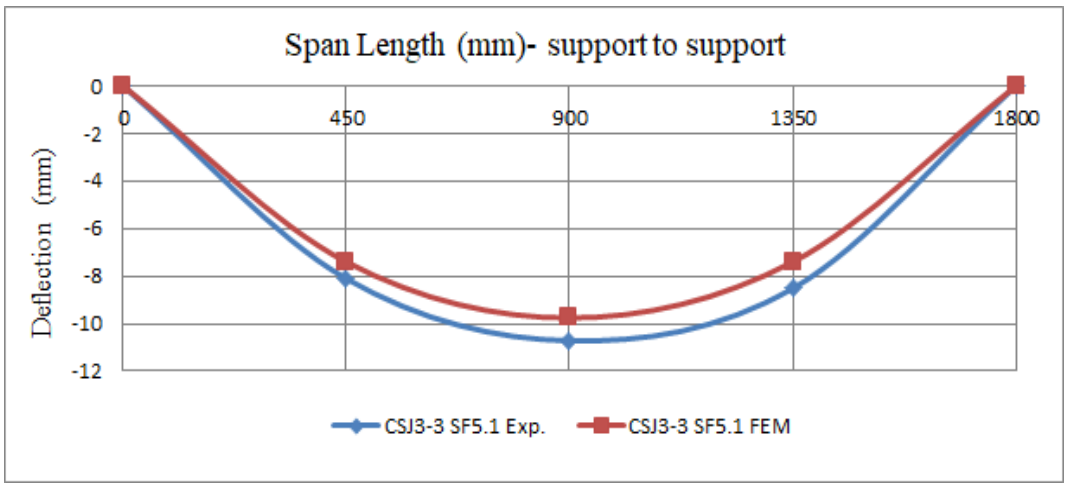

Figure A.8 Longitudinal deflection curves at ultimate load capacity for CSJ3-3 SF5.1 specimen.

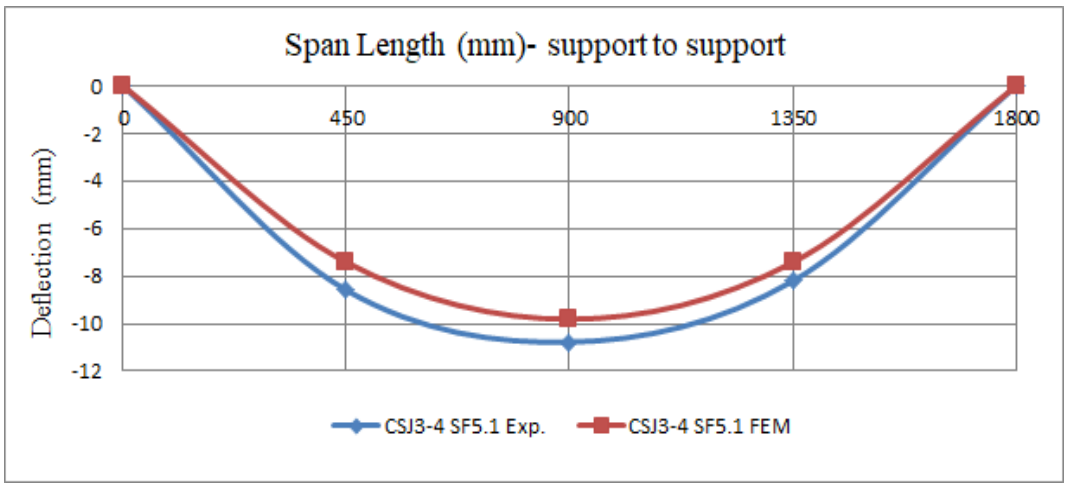

Figure A.9 Longitudinal deflection curves at ultimate load capacity for CSJ3-4 SF5.1 specimen.

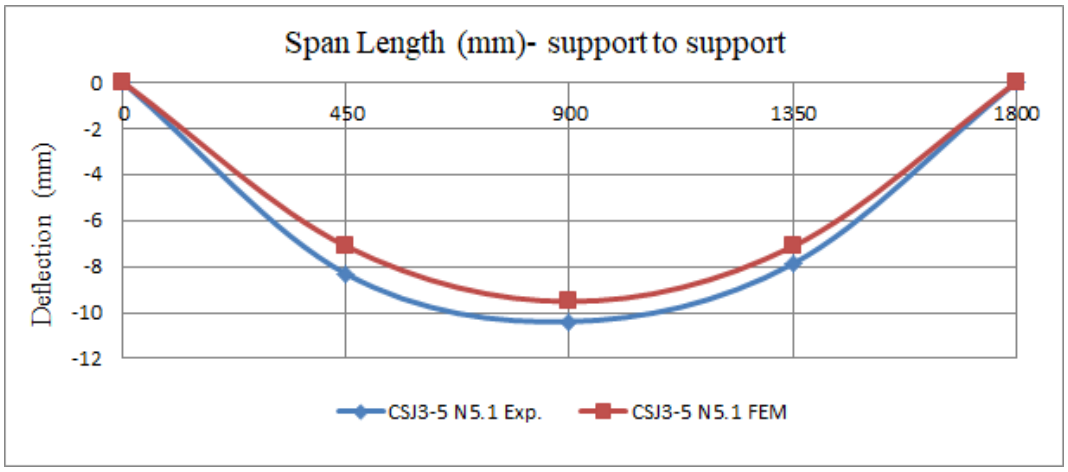

Figure A.10 Longitudinal deflection curves at ultimate load capacity for CSJ3-5 N 5.1 specimen.

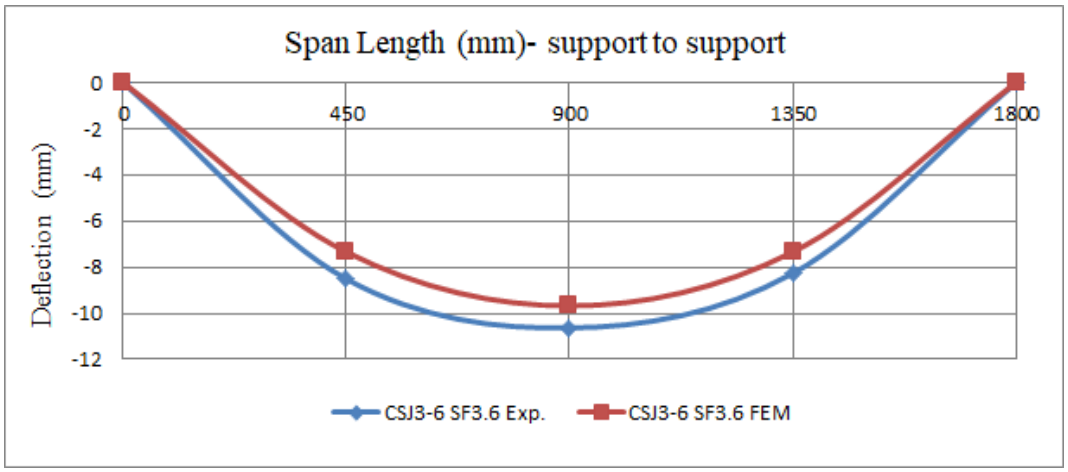

Figure A.11 Longitudinal deflection curves at ultimate load capacity for CSJ3-6 SF3.6 specimen.

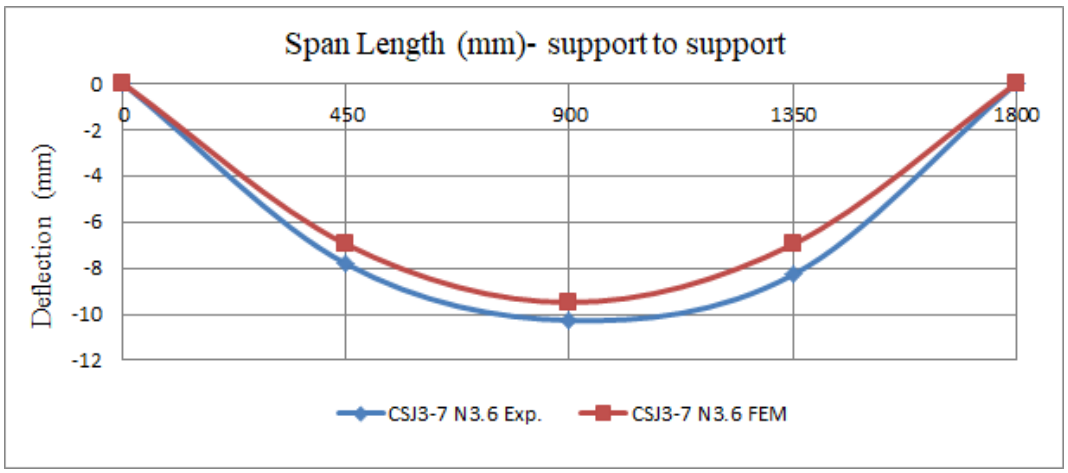

Figure A.12 Longitudinal deflection curves at ultimate load capacity for CSJ3-7 N3.6 specimen.

Appendix B Comparison of the Stud Shear Resistance with Some Design Codes

The shear stud resistance results from this experiment were compared to the ultimate shear resistance calculated from some commonly used design codes. Where the diameter of shear stud connector (d_s) adopted in this study was calculated as follows:

$$d_{stud} = 2\times diameter of (6mm) rebar = 2\times 5.95 = 11.9mm$$

1- The AASHTO LRFD [103] design code of the United States specified the ultimate shear resistance of studs embedded in concrete slabs as follows:

$$Q_r = 0.5 A_{stud}\sqrt{E_c f'_c} \leqslant (A_{stud} F_{ustud})(N) \tag{B.1}$$

2- According to Eurocode [104], the design strength of a shear stud with a height-to-diameter ratio greater than four ($h_{stud}/d_{stud} > 4$) was specified as follows:

$$P_{rd} = Min.[0.8 F_{ustud}(\pi d^2_{stud}/4)/\gamma_v, 0.29\alpha d^2_{stud}\sqrt{f_{ck}E_{cm}}/\gamma_v](N) \tag{B.2}$$

Where in the specimens of this research for ($h_{stud}/d_{stud} = 50/11.9 = 4.2 > 4$), $\alpha = 1.0$, and the partial factor (γ_v) should be equal to one when compared to the test results [74].

3- According to the standard specification for CJ-series composite steel joists [6], after installation, shear studs must extend at least (38 mm) above the top of the steel deck and have at least (13 mm) of concrete cover above the top of the installed studs, with ($d_{stud}/t_f < 2.7$),the shear resistance was specified as follows:

$$Q_n = Min.[o.5 A_{stud}\sqrt{f'_c E_c}, (R_p R_g A_{stud} F_{ustud}/1000)](kN) \tag{B.3}$$

Where: $t_f = 12.7mm$ for the steel section W10*30, thus ($d_{stud}/t_f = 11.9/12.7 = 0.94 < 2.7$) in the specimens of this research. And for no decking condition, $R_p = 0.75$ and $R_g = 1.0$.

4- For calculating shear strength of welded stud connectors, GB 50017 [105] includes Equation (B.4) as:

$$Q_u = 0.5 A_{stud}\sqrt{E_c f'_c} \leqslant 0.7 A_{stud} F_{ustud})(N) \tag{B.4}$$

Appendix C Specification of Superplasticizer

Construction

Product Data Sheet
Edition 2/2018/001
Version 01
Sika ViscoCrete® F180G

Sika ViscoCrete® F180G

High performance super plasticizer

Product Description

Sika ViscoCrete® F180G is a third generation admixture for concrete and Mortar.

Uses

Sika ViscoCrete® F180G is a high range water reducer that provides long Workability times, so it is used for the following applications:

- Ready mix concrete production
- High performance concrete production
- Concrete in hot and windy weather with extended workability time
- Impermeable and dense concrete with smooth surface (Related to concrete job mix).
- Production of complex and fine elements such as floor slabs, foundations, walls, Beams and columns even through congested reinforcement.
- Concrete mixes containing Silica Fume: GGBFS, Fly ash or PFA.
- Self-Compacting Concrete (SCC) production.

Characteristics / Advantages

Sika ViscoCrete® F180G is a dual impact admixture and when it is used, the Surface adsorption and sterical effects will separate the binder particles. This will Result in the achievement of the following properties.

- Extremely high water reduction, resulting in high density and high strength.
- Early and late strength highly increased.
- High plasticizing effect, resulting in improved flow ability, placing and compacting Behavior.
- Suitability for both summer and winter conditions and pump ability thanks to its long time Consistency
- Increased frost resistance
- Chloride-free, thus harmless to the reinforcing steels,
- Reduced rate of carbonation of the concrete
- Reduced tendency of shrinkage
- No need for vibration, thus no noise pollution
- eliminate the heat curing and energy required for placing, compaction and curing.

Tests

Approval/Standards Conforms to the requirements of ASTM C494-Type F &G, C1017 Type I & II

Product Data

Form

Appearance Transparent/Turbid

Packaging	1000 Kg (IBC) /250 KG/20 Kg/4 Kg Jerry cans Bulk Tanks packing available upon request

Storage

Storage Conditions / Shelf Life	12 months from date of production if stored properly in original and unopened Packaging, in dry conditions at temperatures between +5°C and +35°C. Protect From excessive temperature, direct sunlight and frost.

.

Technical Data

Chemical Base	Modified poly carboxylates based polymer
Density	1.061 +/- 0.01 kg/l at liquid Temp. 20°C
pH Value	4.5-6

System Information

Application Details

Consumption / Dosage

Depending on the expected concrete performance, it is used at a rate of:

- For plastic concrete: 0.5 to 1% by weight of binder (500–1000 g for 100 kg Cement).
- For self-compacting concrete: 1 to 1.8% by weight of binder (1000–1800 g for 100 kg cement).

When adjusting the consistency, high water retarding feature of the additive must Be taken into account when using Dosage above than 1.3% and excessive water addition to the mixture must be prevented.

Effect of Over Dosage

The overdosing of Sika Viscocrete F180G may result the Following:

- Delay of initial setting (Related positively with increased quantity of admixture)
- Higher workability
- Higher Early and final Strength

Application Conditions/Limitations

Compatibility

Sika ViscoCrete® F180G may be combined with following Sika admixtures.
-Sika Aer®
-Sika Pump®
-Sika Rapid®
-SikaFume® HR
-Sika Retarder®
-Sika Ferrogard®-901
-Sika Fibre®
-Sika Antifreeze®
Trails are always recommended before combining products.

Application Instructions

Dispensing	Sika ViscoCrete® F180G Can be added to the gauging water at the plant. And can be added into the concrete mixer in situ (Added water amount in plant should be considered in this case to avoid massive concrete fluidity)

Application Method / Tools

The standard rules of good concreting practice, concerning production as well as Placing, are to be followed. Refer to relevant standards. Fresh concrete must be Cured properly.

Cleaning of Tools

Clean all tools and application equipment with water immediately after use.
Hardened / cured material can only be mechanically removed.

Notes on Application / Limitations

When using Sika ViscoCrete® F180G, a suitable mix design has been taken Into account and local material sources should be trialed.
Sika ViscoCrete® F180G should not be added to dry cement.
When using Sika ViscoCrete® F180G for the production of self-compacting Concrete, suitable mix design must be taken into account. Before application, suitability tests must be performed.

Notes

All technical data stated in this Product Data Sheet are based on laboratory tests. Actual measured data may vary due to circumstances beyond our control.

Local Restrictions

Please note that as a result of specific local regulations the performance of this Product may vary from country to country. Please consult the local Product Data Sheet for the exact description of the application fields.

Health and Safety Information

For information and advice on the safe handling, storage and disposal of chemical Products, users should refer to the most recent Material Safety Data Sheet Containing physical, ecological, toxicological and other safety-related data.

Legal Notes

The information, and, in particular, the recommendations relating to the application And end-use of Sika products, are given in good faith based on Sika's current Knowledge and experience of the products when properly stored, handled and Applied under normal condilions in accordance wilh Sika's recommendations. In Practice, the differences in materials, substrates and actual site conditions are such That no warranty in respect of merchantability or of fitness for a particular purpose, Nor any liability arising out of any legal relationship whatsoever, can be inferred Either from this information, or from any written recommendations, or from any Other advice offered. The user of the product must test the product's suitability for The intended application and purpose. Sika reserves the right to change the Properties of its products. The proprietary rights of third parties must be observed. All orders are accepted subject to our current terms of sale and delivery. Users Must always refer to the most recent issue of the local Product Data Sheet for the Product concerned, copies of which will be supplied on request.

Sika IRAQ L.L.C
Erbil,Baghdad
Basrah
IRAQ

info.iraq@iq.sika.com
www.sika.com

جمهورية العراق
وزارة التعليم العالي والبحث العلمي
جامعة بابل
كلية الهندسة
قسم الهندسة المدنية

سلوك القص والانحناء لعوارض الروافد الفولاذية الهجينة المصنعة الساندة لبلاطات خرسانية مسلحة بألياف

أطروحة مقدمه الى جامعة بابل كلية الهندسة قسم الهندسة المدنية كجزء من متطلبات نيل درجة الدكتوراه فلسفة في الهندسة الإنشائية

من قبل

جنان نعمة ياسر الموسوي

بكالوريوس هندسه مدنيه، جامعة الكوفة 1998
ماجستير هندسه إنشائية، جامعة الكوفة 2002

اشراف

الاستاذ الدكتور هيثم حسن متعب الدعمي

1443 ذو الحجة

2022 تموز

الخلاصة

تألف البرنامج التجريبي لهذه الدراسة من تصنيع واختبار مجموعتين من العينات ، تم اختبار جميع العينات تحت الحمل الساكن. تكونت المجموعة الأولى من عشرة روافد فولاذية هجينة مفتوحة الوترات ، و كان لكل زوج من هذه المجموعة نفس المقطع العرضي ودرست ثلاثة متغيرات لكل مقطع عرضي. وكان المتغير الأول هو شكل المقطع العرضي للرافدة ، بينما كان المتغير الثاني هو نسبة الطول إلى العمق للروافد الفولاذية ، وكان المتغير الثالث هو تأثير قطر أعضاء الوترات الداخلية على القص والانثناء والالتواء الجانبي لهذه الروافد.

تكونت المجموعة الثانية من سبع عينات من الروافد الفولاذية المركبة ذات الوترات المفتوحة . تم اختبار ثلاث عينات ذات شكل مقطع عرضي مختلف لـهذه الروافد المركبة، لدراسة تأثير شكل المقطع العرضي للروافد الفولاذية المفتوحة الوترات على سلوك الروافد الفولاذية المركبة ذات الوترات المفتوحة. بينما كانت أربعة منها تمتلك المقطع العرضي ذاته للروافد الفولاذية المفتوحة الوترات ، ولكن في نفس الوقت تم فحص العديد من المتغيرات عند اختبار هذه العينات و هذه المتغيرات كانت ، العرض الفعال لسطح البلاطة الخرسانية ، ونسبة الطول إلى العمق للروافد الفولاذية المفتوحة الوترات ، وكذلك تأثير نوع البلاطة الخرسانية حيث تم استخدام نوعين من الخرسانة في هذه الدراسة لصب البلاطة الخرسانية وهما الخرسانة المسلحة بالألياف الفولاذية والخرسانة غير المسلحة بألياف.

في هذه الدراسة ، تم استخدام نوع جديد من روابط القص ، لذلك تم إجراء اختبار الدفع لتحديد قوة القص وصلابة موصلات القص المطمورة في كل من الخرسانة غير المسلحة بألياف والخرسانة المسلحة بالألياف الفولاذية .تمت مقارنة النتائج التجريبية لمقاومة القص لهذا النوع من مسمار القص مع بعض مدونات التصميم القياسية ، وأظهرت النتائج أنه يمكن استخدام هذه المعادلات لحساب مقاومة القص لمسامير القص لكل من الخرسانة غير المسلحة بألياف والخرسانة المسلحة بألياف فولاذية.

أظهرت النتائج التجريبية للروافد الفولاذية المفتوحة الوترات أن نسبة الطول إلى العمق أثرت على سلوك تحليل الروافد، حيث عند نقصان هذه النسبة ، كان التحسن في قابلية التحمل النهائية للعوارض المركبة ضئيلًا جدًا ، حوالي (1.81٪) فقط ، كانت هذه الزيادة الطفيفة في حالة استخدام نفس القطر للوترات الداخلية المائلة المستخدمة في الروافد الفولاذية ذات نسبة طول/عمق يساوي 5.1 و للروافد التي تمتلك نسبة طول/عمق يساوي 3.6 ، ولكن عندما تم زيادة قطر الاوتار الداخلية بحوالي (24.48٪) و الذي ادى الى انخفاض في نسبة النحافة للوترات الداخلية المائلة أصبحت الزيادة في قابلية التحمل النهائية بحوالي 25.7 \٪ وانخفض الانحراف بنحو 11.3 ٪ . و كان لشكل المقطع العرضي للروافد الفولاذية المفتوحة الوترات أيضًا تأثيراً كبيراً على سلوك الرافدة الفولاذية ، حيث تم زيادة سعة التحمل القصوى تقريبًا (7.4٪) و (14.5٪) عند مقارنتها بالعينات التي تم تصنيعها بلحام الزوايا إما وجهاً لوجه بدون فجوة أو وجهاً لوجه مع فجوة ، بينما كان مؤشر الليونة لعينات الروافد الفولاذية المفتوحة الوترات والتي تم لحام مقاطع الزوايا الفولاذية للأوتار العلوية و

السفلية للرافدة وجهاً لوجه مع فجوة بقدر 1.52 و 1.35 مرة مؤشر ليونة للعينات التي تم لحام الزوايا فيها ظهر لظهر و وجها لوجه بدون فجوة ، على التوالي.

أظهر البحث التجريبي والتحليلي للالتواء الجانبي أن العينات التي كان لها مقطع عرضي وجهًا لوجه مع فجوة كانت أكثر ثباتًا ضد التشوهات الجانبية من المقطعين العرضيين الآخرين ، حيث نتج عنها دوران وانحراف جانبي أقل من العينات ذات المقطع العرضي التي تم لحام زوايا الوتر العلوي و السفلي من الخلف إلى الخلف بحوالي (25.1٪) و (30.7٪) على التوالي. كما نتج عنها انحراف دوران وانحراف جانبي أقل من العينات ذات المقطع العرضي التي تم لحام زوايا الاوتار العلوية و السفلية فيه وجها لوجه بدون فجوة بحوالي (7.3٪) و (11.2٪) على التوالي.

فيما يتعلق بمجموعة الروافد المركبة ذات الوترات الفولاذية المفتوحة ، أظهرت نتائج العمل التجريبي أن استخدام الخرسانة المسلحة بالألياف الفولاذية لصب بلاطة السقف أدى الى تحسين قدرة الروافد الفولاذية المركبة وصلابتها وليونتها قليلاً مقارنة مع استخدام البلاطة الخرسانية غير المسلحة بألياف. من ناحية أخرى ، فإن زيادة نسبة الطول / العمق للروافد الفولاذية المفتوحة الوترات لكلا النوعين من البلاطة الخرسانية تظهر انحرافات طبيعية للهطول بنسبة (31٪) أكبر من النسبة الاقل للطول/ العمق. بينما يؤدي تقليل نسبة الامتداد / العمق إلى تحسين سعة الحمل الأقصى بحدود (3.66٪) و (4.31٪) لبلاطة ذات خرسانة غير مسلحة بألياف وبلاطة ذات خرسانة مسلحة بألياف فولاذية ، على التوالي.

ان استخدام البلاطة الخرسانية في عينات الروافد المركبة ذات الوترات الفولاذية لأشكال المقاطع العرضية الثلاث للروافد الفولاذية الهجينة المفتوحة الوترات المستخدمة في هذه الدراسة، تم تحسين قابلية التحمل القصوى و الصلابة و المتانة وكذلك تم تحسين الاستقرار لأعضاء الوترات الداخلية و ضمن ليونة معقولة مقارنة مع نتائج عينات الروافد الفولاذية المفتوحة الوترات.

أخيرًا ، تم إجراء تحليل العناصر المحددة بالاستعانة ببرنامج ABAQUS لمحاكاة البرنامج التجريبي الذي تم تنفيذه في هذه الدراسة. وجد ان هناك حالة تقارب جيدة بين النتائج العملية و نتائج ABAQUS حيث كان الفرق الاعلى في قابلية التحمل النهائية اقل من 8% و 9.5% للروافد الفولاذية الهجينة مفتوحة الوترات و الروافد المركبة ذات الوترات الفولاذية المفتوحة على التوالي. بينما لم يتجاوز الاختلاف الاكبر في قيم الهطول عند الحمل الاقصى 10.72% لكلا المجموعتين. و كانت الاختلافات في تشوه الدوران والانحراف الجانبي للروافد الفولاذية الهجينة مفتوحة الوترات أقل من (9٪) و (6٪) على التوالي.